

# A highly stable UV clock laser

Von der QUEST-Leibniz-Forschungsschule der  
Gottfried Wilhelm Leibniz Universität Hannover  
zur Erlangung des Grades

Doktor der Naturwissenschaften  
Dr. rer. nat.

genehmigte Dissertation von

Benjamin Kraus, M.Sc.

2023

Referent: Prof. Dr. Piet O. Schmidt  
Koreferent: PD Dr. Christian Lisdat  
Tag der Promotion: 03.11.2023

# Abstract

Optical clocks are the most precise frequency measurement devices, with a systematic fractional frequency uncertainty as low as  $10^{-18}$ . While these clocks are typically operated in stationary laboratories, there is a growing interest in implementing transportable optical clocks. As part of this thesis, a transportable  $^{40}\text{Ca}^+ / ^{27}\text{Al}^+$  quantum logic clock is being developed. For spectroscopy of the  $^{27}\text{Al}^+$  clock transition from  $^1\text{S}_0$  to  $^3\text{P}_0$ , a highly stable UV laser system is required. This thesis focuses on the evaluation of a transportable and highly frequency stable UV laser system built for the  $^{40}\text{Ca}^+ / ^{27}\text{Al}^+$  clock. The laser system includes a highly frequency stable cavity designed for stabilizing the seed laser frequency and a system for quadrupling the laser frequency without introducing phase disturbances. The cavity consists of a Fabry-Pérot resonator, consisting of a 20 cm long spacer made from ultra-low expansion glass (ULE) with  $\text{Al}_{0.92}\text{Ga}_{0.08}\text{As}/\text{GaAs}$  mirror coatings on fused silica substrates, optically bonded to the spacer. The calculated thermal noise floor limit is approximately  $7\text{-}8 \times 10^{-16}$ . The laser is locked to the resonance frequency of the cavity using the Pound-Drever-Hall locking technique. A residual amplitude modulation (RAM) stabilization scheme is employed, and the fractional frequency instability limit due to RAM is evaluated. Optical properties such as finesse, linewidth, and birefringence line splitting of the cavity are measured. Additionally, the main sources of relative length change in the cavity are assessed, including vibration noise, photo-thermal noise, and photo-birefringence noise. These noise sources, including RAM, are found to be at or below the thermal noise limit. The cavity is temperature-stabilized using two passive and one active heat shield and is further isolated against temperature fluctuations. The remaining length changes of the cavity due to thermal expansion of the cavity spacer and thermal stress inside the heat shields is evaluated to be dominant over longer timescales. The frequency stability of the cavity is measured by phase comparison with a more stable reference cavity using an optical frequency comb. A fractional frequency instability, represented by the modified Allen deviation, of  $2 \times 10^{-16}$  is achieved. The seed laser frequency is quadrupled using a transportable and compact setup consisting of two single-pass second harmonic generation stages. The single-pass configuration enables phase stabilization of the seed light and UV light throughout the entire setup. The performance of the system is evaluated, demonstrating negligible phase distribution and sufficient UV output power for operating an optical  $^{27}\text{Al}^+$  clock. Furthermore, the current status of transportable  $^{40}\text{Ca}^+ / ^{27}\text{Al}^+$  ion clock is presented, including the physics package with the ion trap in a vacuum chamber, magnets and coils for magnetic field generation, optical paths for ion integration, and the imaging system all mounted on a breadboard.

Key Words: Transportable  $^{27}\text{Al}^+$  ion clock, ultra-stable optical cavity, SHG for frequency quadrupling





# Contents

<b>1</b>	<b>Introduction</b>	<b>1</b>
<b>2</b>	<b>Optical clocks</b>	<b>5</b>
2.1	Concept of optical ion clocks . . . . .	5
2.2	Characterisation of frequency stability . . . . .	6
2.2.1	Allan deviation . . . . .	6
2.2.2	Statistical and systematic uncertainties of optical clocks . . . . .	9
2.3	An optical $^{40}\text{Ca}^+ / ^{27}\text{Al}^+$ clock using quantum logic spectroscopy . . . . .	15
<b>3</b>	<b>A transportable ultra-stable reference cavity</b>	<b>19</b>
3.1	Theoretical description . . . . .	19
3.1.1	Theory of optical cavities . . . . .	19
3.1.2	Pound Drever Hall stabilization locking scheme . . . . .	21
3.1.3	Residual amplitude modulation and stabilization . . . . .	23
3.1.4	Interferometric optical path length stabilization . . . . .	25
3.1.5	Frequency comparison via optical comb . . . . .	26
3.1.6	Frequency noise sources . . . . .	28
3.2	Setup of the reference cavity . . . . .	36
3.2.1	Design of the stabilization cavity . . . . .	36
3.2.2	Optical setup . . . . .	39
3.2.3	Integration into a standard 19-inch rack . . . . .	44
3.3	Characterisation of the stabilization cavity . . . . .	45
3.3.1	Finesse, cavity linewidth and birefringence . . . . .	45
3.3.2	Vibration sensitivity and vibration noise limit . . . . .	46
3.3.3	Photo-thermal and photo-birefringence noise . . . . .	49
3.3.4	RAM stabilization limit . . . . .	59
3.3.5	Temperature stabilization . . . . .	62
3.3.6	Frequency instability of the laser . . . . .	71
<b>4</b>	<b>Generation of phase stable laser light at 267.4 nm</b>	<b>75</b>
4.1	Concept of frequency quadrupling setup . . . . .	75
4.2	Second harmonic generation stages . . . . .	77
4.2.1	Second harmonic generation theory . . . . .	77
4.2.2	Nonlinear crystals selection . . . . .	80
4.2.3	Crystal temperature controlling system . . . . .	81
4.3	Optical setup . . . . .	83
4.3.1	First SHG stage from 1069.6 nm to 534.8 nm . . . . .	86
4.3.2	Second SHG stage 534.8 nm to 267.4 nm . . . . .	87
4.3.3	Interferometric phase stabilization . . . . .	88
4.4	Characterization of the frequency quadrupling setup . . . . .	89
4.4.1	Second harmonic generation efficiency . . . . .	89
4.4.2	Phase stability of the generated UV light . . . . .	95
4.5	Rack integration of the clock laser system . . . . .	101
4.6	A simplified frequency quadrupling system . . . . .	103

<b>5</b>	<b>Clock setup</b>	<b>107</b>
5.1	Vacuum system . . . . .	107
5.2	The ion trap . . . . .	108
5.3	Magnetic field generation . . . . .	109
5.4	Ablation and ionization calcium and aluminium . . . . .	109
5.5	Integration of the physics package . . . . .	111
5.6	The imaging system . . . . .	116
<b>6</b>	<b>Discussion and conclusion</b>	<b>117</b>

# List of Figures

2.1	Concept of an optical clock . . . . .	6
2.2	Reduced level diagram of $^{27}\text{Al}^+$ . . . . .	15
2.3	Reduced level diagram of $^{40}\text{Ca}^+$ . . . . .	16
2.4	Quantum logic spectroscopy . . . . .	17
3.1	PDH locking technique . . . . .	23
3.2	Ram stabilization scheme . . . . .	25
3.3	Interferometric optical path length stabilization . . . . .	26
3.4	Frequency comparison between two laser . . . . .	27
3.5	Noise sources in optical cavities . . . . .	30
3.6	Thermal noise limit . . . . .	33
3.7	Setup of the cavity . . . . .	37
3.8	Heat shields of the cavity . . . . .	38
3.9	Optical distribution breadboard . . . . .	40
3.10	Schematic drawing of the optical setup . . . . .	41
3.11	Frequency instability of the optical paths . . . . .	43
3.12	Optical finesse measurement of the cavity . . . . .	46
3.13	Flexible suspension of the cavity . . . . .	47
3.14	Vibrations sensitivity measurement . . . . .	48
3.15	Vibration noise on the passive table . . . . .	50
3.16	Vibration noise on the active table . . . . .	51
3.17	Vibration noise on the active table inside a rack . . . . .	52
3.18	Sensitivity to optical power modulation . . . . .	52
3.19	Displacement factor as a function of modulation frequency . . . . .	53
3.20	Frequency response to a step function in optical power . . . . .	55
3.21	Photo-thermal effect and photo-birefringence-effect . . . . .	56
3.22	Displacement factor as a function of optical power . . . . .	57
3.23	Photo-thermal noise induced frequency instability . . . . .	58
3.24	RAM induced frequency instability . . . . .	61
3.25	CTE zero crossing Temperature . . . . .	64
3.26	Thermalization of the cavity . . . . .	68
3.27	Frequency instability due to thermal expansion of the cavity . . . . .	69
3.28	Immediate frequency response due to temperature changes . . . . .	71
3.29	Frequency instability due to thermal stress . . . . .	72
3.30	Spacer aging drift . . . . .	72
3.31	Frequency instability of the laser . . . . .	74
4.1	Setup of the frequency quadrupling system . . . . .	76
4.2	3D drawing of first crystal oven . . . . .	84
4.3	Thermalization time of the crystal ovens . . . . .	85
4.4	Drawing of the second crystal oven . . . . .	85
4.5	Optical scheme of the frequency quadrupling system . . . . .	86
4.6	Temperature dependency of the SHG output power . . . . .	90
4.7	Phase-matching temperature for different pump light power . . . . .	92
4.8	SHG efficiency of both stages . . . . .	93
4.9	Long term UV light power stability . . . . .	94

4.10	Schematic drawing of the phase stability measurement . . . . .	99
4.11	Frequency instability of the frequency quadrupling system . . . . .	100
4.12	Transportable clock laser system . . . . .	102
4.13	3D drawing of the miniaturized frequency quadrupling system . . . . .	104
4.14	Miniaturized frequency quadrupling system . . . . .	105
5.1	Vacuum chamber and ion trap . . . . .	108
5.2	Ablation target and the ion trap . . . . .	110
5.3	Two step ionization process . . . . .	111
5.4	Optical beam path for ion manipulation . . . . .	112
5.5	Imaging system and mounting of the physics package. . . . .	114
5.6	Rack integrated physics package . . . . .	115

## List of Tables

2.1	Power-law scaling of different noise sources. . . . .	8
2.2	Systematic uncertainty budget of different optical clocks. . . . .	10
3.1	Vibration sensitivity of different cavities. . . . .	49
4.1	Key crystal parameters. . . . .	81
4.2	Key parameters of the crystal ovens. . . . .	83

# Acronyms

Acronym	Meaning
AC	alternating current
AlN	aluminum nitride
AOM	acousto-optic modulator
AR	anti reflection
BBO	beta barium borate
BBR	black-body radiation
BGC	background gas collision
BSB	blue sideband transition
CTE	coefficient of thermal expansion
DC	direct current
DDS	direct digital synthesis
DKDP	potassium dideuterium phosphate
EAV	estimated Allan deviation
EMAV	estimated modified Allan deviation
EMM	excess micromotion
EOM	electro-optic modulator
FDA	frequency distribution amplifier
FHG	fourth harmonic generation
FS	fused silica
FHWM	full width half maximum
IR	infrared
NA	numerical aperture
NEG	non-evaporative getter (pump)
MgO:PPLN	magnesium oxide-doped periodically-poled lithium niobate
PBS	polarizing beam splitter
PD	photodiode
PDH	Pound-Drever-Hall
PID	proportional-differential-integral controller
PLL	phase-locked loop
PMT	photomultiplier tube
PPLN	periodically-poled lithium niobate
PSD	power spectral density
PT	photo-thermal
PTE	photo-thermoelastic
PTR	photo-thermorefractive
QPN	quantum projection noise
RAM	residual amplitude modulation
rf	radio-frequency
RSB	red sideband transition
SHG	second-harmonic generation
TE	thermoelastic
TO	thermooptic

<b>Acronym</b>	<b>Meaning</b>
TR	thermorefractive
ULE	ultra low expansion
UV	ultraviolet

---

# Symbols

Symbols	Description	Unit
$A$	area	m
$B$	magnetic field	$\frac{\text{kg}}{\text{A}\cdot\text{s}^2}$
$C$	heat capacity	$\frac{\text{kg}}{\text{s}^2\text{Km}}$
$c$	speed of light	$\frac{\text{m}}{\text{s}}$
$d$	distance, length	m
$d_{ij}$	component of nonlinear dielectric susceptibility tensor	$\frac{\text{A}\cdot\text{s}}{\text{V}^2}$
$E$	electric field	V/m
$F$	finesse	1
$f$	frequency, Fourier frequency	Hz
$f$	focal length	m
$h$	Planck constant	$\frac{\text{kg}\cdot\text{m}^2}{\text{s}}$
$I$	intensity	$\frac{\text{kg}}{\text{s}^3}$
$k$	wavenumber	$\frac{1}{\text{m}}$
$k$	thermal conductivity	$\frac{\text{m}\cdot\text{kgm}}{\text{K}\cdot\text{s}^3}$
$l$	length	m
$n$	refractive index	1
$P$	power	$\frac{\text{kgm}^2}{\text{s}^3}$
$p$	pressure	Pa
$q$	heat flux	$\frac{\text{kg}}{\text{s}^3}$
$r$	reflectivity	1
$r$	radius	m
$S_x$	power spectral density of displacement	$\frac{\text{m}^2}{\text{Hz}}$
$S_y$	power spectral density of fractional frequency	$\frac{1}{\text{Hz}}$
$S_v$	vibration sensitivity	$\frac{1}{\text{g}}$
$T$	temperature	K
$t, T$	transmission	1
$t$	time	s
$U$	voltage	V
$Y$	young's modulus	Pa
$X$	displacement factor	$\frac{\text{s}^3}{\text{kgm}}$
$x$	Cartesian coordinates	m
$y$	Cartesian coordinates	m
$z$	Cartesian coordinates	m
$\epsilon$	emissivity	1
$\alpha$	coefficient of thermal expansion	$\frac{1}{\text{K}}$
$\gamma$	walk-off angle	rad.
$\Delta\dots$	... difference	
$\delta\dots$	... fluctuation	
$\kappa$	SHG conversion coefficient	$\frac{\% \text{s}^3}{\text{kgm}^2}$
$\kappa_B$	Boltzmann constant	$\frac{\text{kgm}^2}{\text{s}^2\text{K}}$



Symbols	Description	Unit
$\lambda$	wavelength	m
$\nu$	frequency	Hz
$\rho$	density	$\frac{\text{kg}}{\text{m}^3}$
$\sigma$	Possion ratio	1
$\sigma_{SB}$	Stefan-Boltzmann constant	$\frac{\text{kg}}{\text{s}^3\text{K}^4}$
$\tau$	averaging time, time constant	s
$\Phi$	mechanical loss factor	1
$\phi$	phase angle	rad.
$\Omega$	angular frequency	Hz
$\omega$	focus beam waist	m

# 1 Introduction

In our everyday life, time is an essential concept that guides our daily activities and facilitates the synchronization of various technological systems. Time is also used to describe any physical process and is measured with clocks. Clocks rely on oscillations with well-defined frequencies, which serve as a standard for comparison with the process of interest. Over time, the precision of measuring time has improved through the development of new technologies. Nowadays, optical atomic clocks provide a systematic fractional frequency uncertainty in the low  $10^{-18}$  regime [1–9]. The unit second has the smallest uncertainty in relative value of all quantities of the in the international system of units (SI) [10], while it is still defined as 9,192,631,770 oscillation periods of the clock transition of  $^{133}\text{Cs}$  [11–14]. Optical clocks outperform the caesium fountain clocks by two orders of magnitude in terms of systematic and statistical fractional frequency uncertainty. Therefore these optical clocks are strong candidates for the re-definition of the second [15–18].

Various types of optical clocks based on different clock atoms or ions have been reported or proposed. Examples include optical clocks using  $^{171}\text{Yb}$  [5, 19],  $^{174}\text{Yb}$  [20],  $^{87}\text{Sr}$  [7, 8], and  $^{199}\text{Hg}$  [21] as clock atoms. Single-ion optical clocks have been reported using ion species such as  $^{27}\text{Al}^+$  [22],  $^{115}\text{In}^+$  [23],  $^{199}\text{Hg}^+$  [24],  $^{40}\text{Ba}^+$  [25],  $^{88}\text{Sr}^+$  [26],  $^{40}\text{Ca}^+$  [27],  $^{176}\text{Lu}^+$  [28] and  $^{171}\text{Yb}^+$  [29]. Additionally, multi-ion optical clocks based on  $^{115}\text{In}^+$  [23, 30, 31] and  $^{40}\text{Ca}^+$  [32] have been developed, while multi-ion clocks with other ions have also been investigated [31–36]. Moreover, optical ion clocks using highly charged  $^{40}\text{Ar}^{13+}$  ions have been developed [37–39]. Another category of optical clocks are nuclear clocks that utilize a laser-accessible transition between two states of the nucleus instead of an electric transition.  $^{229}\text{Th}$  is a promising candidates in this category [40–42].

Due to their high accuracy, optical clocks have applications beyond timekeeping. They are used for tests of fundamental physics, such as the search for variations of fundamental constants [24, 43–47], detection of violations of Lorentz invariance [4, 48], exploration of dark matter [49–54], and testing Einstein’s theories of special and general relativity [4, 55]. The frequency shift of a clock is influenced by the gravitational potential, as predicted by general relativity. This effect can be used in reverse to measure the height relative to the geoid with an optical clock [56–59] or detect time-variable components of the gravity potential field [60]. This technique is particularly useful for height difference measurements between locations without a direct line of sight. To conduct height measurements at a specific point of interest, a transportable optical clock is required. The frequency of this clock is compared to a reference clock at a reference point either via a fibre link [61–65] or via a satellite link [66]. Different groups have developed transportable optical clocks [7, 67–73], and measurement campaigns for height measurements have been reported [5, 9, 27, 74–76]. The most accurate transportable clocks have a frequency uncertainty in the mid  $10^{-18}$  regime [7, 9], but they have not yet reached the equivalent frequency uncertainty of the best laboratory-based optical clocks. Achieving a height resolution of 1 cm in satellite-based geoid measurements is already possible, although the lateral spatial resolution of this

method is limited [77, 78]. To achieve height measurements with the same resolution, an optical clock with a  $10^{-18}$  uncertainty is required.

A promising candidate for a transportable optical clock with a  $10^{-18}$  uncertainty is the  $^{27}\text{Al}^+$  ion clock. This is due to the  $^{27}\text{Al}^+$  ion's resilience against external perturbations. Laboratory-based  $^{27}\text{Al}^+$  ion clocks with an uncertainty of approximately  $10^{-18}$  have already been developed [3, 79–81]. However, one limitation of  $^{27}\text{Al}^+$  is the absence of a suitable transition for laser cooling and state readout. To overcome this limitation, a co-trapped ion of a different species, for example  $^{40}\text{Ca}^+$ , is employed for sympathetic cooling, and quantum logic spectroscopy [82] is used for probing the clock transition of  $^{27}\text{Al}^+$ . The work presented in this thesis is part of our effort in developing such a transportable  $^{40}\text{Ca}^+ / ^{27}\text{Al}^+$  quantum logic clock for measurements of geopotential height difference.

Optical clocks demand stringent phase stability requirements to effectively probe narrow clock transitions, enabling long interrogation times and reducing statistical uncertainties [83]. This is especially crucial for single or few-ion optical clocks, as their limited signal-to-noise ratio requires lifetime-limited interrogation times to achieve competitive statistical uncertainties [84–87]. Achieving long coherence times for clock interrogation light can be accomplished by stabilizing the laser frequency to ultra-stable cavities [88–107], which can provide coherence times exceeding 11 seconds [108]. Furthermore, several schemes have been devised to extend the coherence time of clock interrogation light even further by employing multiple ensembles of clocks [109–115].

However, many optical clock transitions fall within the ultraviolet (UV) spectral range. For instance, the  $^{27}\text{Al}^+$  ion quantum logic optical clock operates at a clock transition wavelength of 267 nm [3, 24, 55, 116–120], the  $^{199}\text{Hg}^+$  ion clock at 282 nm [24, 121, 122], the  $^{115}\text{In}^+$  ion clock at 237 nm [123–125], and the neutral atom mercury lattice clock at 266 nm [21, 126–128]. Unfortunately, ultra-stable cavities are not available in the UV regime due to significant UV light absorption in mirrors, which hampers cavity performance. As an alternative, ultra-stable cavities can be employed to stabilize an infrared (IR) seed laser. Subsequently, UV laser light is typically generated through fourth harmonic generation (FHG) of the IR laser. A commonly used method for FHG involves twofold second harmonic generation (SHG) in non-linear media, often employing pump-beam power enhancement within a cavity to maximize efficiency [129–144]. However, effective phase stabilization is required before, after, and between the SHG units, including active elements like power amplifiers. These additional elements significantly increase the complexity of the experimental setup [145]. A novel approach demonstrated here offers a twofold single-pass SHG method with a comprehensive phase stabilization scheme across the entire optical path [146]. This approach provides phase-stable UV light and substantially reduces the complexity of the system.

This thesis focuses on the development of a highly stable UV clock laser system for a transportable optical  $^{40}\text{Ca}^+ / ^{27}\text{Al}^+$  quantum logic clock. The system comprises a seed laser operating in the infrared (IR) range, which is frequency stabilized using a highly

stable cavity. Additionally, an optical setup is employed for frequency quadrupling while preserving the phase relationship of the laser light.

The structure of this thesis is organized as follows:

Chapter 2 provides an explanation of the fundamental principle of an optical clock. A theoretical concept for describing the statistical uncertainty of frequency measurements is introduced. The chapter also discusses systematic effects that can cause frequency shifts of the clock transition. A comparison of the systematic uncertainties of different optical clocks is presented, along with a motivation for using  $^{27}\text{Al}^+$  as a clock ion. The level diagrams of the  $^{27}\text{Al}^+$  clock ion and  $^{40}\text{Ca}^+$  as the co-trapped logic ion are shown, and an explanation of quantum logic spectroscopy is provided.

Chapter 3 begins with a theoretical description of optical cavities, followed by an explanation of the Pound Drever Hall locking technique. Residual amplitude modulation as a source of noise that limits the frequency stability of a laser locked to the cavity resonance frequency is discussed. An interferometric optical path length stabilization scheme is presented to prevent phase distribution of the laser light in the optical setups. The chapter includes a comparison method of the laser frequency to a second reference cavity using an optical frequency comb. An overview of the cavity design and the optical setup is given, including breadboards for light distribution and optical path length stabilization, Pound Drever Hall locking, and optical intensity stabilization. The setup is designed for transportability and is integrated into a standard 19-inch rack. Measurements are performed to characterize the finesse, cavity linewidth, birefringence, and vibration sensitivity of the cavity. Various sources of frequency noise for a highly stable optical cavity are discussed, including photon noise, electronic noise, vibration noise, thermal noise, photo-thermal noise, pressure fluctuations, photo-birefringence noise, and frequency drifts due to temperature changes and spacer aging. Finally, the frequency instability of the stabilized laser is evaluated through a frequency comparison measurement with a second reference cavity using an optical frequency comb.

Chapter 4 presents an optical setup for frequency quadrupling an infrared (IR) laser to the ultraviolet (UV) regime. The setup consists of two single-pass frequency doubling stages that use second harmonic generation in nonlinear crystals. The concept of second harmonic generation and the selection of appropriate crystals are discussed. The chapter covers the characterization of the UV light output power and the instability of the phase relationship between the fundamental light and the generated UV light. Similar to the stabilization cavity setup described earlier, the frequency quadrupling system is also integrated into the same standard 19-inch rack, along with the laser source and all necessary electric parts, to create a transportable standalone UV clock laser system for a transportable optical  $^{27}\text{Al}^+$  ion clock.

Chapter 5 describes the setup of a transportable optical  $^{27}\text{Al}^+$  clock. It includes the vacuum system, ion trap, magnetic field generation using permanent magnets and compensation coils, and a target for ablation of Ca and Al atoms. These components are placed on an aluminum breadboard inside a standard 19-inch rack. The breadboard

also contains the optical setup for guiding all necessary laser beams for ionizing the Ca and Al atoms, laser cooling the  $^{40}\text{Ca}^+$  ions, and manipulation and interrogation of the electronic states of  $^{40}\text{Ca}^+$  and  $^{27}\text{Al}^+$ . Additionally, the chapter covers the installation of an imaging system for state detection on the bottom of the breadboard.

In Chapter 6 the thesis concludes with a discussion and conclusion of the presented results. It provides a brief outlook on the next steps required to complete the clock setup.

## 2 Optical clocks

In this chapter, the basic concept of optical clocks is presented. Additionally, the statistical and systematic frequency uncertainties of optical clocks is discussed. As a conclusion to this discussion, a motivation for the development of a highly frequency stable clock laser system is provided. Due to its high clock frequency and low sensitivity to external perturbations,  $^{27}\text{Al}^+$  is especially well suited for an optical clock. However, there is no accessible transition for detecting the state of the ion and for cooling the  $^{27}\text{Al}^+$  ion. To address this limitation,  $^{40}\text{Ca}^+$  is used as a co-trapped ion, which can be laser cooled and used for sympathetic cooling of the  $^{27}\text{Al}^+$  ion. Quantum logic spectroscopy can be employed for the readout of the  $^{27}\text{Al}^+$  state, transferring the information to the  $^{40}\text{Ca}^+$  ion, where efficient detection is accomplished.

### 2.1 Concept of optical ion clocks

The principle of every clock is based on counting the number of oscillations in a physical system. These oscillations can be derived from various sources, such as astronomical events like the rotation around the sun (year) or the rotation of the Earth (day), the swinging of a pendulum in a mechanical clock (second), or the electric oscillation of a quartz crystal (microseconds). Another method involves utilizing atomic references, where the transition between two precisely defined atomic energy levels is measured. This is the case for  $^{133}\text{Cs}$  fountain clocks, which currently define the SI second as consisting of 9,192,631,770 oscillation periods. As the oscillation frequency increases, the systematic uncertainty of clocks typically decreases. The most advanced  $^{133}\text{Cs}$  fountain clocks achieve a systematic uncertainty in the range of  $10^{-16}$  [11–14]. Optical clocks, similar to other atomic clocks, operate by examining the transition frequency between two well-defined energy levels of an atom. However, in optical clocks, this transition is probed using light instead of an RF (radio frequency) field, resulting in an oscillation frequency several orders of magnitude higher and thus allow lower statistical and systematic uncertainties of the measured fractional frequency.

Figure 2.1 illustrates the fundamental concept of an optical clock [83, 147]. In neutral atom lattice clocks [7, 8, 45, 67, 148], typically tens or hundreds of thousands of atoms are trapped using the potential created by an optical lattice. In optical ion clocks [1, 3, 22–27, 29, 46, 48, 123, 149, 150], one or more ions are trapped using an ion trap, such as a quadrupole trap. Laser cooling [151–155] is employed to cool the atoms or ions, to ensure effective trapping and to suppress the atoms or ions motion and hence the Doppler shift. The narrow clock transition is probed using a frequency-stabilized laser, and an external stabilization cavity is typically utilized for frequency stabilization [90, 156–158]. Any deviation of the laser frequency from the reference frequency provided by the clock transition is corrected through a feedback loop and frequency shifter integrated into the optical path of the laser beam. Since the oscillations of optical frequencies are too rapid for electronic devices to count, an optical frequency comb [159, 160] is employed to convert the optical oscillation into an RF signal, which can be used as a clock signal and can be compared to other clocks [74]. Furthermore, the optical comb allows for the direct comparison of two optical clocks

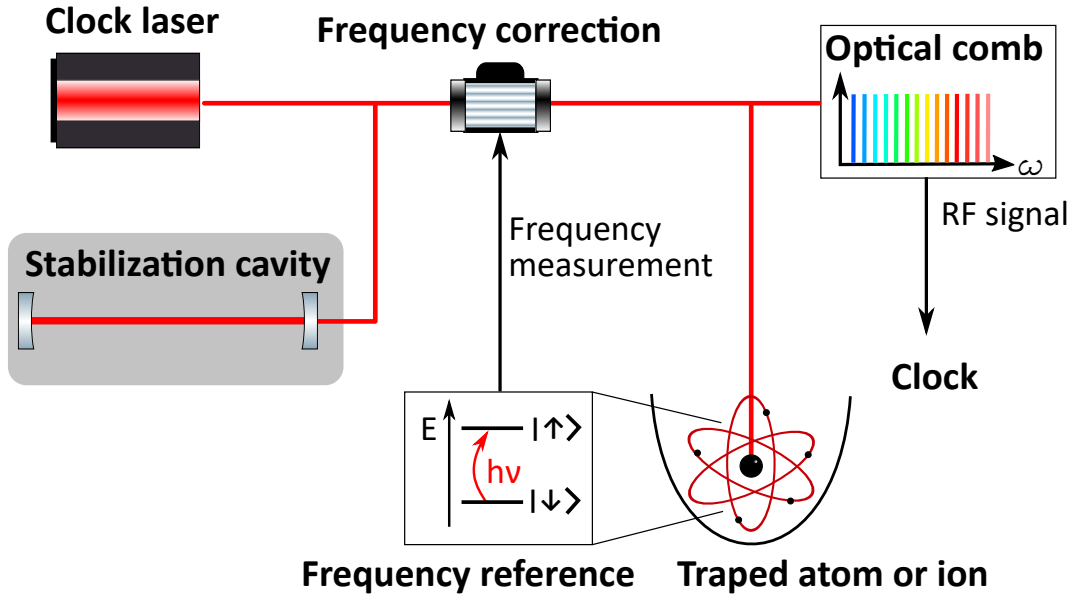


Figure 2.1: Concept of an optical clock. The clock laser serves the purpose of probing the internal state of a trapped atom or ion. The measurement feedback obtained from this interrogation is used to adjust the frequency of the clock laser. Stabilization of the clock laser with an ultra-stable cavity is necessary to enable long coherence times for interrogation approaching the lifetime limit. The frequency of the laser light can be translated into an RF frequency using an optical comb. Adapted from [79].

with different wavelengths of the clock laser [24, 29, 120, 127].

## 2.2 Characterisation of frequency stability

Typically, the frequency stability is the most important value for a local resonator. This is also true for optical clocks in terms of statistical uncertainty of the measured frequency. The Allan deviation or modified Allan deviation serves as a useful tool for describing frequency stability. Furthermore, it is crucial to assess the systematic uncertainties of each optical clock in order to provide an accurate estimation of the clock's measurement accuracy. A more comprehensive explanation of the theory behind frequency standards and clocks can be found in Riehle et al. [161].

### 2.2.1 Allan deviation

When assessing the statistical uncertainty of a measurement, the standard deviation is commonly employed. However, when evaluating the stability of a local resonator, the standard deviation is not the ideal measure because consecutive frequency samples, denoted as  $v_i$  and  $v_{i+1}$ , are generally not independent of each other. The standard deviation for  $N$  measurements is mathematically defined as:

$$\sigma_{std,v} = \sqrt{\frac{1}{N-1} \sum_{i=1}^N (v_i - \bar{v})^2}, \quad (1)$$

where  $\bar{v}$  represents the mean frequency. However, in cases where the noise in the frequency samples  $v_i$  follows a power spectral density (PSD) scaling of  $f^a$ , with  $a \leq -1$ , the standard deviation does not approach a specific value. In resonators, including optical clocks, flicker frequency noise characterized by a scaling of  $f^a$  with  $a = -1$  is a common source of noise. In such scenarios, an alternative definition is required to characterize the stability of the local oscillator. This can be achieved by employing the M-sample variance, which is defined as follows:

$$\sigma_y^2(M, T, \tau) = \frac{1}{M-1} \left\{ \sum_{i=0}^{M-1} \bar{v}_i^2 - \frac{1}{M} \left[ \sum_{i=0}^{M-1} \bar{v}_i \right]^2 \right\}, \quad (2)$$

while  $\bar{v}_i$  is given by the average frequency a frequency sample within the average time  $\tau$ :

$$\bar{v}_i = \frac{1}{\tau} \int_{t_i}^{t_i+\tau} v(t) dt \quad (3)$$

The M-sample variance with  $M=2$  and without dead time  $T = \tau$  is called Allan variance  $\sigma_v^2(\tau)$  [162] and can be written as the expectation value of the difference between two consecutive frequency samples:

$$\sigma_v^2(\tau) = \frac{1}{2} \langle (\bar{v}_{n+1} - \bar{v}_n)^2 \rangle, \quad (4)$$

The Allan deviation  $\sigma_v(\tau) = \sqrt{\sigma_v^2(\tau)}$  can be calculated from  $N$  measured frequency samples by:

$$\sigma_v(\tau) = \sqrt{\frac{1}{2(N-1)} \sum_{i=1}^N (\bar{v}_i - \bar{v}_{i+1})^2}. \quad (5)$$

The Allan deviation is a good choice to describe the frequency stability of an oscillator, as it converges to the expectation value with increasing sample number.

The same method can be applied to the fractional frequency  $y = \frac{v}{v_0}$ , where  $v_0$  is the frequency of the local oscillator:

$$\sigma_y = \frac{\sigma_v}{v_0}. \quad (6)$$

Also the PSD can be normalized by:

$$S_y(f) = \frac{1}{v_0^2} S_v(f) \quad (7)$$

The PSD can be classified by known noise models that are functions of the Fourier



Table 2.1: Power-law scaling of different noise sources (PN= phase noise; FN=frequency noise).

Noise Type/ Analyse Method	White PN	Flicker PN	White FN	Flicker FN	Random walk FN
$S_y(f)$	$h_2 f^2$	$h_1 f^1$	$h_0 f^0$	$h_{-1} f^{-1}$	$h_{-2} f^{-2}$
$\sigma_y^2(\tau)$	$K_2 h_2 \tau^{-2}$	$K_1 h_1 \tau^{-2}$	$K_0 h_0 \tau^{-1}$	$K_{-1} h_{-1} \tau^0$	$K_{-2} h_{-2} \tau^1$
mod $\sigma_y^2(\tau)$	$Km_2 h_2 \tau^{-3}$	$Km_1 h_1 \tau^{-2}$	$Km_0 h_0 \tau^{-1}$	$Km_{-1} h_{-1} \tau^0$	$Km_{-2} h_{-2} \tau^1$

frequency to the power of an integer  $a$  and coefficients  $h_a$ :

$$S_y(f) = \sum_{a=-2}^{a=2} h_a f^a. \quad (8)$$

Similar to the PSD also the Allan variance can be used to identify the dominant noise source of the system. Table 2.1 shows the power law scaling of  $S_y(f)$ ,  $\sigma_y^2(\tau)$ , and the modified Allan variance mod  $\sigma_y^2(\tau)$  with coefficients  $K$  and  $Km$ . However, it can not be differentiated between flicker phase noise and white phase noise by the behaviour of the Allan variance. Therefore, typically the modified Allan variance mod  $\sigma_y^2(\tau)$  is used, where a weighting function for averaging of the frequency samples is applied

$$\text{mod } \sigma_y^2(\tau) = \frac{1}{2} \left\langle \left[ \frac{1}{n} \sum_{i=1}^n \left( \frac{1}{n} \sum_{k=1}^n \bar{y}_{i+k+n} - \frac{1}{n} \sum_{k=1}^n \bar{y}_{i+k} \right) \right]^2 \right\rangle. \quad (9)$$

For a measurement with  $N$  frequency samples the modified Allen deviation can be calculated by:

$$\text{mod } \sigma_y(\tau) = \sqrt{\frac{1}{2m^4(N-3m+2)} \sum_{j=1}^{N-3m+2} \left[ \sum_{i=j}^{j+m-1} \left( \sum_{k=i}^{i+m-1} [\bar{y}_{k+m} - \bar{y}_k] \right) \right]^2}. \quad (10)$$

For the modified Allan variance flicker phase noise shows a  $\tau^{-2}$  behaviour and white phase noise shows a  $\tau^{-3}$  behaviour. In Table the behavior of the PSD, the Allan variance, and the modified Allan variance for different noise sources is shown.

The conversion between PSD and Allan variance and between PSD and modified Allan variance is given by [163]:

$$\sigma_y^2(\tau) = 2 \int_0^\infty S_y(f) \frac{(\sin \pi \tau f)^4}{(\pi \tau f)^4} df \quad (11)$$

and

$$\text{mod } \sigma_y^2(\tau) = 2 \int_0^\infty S_y(f) \frac{(\sin \pi \tau f)^6}{(\pi n \tau f)^2 (\sin \pi \tau_0 f)^2} df. \quad (12)$$

The confidence interval of the estimated Allan variance EAV and the estimated

modified Allan variance EMAV does not only depend on the number of taken sample, it also depends on the dominant frequency noise source [164–166]. As the noise source is often not known, the confidence interval of the Allan variance calculated by  $m$  independent frequency samples is often approximated by:

$$\sigma(\text{EAV}) = \frac{1}{2} \sqrt{\frac{\text{EAV}}{m}} \quad (13)$$

$$\sigma(\text{EMAV}) = \frac{1}{2} \sqrt{\frac{3 \text{EMAV}}{m}} \quad (14)$$

The use of an overlapping Allan deviation and modified Allan deviation calculation method can further improve the confidence factor. In the following an overlapping Allan deviation calculation method is used. For the confidence interval either the approximation in equation 14 is chosen or the calculation methods of [167] is used.

### 2.2.2 Statistical and systematic uncertainties of optical clocks

The Allan deviation is a useful tool for assessing the statistical uncertainty in frequency measurements. In the case of optical clocks, the frequency of the clock laser is measured when it is stabilized on the spectroscopy signal of the clock transition. However, each individual interrogation of the atomic state provides only one bit of information by projecting the probability distribution onto one of the two eigenstates. This statistical uncertainty is known as quantum projection noise (QPN) and it limits the statistical frequency stability of an optical clock. For  $N$  uncorrelated atoms, the Allan deviation of the QPN is given by the following equation [161]:

$$\sigma(\tau) = \frac{1}{K} \frac{1}{2\pi t_{\text{int}} \nu_0} \sqrt{\frac{t_{\text{cy}}}{N\tau}}, \quad (15)$$

here  $\nu_0$  represents the transition frequency. The QPN depends on the interrogation time  $t_{\text{int}}$  of the transition and the cycle time  $t_{\text{cy}} = t_{\text{int}} + t_{\text{dead}}$ , which includes the interrogation time and the dead time between measurements. The factor  $K \lesssim 1$  is dependent on the atom interrogation method used. For Rabi interrogation,  $K = 0.60386$ , while for Ramsey interrogation with a long dark time,  $K \approx 1$  [168–170]. This indicates that Ramsey interrogation is more favorable than Rabi interrogation in terms of achieving lower QPN. Furthermore, the QPN scales down as  $\sqrt{t_{\text{int}}}$ . In particular, for single ion clocks, a long interrogation time is necessary to achieve a sufficiently low QPN and reduce the required average time to reach the systematic uncertainty limit. However, the interrogation time is often limited by the coherence time  $t_{\text{coh}}$  of the clock laser system, defined as [84, 108, 171, 172]:

$$\frac{1 \text{rad}}{2\pi t_{\text{coh}}} \stackrel{!}{=} \sigma_{y, \text{Laser}}(t_{\text{coh}}). \quad (16)$$

In conclusion, frequency stabilization of the clock laser to an ultra-stable cavity is essential to enable long interrogation times and reducing the QPN.

Table 2.2: Systematic uncertainty budget of different optical clocks. Fractional frequency shifts  $\frac{\delta\nu}{\nu_0}$  and corresponding systematic uncertainty  $\sigma(\frac{\delta\nu}{\nu_0})$  in  $10^{-18}$ . (BBR=black body radiation, BGC=background gas collision).

	$^{87}\text{Sr}$		$^{171}\text{Yb}$		$^{171}\text{Yr}^+$		$^{27}\text{Al}^+$	
Reference	[8]		[5]		[4]		[3]	
shift	$\frac{\delta\nu}{\nu_0}$	$\sigma(\frac{\delta\nu}{\nu_0})$	$\frac{\delta\nu}{\nu_0}$	$\sigma(\frac{\delta\nu}{\nu_0})$	$\frac{\delta\nu}{\nu_0}$	$\sigma(\frac{\delta\nu}{\nu_0})$	$\frac{\delta\nu}{\nu_0}$	$\sigma(\frac{\delta\nu}{\nu_0})$
BBR environment (atomic)	-4974 (0)	0.2 (1.5)	-2361	0.9	-70.5	1.8	-3.05	0.42
BGC	-3.7	0.4	-5.5	0.5	0.5	0.5	-0.06	0.24
2 <sup>nd</sup> -order Zeeman	-176.9	0.2	-118	0.2	-10.4	0.2	-924.2	0.37
AC-Stark shift (lattice laser)	0 (-21.3)	< 0.1 (1.2)	0.02 (-1.5)	0.01 (0.8)	0	0.8	0	0.2
DC Stark shift	0	0.3	0	< 0.07	-0.8	0.6		
Servo	0	0.2	0.03	0.05	0	0.2		
AOM chirp	0	< 0.1	0	< 0.1			0	< 0.1
cold collision	-12.3	0.4	-0.21	0.07				
1 <sup>st</sup> -order Doppler							0	0.22
2 <sup>nd</sup> -order Doppler (EMM)	0	< 0.1	0)	< 0.02	-2.3	1.5	-1.73 (-4.58)	0.29 (0.59)
Total	-5188	2	-2487	1.4	-90.2	2.7	-933.6	0.94

Moreover, the clock transition has a finite lifetime determined by the linewidth of the clock transition, denoted as  $\delta\nu$ . This introduces a fundamental limitation on the interrogation time and consequently imposes the quantum projection noise limit:

$$\sigma(\tau) = \frac{1}{K} \frac{\delta\nu}{\nu_0} \sqrt{\frac{t_{\text{cy}}}{N\tau}}. \quad (17)$$

Another source of noise is directly associated with the dead time  $t_{\text{dead}}$ , between clock interrogations. During this period, the clock laser operates without feedback from the atom, allowing for potential frequency drift. This effect is known as the Dick-effect [168, 169, 173]. For effective stabilization of the clock laser to the the atomic resonance several interrogation cycles of the clock transition are necessary. To enable this and to mitigate the influence of the Dick effect the stability of the ultra-stable cavity needs to hold over multiple interrogation cycles

After a sufficiently long measuring time the uncertainty of an optical clock is given by the systematic uncertainties. In Table 2.2 the occurring drifts and the systematic uncertainties budget of some of the best optical clock are shown. The small black body radiation shift of  $^{27}\text{Al}^+$  and the low total systematic uncertainty gives a motivation for building an  $^{27}\text{Al}^+$  ion clock. To stay in focus of the topic of this work the following brief discussion of the shift are concentrating on optical ion clocks and should motivate the later design of the clock setup

- Stark shift: Electric fields interact with the electric moment of the atoms or ions introducing an frequency shift called stark shift. This frequency shift between two energy levels is given by [174]:

$$\Delta\nu_{Stark} = -\frac{1}{2h}(\Delta\alpha_{DC}E_0^2 + \Delta\alpha_{AC}(\Omega)\langle E_0^2(\Omega)\rangle), \quad (18)$$

where  $h$  is the Planck constant. It can be differentiated between the DC-Stark effect with the term  $\Delta\alpha_{DC}E_0^2$  depending on the differential polarizabilities  $\alpha_{DC}$  and the static electric field  $E_0$ , and the AC-Stark effect, which is given by:

$$\Delta\nu_{ACStark} = -\frac{1}{2h}\Delta\alpha_{AC}(\Omega)\langle E_0^2(\Omega)\rangle. \quad (19)$$

The differential polarizabilities  $\alpha_{DC}(\Omega)$  in the AC-Stark shift depends on the oscillation frequency  $\Omega$  of the electric field  $E(\Omega)$ .

For optical clocks static electric fields can be induced external electric field or by electric charge accumulations in dielectric materials close to the atoms or ions [69]. Electric fields oscillating with RF frequencies are introduced by the ion trap [81]. For most of the typically used species the AC Stark shift introduced by the alternating electric field of the probe laser is small [55]. For optical lattice clocks the lattice laser typically introduces a strong AC-Stark shift [174, 175], which needs to be taken into account. Additionally, Black body radiation consists of electromagnetic radiation and leads to an AC-Stark shift.

- Black body radiation (BBR) shift: Every object at finite temperature emits thermal electromagnetic radiation. The spectrum can be described by Planck's law of black-body radiation:

$$B_\nu(T) = \frac{2h\nu^3}{c^2} \frac{1}{e^{h\nu/kT} - 1}. \quad (20)$$

The energy levels involved in the frequency measurement of the optical clock couple similarly to the AC Stark shift differently to electromagnetic field and therefore the clock transition experiences a differential energy shift [176–179]. This shift depends on the temperature of the surrounding material, their emissivity and the polarizability of the energy levels. Typically, the temperature is measured at different positions around the ions and atoms and simulations of the influence of BBR on the ion or atoms are performed to evaluate the frequency shift. For ion clocks the high RF power of the ion trap heats the trap and the surrounding materials which needs to be taken into account. If the clock species is susceptible to BBR often a cryogenic system [45, 174] is used which adds significant complicity to the system. For a transportable clock typically operates at room temperature, clock species with small BBR shifts are favourable.

- Background gas collision (BGC): Remaining gas inside the vacuum chamber leads to collisions of these particles with the trapped atoms or ions. Such a collision

can lead to a momentum transfer and hence motional heating of the clock atoms or ions [180]. Additionally, some atom and ion species are chemically reactive with the background gas, which hinders clock operation. For examples  $^{27}\text{Al}^+$  can react with hydrogen from the background gas forming aluminiumhydrid.

However, the main contribution of BGC to a systematic frequency uncertainty is given by a phase change of the atomic superposition between ground and excited state of the clock transition due to interaction of the atom or ion with the background gas particle [69, 180–182]. The phase change classically occurs due to different interaction potentials of ground and excited state. Additionally, polarization of the colliding molecule results in an electric field that generates an AC Stark shift. Therefore the phase change depends on the polarizability of the clock ion. In general the frequency shift due to BGC depends on the collision rate and hence on the remaining vacuum pressure inside the vacuum chamber. This makes ultra-high vacuum necessary in those experiments.

- Zeeman shifts: Magnetic fields induce an shift of the energy levels of the atom due to the magnetic momentum of the atom. This effect is called Zeeman effect. The coupling to the magnetic field  $B$  depends on the projections of the angular momenta on the magnetic field quantization axis  $|m_f\rangle$  and introduce a frequency splitting of the magnetic hyperfine sub levels of

$$\Delta\nu = C_1B + C_2B^2 + C_3B^3 \dots \quad (21)$$

Here,  $C_1$  is the linear and  $C_2$  the quadratic Zeeman coefficient, while higher order terms can often be neglected. The linear Zeeman coefficient is given by  $C_1 = \frac{\mu_B g_F m_F}{h}$ , where  $g_F$  is the g-factor of each hyperfine state and  $h$  is the Planck constant. Two approaches can be used to sufficiently reduce the first order Zeeman shift. The first one is given by using transitions between lower states  $|F, m_F = 0\rangle$  and upper states  $|F', m_{F'} = 0\rangle$  if possible. The second is given by averaging the frequency shift to zero by probing at least two Zeeman transitions with opposite  $m_F$  sign [6, 67, 183]. In an  $^{27}\text{Al}^+$  clock for example the  $|^1\text{S}_0, F = 5/2, m_F = -5/2\rangle$  to  $|^3\text{P}_0, F = 5/2, m_F = -5/2\rangle$  is alternately probed with the  $|^1\text{S}_0, F = 5/2, m_F = 5/2\rangle$  to  $|^3\text{P}_0, F = 5/2, m_F = -5/2\rangle$  transition [184]. The quadratic Zeeman term still remains and introduces a frequency shift. The strength of the magnetic field needs to be measured to compensate for the frequency drift. The measurement of the magnetic field can be achieved by probing the Zeeman shift of a suitable optical transition. In the case of an optical clock using  $^{40}\text{Ca}^+$  and  $^{27}\text{Al}^+$  ions, it is advantageous to employ calcium transitions for precise magnetic field measurements due to aluminum's insensitivity to magnetic fields [81].

- Time dilation due to ion motion: For ion clocks which are using one or only a few typically motionally coupled ions, thermal motion leads to a frequency shift due to the second order Doppler effect, which is a direct consequence of special

relativity. Relative motion between the laser beam in the laboratory frame and the ion introduces a Doppler shift  $\frac{\Delta\nu}{\nu} = \frac{v_{lab} - \nu}{\nu}$  [83]:

$$\frac{\Delta\nu}{\nu} = \frac{\langle v_{\parallel} \rangle}{c} - \frac{\langle v^2 \rangle}{2c^2} + \frac{\langle v_{\parallel}^2 \rangle}{c^2} + O\left(\frac{1}{c^3}\right), \quad (22)$$

$v_{\parallel}$  is the ion's velocity in the direction of the probe beam and  $v$  the total velocity of the ion. The first term in Equation 22 is the 1<sup>st</sup>-order Doppler shift. The average motion  $\langle v_{\parallel} \rangle$  of the ion in the harmonic trap potential is zero over the probe duration. However, due to thermal drifts or buildup of electric charges [3] during clock probing, the relative position of the ion can change over time and leads to a systematic shift of the clock frequency. By probing the clock transition from both sides this effect can be canceled. The next two terms in Equation 22, referred to as 2<sup>nd</sup>-order Doppler shifts, are a form of time dilation shifts [83]. In an ion trap different types of motion contribute to the trajectory of the ion given by secular motion and intrinsic and excess micromotion (EMM) [79, 185, 186]. The motion of the ion can be suppressed by cooling and ensuring low heating rates [79, 81, 187]. However, even a ground state cooled ion in a quadrupole trap has a finite velocity due to the zero point energy of the corresponding harmonic oscillator modes.

- Tunnel effect and cold collisions: In optical lattice clocks the atoms are trapped relatively weakly in the electromagnetic field of the optical lattice. The potential barrier introduced by the lattice is relative small and atoms can tunnel through the barrier. The effect is especially relevant for shallow lattices. The extended wave function of the atoms connected with high atomic densities leads to collisions between the atoms itself, and hence to an additional collision shift [5, 175, 188, 189].
- Other systematic effects: Technical effects, can be a relevant systematic effects for individual measurement setups. Optical path length changes in the clock laser setup can lead to a change of laser phase. During interrogation this effects can affect the excitation probability of the atoms or ion, resulting in a frequency shift. Optical path length changes in the connection between the experiment and the optical comb can also lead to frequency changes. Therefore those optical paths needs to be length stabilized. Phase shift induced by the rise time of the AOM when probing the clock transition [5, 8, 55] can also induce additional systematic uncertainty. Optical path length changes in the clock laser setup can lead to a change of laser phase. During interrogation this effects can affect the excitation probability of the atoms or ion, resulting in a frequency shift. Optical path length changes in the connection between the experiment and the optical comb can also lead to frequency changes. Therefore those optical paths needs to be length stabilized. The clock laser is stabilized by an ultra stable reference cavity, which typically shows frequency drifts due to spacer aging and temperature changes. While linear drifts are typically compensated for during clock interrogation, remaining frequency second order drifts lead to an offset

inducing a clock servo error [69]. Furthermore the gravitational red shift between two clocks at different positions need to be considered [56–58, 60].

Optical clocks using  $^{27}\text{Al}^+$  ions exhibit an exceptionally low total shift. When compared to other optical clocks, the total systematic uncertainty for  $^{27}\text{Al}^+$  optical clocks is the lowest recorded thus far, around  $1 \times 10^{-18}$  [3, 81]. Particularly noteworthy is the significantly reduced BBR shift for  $^{27}\text{Al}^+$  compared to other clock species. The insensitivity of  $^{27}\text{Al}^+$  to BBR makes it an excellent choice as a clock ion, as BBR often constitutes the dominant systematic uncertainty in optical clocks using different clock species. To further suppress the BBR associated systematic uncertainty, it is crucial to obtain a better understanding of the temperature distribution around the ions or atoms, which can be challenging when heat-inducing elements like ion traps are involved. Measurement of the trap temperature and the carrier board holding the trap is necessary, and the trap itself should have good heat conduction to a heat sink. For design of the carrier board and its mounting, presented in Section 5.2, takes these aspects into account.

By achieving higher vacuum levels in the experimental setup, the remaining systematic uncertainty resulting from BBR can be further mitigated. With the vacuum system presented in Section 5.1 we aim for a pressure below  $10^{-11}$  mbar to suppress black body radiation and chemical reactions between  $^{40}\text{Ca}^+$  ions and hydrogen atoms in the background gas.

The uncertainty associated with the Zeeman shift in  $^{27}\text{Al}^+$  clocks arises from several factors, including the limited accuracy of magnetic field probing using co-trapped  $^{40}\text{Ca}^+$  ions, uncertainty in the quadratic Zeeman coefficient  $C_2$ , and fluctuations in the magnetic field [81]. The uncertainty of the Zeeman shift can be reduce by a more accurate measurement of  $C_2$ . Fluctuations in the magnetic field can be minimized by stabilizing the magnetic field or utilizing permanent magnets, as well as employing a mu-metal shield for isolation from external magnetic fields. The magnetic field can be measured using a magnetic field sensor, and feed-forward or feedback stabilization schemes can be implemented to maintain its stability [190]. For the setup described here, a different approach is chosen. The design presented in Section 5.3 utilizes permanent magnets and a mu-metal shield, along with compensation coils. The mu-metal shield serves to isolate the experiment from environmental magnetic field fluctuations. The magnetic field produced by the magnetic field coils is susceptible to higher frequency noise, including 50 Hz noise, whereas permanent magnets do not exhibit such noise. By combining permanent magnets with compensation coils, it becomes possible to adjust the magnetic field at the ions' position. The contribution of the magnetic field from the coils is small, resulting in low magnetic noise.

Optical lattice clocks like the  $^{87}\text{Sr}$  or  $^{171}\text{Yb}$  lattice clock are using many atoms simultaneously to measure the transition frequency. According to equation 15 the QPN scales down with  $1/\sqrt{N}$  with the atom number. Ion clocks like the  $^{27}\text{Al}^+$  clock typically are using one ion. Consequently, they are limited by QPN and it takes a long measurement time for ion clocks to reach the systematic uncertainty limit. Therefore,



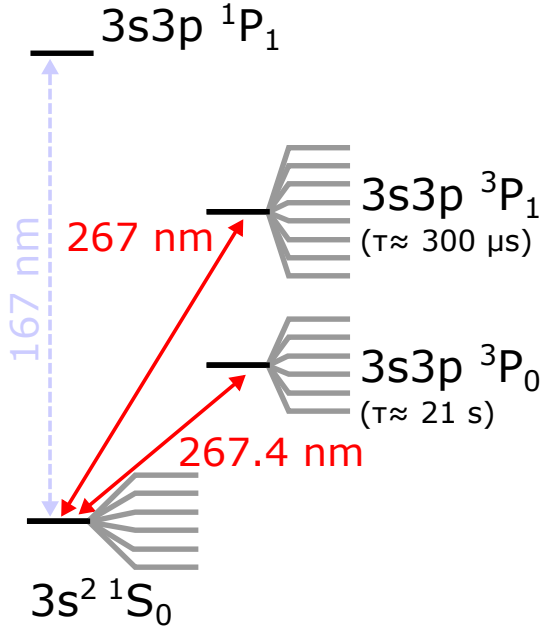


Figure 2.2: Reduced level diagram of  $^{27}\text{Al}^+$  with the clock transition  $^1S_0$  to  $^3P_0$  and the logic transition  $^1S_0$  to  $^3P_1$ . The  $^1S_0$  to  $^1P_1$  transition is in the deep UV and cannot be used for cooling and detection. Taken from [80].

it is important for optical ion clocks to enable long probe times to reduce the QPN. To enable long probe times, an ultra-stable laser system is required. The focus of this thesis is the development of an ultra-stable, transportable clock laser system for an  $^{27}\text{Al}^+$  clock.

### 2.3 An optical $^{40}\text{Ca}^+ / ^{27}\text{Al}^+$ clock using quantum logic spectroscopy

In the preceding section, the systematic uncertainty budgets of various optical clocks, including an  $^{27}\text{Al}^+$  ion clock, are discussed. However, it should be noted that  $^{27}\text{Al}^+$  ions do not possess an available transition suitable for efficient cooling and state detection of the ion. The level diagram for  $^{27}\text{Al}^+$  is depicted in Figure 2.2. The transition from  $^1S_0$  to  $^1P_1$  cannot be utilized for state detection and laser cooling due to the unavailability of stable laser systems at this particular wavelength, despite ongoing efforts to develop lasers in the deep ultraviolet range [191–193]. Furthermore, the clock transition from  $^1S_0$  to  $^3P_0$  at  $267.4 \text{ nm}$  and the logic transition from  $^1S_0$  to  $^3P_1$  at  $267 \text{ nm}$  are shown in the diagram. The logic transition can also be utilized for state preparation of the Zeeman sublevels of the  $^1S_0$  ground state.

To cool the  $^{27}\text{Al}^+$  ion, it is trapped alongside one or more  $^{40}\text{Ca}^+$  ions. The level diagram for  $^{40}\text{Ca}^+$  is presented in Figure 2.3. Direct laser cooling of  $^{40}\text{Ca}^+$  ions is feasible [194]. The  $^{27}\text{Al}^+$  ion is sympathetically cooled through its Coulomb interaction with the  $^{40}\text{Ca}^+$  ion [195–199]. For cooling the  $^{40}\text{Ca}^+$  ion, the transition from  $^2S_{1/2}$  to  $^2P_{1/2}$  at  $397 \text{ nm}$  can be employed, and various cooling techniques such as Doppler cooling and



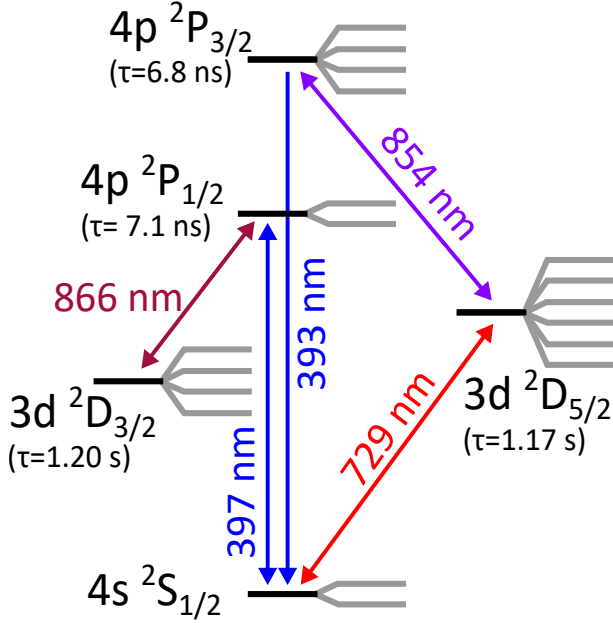


Figure 2.3: Reduced level diagram of  $^{40}\text{Ca}^+$ . The  $^2S_{1/2}$  to  $^2P_{1/2}$  transition can be used for cooling and state detection. To avoid population trapping a repumper laser at 866 nm is used to drive the  $^2P_{1/2}$  to  $^2D_{3/2}$  transition. For sideband cooling and quantum logic spectroscopy the narrow  $^2S_{1/2}$  to  $^2D_{5/2}$  transition can be used and the  $^2D_{5/2}$  level and the quickly decaying  $^2P_{3/2}$  level can be used for state clear out. Taken from [80].

electromagnetically induced transparency (EIT) cooling can be implemented [200, 201]. The  $^2S_{1/2}$  level decays to the metastable  $^2D_{3/2}$  level [202]. A repumper laser operating at 866 nm is necessary to prevent population trapping. Sideband cooling techniques [79, 81, 186, 194] can be applied using the narrow transition between the  $^2S_{1/2}$  and  $^2D_{5/2}$  states at 729 nm. The transition between the  $^2D_{5/2}$  level and the rapidly decaying  $^2P_{3/2}$  level can be utilized to effectively clear the  $^2D_{5/2}$  level and facilitate efficient sideband cooling and micromotion determination.

The choice of  $^{40}\text{Ca}^+$  as the logic and cooling ion in  $^{27}\text{Al}^+$ -based systems is attributed to several factors. Firstly, the mass ratio of 1.48 between  $^{40}\text{Ca}^+$  and  $^{27}\text{Al}^+$  enables efficient sympathetic cooling [197]. Additionally, the cooling transition at 397 nm for  $^{40}\text{Ca}^+$  is easily accessible. Moreover,  $^{40}\text{Ca}^+$  is used in various experiments, and its cooling, state detection, and manipulation have been well-studied [22, 68, 203–209]. Commercial laser systems specifically designed for  $^{40}\text{Ca}^+$  applications are readily available, facilitating experimental setups and implementation. Alternatively, other ion species such as  $\text{Mg}^+$  [3] or  $\text{Be}^+$  [82, 119] have been demonstrated as logic ions for  $^{27}\text{Al}^+$  quantum logic clocks. The mass ratio of  $\text{Mg}^+ / ^{27}\text{Al}^+$  is more favorable than the  $^{40}\text{Ca}^+ / ^{27}\text{Al}^+$  mass ratio. But the mass ratio of  $\text{Be}^+ / ^{27}\text{Al}^+$  provides only insufficient sympathetic cooling capabilities. However, both of these species require deep UV light to address the cooling transition, which necessitates the use of custom-made optical fibers and complex laser systems.

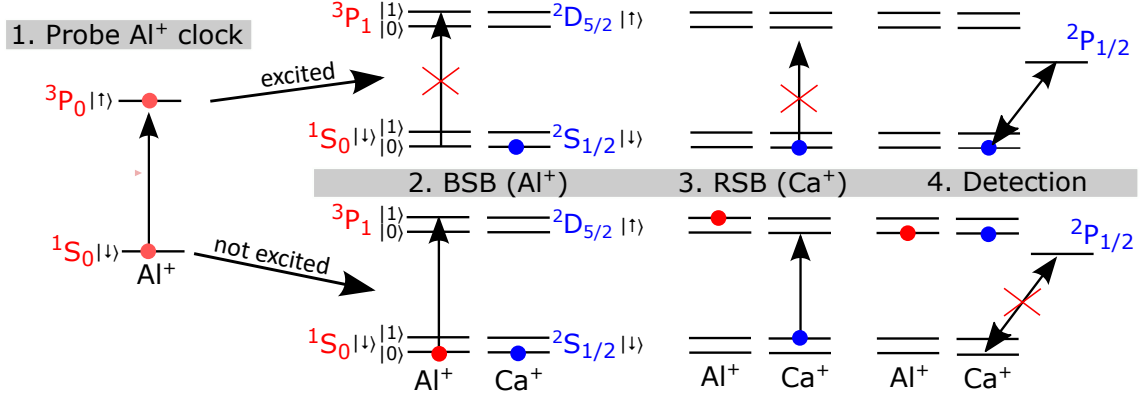


Figure 2.4: Quantum logic spectroscopy protocol. 1. Probing the clock transition  $^1S_0$  to  $^3P_0$ . If it is excited follow the upper line, if excitation failed follow the lower line. 2. Blue sideband (BSB) pulse of the  $^{27}\text{Al}^+$  logic laser is used to excite  $^{27}\text{Al}^+$  to the  $|^3P_{0,1}\rangle$  state with one motional quantum, which is only successfully if the clock transition failed. Due to the motional coupling  $^{40}\text{Ca}^+$  is also in the first motional state  $|1\rangle$ . 3. Red sideband (RSB) pulse with  $^{40}\text{Ca}^+$  quantum logic laser excites  $^{40}\text{Ca}^+$  to the  $^2D_{5/2}$  if it is in the  $|1\rangle$  state. 4. Detection of the  $^{40}\text{Ca}^+$  state, bright fluorescence is obtained if the  $^{40}\text{Ca}^+$  ion is still in the ground state otherwise no fluorescence is obtained. Following the quantum logic scheme, information on whether the clock excitation was successfully or not is gained.

To address the absence of an accessible detection transition in  $^{27}\text{Al}^+$ , quantum logic spectroscopy (QLS) can be employed to probe the  $^{27}\text{Al}^+$  clock transition. Figure 2.4 illustrates the quantum logic scheme for using  $^{27}\text{Al}^+$  as the clock ion and  $^{40}\text{Ca}^+$  as the logic ion. Prior to the QLS protocol, the ions are cooled to their motional ground state. The  $^{27}\text{Al}^+$  ion is prepared in the desired Zeeman sublevel of the ground state, typically  $|^1S_0, m = -\frac{5}{2}\rangle$  or  $|^1S_0, m = \frac{5}{2}\rangle$ , using a circularly polarized  $^{27}\text{Al}^+$  logic laser. The clock laser is then utilized to interrogate the  $^{27}\text{Al}^+$  clock transition from  $^1S_0$  to  $^3P_0$ . Depending on the interrogation scheme and the laser frequency detuning, the ground state  $^1S_0$  and the upper  $^3P_0$  state are excited with a certain probability. If the excitation fails, the  $^{27}\text{Al}^+$  ion remains in the ground state  $^1S_0$  (lower lane in Figure 2.4).

To read out the clock transition, a blue sideband pulse (BSB) of the logic laser is applied to excite the  $^{27}\text{Al}^+$  ion to the  $^3P_1$  state. Due to the blue detuning of the logic laser, one motional quantum is added, resulting in the  $^{27}\text{Al}^+$  ion being in the first motional state  $|^3P_1, 1\rangle$ . Due to the motional coupling between the  $^{40}\text{Ca}^+$  and  $^{27}\text{Al}^+$  ions, the  $^{40}\text{Ca}^+$  ion is also driven to the first motional state  $|^2S_{1/2}, 1\rangle$ . However, if the excitation of the clock transition is successful, the  $^{27}\text{Al}^+$  ion remains in the upper state  $^3P_0$ , and the logic laser has no influence on the  $^{27}\text{Al}^+$  state (upper lane in Figure 2.4). Both ions remain in the motional ground state  $|0\rangle$ . A red sideband pulse (RSB) of the  $^{40}\text{Ca}^+$  quantum logic laser at 729 nm is then employed to drive the  $^2S_{1/2}$  to  $^2D_{5/2}$  transition. Due to the red detuning of the laser, one motional quantum is removed. If the  $^{40}\text{Ca}^+$  ion was initially in the motional ground state (clock transition excited),

the excitation to the  $^2D_{5/2}$  state fails, and the  $^{40}\text{Ca}^+$  ion remains in the ground state. In contrast, if the  $^{40}\text{Ca}^+$  ion is in the  $^2D_{5/2}$  state (clock transition not excited), the interrogation of the  $^2S_{1/2}$  to  $^2P_{1/2}$  transition is dark. The readout process can be repeated, which allows for quantum non-demolition measurements and, enables a high fidelity. In summary, the excitation probability of the  $^1S_0$  to  $^3P_0$  transition is measured by transferring the information to the  $^{40}\text{Ca}^+$  ion via their motional states and detecting the  $^{40}\text{Ca}^+$  state.

### 3 A transportable ultra-stable reference cavity

In this chapter, a transportable ultra-stable stabilization cavity is presented. Firstly, the theoretical foundation of optical cavities is discussed, including the examination of major noise sources that affect the frequency stability of the laser. Secondly, the setup of the optical cavity is outlined, including the optical setup for locking the laser frequency to the resonance frequency of the cavity. The entire setup is integrated into a rack. The main focus of this chapter is the characterization of the frequency stability of the optical cavity. As the major noise sources vibration noise, photo-thermal noise, RAM and the temperature stability are investigated.

#### 3.1 Theoretical description

The theoretical consideration of optical cavities begins with the general concept of an optical resonator. Furthermore, the Pound-Drever Hall (PDH) locking technique is explained. Residual amplitude modulation (RAM) is described, and an active stabilization scheme for RAM is presented. Additionally, a stabilization scheme for optical path length changes is discussed. Finally, the main contributions of noise that affect the frequency stability of the laser are presented.

##### 3.1.1 Theory of optical cavities

A detailed discussion of the theory of optical resonators can be found in various literature, for example, by Saleh and Teich [210]. Here, the basic theoretical concepts are reproduced.

Considering a laser beam with an electric field  $E_{\text{in}} = E_0 e^{i\nu t}$  assuming a plane wave, where  $\nu$  represents the frequency. When this laser beam is directed into an optical resonator, a fraction  $t_1 E_{\text{in}}$  passes through the first mirror. The beam is then reflected by the second mirror and, after completing a full round trip, it is reflected once again by the first mirror. The resulting beam  $r_1 r_2 t_1 E_{\text{in}}$  interferes with the laser beam transmitted by the first mirror. This process repeats for numerous circulations of light within the cavity, while a portion of the light leaks out through the second mirror. Perfect coupling is indeed achieved by ensuring perfect destructive interference between the input light reflected off the first mirror and the light from the cavity transmitted through it. This interference results in optimal coupling efficiency, maximizing the transmission of light into and through the cavity. This resonance condition is met when  $n\lambda = 2l_0$ , where  $n$  is an integer,  $\lambda$  is the wavelength of light, and  $l_0$  is the length of the optical resonator. In the frequency domain, a transmission peak appears for each axial mode, with the frequency separation between these modes referred to as the free spectral range  $\nu_{\text{FSR}}$ , which is fully determined by the resonance condition. The free spectral range can be calculated using the equation:

$$\nu_{\text{FSR}} = \frac{c}{\lambda} = \frac{c}{2l_0} \quad (23)$$

In a broader perspective, the circulating light accumulates a phase change of  $\Delta\phi =$

$\exp(-i\nu \cdot \frac{2l_0}{c})$  with each circulation within the optical resonator. In the case of a perfect cavity without losses, the electric field coupled into the cavity  $E_c$ , can be calculated by summing up the round trips of the field:

$$E_c = t_1 E_{\text{in}} \sum_{n=0}^{\infty} (r_1 r_2 \exp(-i \frac{\nu}{\nu_{\text{FSR}}}))^n = E_0 \frac{t_1}{1 - r_1 r_2 \exp(\frac{-i\delta\nu}{\nu_{\text{FSR}}})}. \quad (24)$$

The transmission is given by:

$$E_t = \exp(-i \frac{\nu}{\nu_{\text{FSR}}}) \dot{E}_c = E_{\text{in}} \frac{t_1 t_2 \exp(-i \frac{\nu}{\nu_{\text{FSR}}})}{1 - r_1 r_2 \exp(-i \frac{\nu}{\nu_{\text{FSR}}})} \quad (25)$$

and the reflection is given by:

$$E_r = -r E_{\text{in}} + E_{\text{in}} \frac{t_1^2 r_2 \exp(-i \frac{\nu}{\nu_{\text{FSR}}})}{1 - r_1 r_2 \exp(-i \frac{\nu}{\nu_{\text{FSR}}})} \quad (26)$$

The reflection coefficient is defined as the ratio between the incident beam  $E_{\text{in}}$  and the reflected beam  $E_{\text{ref}}$ . For a lossless optical resonator with identical mirrors, the reflection coefficient can be calculated using the equation:

$$R(\nu) = \frac{E_r}{E_{\text{in}}} = r \frac{1 - \exp(i \frac{\nu}{\nu_{\text{FSR}}}) - 1}{1 - r^2 \exp(i \frac{\nu}{\nu_{\text{FSR}}})} \quad (27)$$

The full width at half maximum of the light intensity transmitted by the cavity represents the linewidth  $\delta\nu$  of the cavity and can be calculated as:

$$\delta\nu = \frac{c}{2L} \frac{1 - r_1 r_2}{\sqrt{\pi r_1 r_2}} \quad (28)$$

The finesse of the cavity is defined as:

$$F = \frac{\nu_{\text{FSR}}}{\delta\nu} = \frac{\sqrt{\pi r_1 r_2}}{1 - r_1 r_2} \quad (29)$$

The description provided above applies to a cavity with two planar mirrors. However, in practice, a high-finesse cavity with planar mirrors is highly sensitive to misalignment, making it difficult to successfully confine the field between the mirrors. For stable operation, at least one of the mirrors should have curvature. In an optical resonator with two curved mirrors with radii  $R_i$ , stability parameters  $g_i = \frac{l_0}{R_i}$  can be defined. In such an optical resonator, the stability condition

$$0 \leq g_1 g_2 \leq 1 \quad (30)$$

must be fulfilled to form stable optical modes. As a consequence of this geometry, higher-order transverse modes appear in the cavity. The phase of such modes inside the cavity is modified by the Gouy phase shift. Therefore, the resonance conditions of these modes change to:

$$\nu_{qnm} = (1 + q)\nu_{\text{FSR}} + (n + m)\Delta\nu_{qnm}, \quad (31)$$

where

$$\Delta\nu_{qnm} = \frac{c}{2l_0} \left( \frac{\arccos \sqrt{g_1 g_2}}{\pi} \right). \quad (32)$$

The integer  $q$  represents the longitudinal mode number, while the integers  $n$  and  $m$  represent the transverse mode numbers. When constructing an optical cavity, it is essential to ensure that the desired mode and other modes are not degenerate, and that the spacing between them is sufficient to prevent a reduction in laser stability.

The stability of the resonance frequency  $f_0$  of an optical cavity is directly related to the stability of its length. This can be expressed by the equation:

$$\frac{\delta f}{f_0} = -\frac{\delta l}{l_0}, \quad (33)$$

where  $\frac{\delta f}{f_0}$  represents the fractional frequency instability and  $\frac{\delta l}{l_0}$  denotes the relative length change of the cavity.

The same conversion can be applied for the power spectral density (PSD) of displacement  $S_x$  to the PSD of fractional frequency noise  $S_y$  given by:

$$S_y = \frac{S_x}{l_0^2}. \quad (34)$$

It is essential to minimize the length fluctuations caused by various noise sources in order to achieve a highly frequency-stable optical cavity. Furthermore, it is necessary to implement frequency locking between the laser source and the optical cavity to ensure that the stable resonance frequency of the cavity is accurately transferred to the laser frequency.

### 3.1.2 Pound Drever Hall stabilization locking scheme

To stabilize the frequency of laser light to an external reference cavity, the Pound-Drever-Hall (PDH) locking scheme [211–213] can be employed. The PDH locking scheme is illustrated in Figure 3.1. In this setup, a fiber laser is used, and its frequency can be adjusted by applying voltage to a built-in piezo actuator. However the response of laser frequency is too slow to suppress high frequency noise. To achieve faster frequency control, an acousto-optical modulator (AOM) is included. An electro-optical modulator (EOM) is used to introduce additional sidebands to the laser light. The frequency of the sidebands is determined by the laser frequency plus or minus the frequency of the modulation signal generated by a local oscillator.

The laser beam undergoes polarization cleaning by a polarizing beamsplitter (PBS) and then passes through a quarter-wave plate. Close to resonance, a laser light with the carrier frequency is partially coupled into the reference cavity and partially reflected, while the sidebands are fully reflected. The reflected light then passes through the quarter-wave plate again and is reflected by the PBS. The interfering light, consisting of the carrier and sideband, is detected by a photodetector. The measured

signal is demodulated using an rf mixer, utilizing the phase-matched sideband modulation signal from the local oscillator. By applying low-pass filtering, a typical error signal denoted as  $\epsilon$  (depicted on the right side of Figure 3.1) is generated. The error signal is fed to a PID controller, which is used to control the frequency of the laser light.

The difference between the carrier frequency and the resonance frequency of the cavity leads to a phase shift of the reflected light with the carrier frequency. This phase shift of the carrier, relative to the two sidebands, results in the detected error signal. A brief mathematical derivation of the error signal and the demodulation process is given considering phase modulation by the EOM,

$$E_{in} = E_0 e^{i(\nu t + \beta \sin \Omega t)}. \quad (35)$$

This can be approximated using the Bessel functions  $J_0$  by

$$E_{in} \approx E_0 [J_0(\beta) e^{i\nu t} + J_1(\beta) e^{i(\nu + \Omega)t} - J_1(\beta) e^{i(\nu - \Omega)t}] \quad (36)$$

Taking the response function  $R(\nu)$  of the cavity into account, the reflected light can be written as:

$$E_r = E_0 [R(\nu) J_0(\beta) e^{i\nu t} + R(\nu + \Omega) J_1(\beta) e^{i(\nu + \Omega)t} - R(\nu - \Omega) J_1(\beta) e^{i(\nu - \Omega)t}]. \quad (37)$$

The optical power detected by the PDH photodiode  $P_r$  is given by

$$\begin{aligned} P_r &= |E_r|^2 \\ &= P_c |R(\nu)|^2 + P_s (|R(\nu + \Omega)|^2 + |R(\nu - \Omega)|^2) \\ &\quad + 2\sqrt{P_c P_s} \operatorname{Re} [R(\nu) R^*(\nu + \Omega) - R^*(\nu) R(\nu - \Omega)] \cos(\Omega t) \\ &\quad + 2\sqrt{P_c P_s} \operatorname{Im} [R(\nu) R^*(\nu + \Omega) - R^*(\nu) R(\nu - \Omega)] \sin(\Omega t) \\ &\quad + (O[2\Omega]). \end{aligned} \quad (38)$$

Here,  $P_c$  and  $P_s$  represent the optical power of the carrier and the optical power of one sideband, respectively. The frequency mixing with frequency  $\Omega$  is mathematically expressed by multiplying with a  $\sin(\Omega t)$  term. After frequency mixing and applying a low-pass filter, the following error signal arises

$$\epsilon = 2\sqrt{P_c P_s} \operatorname{Im} [R(\nu) R^*(\nu + \Omega) - R^*(\nu) R(\nu - \Omega)] \quad (39)$$

If the frequency difference  $\Delta\nu = \nu_0 - \nu$  between the laser frequency  $\nu$  and resonance frequency of the cavity  $\nu_0$  is small,  $R(\nu)$  can be approximated as

$$\operatorname{Im} [R(\nu)] \approx \frac{1}{\pi} \frac{\Delta\nu}{\delta\nu}. \quad (40)$$

The error signal is given by:

$$\epsilon = -\frac{4\sqrt{P_c P_s}}{\pi \delta\nu} \Delta\nu \quad (41)$$

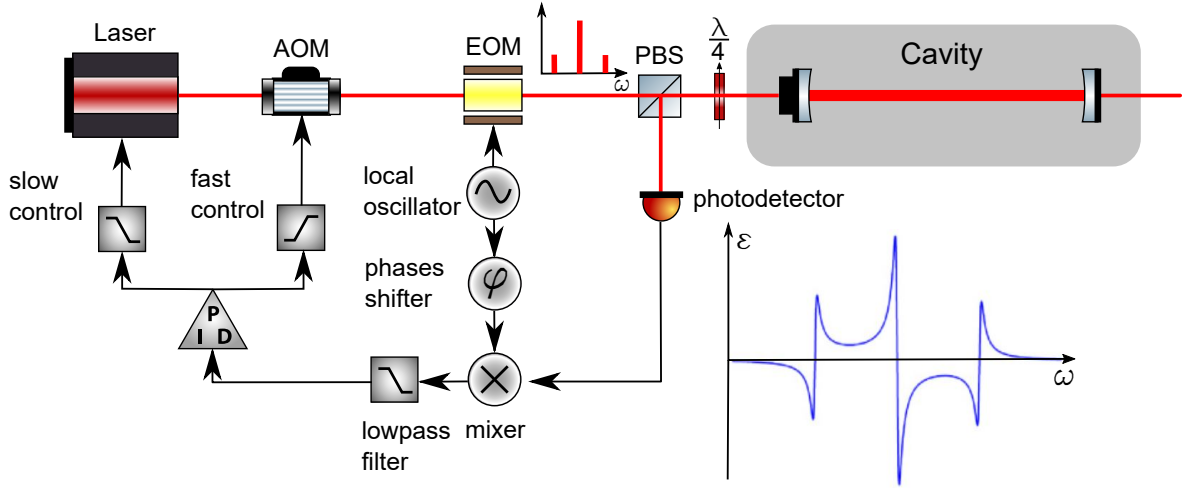


Figure 3.1: Schematic drawing of the PDH locking technique. The laser beam is modulated with sidebands in frequency space using the EOM (electro-optical modulator). The light reflected from the cavity is measured by a photodetector, and this signal is used to generate the error signal  $\epsilon$ . A detailed description of the PDH locking technique is provided in the text.

By using this error signal and enforcing  $\epsilon = 0$ , the frequency of the laser is locked to the cavity resonance frequency  $\Delta\nu = 0$ . In the optimal case, the error function  $\epsilon$  is asymmetry around the resonant frequency of the cavity. This means that the error signal is zero when the laser light is in resonance with the cavity. This point represents the optimal locking point because amplification of the PDH error signal have no effect on the frequency of the laser.

### 3.1.3 Residual amplitude modulation and stabilization

The frequency sidebands for the PDH locking scheme are produced by phase modulation with an EOM. In practice, residual amplitude modulation (RAM) at the modulation frequency is unavoidable in such a process [214, 215]. The presence of RAM is detected by the PDH photodiode and leads to an offset in the PDH signal due to the demodulation scheme. As a consequence, this offset in the PDH error signal causes a shift in the laser frequency. A change in the magnitude of the error signal results in a corresponding shift of the laser frequency. For a more detailed description of RAM, one can refer to various sources, such as Shen et al. [216].

In the case of RAM is induced by the birefringence of the EOM, the following explanation can be provided: The phase modulation of the EOM is generated by modulating the length of the crystal by applying a electric field. Due to the birefringent nature of the EOM crystal, when linearly polarized light at an angle with respect to the extraordinary axis enters the EOM, the birefringence and length modulation of the crystal cause different phase shifts for light polarized along the extraordinary and ordinary axes. Consequently, the polarization of the combined light wave after passing through the EOM is also modulated. This polarization modulation is then converted



into intensity amplitude modulation when it undergoes polarization analysis. The frequency of this modulation corresponds to the PDH sideband modulation frequency, resulting in RAM.

Fluctuations in the polarization angle of the incident light, light power, EOM modulation power, or the birefringence of the EOM can introduce fluctuations in the locking point, leading to a degradation of laser stability. Therefore, it becomes necessary to stabilize these physical quantities. To minimize RAM caused by the birefringence of the EOM, one approach is to select an EOM with a low temperature dependency of the birefringence [217]. Careful alignment of the polarization axis of the incident light, the crystal axis, and the polarization analyzer axis is also important. It is worth noting that birefringent materials like optical fibers can cause polarization changes. Hence, it is recommended to place a polarizer in close proximity to the EOM, both before and after it. Additionally, temperature stabilization of the EOM is crucial to prevent RAM fluctuations arising from the temperature dependence of the EOM's birefringence.

To stabilize RAM, an active control approach [214, 218–221] can be implemented. Figure 3.2 illustrates a RAM stabilization scheme, which operates alongside the PDH setup. In this scheme, an additional PBS is incorporated as a polarization analyzer to convert any polarization modulation into intensity modulation. A beamsplitter is utilized to direct a portion of the light to the RAM stabilization diode. The demodulation of the signal measured on the RAM stabilization diode follows a similar process to the demodulation of the PDH error signal. The measured signal is mixed with the phase-matched PDH sideband modulation signal and then filtered using a low-pass filter. The demodulated signal is employed to control the optical length of the EOM through a PID controller and the application of a near dc electric field using a bias tee. The signal changes the crystal's length, which stabilizes the phase shifts for light with different polarizations. This signal acts as a countermeasure to the RAM signal, effectively nullifying the measured RAM and suppressing RAM caused by the birefringence of the EOM.

Another effect contributing to RAM is the presence of etalons. To gain a deeper insight into this phenomenon, it is helpful to examine the PDH modulation from a Fourier space perspective. The EOM introduces modulation to the laser light by generating two symmetrical sidebands with opposite phases: one at the laser frequency plus the modulation frequency and the other at the laser frequency minus the modulation frequency, as shown in Equation 37. In this context, RAM occurs when the sidebands have unequal amplitudes or phases that are not exactly opposite. The etalons in the optical setup apply differently to light with different frequencies. The frequency difference between the two sidebands can cause an asymmetric reduction in their amplitudes and induce a phase shift, which was previously described as RAM. Fluctuations in the conditions of the etalons within the optical setup, such as temperature variations, lead to additional fluctuations in the RAM offset. Therefore, it is crucial to strictly avoid the presence of etalons in the optical setup. This can be achieved by tilting potentially parallel surfaces or adding optical isolators to avoid reflected light to propagate back and forth to form an etalon.

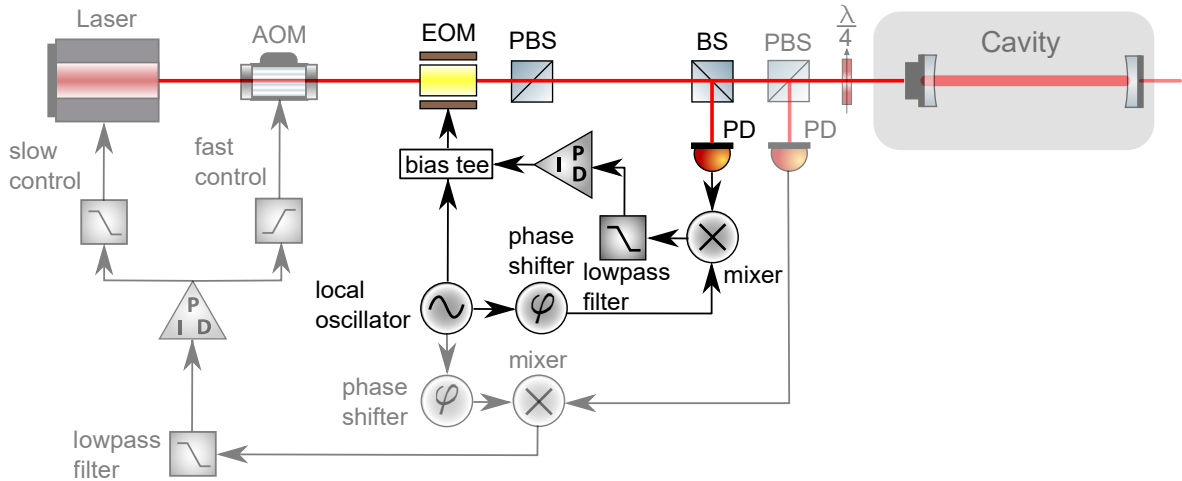


Figure 3.2: Schematic drawing of the PDH locking technique from Figure 3.1 (light components) updated by the RAM stabilization scheme (saturated components). The RAM stabilization scheme consists of an additional polarisation beamsplitter (PBS) and a beamsplitter (BS) used to reflect part of the light to the RAM photodiode (PD). The RAM signal is electrically demodulated and used to cancel RAM by controlling the phase shift induced by the EOM. A detailed description is given in the text.

However, for RAM induced by etalons, effective suppression can only be achieved if the etalon is positioned between two surfaces that are both part of the RAM stabilization path and the optical path of the PDH locking scheme [216]. Ideally, optical isolators should be inserted into all optical paths that are not shared by both the RAM stabilization scheme and the PDH locking scheme. Shen et al. [216] provide a comprehensive discussion on the influence of etalons on RAM, considering their position and the RAM stabilization scheme.

### 3.1.4 Interferometric optical path length stabilization

In an optical setup, variations in temperature, pressure, and mechanical alignment can lead to changes in the optical path length. These changes affect the phase of the laser light and limit the frequency stability. To stabilize the length of all optical paths, particularly in the case of optical fibers, a phase stabilization technique is employed.

Phase stabilization is typically achieved through a strongly asymmetric Michelson interferometer, where the light in a short reference arm interferes with light traveling back and forth in a long arm. In this configuration, the frequency of the frequency-shifted light at a distant position at the end of the main path of the setup is compared with the frequency of the light at the reference point [222, 223].

In Figure 3.3 such a interferometric setup for phase stabilization is depicted. In this setup, a portion of the laser light is directed towards a mirror and back reflected, interfering with the back reflected light from the main path. The majority of the laser

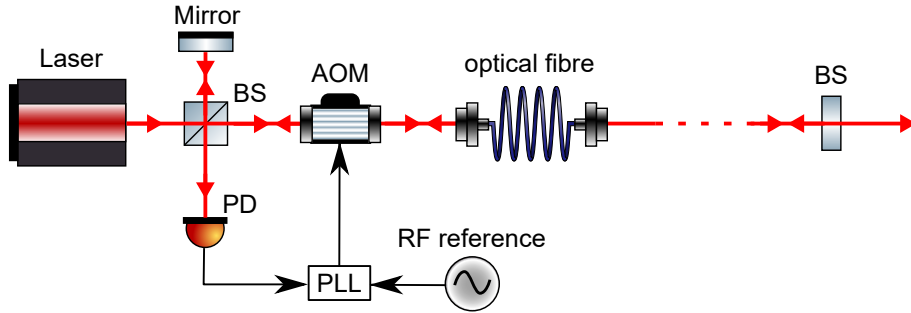


Figure 3.3: Schematic drawing of an interferometric optical path length stabilization schema. The incident light is divided into two paths using a beamsplitter (BS): the main path and a reference path. In the main path, the light undergoes a frequency shift by passing through an acousto-optic modulator (AOM), and at the end of this path, a portion of the light is partially reflected back by another beamsplitter (BS). In the reference path, the light is directly reflected back by a mirror. The back reflected light from both paths interferes on a photodiode (PD), resulting in the generation of a beat signal. This beat signal is utilized within a phase-locked loop (PLL) to stabilize the phase of the light via a phase shift created by the AOM.

light continues along the main path. Close to the desired point where phase-stabilized light is required, another beamsplitter is placed, which reflects a small fraction of the light. Additionally, an AOM is inserted in the main path. The AOM induces a frequency shift in the laser light within the main path, and the back reflected light undergoes a second frequency shift. The back reflected light partially reflects off the first beamsplitter and interferes with the light from the reference arm. The resulting interference is detected by a photodiode, generating a beat signal due to the frequency difference of the two light beams. Any changes in the optical length of the main path cause a frequency variation in the beat signal. This electric signal is compared to a reference signal with a stable radio frequency (rf) by a phase-locked loop (PLL). The corrected RF signal is then used to drive the AOM, compensating the frequency shift and ensuring that the phase of the laser light at the second beamsplitter is referenced to the phase at the first beamsplitter. It is important to minimize additional reflections from other optical components that can interfere with the reference beam and disrupt the electronic phase stabilization. Alternatively, the AOM can be placed behind the reflection, providing a frequency marker for the desired reflection. In this setup, the laser light that requires stabilization traverses the main path twice, experiencing the same phase variation and frequency correction by another AOM twice. Alternative phase stabilization schemes are also possible. For example, if the main path forms a loop where the distance between the starting point and endpoint of the laser light is small, direct interferometric phase stabilization can be achieved by measuring the beat between the laser light at the start point and the endpoint.

### 3.1.5 Frequency comparison via optical comb

To accurately measure the frequency stability of the cavity, a second reference cavity with higher stability is required. The laser light stabilized by the first cavity is combined

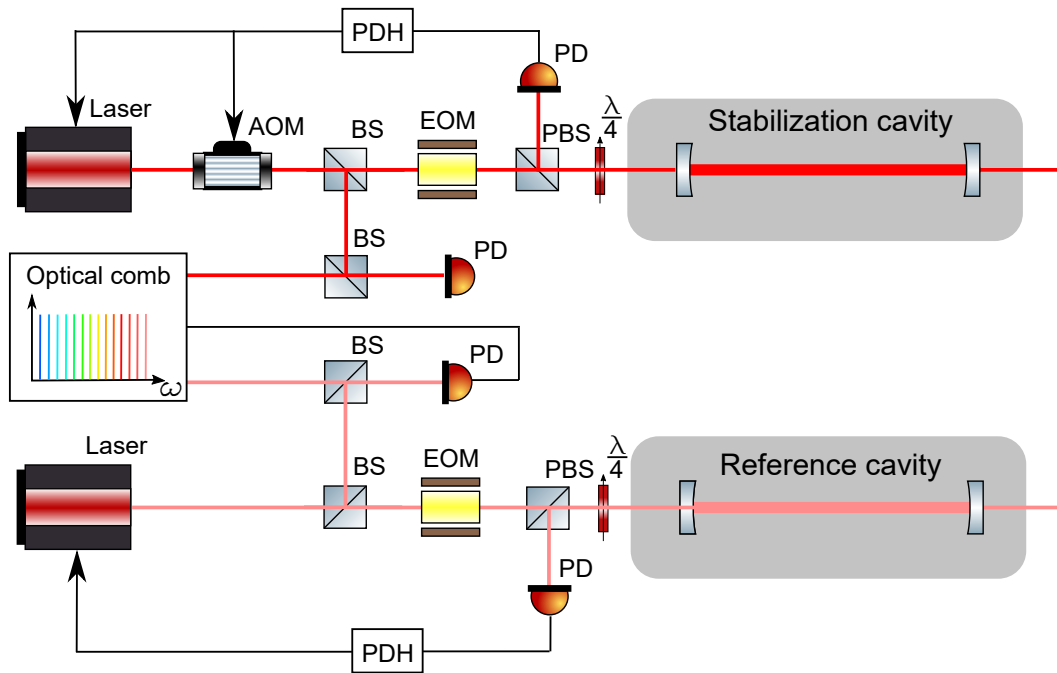


Figure 3.4: Schematic drawing of a frequency comparison between two lasers with different wavelength via an optical frequency comb. Both lasers are stabilized using a PDH locking scheme on respective cavities. In this setup, the laser light from each cavity is split using a beamsplitter (BS). One portion of the laser light is combined with a tooth of the optical comb, and the interference beat between them is detected by a photodiode (PD). The optical comb itself is stabilized to the laser light that is stabilized by the reference cavity. The second photodiode (PD) measures the frequency difference between the two lasers.

with the laser light stabilized by the reference cavity. The frequency difference between these two overlapping laser beams is measured using a photodiode, which detects the beat signal resulting from their interference. In order to achieve precise frequency comparison, it is essential to implement optical path length stabilization for all optical paths, as discussed in Section 3.1.4. We have only access to, a highly stable reference cavity for laser light at a wavelength of 1542 nm. To bridge the frequency gap between the reference cavity at 1542 nm and the stabilization cavity at 1069.6 nm, an optical frequency comb [159, 160] is employed. An optical frequency comb provides light with sharp peaks in the frequency domain with a constant spacing  $f_r$  between each tooth of the optical frequency comb.

$$f_n = f_0 + n f_r. \quad (42)$$

For an optimal optical frequency comb, the carrier offset frequency  $f_0$  is smaller than  $f_r$ , both frequencies are constant and in the rf regime.  $f_r$  is also known as the repetition rate, referencing to mode-locked lasers. A schematic diagram of the setup is provided in Figure 3.4. Both cavities are utilized to stabilize a single laser using the PDH technique. A portion of the light stabilized by the reference cavity is overlapped with the light from the optical frequency comb. The beat signal resulting from the interference between the laser light and the nearest frequency tooth of the optical comb is detected by a photodiode. This signal is then fed back to the optical comb to stabilize it to the reference laser. The light from the stabilized optical comb is combined with the light stabilized by the stabilization cavity. The beat signal arising from the interference between the laser light and another frequency tooth of the comb, which is close to the laser frequency, is measured using a second photodiode. The frequency spacing between each tooth of the optical comb is equal and stable. Therefore, the measured signal provides information about the frequency stability of the stabilization cavity. For the direct measurement of the resonance frequency of the cavity in this thesis, the described method is used. A tracking oscillator and a frequency counter<sup>1</sup> is used to record the frequency of the beat note measurement on the photodiode.

### 3.1.6 Frequency noise sources

The following discussion focuses on the most common noise sources that can limit the frequency stability of a highly stable stabilization cavity. Figure 3.5 presents a general overview of these noise sources and their relevant timescales.

**Photon shot noise and electronic noise:** On small timescales, the dominant noise sources that limit the performance of highly stable optical cavities are photon shot noise and electrical noise. Photon noise arises from the quantum nature of light and follows a Poisson distribution, therefore it is often referred to as shot noise. The PDH signal is produced by the interference signal of the carrier and the sidebands on the PDH photodiode. On resonance, the reflected carrier will vanish, and only the sidebands are reflected to the photodiode. Photon noise of the light detected by the photodiode

---

<sup>1</sup>K+K Messtechnik, FXE Phase + Frequency Meter

affects the error signal in the PDH locking scheme, setting a fundamental limit on the frequency instability of the cavity. The noise power spectral density (PSD) of the fractional frequency instability  $S_{y,SN}$  caused by shot noise is given by the expression [213]:

$$S_{y,SN} = \frac{hc^2}{8^2 F^2 \nu_0 P_c} \quad (43)$$

This fractional frequency noise PSD remains constant across all frequencies where shot noise is present. As a result, shot noise can be characterized as white frequency noise, exhibiting a  $\tau^{-\frac{1}{2}}$  behavior in the Allan deviation.

In addition to photon shot noise, electronic noise is also present in the electronic components of the PDH locking scheme. The main electronic noise sources of importance are thermal noise, electric shot noise, and flicker noise. As such noise in the error signal is indistinguishable from noise in the laser's frequency, the PDH feedback loop modulates the in-loop noise on the laser frequency similar to any controller with disturbed error signal. The first two types of electronic noise exhibit frequency-independent behavior and are only relevant on smaller timescales. Thermal noise is generated due to the random thermal motion of electrons within an electrical conductor. Similar to photon shot noise, electronic shot noise originates from the discrete nature of electric charge. Flicker noise follows a  $\frac{1}{f}$  behavior, consequently it is often referred to as  $\frac{1}{f}$  noise. In practical applications, electronic noise and photon noise are often amplified by electrical amplifiers. However, for reasonable optical power coupled into the stabilization cavity, these noise sources can be neglected in terms of the cavity's performance. For high-finesse cavities with finesse on the order of  $10^5$ , optical powers in the range of  $10^{-5}$  Watt are commonly used, resulting in a fractional frequency noise PSD caused by photon shot noise  $S_{y,SN}$  on the order of  $10^{-38} \text{ Hz}^{-1}$ . At frequencies around 1 Hz, this noise level is several orders of magnitude smaller than the frequency stability achieved by the best-known cavities to date [157]. Typically, the same holds true for electronic noise when a strong PDH signal is detected by the PDH diode, and adequate electronic devices are employed.

**Limits of optical path length stabilization:** Temperature and pressure fluctuations, as well as vibrations and distortion of optical components in a non-stabilized optical path, can introduce a significant amount of phase noise into the system. To mitigate these effects, phase stabilization, as discussed in Section 3.1.4, needs to be implemented. Nevertheless, unstabilized optical paths may persist, and disturbances in the reference path can also introduce phase noise through the stabilization feedback loop. Photon noise and electrical noise can also impact the accuracy of phase measurements through optical beats, and electrical noise in the phase-locked loop (PLL) can introduce additional phase noise to the laser. The latter can be assessed by analyzing the beat signal on the photodetector, which serves as an in-loop signal for phase stabilization. These noise sources are particularly pronounced on smaller timescales.

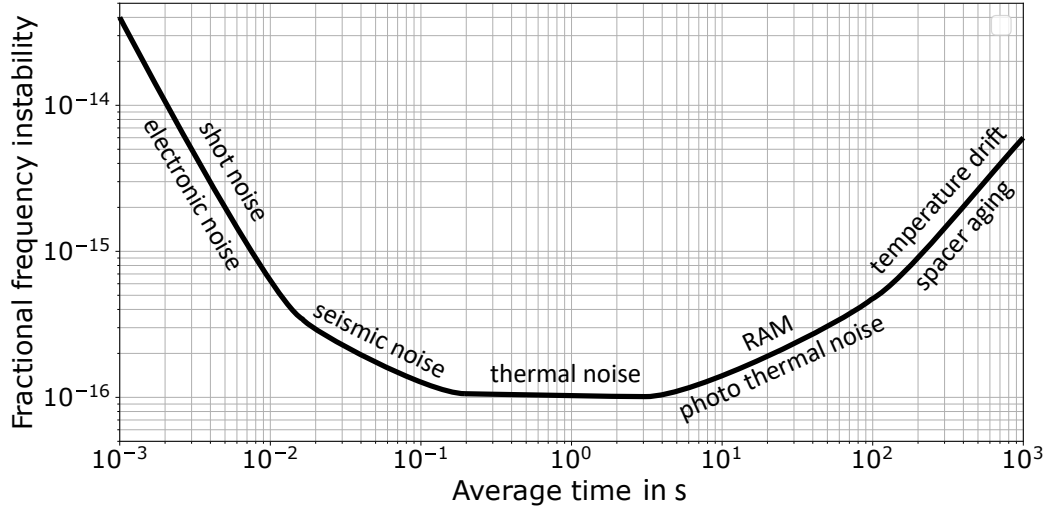


Figure 3.5: Noise sources reducing the frequency stability of highly stable optical cavities and their timescales. The identified noise sources include photon shot noise, electric shot noise, other electrical noise, seismic noise, thermal noise, RAM (Residual Amplitude Modulation), photo-thermal noise, temperature drift, and spacer aging. Each of these noise sources will be explained in detail in the text.

When employing a frequency comparison between two optical cavities via an optical comb, as explained in Section 3.1.5, these noise sources also affect the optical path of the reference cavity. Moreover, fluctuations in the carrier frequency and the repetition rate of the optical comb can introduce additional noise to the measurement and require stabilization. In such scenarios, the frequency noise induced by the optical path and the optical frequency comb may limit the measured fractional frequency instability, even if the laser frequency under investigation is more stable.

**Vibration noise:** Another noise source that can limit the frequency stability of the stabilization cavity is due to acceleration of the cavity. Acceleration introduces mechanical stress on the cavity, leading to displacement and misalignment of the two cavity mirrors. This results in an effective change in the optical length of the cavity and, therefore, in a shift in its resonance frequency. The acceleration, typically in the form of vibrations, is often caused by seismic activity, or mechanical devices with moving parts. Seismic noise often increase at frequencies higher than 1 Hz. Depending on the magnitude of vibrations, the effectiveness of vibration isolation of the cavity, and the frequency distribution, the frequency noise due to vibrations may compete with or exceed photon and electrical noise at timescales between 0.01 s and 1 s. To make the optical length of the cavity insensitive to vibrations, a special cavity mounting, along with vibration isolation platforms, is employed. Such mountings are reported for spherical [91, 224], cubical [97, 225], cylindrical [104, 107, 226–229] and double tetrahedral [104] cavities. Additionally, vibration isolation platforms are used to suppress the magnitude of the vibrations acting on the cavity.



**Thermal noise:** Another lower limit for the laser frequency instability is imposed by thermal noise. Thermal fluctuations in different parts of the cavity result in length variations, consequently leading to fluctuations in the cavity's resonance frequency. Thermal noise, along with its corresponding length changes, depends solely on the materials and geometry of the cavity. Therefore, it represents a fundamental limit specific to each cavity and cannot be technically mitigated like most other noise sources. Thermal noise encompasses various types of noise sources, such as Brownian noise, thermorefractive (TR) noise, and thermo-elastic (TE) noise, each affecting different components of the cavity.

Following fluctuation-dissipation theorem [230, 231], Brownian noise arises from the Brownian motion of particles within the cavity materials. The power spectral density (PSD) of the displacement  $S_x$  can be calculated using [232]:

$$S_{x,B} = \frac{4k_B T}{2\pi f} \text{Im}[H(f)] \quad (44)$$

Here,  $T$  represents the temperature, and  $\text{Im}[H(f)]$  is the transfer function relating the applied force to the resulting displacement.  $\text{Im}[H(f)]$  is proportional to the system's loss, which includes the mechanical loss factor  $\Phi$  representing energy damping in the material, as well as the elastic properties of the cavity material such as Young's modulus  $Y$  and Poisson's ratio  $\sigma$  [233]. For practical applications with complex cavity geometries, a finite element method is often utilized to calculate  $\text{Im}[H(f)]$  [234]. More detailed distributions of  $S_{y,B}$  can be found in various literature sources [232, 235–238]. As Brownian noise occurs in all cavity components, the total Brownian noise  $S_{x,B}$  is the sum of contributions from the spacer  $S_{x,B}^{(sp)}$ , the two mirror substrates  $S_{x,B}^{(sb)}$ , and the two mirror coatings  $S_{x,B}^{(ct)}$ :

$$S_{x,B} = S_{x,B}^{(sp)} + S_{x,B}^{(sb)} + S_{x,B}^{(ct)}. \quad (45)$$

Analytical expressions for each component have been derived [234]:

$$S_{x,B}^{(sp)} = \frac{4k_B T}{2\pi f} \frac{l_0}{AY} \Phi_{sp}, \quad (46)$$

$$S_{x,B}^{(sb)} = \frac{4k_B T}{2\pi f} \frac{1 - \sigma^2}{\pi Y} \frac{\Phi_{sp}}{\omega}, \quad (47)$$

$$S_{x,B}^{(ct)} = \frac{4k_B T}{2\pi f} \frac{2(1 + \sigma)(1 - 2\sigma)}{\pi Y} \frac{d}{\omega^2} \Phi_{sp}. \quad (48)$$

$\omega$  represents the beam radius,  $d$  denotes the coating thickness, and  $A$  corresponds to the end face area of the cylindrical spacer. For a cylinder with a hole, the area is given by  $A = \pi(r_{\text{out}}^2 - r_{\text{in}}^2)$ . Notably, improvements have been proposed by Harry et al. [235] to account for different elastic properties between the substrate and the coating. The calculation of Brownian noise in this work follows the method described by Herbers et al. [156, 239].



Taking the conversion  $S_x$  to  $S_y$  (Equation 34),  $S_{y,B}$  decreases for all three components with an increase in spacer length  $l_0$ . Furthermore, it can be shown that both  $S_{x,B}^{(sp)}$  and  $S_{x,B}^{(ct)}$  also decrease with a larger beam waist  $\omega$ , which is associated with a longer spacer length  $l_0$ . The fractional frequency noise  $S_{y,B}$  resulting from Brownian noise exhibits a typical 1/f behavior, commonly referred to as flicker frequency noise. In the time domain the fractional frequency instability of the cavity, calculated using the modified Allan deviation, remains constant for flicker noise, as demonstrated in Section 3.1.6. Since Brownian noise is influenced by the mechanical loss factor  $\Phi$ , Poisson's ratio  $\sigma$ , and Young's modulus  $Y$ , the choice of suitable materials can help reduce Brownian noise. Specifically, low-mechanical-loss materials are commonly utilized to minimize the effects of Brownian noise. A comprehensive discussion on appropriate materials for cavity construction can be found in [156, 233].

Additionally, thermal dissipation results in temperature fluctuations in the cavity components [240]. Thermal expansion of these components leads to fluctuations in the cavity length and, hence, in frequency. This noise is known as thermo-elastic (TE) noise. Temperature fluctuations also affect the refractive index of the mirror coating, resulting in a change of the optical length of the cavity and leading to frequency noise. This noise is known as thermo-reflective (TR) noise. Collectively, TE and TR noise are referred to as thermo-optic (TO) noise.

In the case of TE noise, the thermal expansion of all cavity components induces deformation and strain, impacting the length of the cavity between the two mirrors. However, for TR noise, only the components traversed by the laser beam contribute to the total TO noise of the cavity. Since the light passes through the mirror substrate only twice when entering or leaving the cavity, TE noise from the substrate can be neglected compared to TE noise. As the light penetrates the coating during each round trip, TO noise in the coating strongly affects the effective cavity length experienced by the laser beam. Due to the opposite effects of TE and TR noise in the coating, careful selection of cavity coatings can lead to a partial cancellation of TO noise [241–243]. The resulting fractional frequency power spectral density (PSD) due to TO noise can be calculated by summing its individual components:

$$S_{y,TO} = S_{y,TE}^{(sp)} + 2S_{y,TE}^{(sb)} + 2S_{y,TO}^{(ct)}. \quad (49)$$

Thermal noise of each component is discussed in various literature sources [232, 234, 235, 237, 238, 240, 241, 243–251]. In this work, the same method as presented by Herbers et al. [156, 239] is employed to calculate the thermal noise. The cavity examined in this study consists of an ultra-low expansion (ULE) glass spacer, fused silica mirror substrates, and single crystal GaAs/AlGaAs coatings. The PSD fractional frequency instability resulting from thermal noise and its components for this cavity are calculated and shown in Figure 3.6 (right). As Brownian noise is the main contributor, the thermal noise exhibits a frequency-dependent flicker noise behavior with a 1/f power spectral density. The corresponding modified Allan deviation, depicted in Figure 3.6 (left), remains nearly constant. When all other noise sources are sufficiently suppressed, thermal noise becomes the limiting factor for the frequency stability of the cavity.

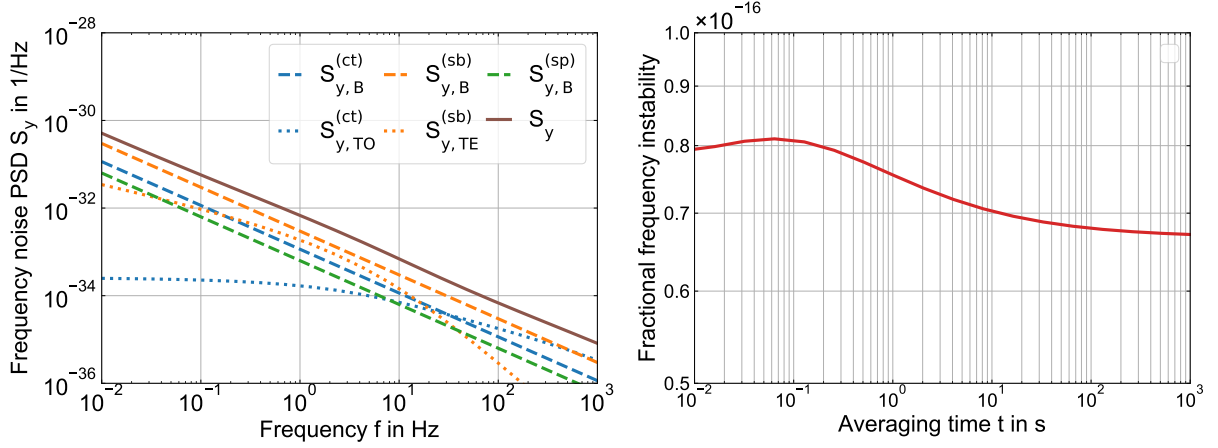


Figure 3.6: Calculation of cavity frequency instability resulting from thermal noise. Right: Power spectral density (PSD) of the fractional frequency instability for various thermal noise components. These include the Brownian noise of the coating  $S_{y,B}^{ct}$  (blue dashed line), Brownian noise of the substrate  $S_{y,B}^{sb}$  (orange dashed line), Brownian noise of the spacer  $S_{y,B}^{sp}$  (green dashed line), thermal-optic noise of the coating  $S_{y,TO}^{ct}$  (blue dotted line), and thermo-elastic noise of the spacer  $S_{y,TE}^{sb}$  (orange dotted line). The overall thermal noise of the cavity  $S_y$  is shown by the brown line. Left: Modified Allan deviation of the fractional frequency instability caused by thermal noise.

This is typical the cause on medium timescales, approximately between  $1 \times 10^{-1}$  s and  $1 \times 10^2$  s, as shown in Figure 3.5 (left). For a given cavity, thermal noise represents a fundamental lower limit for the frequency stability. In this work, all other noise sources are compared to this thermal noise limit for evaluation purposes.

**Photo-thermal noise:** The physical nature of photo-thermal (PT) noise is the same as that of thermo-optic noise. However, photo-thermal noise is not driven by intrinsic heat dissipation. Instead, it arises due to fluctuations in the optical power inside the cavity, leading to variations in the heat absorbed by the mirrors. When the optical power remains constant, the fundamental limit is determined by the shot noise of the absorbed radiation [240]. However, any change in the optical power of the laser beam coupled into the cavity leads to a variation in the cavity's optical length following the same mechanisms as thermal-optic noise. Similar to TO, PT noise can be further categorized into photon-thermo-elastic noise (PTE), which arises from the thermal expansion of the material, and photo-thermal-refractive noise (PTR), which results from the thermal effect on the material's refractive index. Since light absorption occurs only in the two mirror coatings and substrates, the fractional frequency power spectral density (PSD) attributed to photo-thermal noise is expressed as follows:

$$S_{y,PT} = 2S_{y,PTE}^{(sb)} + 2S_{y,PTE}^{(ct)} + 2S_{y,PTR}^{(ct)}. \quad (50)$$

In a steady-state cavity, the absorbed optical power  $P_{ab}$  at one mirror is proportional to the intracavity power  $P_{cav}$ , which in turn is proportional to the coupling power  $P_{in}$ . This relationship can be calculated as follows:

$$P_{ab} = aP_{cav} = \frac{aF}{\pi}P_{in}. \quad (51)$$

Here,  $a$  represents the absorption coefficient of one mirror. The total losses  $L$  of the cavity consist of the sum of the losses  $l$  of each mirror and the transition  $T$  at each mirror. The loss at each mirror  $l$  includes both the absorption coefficient  $a$  and the scattering coefficient  $s$ . Mathematically, we can express the total losses as  $L = l_1 + l_2 + T_1 + T_2$ . For a cavity with two similar mirrors, this simplifies to  $L = 2l + 2T$ . The finesse of the cavity, denoted as  $F$ , can be calculated as  $F = \frac{2\pi}{L}$ . The losses of the mirror can be directly measured before constructing the cavity, or they can be calculated if the finesse, transmitted cavity power  $P_t$ , and coupled power  $P_{in}$  are known, using the following formula [252]:

$$\frac{P_t}{P_{in} - P_t} = \frac{T^2 \frac{F^2}{\pi}}{1 - l^2 \frac{F^2}{\pi}}. \quad (52)$$

The transmitted power  $P_t$  can be measured behind the cavity, while the power difference  $P_{in} - P_t = P_{inc} - P_r$  can be obtained by measuring the incoming light power  $P_{inc}$  and the reflected light power  $P_r$  before the cavity. However, the scattering coefficient  $s$  and the absorption coefficient  $a$  are often not precisely known. It is worth noting that for fluctuations of the coupling power  $\delta P_{in}$  with frequencies lower than the cutoff frequency of the cavity, Equation 51 still holds. However, for higher frequencies, the cavity behaves as a low-pass filter for optical power fluctuations  $\delta P_{ab}$ :

$$\delta P_{ab}(f) = \frac{aF}{\pi} \frac{\delta P_{in}}{1 + \frac{if}{f_c^{cav}}}. \quad (53)$$

The cut off frequency of the cavity  $f_c^{cav} = \frac{\delta\nu}{2}$  is given by the FWHM linewidth  $\delta\nu$ . For a high finesse cavity this is usually on the order of kHz. An additional low-pass effect arises due to the delayed thermal response of the mirror to changes in absorbed optical power. The heating response time of the mirror is determined by the material's heat conductivity  $k$  and thermal capacity  $C$ . The corresponding cutoff frequency can be estimated as follows:

$$f_c = \frac{k}{2\pi\omega^2\rho C}, \quad (54)$$

where  $k$  represents the heat conductivity and  $C$  represents the thermal capacity. The cutoff frequency  $f_c$  depends on the material properties and the beam waist  $\omega$ . Typically, the cutoff frequency  $f_c$  is smaller than the cavity cutoff frequency  $f_c^{cav}$  of the cavity and the latter can be neglected. The photo-thermo-elastic noise  $S_{y,PTE}$  can be calculated using the following equation:

$$S_{y,PTE} = \frac{\sqrt{2}\alpha(1 + \sigma)}{\pi l^2} \frac{\delta P_{ab}(f)}{(\rho C \pi \omega^2) i f}. \quad (55)$$

In this equation,  $\alpha$  represents the thermal expansion coefficient,  $\sigma$  represents Poisson's ratio,  $l$  is the length of the cavity,  $\delta P_{ab}(f)$  denotes the fluctuations in absorbed

power,  $\rho$  is the density,  $C$  is the heat capacity,  $\omega$  represents the beam waist, and  $f$  denotes the frequency. Theoretical models and a comprehensive description of photo-thermal noise can be found in various literature sources [241, 250, 253, 254]. The transfer function  $\chi_{PT}$  scales with  $1/f$  for higher frequencies and becomes constant for lower frequencies. This characteristic helps in suppressing the effect of fluctuations in the absorbed optical power  $\delta P_{ab}(f)$  on the optical length fluctuation of the cavity for higher fluctuation frequencies. However, fluctuations or drifts in the coupled optical power  $\delta P_{ab}(f)$  usually occur at longer timescales. Therefore, photo-thermal noise becomes a significant noise source at longer timescales, as illustrated in Figure 3.5. To achieve high stability in a cavity, it is essential to mitigate photo-thermal noise through power stabilization techniques. This can be accomplished by ensuring that the optical power within the cavity remains stable.

**RAM:** An explanation of RAM and a RAM stabilization scheme is presented in Section 3.1.3. RAM is frequently caused indirectly by temperature-related processes in the optical components involved. Consequently, the timescale of RAM is comparable to the timescale of temperature fluctuations. As a result, unstabilized RAM usually imposes limitations on laser frequency stability at longer timescales, similar to photo-thermal noise. To mitigate RAM, temperature stabilization of the EOM and shielding of optical elements against temperature fluctuations can be employed.

**Temperature drift:** Temperature drifts can impose limitations on the frequency stability of the cavity. The coefficient of thermal expansion (CTE) of the cavity, primarily determined by the thermal expansion of the spacer, plays a crucial role in the influence of temperature fluctuations and drift. Therefore, materials with low thermal expansion coefficients are utilized. Ultra-low expansion (ULE) glass is commonly used for the spacer, as it exhibits a low CTE and even reaches zero at the CTE zero crossing temperature. To suppress frequency variations caused by temperature changes, it is beneficial to employ multiple passive heat shields to shield the cavity. These shields act as low-pass filters for temperature changes. Additionally, the temperature should be actively stabilized using an active heat shield set at the zero crossing temperature. The remaining frequency variations due to temperature changes are typically small but typically become relevant for longer averaging times of more than 100 s, as depicted in Figure 3.5.

**Spacer aging:** In addition to temperature drift, frequency drifts resulting from the aging of the cavity spacer made of ULE glass have been observed. These aging effects lead to a continuous drift of the resonance frequency of the cavity over time. On time scales of several years the drift decays exponentially and is attributed to the ongoing crystallization of the glass [255, 256]. For a similar cavity, a drift of  $23 \text{ mHz s}^{-1}$  has been observed [156]. Although the drift is relatively small, the effect becomes most significant for long averaging times, similar to temperature drift, as shown in Figure 3.5.

**Pressure fluctuations:** The optical length of the cavity depend on the refractive index  $n$  of the material located between the two mirrors. A change in the refractive index  $\delta n$  results in a change in the optical cavity length  $\delta l = l_0 \delta n$ . This, in turn, leads to a change in the fractional frequency  $\delta f/f_0 = -\delta n$ . The refractive index of air is influenced by pressure and temperature and can be described by the Edlén equation [257]. For light at a wavelength of 1070 nm and under standard conditions, the equation is given by:

$$n - 1 = [2.81 \times 10^{-9} \text{ Pa}] \cdot p, \quad (56)$$

which results in a fractional frequency fluctuation of:

$$\delta f/f_0 \approx [2.81 \times 10^{-9} \text{ Pa}] \cdot \delta p. \quad (57)$$

To achieve a fractional frequency stability below  $10^{-16}$ , pressure fluctuations need to be suppressed to  $\delta p < 3.5 \times 10^{-8} \text{ Pa}$ . This can be achieved by evacuating the cavity. With modern pumps, vacuum pressures in the  $10^{-7} \text{ Pa}$  range can be easily achieved, and pressure fluctuations between the two mirrors are expected to be well below  $10^{-8} \text{ Pa}$ .

**Birefringence and photo-birefringence noise:** For some materials the refractive index depends on the polarization of the light, this effect is known as birefringence. Crystalline mirror coatings, in particular, demonstrate a significant birefringence effect due to the orientation of their crystal structure relative to the polarization of the incident light. During circulation inside the cavity light penetrate the mirror coating, while the effective penetration length depends on the refractive index of the mirror coating. As a result, the optical length of the cavity depends on the polarization of the light inside the cavity. Hence, two degenerate polarization modes of the cavity, separated by the birefringence line splitting exist. Standard theory considers the line splitting to be constant and independent of external influences like the power of the coupled light. However, changes in the birefringence line splitting depending on the optical power in the cavity have been observed for crystalline AlGaAs/GaAs coating [258, 259]. This effect is known as photo-birefringence noise. Furthermore, intrinsic birefringence noise, independent of optical power fluctuations, has also been observed [258, 259]. The physical reason behind this process is not yet known.

## 3.2 Setup of the reference cavity

The cavity is specifically designed for a wavelength of 1070 nm. The cavity was built by Sofia Herbers and its design closely follows the design of another cavity operating at 1397 nm as presented in the work by Herbers et al. [156, 239]. In this section, a brief overview of the mechanical design of the cavity and the optical setup is provided. The stabilization cavity is intended for use in a portable optical clock, and the entire setup is integrated into a 19-inch rack configuration.

### 3.2.1 Design of the stabilization cavity

The cavity primarily consists of a cylindrical cavity spacer made of ULE glass, measuring 20 cm in length, shown in Figure 3.7 (top left). Two coated mirrors are optically



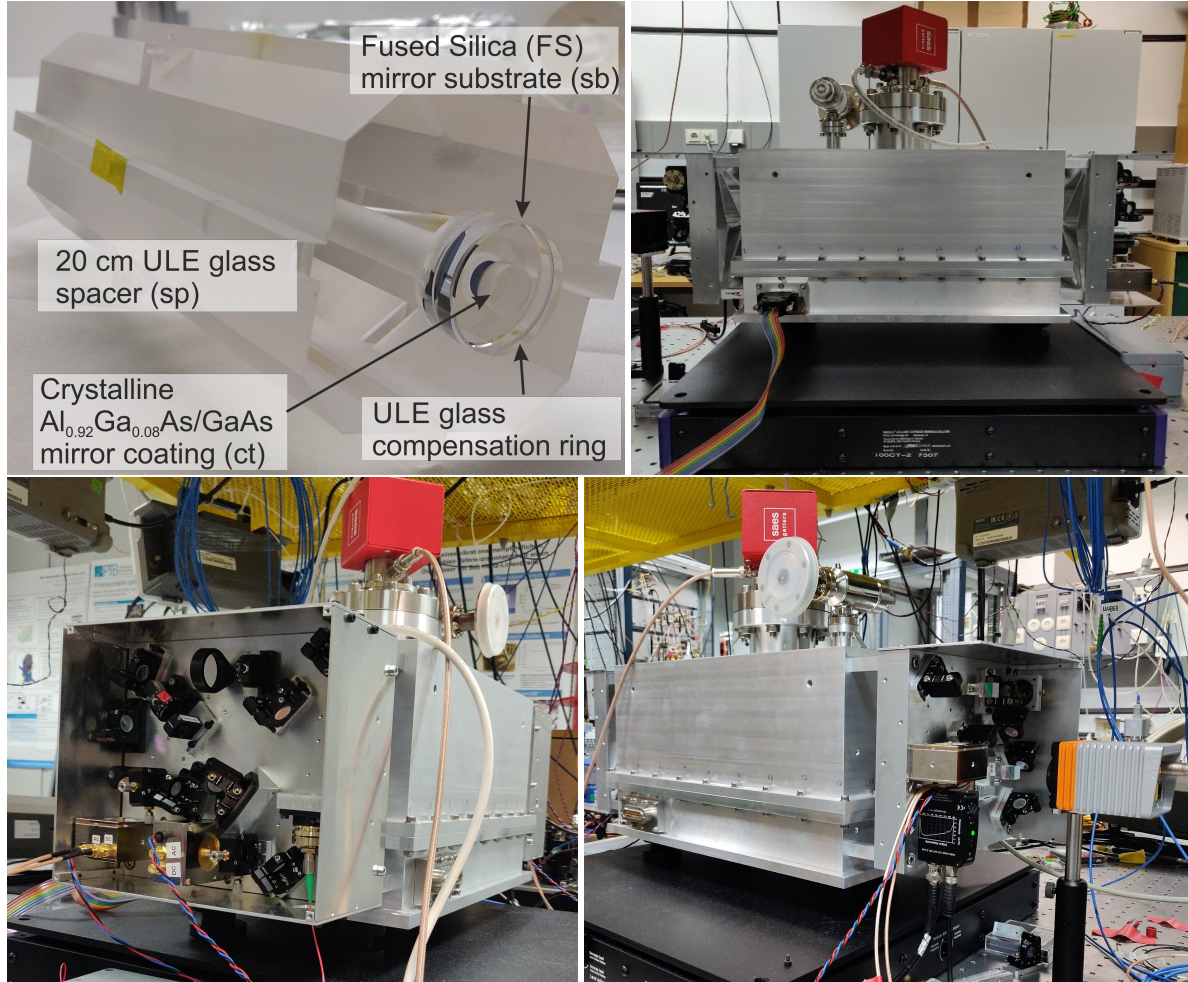


Figure 3.7: Image of the optical cavity. Top left: Cavity spacer with fused silica mirrors with crystalline AlGaAs/GaAs coating and ULE compensation rings. Top left: The cavity is inside the vacuum chamber placed on a passive vibration isolation table. The vacuum system comprises a valve and a combination of a NEG and an ion pump<sup>2</sup> to facilitate the pumping down process and maintain the desired vacuum within the chamber. Bottom left: PDH breadboard and cavity system from the front side. Bottom right: Power stabilization breadboard and cavity system from the back side. A detailed description is given in the text. Images are provided by Sofia Herbers [156].

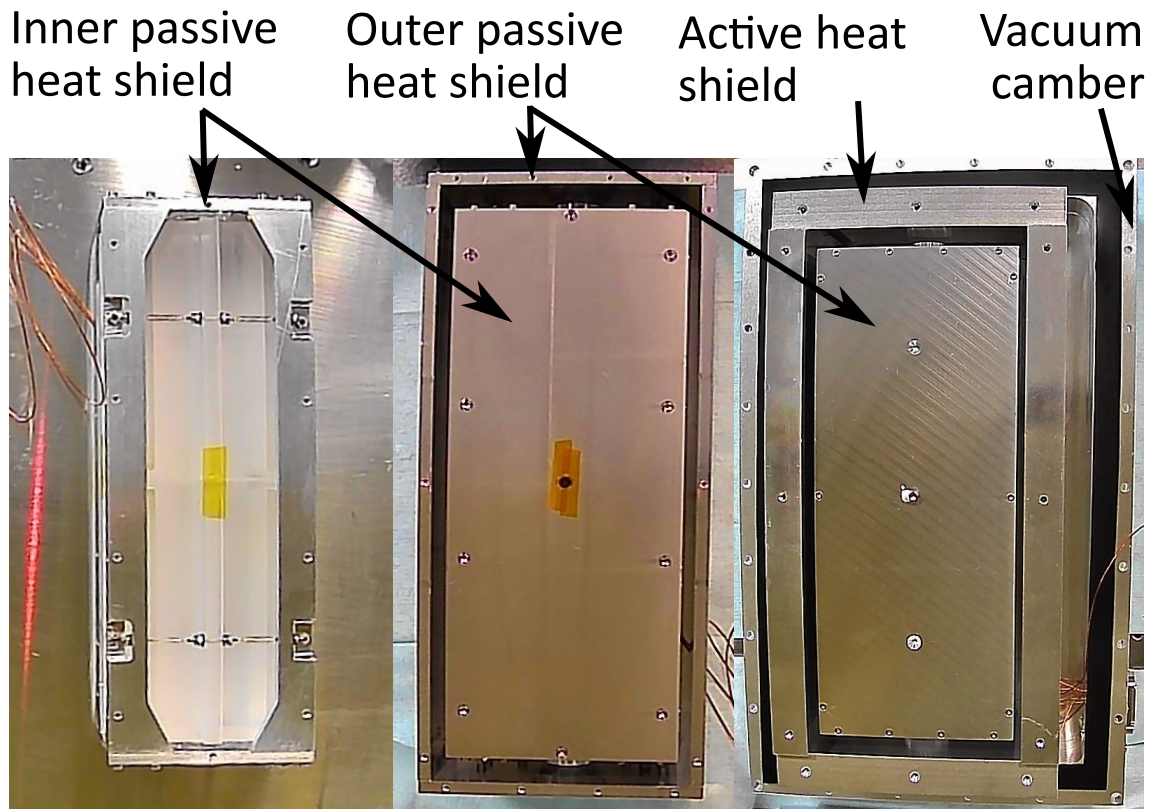


Figure 3.8: Active and passive heat shields of the cavity. The Vacuum chamber and the shield (active heat shield) are temperature stabilized with Peltier elements. Images are provided by Sofia Herbers [156].

contacted to the spacer using ULE glass compensation rings [260]. The mirror substrate is made of fused silica, and a high reflectivity coating (AlGaAs/GaAs single crystalline) [248, 261–263] is applied. The cavity is housed within two passive heat shields, which are further enclosed within an active heat shield. This entire assembly is placed inside a vacuum chamber, as depicted in Figure 3.7 (top right). To ensure proper mechanical stability and vibration isolation, the cavity spacer is attached to the inner passive heat shield using a flexible spring suspension. This allows transportation of the cavity without risk of damaging the optical alignment and provides a good vibration isolation of the cavity. The mounting concept uses the optimal suspension points to minimize optical displacement of the mirrors under acceleration, providing additional vibration insensitivity [101, 107, 156].

NTC5K temperature sensors are strategically placed within the passive heat shields, near the cavity, and at various positions on the active heat shields. The active heat shield is heated or cooled using four Peltier elements positioned between the active heat shield and the vacuum chamber. The vacuum chamber itself is also temperature stabilized using Peltier elements positioned between the chamber and a breadboard that holds the vacuum chamber. All shields, including the passive and active heat shields, are made of aluminum for efficient thermal conductivity. Glass spheres are used to separate the shields, ensuring good thermal isolation. The vacuum chamber,

also made of aluminum, is equipped with a valve to connect it to a turbo pump. Initially, the turbo pump is used to evacuate the vacuum chamber, but it is disconnected afterwards. Additionally, a combination of a non-evaporable getter (NEG) and an ion pump<sup>3</sup> is installed on the vacuum chamber (see Figure 3.7, top right). This pump continuously operates to maintain the vacuum at a level of  $10^{-7}$  Pa. The advantage of using the NEG and ion pump combination over a turbo pump is the minimal mechanical vibration noise. As the mechanical vibrations of a turbo pump can significantly affect the frequency stability of the cavity.

### 3.2.2 Optical setup

The optical setup for laser frequency stabilization is constructed on four separate breadboards, namely the double-pass AOM setup, the distribution board, the PDH locking board, and the optical power stabilization board. The distribution board was designed and set up by Eileen Klocke as part of her master thesis [264]. The PDH locking board, and the optical power stabilization board was build by Dewni Pathegama as part of a student project. A schematic representation of the optical path can be seen in Figure 3.10.

**Double-pass AOM board:** A fiber laser with an instantaneous linewidth of 10 kHz serves as the light source, and its output is amplified by a fiber amplifier. To compensate for slow frequency drifts of the laser, the PDH scheme employs direct control of the laser frequency. In addition to the PDH slow control, a double-pass AOM setup is utilized to lock the frequency of the fiber laser to the resonance frequency of the cavity using the fast control of the PDH locking technique. The double-pass AOM setup is constructed on a dedicated breadboard, with the input and output being fiber coupled. Since the laser power can reach up to 5 W, a free-space setup is chosen. However, there are plans to change to a commercial fiber-coupled AOM setup if feasible.

**Distribution board:** The distribution board, shown in Figure 3.9, is a standalone breadboard designed to be integrated into a standard 19-inch rack configuration. To maintain a compact setup, half-inch optics are utilized. The board itself is constructed from aluminum and features individually drilled threads for each optical component. It is designed to be robust and incorporates support structures at the bottom to strike a balance between mechanical stability and weight. The board is enclosed by walls made of aluminum sheeting, with a flexible plastic lid. It is connected to the bracket using three vibration-isolated connectors, which ensures secure mounting. The bracket, in turn, is connected to the 19-inch rack using rails, enabling the board to be easily slid out for improved accessibility to the optical setup.

The optical setup on the board is connected with other optical setups via optical fibers. The light from the double-pass AOM setup is coupled onto the distribution board through an input fiber using a beam collimator. A Faraday isolator is employed to prevent any detrimental back-reflections from reaching the laser system. The light is

---

<sup>3</sup>SAES, Nextorr Z200



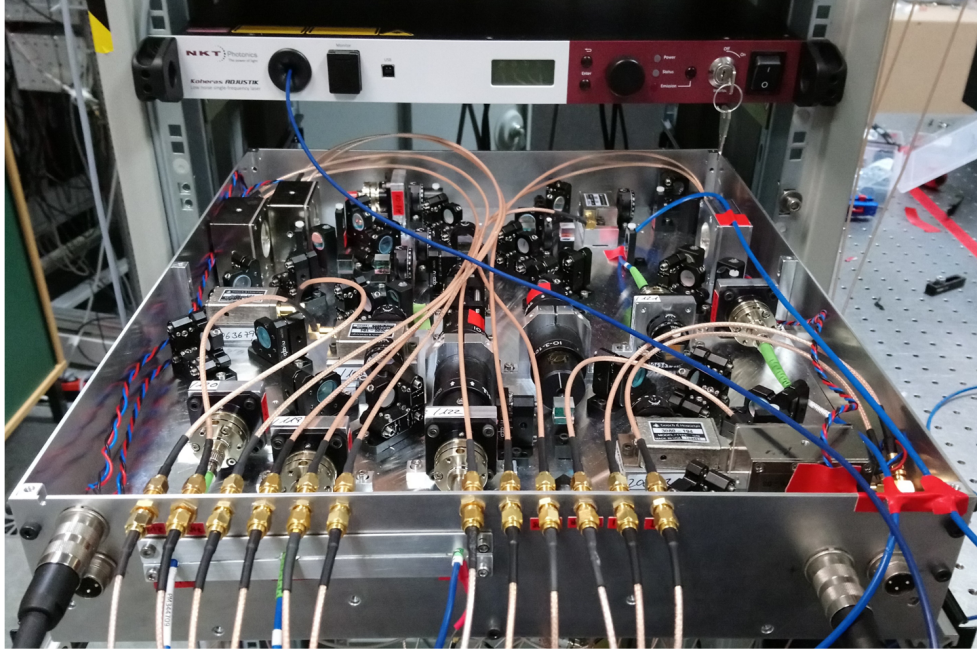


Figure 3.9: Optical distribution breadboard. The light is divided and directed to multiple fiber ports. Each optical path on the breadboard is equipped with an optical path length stabilization mechanism. The breadboard itself is designed in a robust manner and seamlessly integrated into a rack for convenient use and stability. Image was provided by Sofia Herbers [156].

divided into four paths using a waveplate and a polarized beamsplitter (PBS) for each path. Each path features an interferometric optical path length stabilization scheme, similar to the one discussed in Section 3.1.4, with the reference points closely together on the distribution board. For specific details on the setup of each path, refer to the optical setup outlined in the gray area in Figure 3.10. In the first path, a double-pass AOM setup is employed to shift the laser frequency to nearly half of the cavity's free spectral range, if necessary. Each output port is equipped with a collimator to couple the laser beam into an optical fiber. The first port is connected to the PDH breadboard via a fiber-coupled waveguide EOM, supplying light to the cavity. Here, the optical path length can not be directly stabilized, as a back reflection mirror before the cavity would affect the PDH locking. The second port is linked to the power stabilization breadboard positioned behind the cavity. The back reflection mirror for the optical length stabilisation scheme is on the power stabilization breadboard. This connection is crucial for the phase stabilization scheme implemented in this setup. The third port is connected to a frequency comb, which can be used for clock operation or for comparison measurements with a second reference cavity or another optical clock. Here, the back reflection mirror is positioned in the optical set up of the frequency comb. The fourth port is connected to the ion spectroscopy experiment via a frequency quadrupling stage, which will be discussed in the second part of this work. The back reflection mirror, for phase stabilization, is placed behind the frequency quadrupling system as close to the ions as possible.

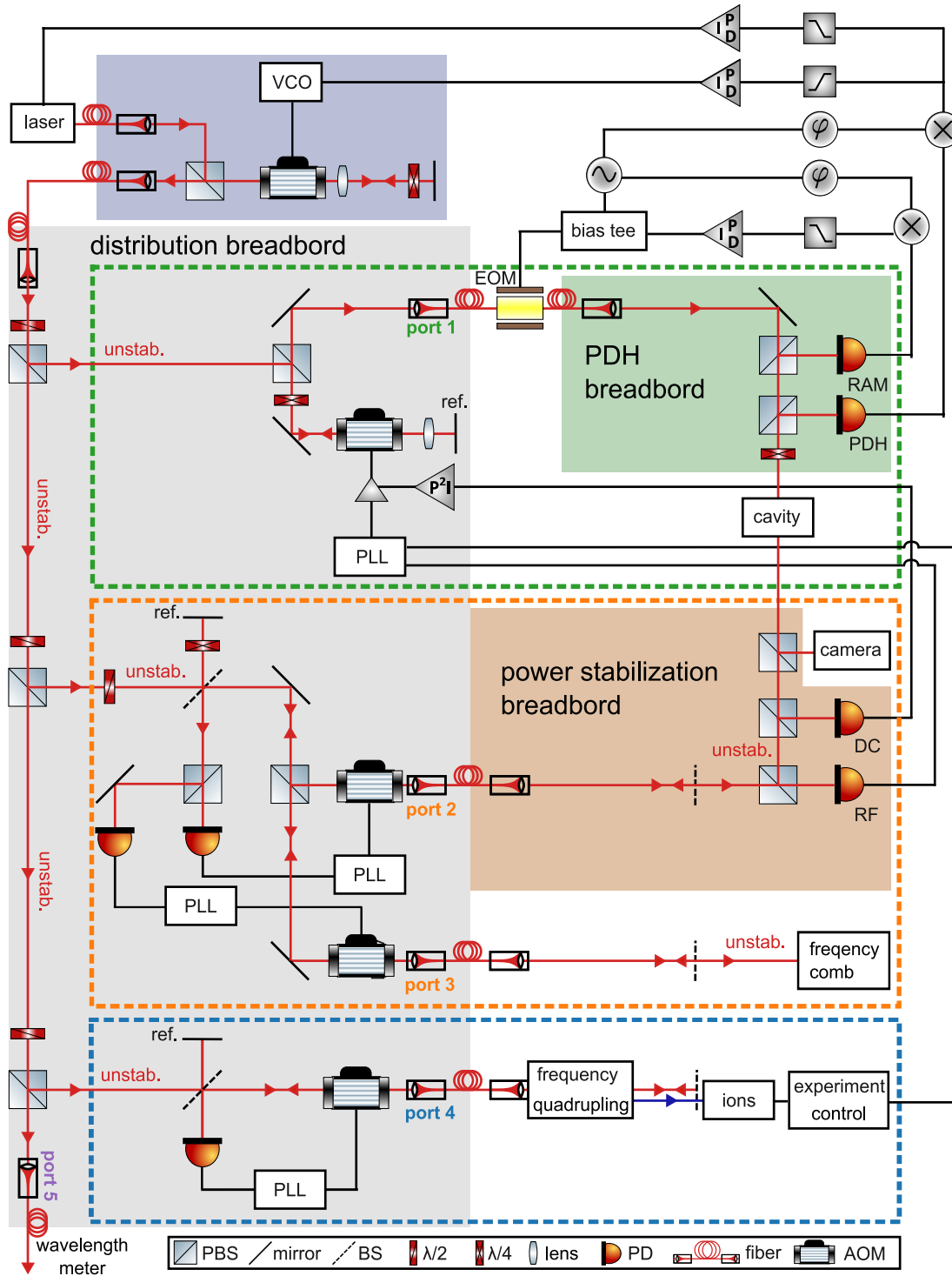


Figure 3.10: Schematic drawing of the locking setup of the reference cavity. The distribution board (grey area) houses four optical paths, each equipped with optical path length stabilization. These paths are connected to the PDH breadboard (green area) located on the front side of the cavity, as well as the power stabilization breadboard (orange area) through optical fibers connected to port 1 and port 2, respectively. Port 3 serves as a connection to an optical frequency comb, while port 4 is linked to a frequency quadrupling system and an associated experiment. The reference point (ref.) for phase stabilization and the remaining unstabilized (unstab.) optical paths are marked.

The limit of the phase stabilization is measured using a beat measurement with a common laser source. This involves overlapping the light from two different ports using a 50:50 beamsplitter after it leaves the optical fiber. A partially transparent mirror is placed behind the beamsplitter to create the necessary reflection for optical path length stabilization. A photodiode is positioned after the mirror to measure the beat frequency resulting from the interference of the laser beams from the two ports. It is important to note that the frequency shift is different for each port. Port 3 is designated as a link to the frequency comb. Beat measurements are carried out for each port against port 3. In addition to measuring the out-of-loop beat signal, the in-loop control signal is actively phase stabilized and recorded [264]. The results are presented in Figure 3.11, showing the fractional frequency instability of the different optical paths. The fractional frequency instability is calculated using the modified Allan deviation. The in-loop signal of port 3 and the compared port are limited by electronic noise in the optical path stabilization electronics. This noise also limits the phase stability of the out-of-loop measurement between the two ports. The reason for this is given by electronic noise in the PLL. The fundamental limit is given by the phase different accumulated during the delay time of the phase measurement signal. This delay time is fundamentally given by delay time of the light running through the optical setup twice, and the delay time of the electric signal. Moreover, non-compensated phase noise in the optical path contributes additional frequency noise to the out-of-loop measurement. To stabilize the laser frequency on the resonance frequency of the cavity, a fractional frequency instability below  $1 \times 10^{-17}$  is required. The measured fractional frequency instability for all optical paths is more than one magnitude lower than this value on the relevant timescales. Furthermore, the required fractional frequency instability of  $1 \times 10^{-18}$  for clock operation is achieved for all ports when longer averaging times are considered.

**PDH breadboard:** The PDH breadboard houses the optics necessary for the PDH locking scheme, as explained in Section 3.1.2. It also includes the RAM stabilization scheme described in Section 3.1.3. The breadboard is directly connected to the front side of the cavity using four robust connectors, as depicted in Figure 3.7 (bottom left). The PDH breadboard incorporates the PDH photodiode and the RAM photodiode. To prevent the formation of etalons, several Faraday isolators are implemented within the setup. The laser beam is coupled into the cavity through a hole in the breadboard. The breadboard itself is constructed from aluminum, and support structures are employed to enhance its mechanical stability. It is enclosed by walls made of aluminum sheeting, with a flexible plastic lid. It is important to note that the optical path length of the first port cannot be directly interferometrically stabilized, as this would disrupt the PDH locking scheme. However, a phase stabilization of the laser to the light transmitted by the cavity is implemented on the power stabilization breadboard behind the cavity.

**Power stabilization breadboard:** The power stabilization breadboard is positioned at the backside of the cavity, following a similar configuration as the PDH breadboard. The setup of the power stabilization breadboard is depicted in Figure 3.7 (bottom right). The light transmitted through the cavity is divided by a 90:10

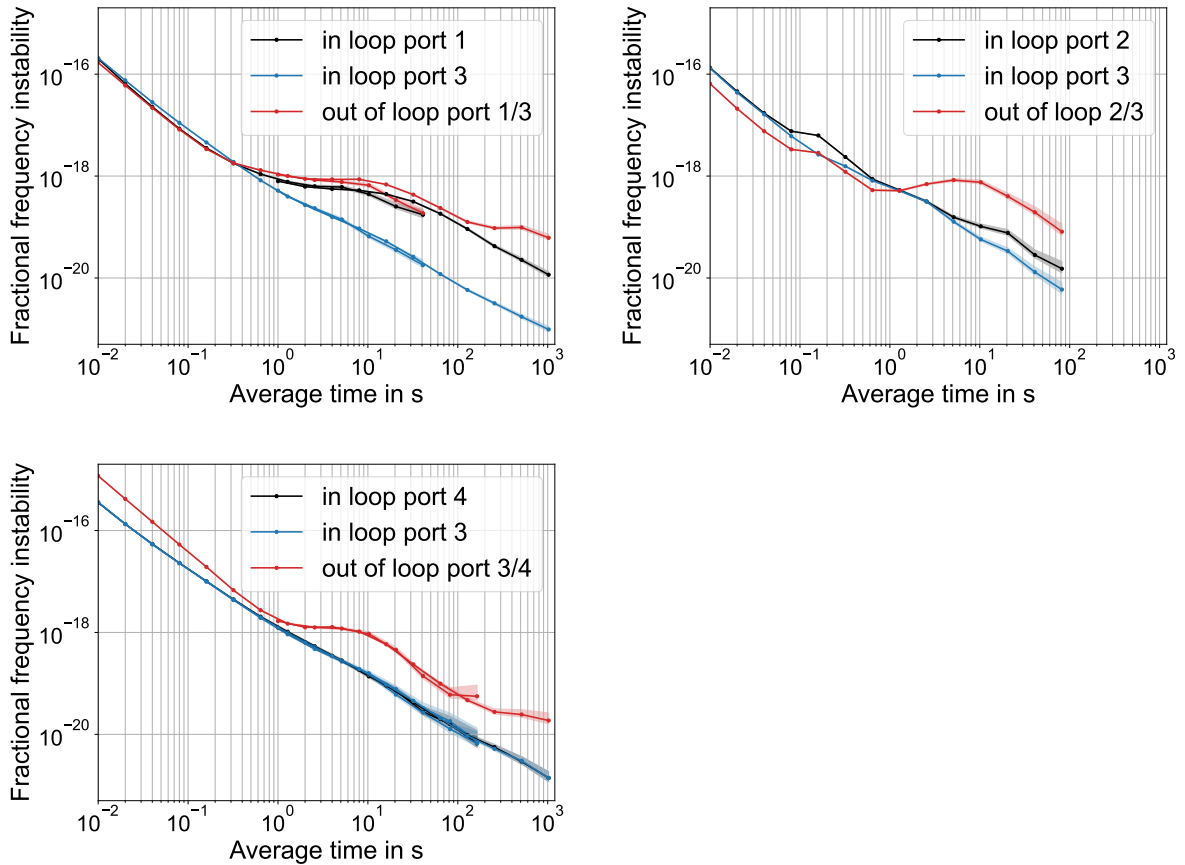


Figure 3.11: Modified Allan deviation of the fractional frequency instability of the different optical paths on the distribution board. Top left: Measurement of the out of loop frequency instability of port 1 compared to port 3 (red line). Also shown the in-loop signal of the active optical path length stabilization of port 1 (black) and of port 3 (blue). Top right: Measurement of the frequency instability of port 2 compared to port 3 (same color coding). Bottom left: Measurement of the frequency instability of port 4 compared to port 3 (same color coding).

beamsplitter, with 10% of the light directed outside the breadboard. This allows for positioning a camera to monitor the stimulated mode of the cavity. The majority of the light is directed to a photodiode, which measures the intensity of the optical light transmitted through the cavity. The signal from the photodiode is then used to stabilize the optical power within the cavity. To achieve power stabilization, a PID controller is employed to regulate the power of the RF amplifier for the double-pass AOM located before the cavity. The power stabilization breadboard is connected to port 2 via an optical fiber. The optical length of the light path at port 2 is stabilized using a reflective beamsplitter located on the PDH breadboard. By interfering the light from port 2 with the light transmitted by the cavity, any phase shift between these two beams can be measured. This is achieved by superimposing the two beams and detecting the resulting beat signal on a photodiode. The beat signal detected by the photodiode is used for phase stabilization of the light that is coupled into the cavity.

### **3.2.3 Integration into a standard 19-inch rack**

The stabilization cavity and the distribution board are both integrated into a standard 19-inch rack. The distribution board is mounted on a construction with retractable rails, allowing it to be slid out of the rack for easy access and modification of the optical alignment. Similarly, the stabilization cavity is placed on an aluminium breadboard, which is also mounted on rails to facilitate sliding out of the rack if needed. The active vibration isolation table is positioned on top of the breadboard. Another breadboard is placed on top of the vibration isolation table, serving as the platform for the stabilization cavity. The cavity is secured to this breadboard using flexible clamps. Four Peltier elements are installed between the stabilization cavity and the breadboard, enabling temperature stabilization of the outer shield of the cavity. Two PT1000 temperature sensors are also placed on the outer shield to monitor and control the temperature. This temperature stabilization helps to minimize temperature fluctuations within the various heat shields, resulting in lower temperature instability of the cavity itself and reduced temperature-induced mechanical stress on the heat shields and vacuum shield. To further protect the system from temperature fluctuations and vibrations in the environment, the cavity is isolated and the entire setup is enclosed within an isolated wooden box. Placing the construction on the bottom of the rack helps to minimize temperature fluctuations and vibrations as well.

During transportation, all the rails, including those for the distribution board and the stabilization cavity, are secured to prevent sliding or movement. In addition, inflatable passive vibration isolation mounts are installed between the first and second breadboards. To protect the active vibration isolation table during transport, these mounts are inflated during transportation, effectively supporting the weight of the cavity and providing vibration isolation. Once the rack reaches its destination and before the measurements begin, the inflatable mounts are vented, allowing the stabilization cavity breadboard to be fully supported by the active vibration isolation table. This setup provides optimal vibration isolation and stability for the cavity during the measurement process.

### 3.3 Characterisation of the stabilization cavity

In the following section the stabilization cavity is characterized. First the finesse of the cavity and the separation frequency of modes with different polarization due to birefringence of the crystalline mirrors are measured. Afterwards the most important frequency noise sources as explained in Section 3.1.6 are characterized. This includes frequency noise due to vibration, photo-thermal noise, temperature drifts and RAM. Finally the frequency instability of the stabilized laser is measured against a more stable optical reference and compared to the characterized frequency noise limits.

#### 3.3.1 Finesse, cavity linewidth and birefringence

The finesse of a cavity can be determined using the ring-down method. When the laser light directed into the cavity is abruptly switched off, the electric field inside the cavity decreases. This decay process takes time due to the finite speed of light and the multiple reflections between the two mirrors. The decay of the electric field inside the cavity follows an exponential decay, characterized by  $e^{-t/t_d}$ . The decay time  $t_d$  is related to the losses of the cavity and is proportional to the finesse. Therefore, the finesse can be calculated using the equation:

$$F = 2\pi\nu_{FSR}t_d \quad (58)$$

The free spectral range of the cavity, denoted as  $\nu_{FSR}$ , can be determined from its length, which is  $l = 200$  mm resulting in  $\nu_{FSR} = 750$  MHz. To observe the decay of the transmitted light, a photodiode is used. Figure 3.12 displays the results of one of the measurements (black line). The data is fitted with a double exponential function (orange line), taking into account the decay time of the photodiode, which is approximately  $20 \mu\text{s}$ . From the measured decay time  $t_d = (43 \pm 1) \mu\text{s}$  of the  $\text{TM}_{00}$  mode of the cavity, the finesse  $F = 202000 \pm 5000$  is calculated. The linewidth of the cavity can be determined as  $\delta\nu = \nu_{FSR}/F = (3.7 \pm 0.1)$  kHz.

The birefringence of crystalline mirrors  $\Delta n_{bi} = n_{slow} - n_{fast}$  results in a splitting of the frequency of the cavity modes corresponding to the two different polarization. The birefringence frequency splitting  $\Delta\nu_{bi}$  between the fast and slow polarization modes is given by

$$\Delta\nu_{bi} = 2f_0\Delta n_{bi}\frac{l_{pen}}{l_0}. \quad (59)$$

The penetration depth  $l_{pen}$  of the light into the coating can be expressed by the delay time  $t_{delay}$  and the average refractive index of the coating  $n_{ct}$ .

$$l_{pen} = \frac{ct_{delay}}{2n_{ct}}. \quad (60)$$

For a coating with alternating layers with reflective index  $n_H$  and  $n_L$ , the delay time is approximately given by [265]:

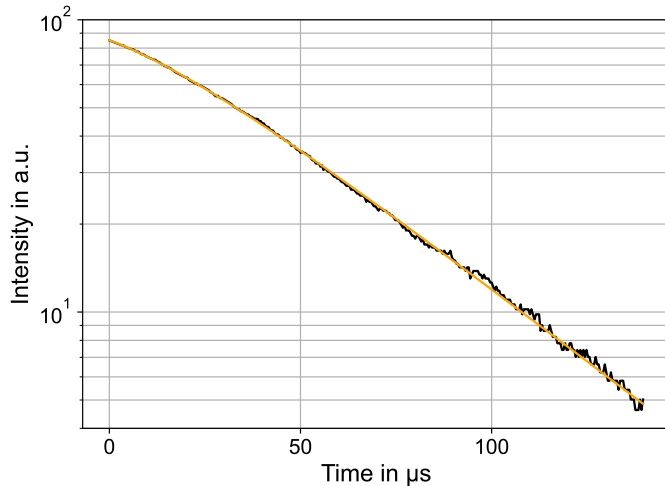


Figure 3.12: Ring down measurement of the finesse of the cavity (black line). A double exponential function is used to fit the measurement data with taking a delay time of the photodiode of  $20 \mu\text{s}$  into account (orange line).

$$t_{\text{delay}} = \frac{1}{2f_0(n_H - n_L)}, \quad (61)$$

assuming a first layer with high refractive index  $N_H$ . The frequency splitting of the cavity is measured to be  $345 \text{ kHz}$ . This frequency splitting is attributed to a birefringence value of  $\Delta n_{bi} = 7.6 \times 10^{-4}$ , for the given mirror coatings. It is noteworthy that the measured birefringence frequency splitting is significantly larger than the linewidth of the cavity, which is  $\delta\nu = (3.7 \pm 0.1) \text{ kHz}$ . Consequently, a clear separation between the two polarization modes is given.

### 3.3.2 Vibration sensitivity and vibration noise limit

Vibrations and seismic noise can limit the performance of a stabilization cavity, as discussed in Section 3.1.6. Since the cavity is designed as a transportable system, special attention must be given to ensuring effective vibration isolation. The spring mounting design of the cavity incorporates optimized suspension points to minimize cavity deformation and reduce sensitivity to vibrations. The flexible suspension is shown in Figure 3.13. Additionally, a vibration isolation platform is employed to mitigate the frequency instability caused by vibrations.

In the following sections, the vibration sensitivity of the cavity is being measured. For this measurement, the cavity on the passive table is accelerated, and the frequency response is recorded. Afterward, the remaining seismic noise on both the active and the passive table is measured, and the resulting frequency noise is calculated. The active table is chosen for the later setup; therefore, the remaining vibration noise on the active table inside the rack is also measured.

To assess the vibration sensitivity of the cavity, the cavity is placed on the passive



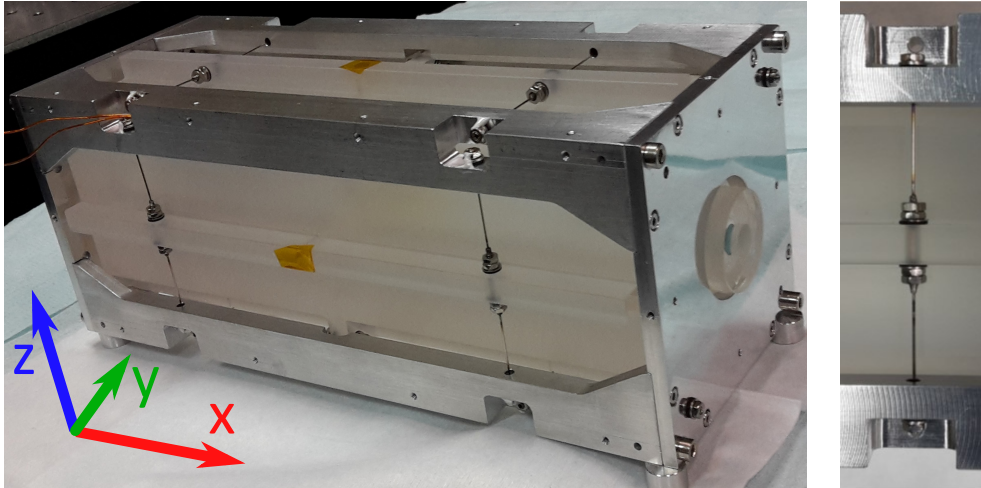


Figure 3.13: Image of the flexible suspension of the cavity. The flexible provides vibration isolation and ensures transportability of the cavity. Images are provided by Sofia Herbers [156].

vibration isolation table. The table is deliberately excited, while the velocity of the vibrations is measured using a seismometer<sup>4</sup>. Concurrently, the change in optical resonance frequency of the stabilization cavity is determined, using the method detailed in Section 3.1.5. The measurements are conducted using the passive vibration isolation table, which can only be manually excited. Its resonance frequency is approximately 2 Hz.

The results of these measurements are presented in Figure 3.14, providing an exemplary illustration. Due to the manual acceleration of the passive vibration isolation table, it is not possible to stimulate a single direction nor a well-defined frequency. However, by conducting multiple measurements, it is possible to estimate the sensitivity of the cavity to vibrations at the resonance frequency of the passive vibration isolation table. The vibration sensitivity  $S_v = \frac{f}{f_0} \frac{1}{a}$  for each axis is determined to be as followed: along the optical axis (x-direction),  $S_{v,x} = 1(1) \times 10^{-11} 1/g$ ; horizontal and perpendicular to the optical axis (y-direction),  $S_{v,y} = 4(2) \times 10^{-11} 1/g$ ; and vertical (z-direction),  $S_{v,z} = 3(2) \times 10^{-11} 1/g$ . In Table 3.1, these vibration sensitivity results are compared with those of other cavities, including an identical cavity. The measured vibration sensitivities in this study agree with the previous measurements of the identical cavity, within the uncertainty range. The active vibration table can be used for automatic vibration modulation with different frequencies. If the frequency response of the cavity is measured simultaneously, the transfer function between vibrations and cavity frequency can be calculated for all modulation frequencies. This measurement has not yet been carried out. As the vibration eigenfrequency of the spacer is expected in the kHz regime [156], a constant vibration sensitivity can be assumed for much lower modulation frequencies.

<sup>4</sup>Nanometrics, Trillium compact 120s



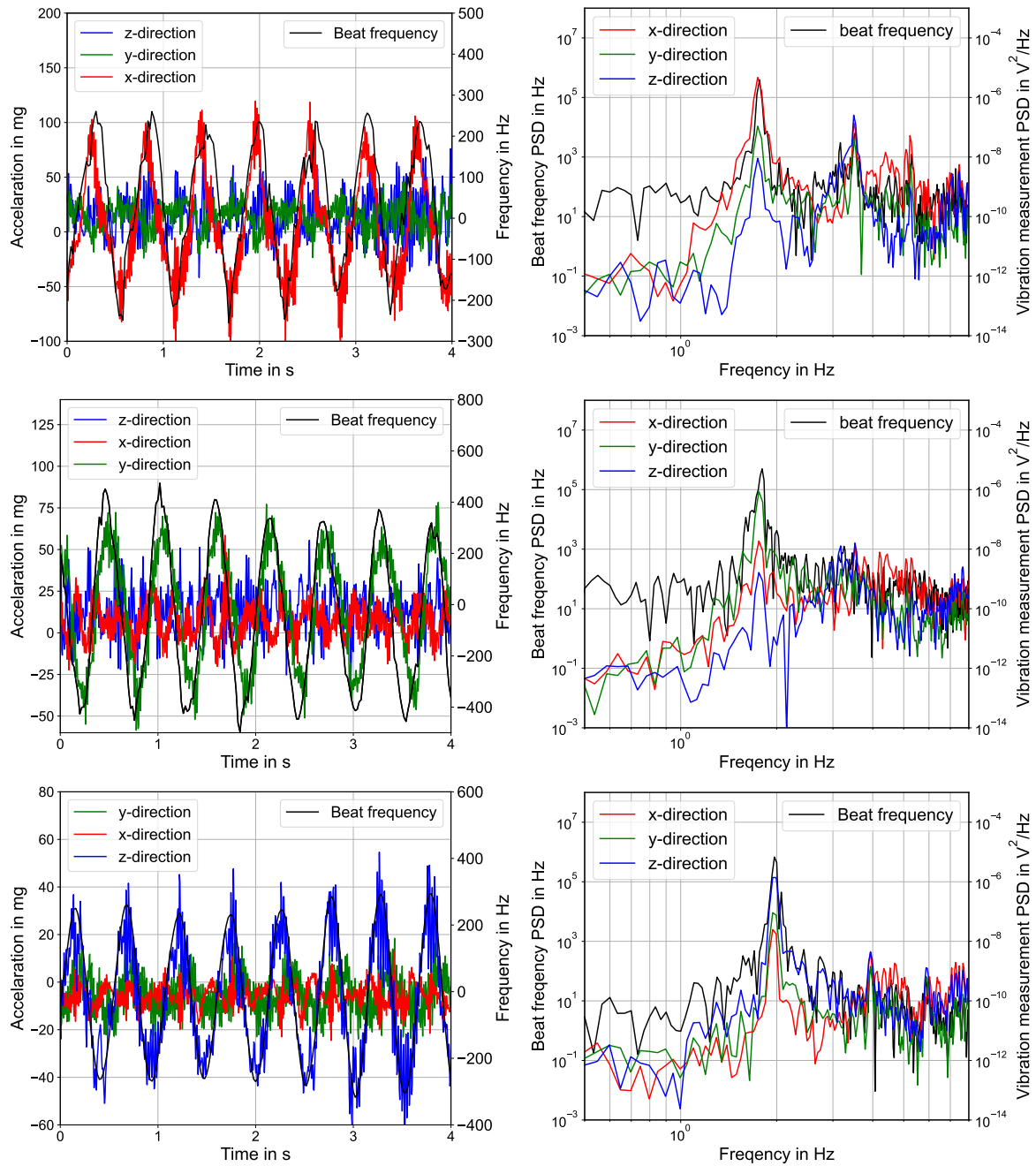


Figure 3.14: Measurement of vibration sensitivity of the cavity for excitation of the passive vibration isolation table in different directions. On the left side the PSD is shown while on the right side the fractional frequency instability calculated by the modified Allan deviation is shown. Top: direct measurement of the resonance frequency (black line) of the cavity during acceleration of the cavity in  $x$  direction (red line), (left). Residual acceleration in  $z$  direction (blue line) and in  $y$  direction (green line) is also shown. Center: measurement of the resonance frequency of the cavity during acceleration of the cavity in  $y$  direction. Bottom: Measurement of the resonance frequency of the cavity during acceleration of the cavity in  $z$  direction. The orientation of the  $xyz$  direction in respect to the cavity as shown in Figure 3.13 is the following: The  $x$  axis is horizontal and parallel to the optical axis of the cavity. The  $y$  axis is horizontal and orthogonal to the optical axis of the cavity. The  $z$  axis is orientated vertically.

Table 3.1: Vibration sensitivity of different cavities.

Cavity design	This work	Identical cavity	Cylindrical			Cubic	
Length	20 cm	20 cm	21 cm	12 cm	10 cm	10 cm	5 cm
Reference		[156, 239]	[90]	[107]	[226]	[225]	[97]
$S_{v,x}$ in $10^{-11}$ 1/g	1(1)	3(1)	5.5	23	8	9	2.5
$S_{v,y}$ in $10^{-11}$ 1/g	4(2)	2(1)	6.7	7	1.7	20	0.2
$S_{v,z}$ in $10^{-11}$ 1/g	3(2)	3(3)	8.4	123	39	20	0.01

For evaluation of the frequency instability of the cavity the residual Vibrations noise floor is measured on the passive and active vibration isolation table. For this measurement, the seismometer is placed on the vibration isolation table next to the cavity. The fractional frequency instability caused by vibration noise is calculated, assuming a constant vibration sensitivity for the relevant Fourier frequencies. The results for the passive vibration isolation table are displayed in Figure 3.15, while the results for the active vibration isolation table are presented in Figure 3.16. It can be observed that the fractional frequency instability due to vibration on both the passive and non-activated active vibration isolation tables exceeds the thermal noise limit for average times shorter than 0.2s. However, the active vibration isolation table effectively suppresses the vibration noise at these timescales, resulting in a fractional frequency instability below  $7 \times 10^{-17}$  for average times ranging from 0.01 s to 100 s. As a result, the active table is chosen for vibration isolation in the subsequent clock laser system. It is important to note that the active vibration isolation table exhibits an increase in vibration noise for frequencies lower than 1 Hz. These oscillations are caused by the table itself during active vibration isolation.

The vibration noise floor of the cavity, while placed on the active vibration isolation table inside the rack, is measured. The power spectral density (PSD) and modified Allan deviation for the fractional frequency instability caused by vibrations are calculated and are presented in Figure 3.17. For comparison, the calculated PSD and modified Allan deviation of the active vibration isolation table with the cavity placed on a lab table as shown in Figure 3.16 can be used. The increase of the vibration noise floor, when the vibration isolation table and the cavity is inside the rack is not significant. The frequency instability of the cavity due vibrations is in the some order of the thermal noise limit or below for average times longer than 0.02 s considering all three axis. Further improvements could be achieved by correction of the low frequency oscillation of the actively controlled vibration isolation table by using an external seismometer.

### 3.3.3 Photo-thermal and photo-birefringence noise

As explained in Section 3.1.6, the absorption of light at the two mirrors of the cavity leads to the heating of the mirrors. This temperature change causes a variation in the optical path length within the cavity, subsequently altering the resonance frequency of the cavity. Fluctuations in the optical power and the consequent frequency noise of the laser are referred to as photo-thermal noise. To determine the relationship between op-

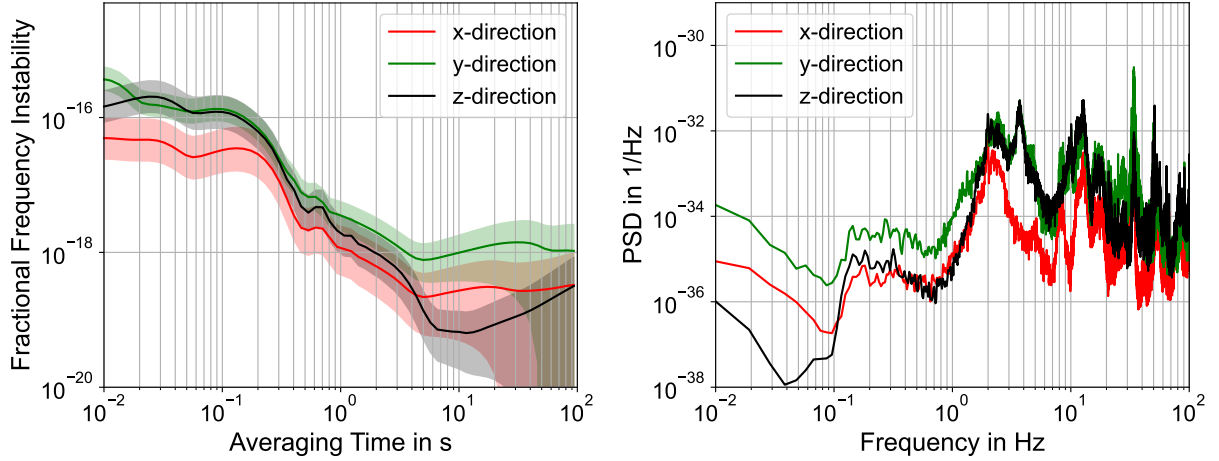


Figure 3.15: Fractional frequency instability of the cavity on the passive vibration isolation table, resulting from vibration noise. Right: Modified Allan deviation of the fractional frequency instability due to vibration noise in  $x$  direction (red line), in  $y$  direction (green line) and in  $z$  direction (black line). Coordinates and cavity orientation are shown in Figure 3.13. Left: Power spectral density of the fractional frequency instability due to vibration noise (same color coding).

tical power modulation and frequency modulation, the optical light power coupled into the cavity is modulated while measuring the frequency response. A conversion factor for this optical power modulation and frequency modulation is derived and compared to theoretical values. The observed results indicate the presence of photo-birefringence noise within the cavity. The optimization of the optical power setting of the cavity is performed. In order to investigate the limitation of the frequency stability of the cavity due to photo-thermal noise, optical power fluctuations are measured both with and without optical power stabilization.

In order to measure the displacement factor and the photo-thermal noise of the cavity, a modulation signal is applied to the RF amplifier of the AOM before the cavity. This induces an oscillation of the coupled optical power to the cavity at a chosen frequency. The transmitted light behind the cavity is detected by a photodiode, which can also be used for power stabilization. Another photodiode is placed behind the cavity for out-of-loop measurements. Simultaneously, the resonance frequency of the cavity is measured. Figure 3.18 (left) shows the typical results of such a measurement with a modulation frequency of 0.5 Hz. A strong correlation between the voltage of the photodiode and the resonance frequency of the cavity is observed, from which a conversion factor can be calculated. Alternatively, the conversion factor can also be determined using the PSD of the two signals, as shown in Figure 3.18 (right).

The measured voltage of the photodiode is proportional to the non-reflected optical power  $P_{in} - P_t$  with a factor of  $16.7 \mu\text{W V}^{-1}$  for the in-loop diode and  $7.1 \mu\text{W V}^{-1}$  for the out-of-loop diode. The measured transmission power of the cavity is approximately  $P_t = 2.4 \mu\text{W}$  at a non-reflected optical power of  $P_{in} - P_t = 11 \mu\text{W}$ . Using Equation 52

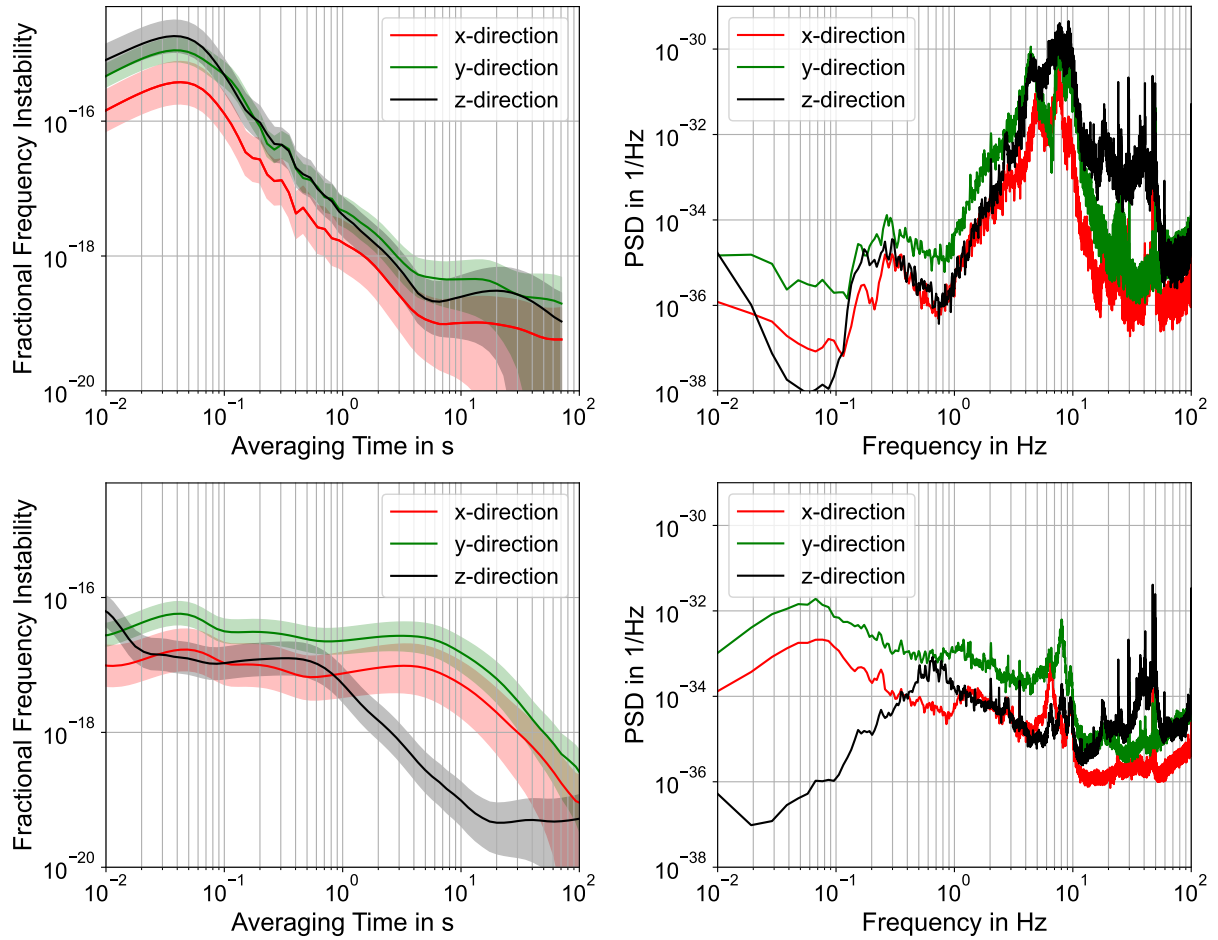


Figure 3.16: Fractional frequency instability of the cavity on the active vibration isolation table, resulting from vibration noise. Top: Measurement of the vibration noise with the active table turned off. Bottom: Measurement of the vibration noise with the active table turned on. Right: modified Allan deviation of the fractional frequency instability due to vibration noise. Left: Power spectral density of the fractional frequency instability due to vibration noise.

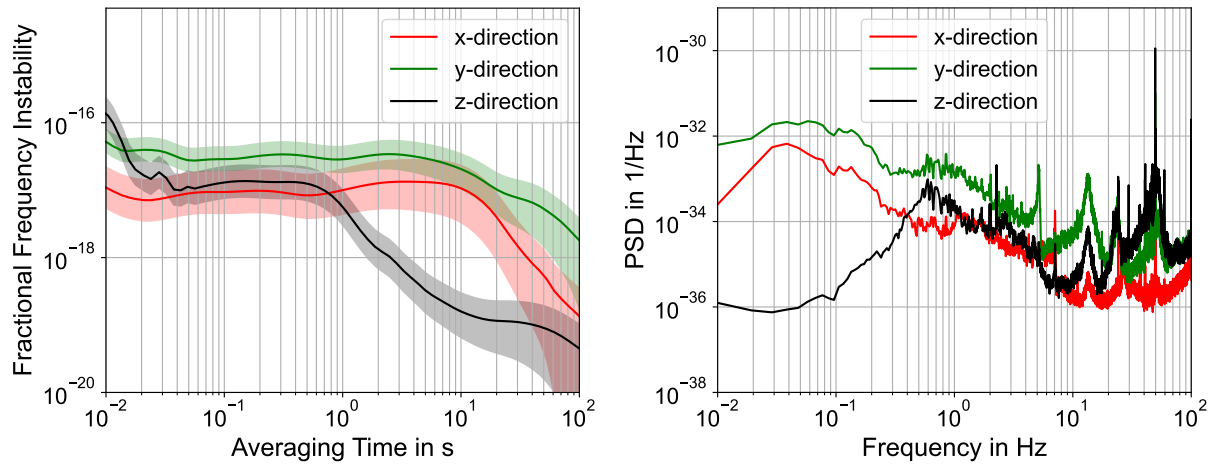


Figure 3.17: Fractional frequency instability of the cavity on the active vibration isolation table placed inside the 19-inch rack, resulting from vibration noise. Right: Modified Allan deviation of the fractional frequency instability due to vibration noise. Left: Power spectral density of the fractional frequency instability due to vibration noise.

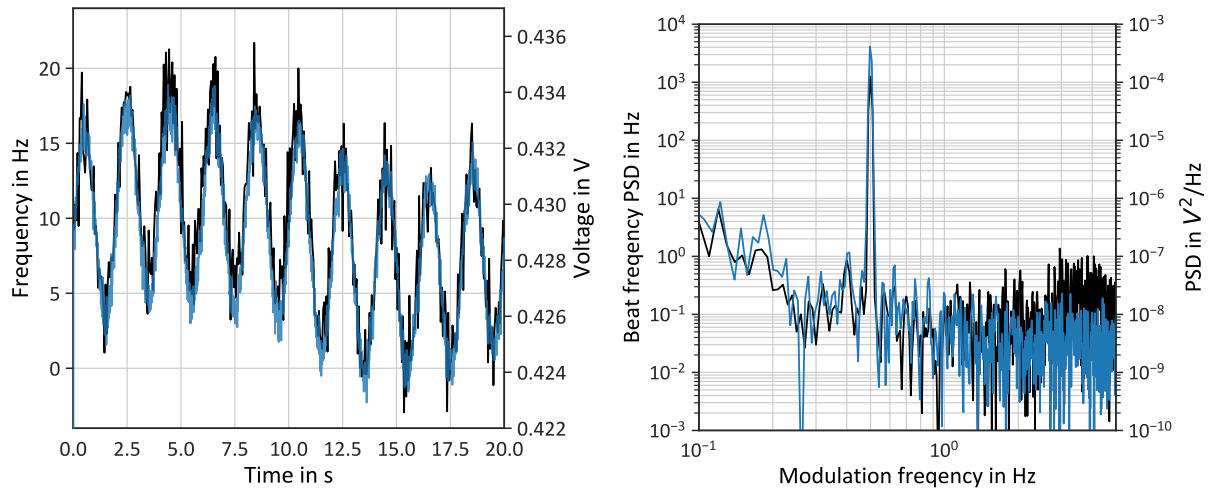


Figure 3.18: Sensitivity of the cavity resonance frequency to optical power modulation. Left: The measured resonance frequency of the cavity (black line) is compared to the modulation of the coupled optical power (blue line) measured by the photodiode. Right: Power spectral density of the the resonance frequency (black line) and the optical power (blue line) during modulation of the optical power with 0.5 Hz. The ratio between the resonance frequency and the optical power modulation signal gives the displacement factor.

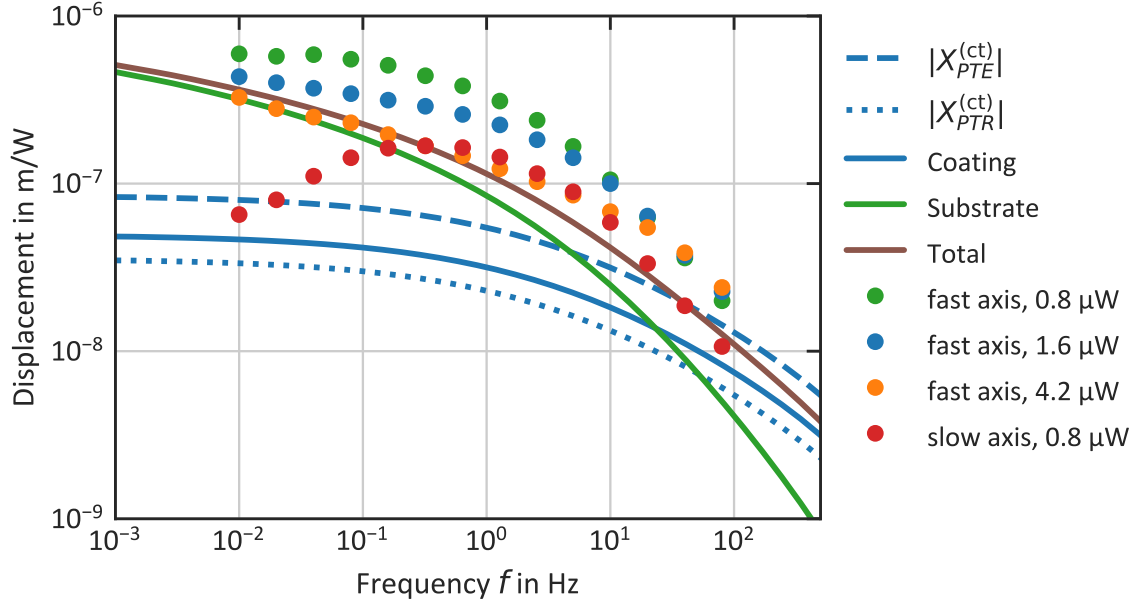


Figure 3.19: Measurement of the displacement factor of the cavity as a function of modulation frequency of the optical power coupled to the cavity for different average optical power and polarization modes. For the fast polarisation mode the displacement factor is shown for an average optical power of 0.8  $\mu$ W (green dots), 1.6  $\mu$ W (blue dots), and 4.2  $\mu$ W (orange dots). For the fast polarisation mode the displacement factor is shown for an average absorbed optical power of 0.8  $\mu$ W (red dots). Additionally, the theoretical results for photo-thermal noise (brown line) and for the individual components; photo-thermal noise of the substrate (green line), photo-thermal noise of the coating (blue line), photo-elastic noise of the coating (blue dashed line) and photo-reflective noise of the coating (blue dotted line) are shown. Deviations of the measurement from the theoretical expectations indicates an additional noise source.

and the finesse of the cavity  $F = 202,000$ , the losses and transmission of one mirror can be calculated, resulting in  $l = 9.6(5)$  ppm and  $T = 6.1(5)$  ppm. These values deviate from the information on the data sheet, which states  $l = 8.3$  ppm and  $T = 7$  ppm for these mirrors. The discrepancy may be attributed to measurement uncertainties or absorption at additional optical elements between the measurement points and the cavity mirrors. Since the precise values of the absorption coefficient  $a$  and the scattering coefficient  $s$  are unknown, an assumption for the absorbed optical power has to be made. As a conservative estimate, we assume that 50% of the lost optical power, is scattered by the two mirrors in all directions. This assumption implies that approximately 75% of the transmitted optical power is absorbed at each mirror. Henceforth, all references to the absorbed optical power will be based on this assumption.

The measurement is repeated for various modulation frequencies, and the corresponding displacement factor is presented in Figure 3.19 for different average absorbed optical powers. The measurements are conducted under fast polarization mode and include data for an average absorbed optical power of 0.8  $\mu$ W (green dots), 1.6  $\mu$ W

(blue dots), and  $4.2\ \mu\text{W}$  (orange dots). In addition, the theoretical calculations for the components of photo-thermal noise, as explained in Section 3.1.6, are displayed. These include the displacement factor due to photo-elastic effects of the coating ( $X_{PTE}^{(ct)}$ ) (blue dashed line), the photo-refractive effects of the coating ( $X_{PTR}^{(ct)}$ ) (blue dotted line), both effects combined ( $X_{PT}^{(ct)}$ ) (solid blue line), the photo-elastic effects of the substrate ( $X_{PT}^{(sb)}$ ) (green dashed line), and the overall photo-thermal noise ( $X_{PT}$ ) (brown line). Although the theoretical calculations do not entirely align with the measurements, they provide valuable insights. The measurements indicate a larger optical power-dependent displacement factor than expected from theory. One potential reason for this discrepancy can be the conservative assumption regarding the absorbed power. Nevertheless, the theoretical and measurement results can not be fully matched across all modulation frequencies. Furthermore, the measurements reveal an increase in the displacement factor with smaller average absorbed optical power for smaller modulation frequencies. This observation cannot be explained by the existing theory, suggesting limitations in the current understanding of the phenomenon. One possible contributing factor to these limitations is photo-birefringence [258, 259]. It is worth mentioning that the displacement factor has also been measured by Chalermongsak et al. [248] and Herbers et al. [239] for AlGaAs/GaAs mirror coatings. Both studies also reported a small discrepancy between their measurements and the theoretically expected values.

In the case of crystalline coatings, the intrinsic birefringence of the coatings causes a splitting of the resonator's polarization eigenmodes, resulting in a difference in the refractive index denoted as  $\Delta n_{bi}$ . This splitting can be expressed as  $\Delta n_{bi} = \frac{\Delta \nu_{bi}}{2\nu_0} \frac{l_0}{l_{pen}}$ , as shown in Section 3.3.1. Consistent with the higher and lower resonance frequency of the two polarization eigenmodes, they are referred to as slow polarization mode and fast polarization mode. If the birefringence splitting of the refractive index ( $\Delta n_{bi}$ ) changes with the optical power inside the cavity, the resonant frequency of the cavity shifts differently for light with ordinary and extraordinary polarization in relation to the crystal orientation, but with opposite signs. This phenomenon is known as photo-birefringence noise. The physical nature of this effect is currently unknown, but it has been observed in various cavities with crystalline coatings. Ongoing experimental investigations are being conducted to further explore photo-birefringence noise. For further investigation of birefringence noise the displacement factor is measured for slow polarization mode at an average absorbed optical power of  $0.8\ \mu\text{W}$ , as depicted in Figure 3.22 (red dots). This measurement shows a significantly lower displacement factor compared to the measured displacement factor for the fast polarization mode at the same average absorbed optical power (green dots). This difference can be attributed to a phase shift of  $\pi$  between the displacement responses of the two polarization modes caused by photo-birefringence noise. As a result, the phase difference between photo-birefringence noise and photo-thermal noise leads to an enhanced or reduced displacement factor.

Next the response of the resonance frequency of the cavity is measured if the coupled optical power is abruptly changed. The results are shown in Figure 3.20 for fast polarization mode and for slow polarization mode. The change of optical power results in an immediate response of the resonance frequency with different sign for different



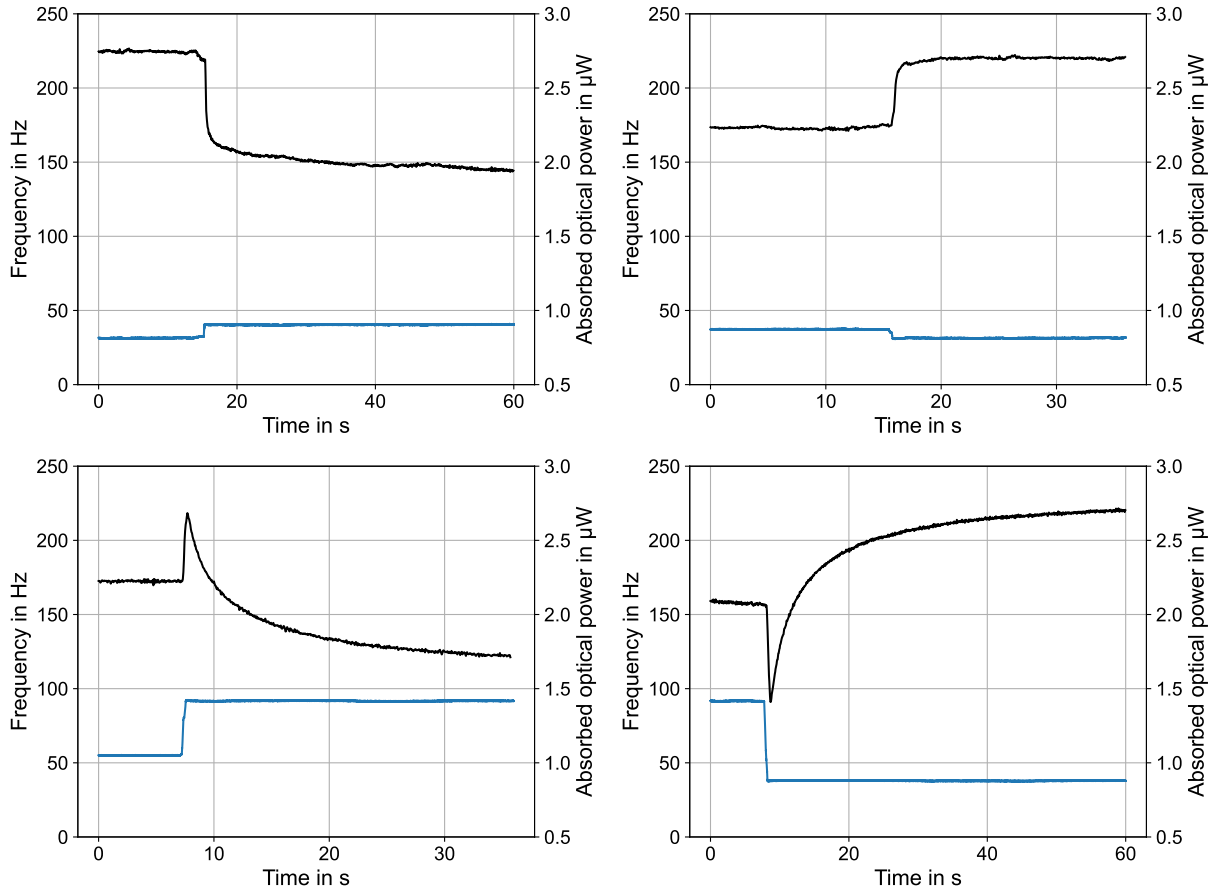


Figure 3.20: Response of the resonance frequency of the cavity due to a step change of optical power coupled to the cavity for different polarization. The measured resonance frequency of the cavity (black line) and the absorbed optical power (blue line) are shown for increasing power (left side) and decreasing power (right side). The measurement is accomplished for the fast polarization mode (top) and the slow polarization mode (bottom).



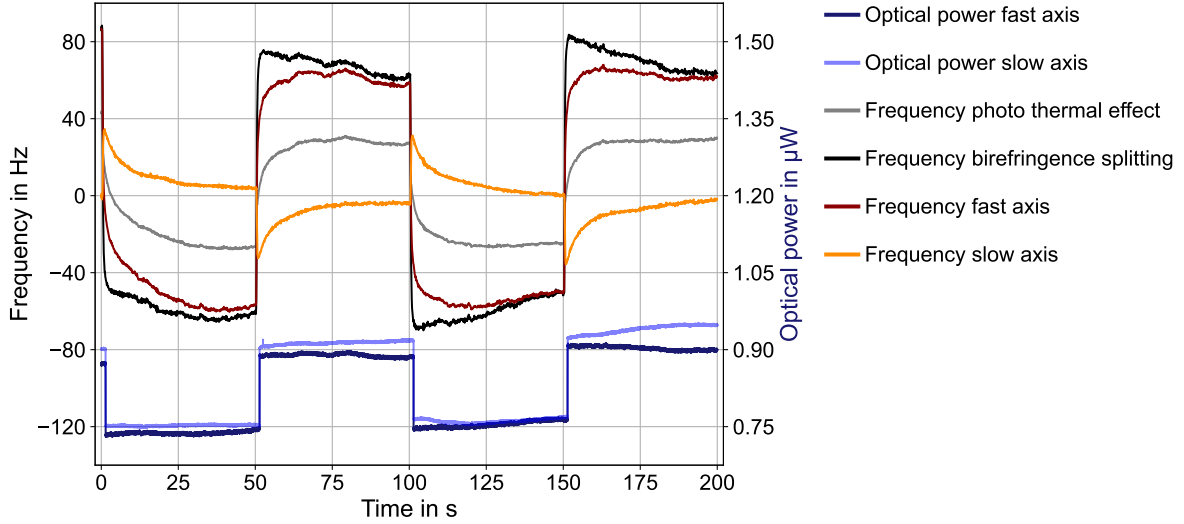


Figure 3.21: Frequency response of the cavity due to photo-thermal effect and photo-birefringence-effect. Frequency response is measured for the slow polarisation mode of the cavity (orange line) and the fast polarisation mode of the cavity (red line). The calculated line-splitting of the two modes; fast polarisation mode - slow polarisation mode (black line) and the portion due to the photo-thermal effect (fast polarisation mode + slow polarisation mode)/2 (grey line) is shown. The absorbed optical power for the fast polarisation mode (dark blue line) and the slow polarisation mode (light blue line) are modulated with a step function.

polarization modes as it is expected for photo-birefringence noise. Afterwards a slower exponential frequency response with the same sign for both polarization modes appears as it is expected for photo-thermal noise. If the optical power and the change of optical power coupled to the cavity is almost the same, the effect of birefringence line splitting and photo-thermal noise on the resonance frequency can be calculated. The results are shown in Figure 3.21. The birefringence line splitting between fast and slow modes increases for increasing optical power and shows a smaller time constant than the frequency shift due to the photo-thermal effect. The displacement due to the photo-thermal effect 10 s after the optical power step is given by  $(2.6 \pm 0.5) \times 10^{-7} \text{ m/W}$  which is in the same order than the theoretical value for small frequencies shown in Figure 3.19. As crystalline cavity mirrors are developed only recently, literature for birefringence noise from a crystalline cavity is very limited and its investigation is still ongoing. However, a similar behaviour as presented here is observed for different cavities and might be published soon [266].

For further investigations of photo-birefringence noise the dependency of the displacement factor to the average absorbed optical power is measured. The results are shown in Figure 3.22 for a modulation frequency of 0.5 Hz and fast polarization mode (blue dots) and slow polarization mode (green dots). The displacement factor is also shown for a modulation frequency of 0.05 Hz and slow polarization mode (yellow dots). For fast polarization mode the displacement factor decreases at higher average absorbed power. From the standard theory for photo-thermal noise no dependency of

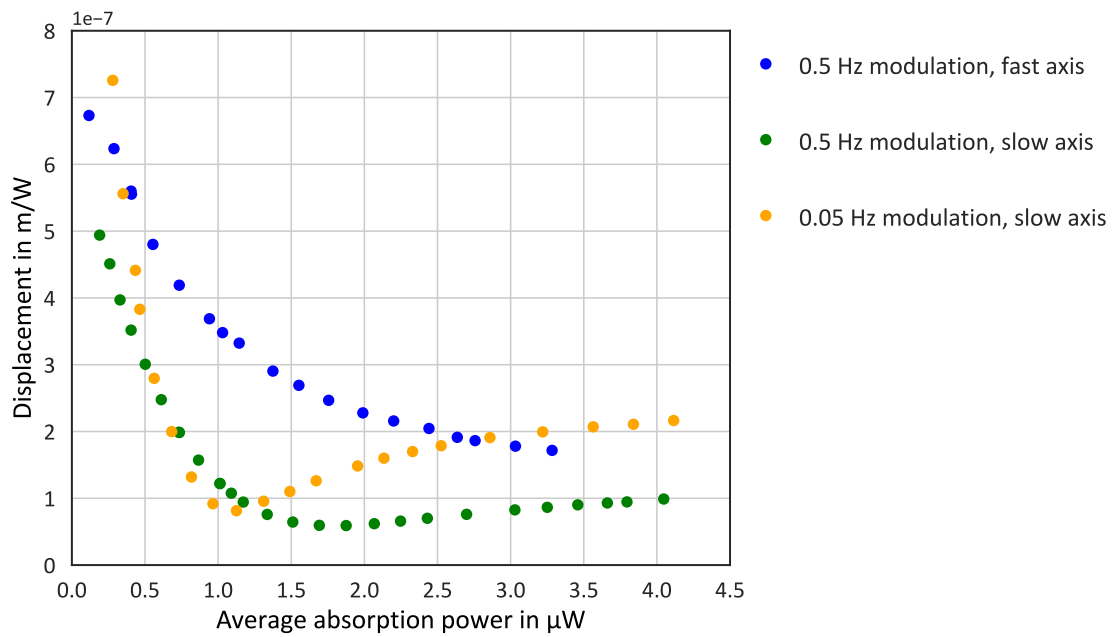


Figure 3.22: Measurement of the displacement factor of the cavity as a function of the average optical power absorbed by each mirror. The displacement factor for the fast polarisation mode of the cavity with a modulation frequency of 0.5 Hz (blue dots), for the slow polarisation mode of the cavity with a modulation frequency of 0.5 Hz (orange dots) and for the slow polarisation mode of the cavity with a modulation frequency of 0.05 Hz (green dots). In contrast to the standard theory the displacement factor is not constant for different optical power coupled to the cavity.

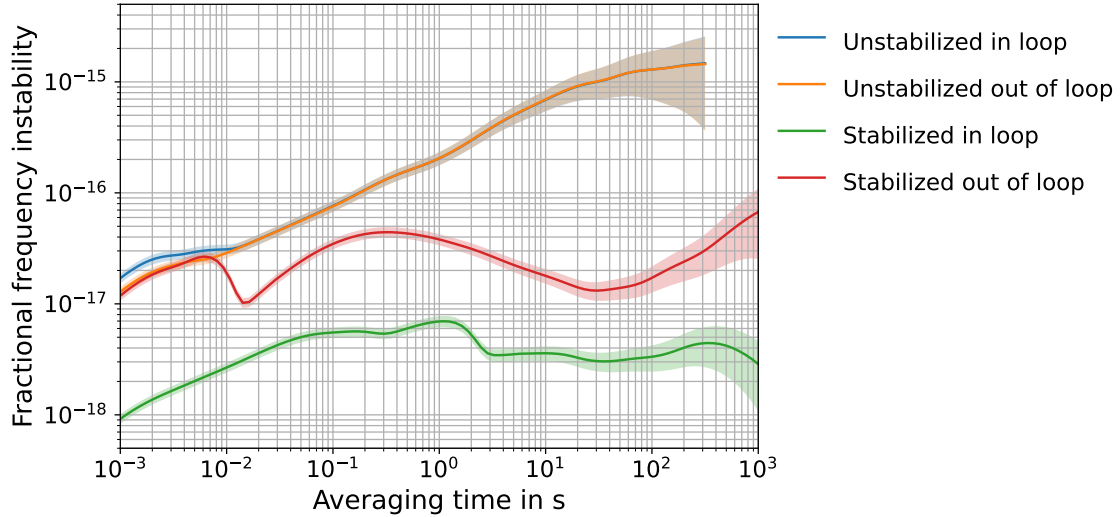


Figure 3.23: Fractional frequency instability of the cavity due to photo-thermal noise. The fractional frequency instability is calculated using the modified Allan deviation based on measured optical power fluctuations coupled into the cavity. The analysis considers the slow polarization mode with an average optical power of  $0.8 \mu\text{W}$ . The results are presented for two scenarios: without active optical power stabilization on the in-loop diode (blue line) and on the out-of-loop diode (orange line), and with active optical power stabilization on the in-loop diode (green line) and on the out-of-loop diode (red line).

the displacement factor to the average power is expected. Additionally, the measured displacement factor is higher than expected from theory (theoretical value:  $1.5 \text{ m W}^{-1}$ , for modulation frequency of  $0.5 \text{ Hz}$ ). For the slow polarization mode the displacement factor also decreases with increasing average absorbed power but reaches a minimum at  $1.1 \mu\text{W}$  and  $1.7 \mu\text{W}$  for modulation frequency of  $0.5 \text{ Hz}$  and  $0.05 \text{ Hz}$ , respectively, and increases for higher average absorbed power. Important to note is that frequency response for small average optical power has again a different sign for the different polarisation modes. This means that the influence of photo-birefringence noise on the displacement factor increases with decreasing average optical power. For the slow polarization mode photo-birefringence noise and photo-thermal noise cancel each other partially. However, the step response shows a faster response for photo-birefringence noise as for photo-thermal noise, therefore an effective cancellation of these two noise sources can be achieved best for low frequency noise as shown in Figure 3.19 (red dots). For minimal frequency instability due to photo-thermal noise and birefringence noise small optical power fluctuations and a small displacement factor are advantageous. The first one is given for small average optical power in the cavity. Small displacement factor can be ensured when the photo-thermal effect and the photo-birefringence-effect cancel each other. This is the case for average absorbed power around  $1.0 \mu\text{W}$  and slow polarization mode, considered optical power fluctuations with small Fourier frequencies. This setting represents the optimal operating point of the cavity.

The transmitted light power is measured with the power stabilization diode (in loop)

and a second diode (out of loop), with active optical power stabilization and without optical power stabilization. With the displacement factor the fractional frequency instability due to photo-thermal noise can be calculated from the measurements using the modified Allan deviation. The results for the slow polarization mode and an average optical power of  $0.8 \mu\text{W}$  are shown in Figure 3.23. In the unstabilized case the frequency instability measured by the in loop diode (blue line) and the out of loop diode (orange line) is the same for averaging times longer than 10 ms. For averaging times higher than 0.2 s the fractional frequency instability due to photo-thermal noise is higher than the thermal noise limit. To reach this level, an active stabilization of the optical power is necessary as it is shown in Section 3.2.2. With active optical power stabilization the remaining fractional frequency instability measured by the out-of-loop diode (red line) and the in-loop diode (green line). The measurement of the in-loop diode is also the signal of the active stabilization. It serves as a lower limit for the electronic noise of the stabilization scheme. However other noise sources like photon shot noise, electronic noise and beam pointing also lead to a limitation of the stabilization scheme. This can only be measured by the out-of-loop diode. For averaging times below 0.01 s, the frequency stability is not significantly improved with active power stabilization. The reason, is given by electronic noise in the measurement and control systems which limits the optical power stability, while the fundamental limit of the optical power stabilization is given by the shot noise on the photodiode. For average times longer than 0.01 s the active power stabilization significantly improves the measured frequency stability. In conclusion, the measured fractional frequency instability is below the thermal noise limit, if the active power stabilization is used. Hence, optical power fluctuations are no longer the primary limiting factor for the frequency stability of the cavity.

### 3.3.4 RAM stabilization limit

As discussed in Section 3.1.3, the frequency stability of the stabilization cavity can be affected by RAM. To mitigate this instability, passive reduction of RAM is often the preferred solution, especially in transportable setups. This approach eliminates the need for additional electronic and optical components for RAM stabilization. Nevertheless RAM is often a major limitation to the frequency stability. This was also the cause in a setup with identically designed cavity [156]. This cavity operates at a wavelength of 1397 nm exhibiting a fractional frequency instability limitation due to RAM of  $8 \times 10^{-16}$  at 1 s in the unstabilized case using a commercial free-space EOM. Additionally, a homemade EOM is investigated with a limitation of the fractional frequency instability in the mid  $10^{-17}$  range. Using an active RAM stabilization with a temperature-stabilized waveguide EOM, a limitation of the fractional frequency instability of  $4 \times 10^{-18}$  at 1 s is reported. In this work, such a temperature-stabilized waveguide EOM is employed.

In the following sections, the EOM is modulated, inducing a corresponding modulation of RAM. A conversion factor between the frequency response of the cavity and the measured signal at the RAM diode and PDH diode is determined. The RAM signal without modulation is measured on the RAM control diode while the laser is locked

to the cavity, both with and without active RAM stabilization. Next, the RAM signal is measured on both the RAM control diode and the PDH diode, again for both the unstabilized and stabilized cases, when the laser is not locked to the cavity. Using the established conversion factor, the frequency stability limit due to RAM is calculated, with and without active RAM stabilization.

To measure the conversion factor, a modulation signal is generated at the DC input of the bias tee connected to the EOM. This signal caused the EOM to produce a modulated RAM signal at a specific frequency, which is then measured by the RAM control diode. When the laser is locked to the cavity, the laser frequency is also modulated by the RAM signal. The laser frequency is determined by performing a beat-note measurement with a second, more stable reference cavity via an optical comb. By comparing the amplified signals from the RAM control diode and the laser frequency measurement, a conversion factor of  $(0.79 \pm 0.04) \text{ Hz V}^{-1}$  is obtained. This conversion factor remained constant within the uncertainty range for modulation frequencies between 0.1 Hz and 10 Hz.

In cases where the laser frequency deviated from the resonance frequency of the stabilization cavity and no PDH signal is detected. This time the modulated RAM signal can also be measured on the PDH diode. The measurement with EOM modulation is repeated which allows to determine conversion factor between PDH and RAM diode. In this measurement, the demodulated PDH signal is further amplified by a factor of 100. A conversion factor of 0.077 is determined amplified signals of the PDH diode and the RAM diode, resulting in a conversion factor of  $(10.3 \pm 0.5) \text{ Hz V}^{-1}$  between the laser frequency and the amplified signal of the PDH diode.

The frequency stability limit due to RAM, the RAM signal without modulation is measured on the RAM control diode when the laser is locked to the cavity, both with and without active RAM stabilization. This represents the in-loop signal of the RAM control scheme. When the laser is off-resonance with the stabilization cavity, the RAM signal is measured on both the RAM control diode and the PDH diode, again for both the unstabilized and stabilized cases. The signal on the PDH diode serves as the out-of-loop signal in the stabilized case.

The results presented in Figure 3.24 illustrate the fractional frequency instability of the stabilization cavity caused by RAM, as calculated using the modified Allan deviation. Without RAM stabilization, the limitations of the fractional frequency uncertainty for the stabilization cavity are shown for the signal recorded on the RAM control diode with locked and unlocked laser. Additionally, the measurement on the PDH diode is shown for an unlocked laser without RAM stabilization. It is important to note that the data obtained from the RAM and PDH diodes for the unlocked laser are derived from the same measurement, while the data for the locked laser is from a separate measurement. Although there may be slight differences in the measurement conditions between the two sets of data, such as variations in laser frequency and temperature changes in the optical setup and EOM, the limitation of the fractional frequency instability due to unstabilized RAM is similar for all three data sets when

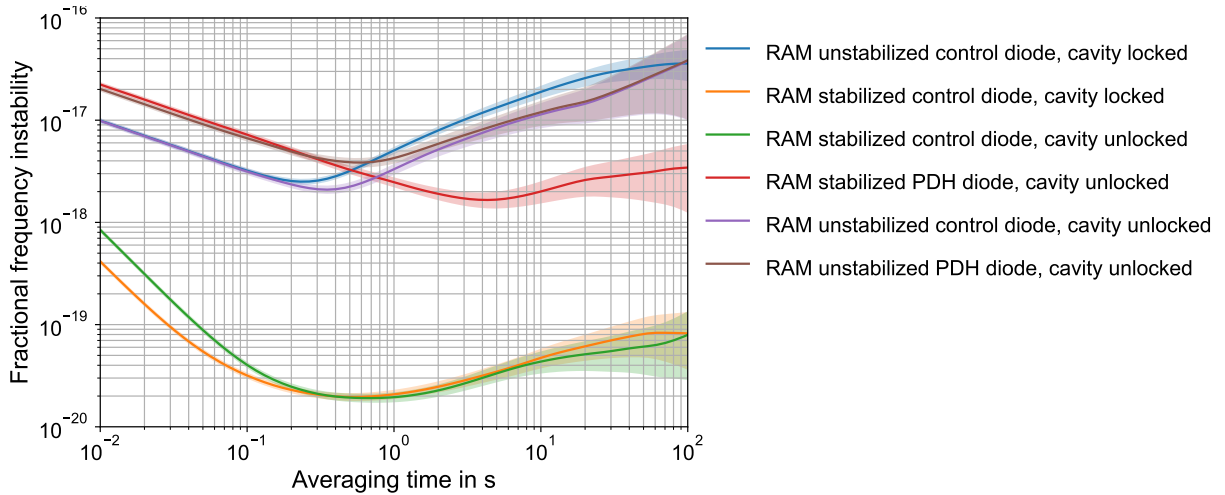


Figure 3.24: Fractional frequency instability caused by RAM. The fractional frequency instability of the cavity due to RAM is determined using the modified Allan deviation. RAM is measured using the RAM control diode when the laser is locked to the cavity, both without RAM stabilization (blue line) and with RAM stabilization (orange line). In the absence of laser locking to the cavity, RAM is measured with stabilization by the RAM photodiode (green line) and the PDH photodiode (red line). Additionally, in the absence of active RAM stabilization and an unlocked laser, RAM is measured by the RAM photodiode (violet) and the PDH photodiode (brown).

averaging times exceed 1 s. The fractional frequency instability attributed to RAM is on the order of  $(3 \pm 1) \times 10^{-18}$  at 1 s without RAM stabilization. For longer averaging times it increases and reaches the low  $10^{-17}$  regime. For shorter averaging times (1 s), the measurement is dominated by the electrical noise of the diodes and electronic systems, limiting the accuracy.

With active RAM stabilization, the measurements obtained using the RAM control diode provide an in-loop signal for the control loop and demonstrate the electronic limitations of the PI controller. The in-loop measurements for both the locked laser (yellow line) and the unlocked laser (green line) exhibit the same level of instability in the  $10^{-20}$  regime for averaging times above 0.2 s. For active RAM stabilization and a locked laser, the out-of-loop measurement obtained from the PDH diode (red line) sets an upper limit on the fractional frequency instability due to RAM in the laser system. Similar to the previous measurements, this measurement is limited by electronic noise for small averaging times. For averaging times exceeding 1 s, the fractional frequency instability is below  $3 \times 10^{-17}$ . Notably, for averaging times of 10 s and longer, active RAM stabilization demonstrates an improvement of approximately one order of magnitude compared to the unstabilized system.

In conclusion, RAM does not significantly limit the frequency stability of the stabilization cavity in the transportable clock laser system with temperature stabilization of the waveguide EOM. The system is expected to achieve a fractional frequency instability in the lower  $10^{-16}$  range for averaging times around 1 s, primarily limited by

thermal noise and other discussed noise sources. Therefore, active RAM stabilization is not necessary for the aforementioned system configuration. It should be noted that the results may vary for different temperature stabilization points of the waveguide EOM and different operating voltages of the EOM.

### 3.3.5 Temperature stabilization

Changes in temperature generally result in thermal expansion of materials. The relationship between temperature and expansion is quantified by the coefficient of linear thermal expansion (CTE). In the case of optical cavities, thermal expansion causes a shift in the resonance frequency [267–269]. Therefore, it is crucial to select a material with minimal CTE. Among the various components of the cavity, the choice of material for the cavity spacer is particularly important due to its relatively longer length. For this purpose, ultra-low thermal expansion (ULE) glass is utilized due to its low thermal expansion properties [260, 270]. ULE glass not only exhibits a small CTE but also demonstrates temperature-dependent behavior, transitioning from negative to positive values [271]. The temperature at which the CTE becomes zero is referred to as the CTE zero crossing temperature, denoted as  $T_0$ .

ULE glass is an ideal choice for the cavity spacer in a transportable setup because its CTE zero crossing temperature is at room temperature. In contrast, materials like sapphire and silicon have CTE zero crossing temperatures at cryogenic temperatures. By operating the cavity at the CTE zero crossing temperature, the influence of temperature fluctuations on the cavity length is minimized. However, ULE glass cannot be used as the mirror substrate due to its high mechanical loss factor. Instead, fused silica glass is employed for the mirror substrate, which has a CTE of approximately  $5 \times 10^{-7} \text{ K}^{-1}$ . Although the higher CTE of fused silica glass reduces the thermal length stability of the cavity, it shifts the CTE zero crossing temperature of the cavity to lower temperatures, as described by Legero et al. [260]. ULE glass compensation rings are used to shift CTE zero crossing temperature back, close to the one of a pure ULE glass cavity. This approach effectively minimizes the impact of the fused silica glass mirror substrate on the thermal length stability of the cavity.

The fractional length change of the cavity spacer resulting from thermal expansion is solely determined by the coefficient of linear thermal expansion (CTE)  $\alpha$ . When operating the cavity close to the CTE zero crossing temperature, it is typically assumed that the CTE follows a quadratic temperature dependency:

$$\begin{aligned}\alpha(T) &= \alpha'(T - T_0) + \alpha''(T - T_0)^2 \\ \frac{l(T)}{l_0} &= \frac{1}{2}\alpha'(T - T_0)^2 + \frac{1}{3}\alpha''(T - T_0)^3.\end{aligned}\tag{62}$$

For ULE glass, it is typical to assume values of  $\alpha' = 1.8 \times 10^{-9} \text{ K}^{-2}$  and  $\alpha'' = -1 \times 10^{-11} \text{ K}^{-3}$ .



To achieve a fractional length instability below  $10^{-16}$ , it is necessary to maintain a stability of below  $0.3\ \mu\text{K}$ , when the temperature of the cavity is stabilized to the CTE zero crossing temperature within a range of  $0.2\ \text{K}$ . For better length stability, the cavity temperature should be stabilized as close as possible to  $T_0$ . Therefore, it is essential to measure its value accurately.

To determine the CTE zero crossing temperature, a gradual change in the cavity temperature is performed. The resonance frequency of the stabilization cavity is measured by locking a laser to the resonance and using a beat note measurement with a more stable reference cavity via an optical comb, as described in Section 3.1.5. At the CTE zero crossing temperature, the measured frequency reaches a minimum value. The temperature of the cavity is measured using a temperature sensor. However, this sensor is not placed inside the cavity itself; it is integrated next to the cavity spacer on the suspension of the cavity, which is thermally connected to the inner passive heat shield. Therefore, it can only provide the temperature measurement at that specific location. It is important to note that the temperature may vary at different points within the cavity. During the temperature sweep, reaching the CTE zero crossing temperature in the cavity experiences a time delay compared to the temperature measured by the sensor. This time delay manifests as a hysteresis between the temperature measurement during temperature increase and temperature decrease. The magnitude of the hysteresis depends on the ratio between the thermalization time of the cavity and the heating or cooling rate applied.

The results of the temperature measurement, as shown in Figure 3.25 (left), reveal a significant hysteresis of approximately  $4\ ^\circ\text{C}$  as a relatively rapid temperature change is applied (approximately  $0.1\ ^\circ\text{C h}^{-1}$  for cooling and  $0.4\ ^\circ\text{C h}^{-1}$  for heating). Taking the delay time of 8 hours between the measured temperature at the sensor and the actual temperature of the cavity into account, the minimum of both curves can be reconciled, yielding a CTE zero crossing temperature of  $T_0 = 26.2\ ^\circ\text{C}$ . By fitting measurement with the polynomial function described in Equation 62, the calculated values for the coefficients are  $a' = 1.0 \times 10^{-9}\ \text{K}^{-2}$ ,  $a' = 1.2 \times 10^{-9}\ \text{K}^{-2}$ ,  $a'' = 2.8 \times 10^{-11}\ \text{K}^{-3}$ , and  $a'' = -0.7 \times 10^{-11}\ \text{K}^{-3}$ . It is important to note that the accuracy of the measurement is limited by the temperature variations within the cavity, as well as drifts in the beat frequency. Additionally, the fused silica mirror substrate with a higher CTE and the ULE compensation rings can affect the temperature dependence of the cavity's resonance frequency. Consequently, temperature changes at the mirrors can introduce deviations from the theoretical values. The influence of mechanical stress on the heat shields and suspension due to temperature changes also contributes to changes in the cavity's resonance frequency and affects the measurement. Further investigations of these effects are conducted below. For a cavity with a similar design, a CTE of  $a' = 1.2 \times 10^{-9}\ \text{K}^{-2}$  and  $a'' = 8 \times 10^{-11}\ \text{K}^{-3}$  were found [156], while previous cavities with an ULE spacer, FS mirror substrates, and ULE compensation rings exhibited  $a' = 0.86 \times 10^{-9}\ \text{K}^{-2}$  for a 12 cm long cavity and  $a' = 2.2 \times 10^{-9}\ \text{K}^{-2}$  for a 48 cm long cavity [157].

To obtain a more precise determination of the CTE zero crossing temperature, a second measurement is conducted with a slower rate of temperature change in the



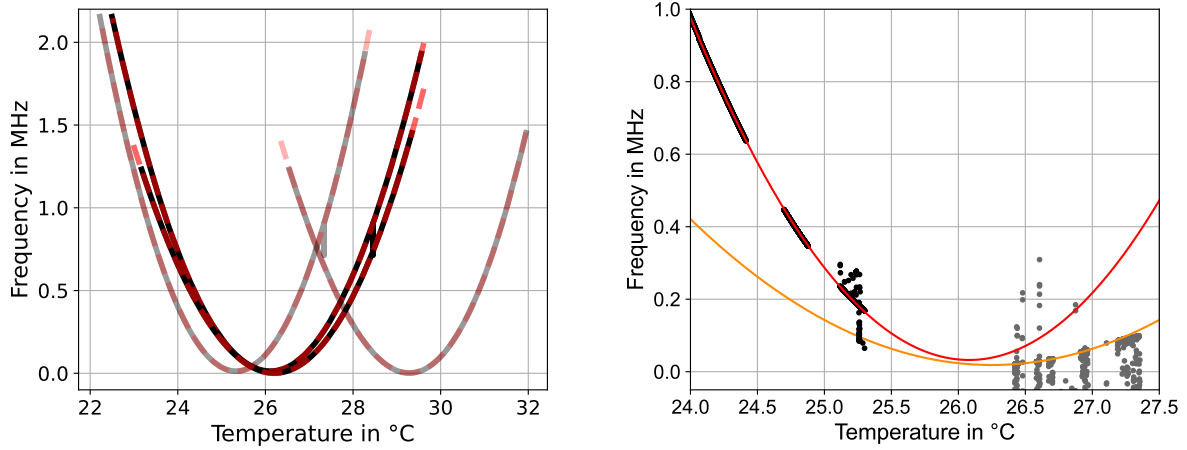


Figure 3.25: Measurement of the CTE zero crossing temperature. Left: Employing a rapid temperature change of the cavity, its frequency response exhibits a significant hysteresis of approximately 4 °C (grey lines). The obtained results are fitted using a third-order polynomial function given by Equation 62 (light red lines). By considering a thermal low-pass-induced delay of 8 h, the two curves (black lines) and the corresponding fit (dashed red lines) nearly overlap, yielding a CTE zero crossing temperature of  $T_0 = 26.2\text{ °C}$ . Right: For a more precise measurement, the temperature of the cavity is gradually changed. When the temperature increases, the measured frequency curves (black dots) with the fit (dashed red line) yield a CTE zero crossing temperature of  $T_0 = 26.08\text{ °C}$ . Conversely, when the temperature decreases, the measured frequency data (grey dots) indicates a CTE zero crossing temperature of  $T_0 = 26.25\text{ °C}$  (orange line). A delay of 8 h is accounted for, and a linear drift of 90 mHz is observed and removed from the data. Isolated outliers in the frequency measurement and missing data points occur when the optical comb is not stabilized or when the measured beat signal becomes too weak to track accurately.

cavity (approximately  $0.002\text{ }^\circ\text{C h}^{-1}$  for cooling and  $0.02\text{ }^\circ\text{C h}^{-1}$  for heating). The temperature dependence of the cavity's resonance frequency is once again measured for both increasing and decreasing cavity temperatures, considering an 8-hour delay. Additionally, a linear drift of  $90\text{ mHz s}^{-1}$  is observed and accounted for in the data. The results of this measurement yield CTE zero crossing temperatures of  $T_0 = 26.08\text{ }^\circ\text{C}$  and  $T_0 = 26.25\text{ }^\circ\text{C}$ , as depicted in Figure 3.25 (right). For these measurements, the coefficients are determined as  $a' = 1.6 \times 10^{-9}\text{ K}^{-2}$  and  $a' = 0.6 \times 10^{-9}\text{ K}^{-2}$ , while  $a''$  is not considered. Similar to the previous measurement, deviations from the theoretical values are introduced by drifts in the beat frequency and thermal stress on the heat shields and suspension of the cavity. Given the slow temperature changes in the cavity during this measurement, these effects have a significant impact on the measurement accuracy. However, the temperature inhomogeneity within the cavity is considered to be small, due to the small heating and cooling rates. The corrected hysteresis, is less than  $0.2\text{ }^\circ\text{C}$  for heating, and less than  $0.02\text{ }^\circ\text{C}$  for heating the cavity. With these measurements, it can be expected that the CTE zero crossing temperature is known with an accuracy of less than  $\Delta T_0 = 0.2\text{ }^\circ\text{C}$ .

For effective temperature stabilization of the cavity, it is necessary to minimize heat transfer between the cavity and its surroundings on shorter timescales. A simplified model assumes that the heat transfer between the cavity and its heat shields occurs primarily through thermal conduction and radiation between the shields. Thermal convection and radiation directly from outside the vacuum chamber through the windows to the cavity can be neglected in this model. Conductive heat transfer, denoted as  $q_c$ , between two systems with fixed temperatures  $T_1$  and  $T_2$  can be described by the following law:

$$q_c = k \frac{A}{d} (T_1 - T_2(t)), \quad (63)$$

where  $A$  is the contact surface,  $d$  the length of the conduction and  $k$  the thermal conductivity of the conduction material. For thermal radiation the heat transfer  $q_{rad}$  follows the Stefan–Boltzmann law:

$$q_{rad} = A\sigma_{SB}\epsilon(T_1^4 - T_2(t)^4), \quad (64)$$

with the Stefan-Boltzmann constant  $\sigma$  and the emissivity  $\epsilon$  of the material under the assumption of same materials and same surface for both systems. For small temperature difference between the two system with respect of the absolute temperature, this equation can be linearized to

$$q_{rad} = 4A\sigma_{SB}\epsilon T_1^3 (T_1 - T_2(t)). \quad (65)$$

The total heat transfer  $q_{tot}$  is given by

$$q_{tot} = q_{rad} + q_c = \left(4A\sigma_{SB}\epsilon T_1^3 + k \frac{A}{d}\right) (T_1 - T_2(t)). \quad (66)$$

Due to the heat transfer the temperature of the second system changes according to

$$\frac{\delta T_2}{\delta t} = \frac{q_{tot}}{C} \quad (67)$$

where  $C$  is the heat capacity of the second system. By solving the linear differential equation

$$\frac{\delta T_2}{\delta t} = \frac{1}{C} \left( 4A\sigma_{SB}\epsilon T_1^3 + k\frac{A}{d} \right) (T_1 - T_2(t)) = \frac{1}{\tau} (T_1 - T_2(t)), \quad (68)$$

an exponential behavior of the system is found with the time constant  $\tau$ . In the case of the cavity, a large value of  $\tau$  is desired to effectively suppress temperature changes on shorter timescales. This can be achieved by either increasing the heat capacity or reducing the heat transfer rate. To increase the heat capacity, more material can be used for the cavity. However, this contradicts the concept of a transportable cavity, as it would make the cavity heavier and less portable. To reduce the heat transfer rate, materials with small thermal conductivity  $k$  and minimal contact surface should be employed. For the cavity, glass spheres are used to separate the different heat shields and the cavity, minimizing conductive heat transfer. To suppress radiation heat transfer, the cavity is placed within two passive heat shields and one active heat shield, as described in Section 3.2.1. The heat is radiated from one heat shield to another, but it takes several hours for the second heat shield to reach the temperature of the first heat shield. No heat transfer due to thermal convection is assumed, as the cavity is placed in ultra-high vacuum. During this time, the effective heat transfer to the cavity is suppressed. To model this behavior, a simplified model is presented next.

The temperature within each heat shield and within the cavity is considered homogeneous, while the active heat shield temperature  $T_a$  remains fixed, the temperature of the outer  $T_o(t)$  and inner  $T_i(t)$  change with time. Thermal radiation through the windows to the cavity is neglected, which is a good approximation if the cavity temperature is close to room temperature. Considering heat transfer from the active heat shield to the outer passive heat shield with time constant  $\tau_{ao}$  and the other way around ( $\tau_{oa}$ ), from the heater shield to the inner shield ( $\tau_{oi}$ ) and back ( $\tau_{io}$ ), and from the inner shield to the cavity ( $\tau_{ic}$ ) and back ( $\tau_{ci}$ ), the following set of differential equations are found:

$$\begin{aligned} \frac{\delta T_o}{\delta t} &= \frac{1}{\tau_{ao}} (T_a - T_o(t)) + \frac{1}{\tau_{ia}} (T_i - T_o(t)) \\ \frac{\delta T_i}{\delta t} &= \frac{1}{\tau_{oi}} (T_o(t) - T_i(t)) + \frac{1}{\tau_{ci}} (T_c - T_i(t)) \\ \frac{\delta T_c}{\delta t} &= \frac{1}{\tau_{ic}} (T_i(t) - T_c(t)). \end{aligned} \quad (69)$$

Here, a simplified model is applied to partially decouple the differential equations:

$$\begin{aligned}
\frac{\delta T_o}{\delta t} &= \frac{1}{\tau_1}(T_a - T_o(t)) \\
\frac{\delta T_i}{\delta t} &= \frac{1}{\tau_2}(T_o(t) - T_i(t)) \\
\frac{\delta T_c}{\delta t} &= \frac{1}{\tau_3}(T_i(t) - T_c(t)).
\end{aligned} \tag{70}$$

If the time constant representing heat flow from the cavity to the inner shield and from the inner shield to the outer shield is large the simplified model agree with Equation 69. In this cause,  $\tau_1 = \tau_{ao}$ ,  $\tau_2 = \tau_{oi}$ , and  $\tau_3 = \tau_{ic}$ . In the other extreme case, the outer passive shield, the inner passive shield, and the cavity are thermally connected. Therefore,  $T_o \approx T_i \approx T_c$  and the model is also valid, taking the heat capacity of both passive shields and the cavity into account for  $\tau_1$ .

A solution of the differential equation is given by:

$$\begin{aligned}
\frac{T_{po}(t) - T_{po}(0)}{\Delta T} &= 1 - \exp\left(-\frac{t}{\tau_1}\right) \\
\frac{T_{pi}(t) - T_{pi}(0)}{\Delta T} &= 1 - \frac{\tau_1}{(\tau_1 - \tau_2)} \exp\left(-\frac{t}{\tau_1}\right) + \frac{\tau_2}{(\tau_1 - \tau_2)} \exp\left(-\frac{t}{\tau_2}\right) \\
\frac{T_c(t) - T_c(0)}{\Delta T} &= 1 - \frac{\tau_1^2}{(\tau_1 - \tau_2)(\tau_1 - \tau_3)} \exp\left(-\frac{t}{\tau_1}\right) + \frac{\tau_2^2}{(\tau_1 - \tau_2)(\tau_2 - \tau_3)} \exp\left(-\frac{t}{\tau_2}\right) \\
&\quad - \frac{\tau_3^2}{(\tau_1 - \tau_3)(\tau_2 - \tau_3)} \exp\left(-\frac{t}{\tau_3}\right)
\end{aligned} \tag{71}$$

This equation represents the temperature responses of the cavity, the inner and the outer heat shield when the temperature of the active heat shield is changed with a normalized step function. The temperature inside the inner heat shield is measured with a temperature sensor. However, the sensor is thermally connected to the inner shield. Therefore, it does not measure the temperature of the cavity, accurately. Nevertheless, the measurement can be used to understand the low pass behaviour of the cavity. Figure 3.26 (left) shows the measured temperature response at the point of the temperature sensor after the temperature of the active heat shield is reduced. The measured temperature behaviour is fitted with the second equation in 71, assuming that the measured temperature is closer to the temperature of the inner shield than to the temperature of the cavity. The resulting thermalization time constants are  $\tau_1 = 47.2$  h and  $\tau_2 = 0.9$  h. For an identical cavity, all three thermalization time constant  $\tau_3 = 2.6$  h,  $\tau_2 = 8.2$  h, and  $\tau_1 = 87.4$  h, are directly measured by the frequency response of the cavity [156]. The results are only comparable to a limited extent as the temperature of the cavity or the frequency response could not be measured for the cavity under investigation. During the measurement of the CTE zero crossing temperature, a time delay of 8 h is observed. This time delay needs to be taken into account when consid-

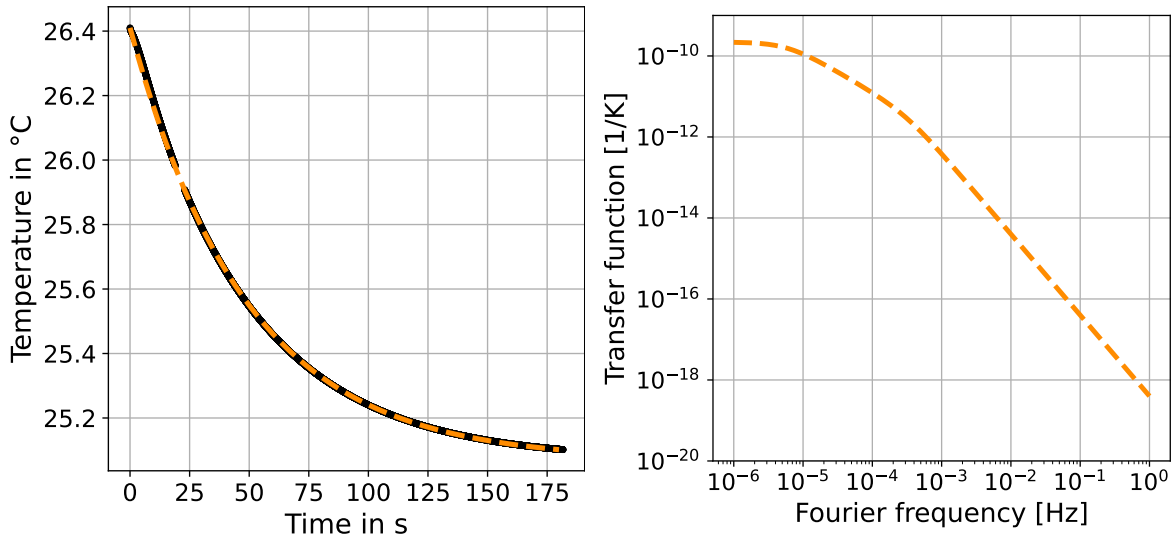


Figure 3.26: Thermalization of the cavity after changing the stabilization temperature of the active heat shield. Right: The measured temperature of the cavity (black lines) decrease exponentially. The fit function given by Equation 71 (orange dashed line) gives a thermalization time constant of  $\tau_1 = 47.2$  h and  $\tau_2 = 0.9$  h. Left: The transfer function between the temperature of the active heat shield and the resonance frequency of the cavity is calculated using the Fourier transform of the temperature response and the thermal expansion of the cavity, when the cavity temperature differs by  $0.2^\circ\text{C}$  from the CTE zero crossing temperature. A cutoff frequency of  $\frac{1}{\tau_1} = \frac{1}{0.9\text{h}}$  and  $\frac{1}{\tau_2} = \frac{1}{47.2\text{h}}$  is employed.

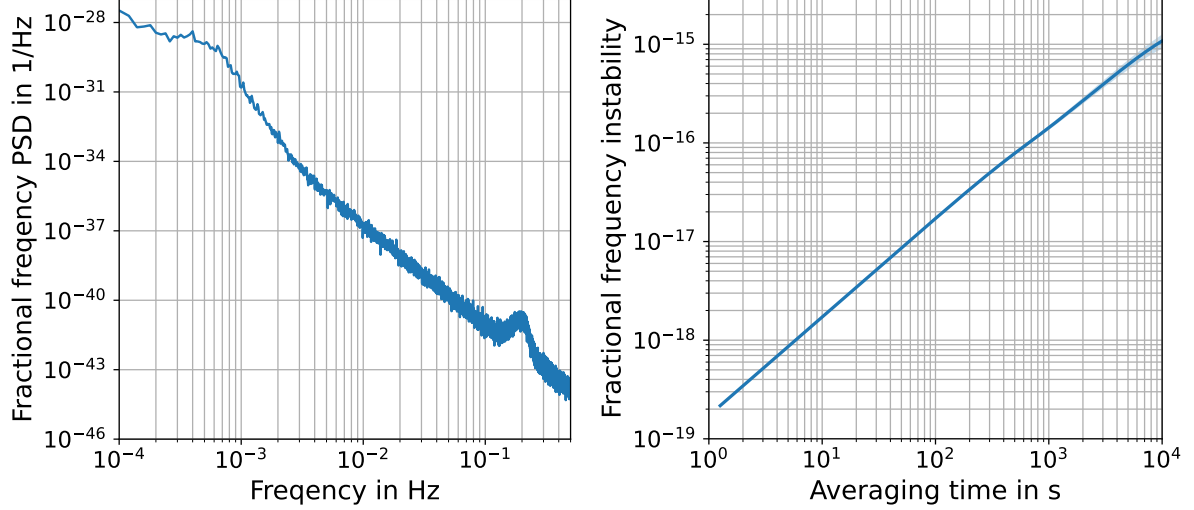


Figure 3.27: Fractional frequency instability of the cavity resonance frequency due to thermal expansion of the cavity. The temperature is actively stabilized, a stabilization temperature within  $\Delta T = 0.2^\circ\text{C}$  deviation from the CTE zero crossing temperature is assumed. Left: PSD of the fractional frequency. Right: modified Allan deviation of the fractional frequency instability.

ering the thermalization time constants. The different results for the thermalization times could also be caused by a inhomogeneous temperature distribution inside the cavity. Moreover, the sensor is connected to the vacuum chamber via copper wires, which introduce additional heat transfer and can influence the sensor temperature.

Applying the Fourier transformation provides the transfer function  $F(\nu)$ . Between the temperature at the sensor position and the active heat shield the transfer function is given by:

$$F(\nu) = \frac{1}{\sqrt{1 + (\nu\tau_1)^2}} \cdot \frac{1}{\sqrt{1 + (\nu\tau_2)^2}}. \quad (72)$$

Which is consistent with the expected low pass behaviour of the heat shields. The frequency response of the cavity for temperature fluctuations at the outer heat shield is even stronger suppressed. Therefore, the function 72 can be chosen as a upper limit for frequency fluctuations due to temperature associated length changes of the cavity. Figure 3.26 (right) shows the transfer function for the resonance frequency of the cavity assuming that the cavity temperature is stabilized within  $\Delta T_0 = 0.2^\circ\text{C}$  of the CTE zero crossing temperature  $T_0 = 26.2^\circ\text{C}$ . Due to the passive heat shield fluctuations of the cavity frequency due to temperature fluctuations are strongly suppressed for frequency larger than  $1/\tau_1$ . Furthermore, an active temperature stabilization is implemented on the active heat shield which is crucial for mitigating temperature fluctuations at low frequencies.

To evaluate the remaining frequency instability with temperature stabilization, it

is necessary to measure the remaining temperature fluctuations. However, due to limitations in the built-in temperature sensor, it is not possible to directly measure the temperature fluctuation of the cavity accurately. Those limitations are given by electronic noise of the sensor and the measurement device and additional heating of the sensor due to heat flow through the wires. The temperature fluctuations at the active heat shield, on the other hand, can be measured with sufficient accuracy using an out-of-loop temperature sensor. The transfer function is used to calculate the expected frequency fluctuations, expecting a difference between cavity temperature and the CTE zero crossing temperature  $T_0 = 26.2^\circ\text{C}$  of less than  $\Delta T_0 = 0.2^\circ\text{C}$ . The resulting fractional frequency instability due to temperature fluctuations is depicted in Figure 3.27, showing the PSD on the left and the modified Allan deviation on the right. The low-pass behavior of the cavity strongly suppresses temperature fluctuations at higher frequencies. However, it is not possible to completely eliminate temperature drifts occurring over hours and days. As a result, the fractional frequency instability increases for longer averaging times. Nevertheless, the fractional frequency instability remains below the thermal noise limit for averaging times below than  $5 \times 10^2$  s.

While the measured temperature of the cavity exhibits the expected low-pass behavior, an almost immediate response of the resonance frequency of the cavity to a temperature change in the active heat shield is observed. Figure 3.28 (left) shows the frequency response (grey and black dots) for a temperature step at the active heat shield of  $\Delta T = 0.2^\circ\text{C}$  (light blue line) and  $\Delta T = 0.4^\circ\text{C}$  (dark blue line). This behavior can be explained by the thermal expansion of the heat shields, which induces mechanical stress in the mounting structure, deforming the cavity. To assess the impact of thermal stress on the fractional frequency instability of the cavity caused by temperature fluctuations at the active heat shield, the transfer function is calculated. This transfer function, denoted as  $F(\nu)$ , is obtained by Fourier transforming the frequency response of the cavity. For simplicity, the frequency response is approximated by an exponential asymptotic function with a time constant of  $\tau = 1.4$  h (orange dashed line).

Using the transfer function, the effect of temperature fluctuations at the active heat shield on the fractional frequency instability of the cavity can be determined. Figure 3.29 illustrates the resulting fractional frequency instability, attributed to stress induced by temperature fluctuations. Notably, the low-pass behavior can only be observed for temperature fluctuations occurring on timescales below  $1 \times 10^3$  s. Beyond this timescale, an increased fractional frequency instability due to temperature fluctuations is observed. The fractional frequency instability exceeds the thermal noise limit for averaging times longer than 20 s. This limitation poses a significant constraint on the use of the laser for clock operation with extended interrogation times. It is important to acknowledge that the measurements only capture temperature fluctuations at a single point on the active heat shield, which may overestimate the average temperature of the heat shield. Moreover, if the length change of the cavity is influenced by thermal stress, temperature gradients become more critical than temperature fluctuations themselves. It is thus crucial to avoid temperature gradients within the heat shield. One approach is to achieve homogeneous heating of the active heat shield and further isolate the cavity. Another approach to reduce the effect of thermal stress is given by

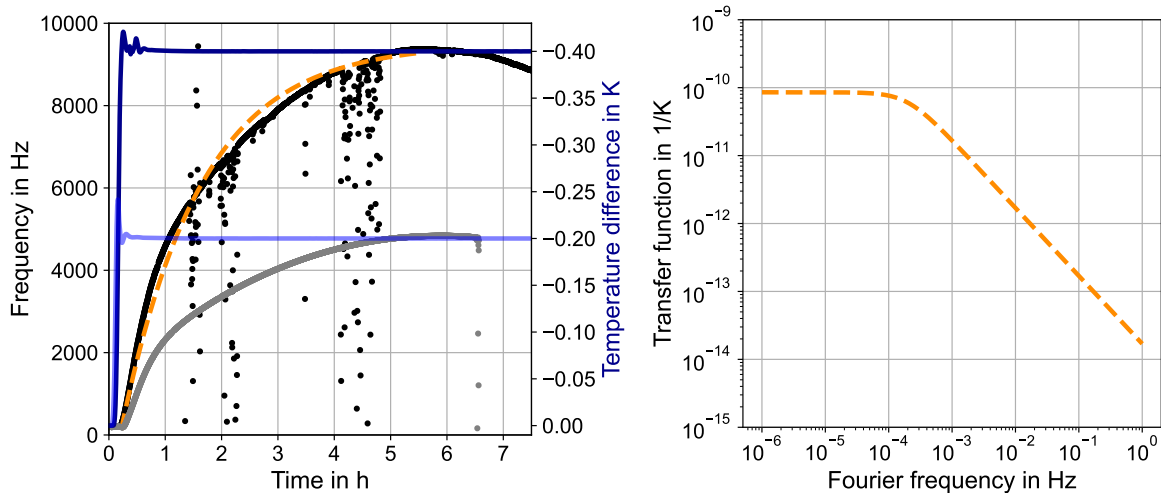


Figure 3.28: Frequency response of the cavity. Right: Response of the resonance frequency of the cavity (black dots) for a temperature step of  $0.4^{\circ}\text{C}$  (dark blue line) and resonance frequency of the cavity (grey dots) for a temperature step of  $0.2^{\circ}\text{C}$  (light blue line) at the active heat shield. An exponential function (dashed orange line) is used as an approximation. Left: The calculated transfer function (orange dashed line) is calculated with a cutoff frequency of  $\frac{1}{\tau} = \frac{1}{1.4\text{h}}$ . Isolated outliers in the frequency measurements appear when the measured beat signal becomes too weak to track accurately.

implementing a more complex cavity mounting [107].

### 3.3.6 Frequency instability of the laser

The frequency stability of the laser, which is locked to the resonance frequency of the stabilization cavity, is assessed by comparing it to a highly stable reference cavity, see Section 3.1.5. To ensure accurate measurements, a linear drift is eliminated from the data. As the temperature stabilization is active the linear drift of  $30.5(1)\text{mHz s}^{-1}$  is caused primarily by spacer aging. In Figure 3.30 a measurement of this drift prior to the stability measurement is shown.

Figure 3.31 (top) shows the PSD of this measurement. It is important to note that during this measurement, several noise sources are actively controlled, including RAM stabilization, optical power stabilization, and temperature stabilization at the zero crossing point. In addition, an active vibration isolation table is utilized. To provide a reference for comparison, the expected limitations arising from the accumulated frequency sources (violet line) is displayed. The PSD graph also depicts the noise contributions from various sources, including the remaining frequency noise of the fiber length stabilization (blue line), photo-thermal noise (orange line), RAM noise (green line), thermal noise (red line), cavity length changes due to temperature fluctuation (purple line), thermal stress contribution (brown line), seismic noise in the  $x$  (pink line),  $y$  (olive line), and  $z$  (purple line) components. Two measurements of the laser



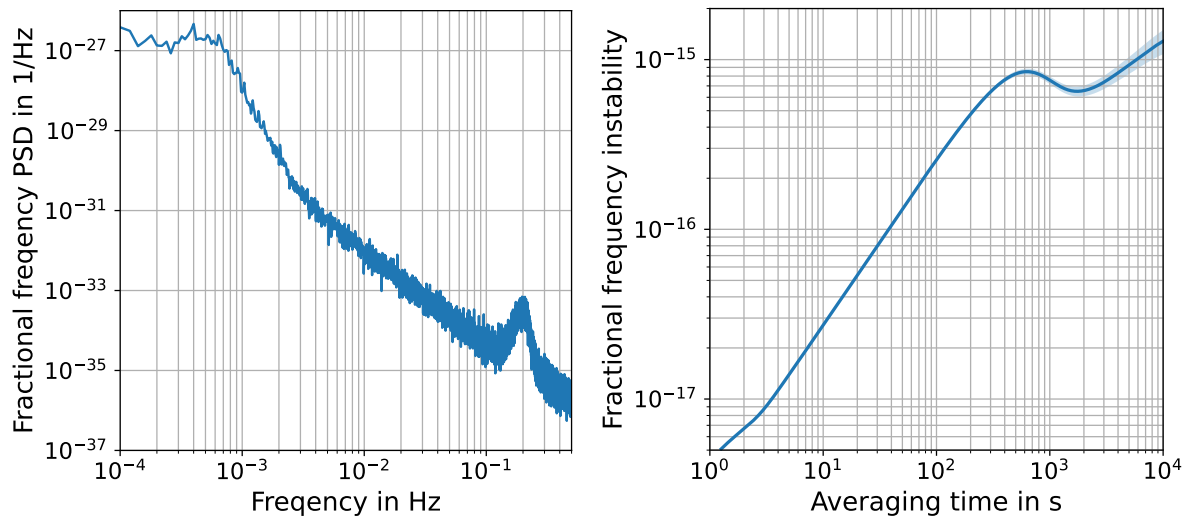


Figure 3.29: Fractional frequency instability of the cavity resonance frequency due to thermal stress due to temperature changes on the heat shields. The temperature is actively stabilized. Left: PSD of the fractional frequency. Right modified Allan deviation of the fractional frequency instability.

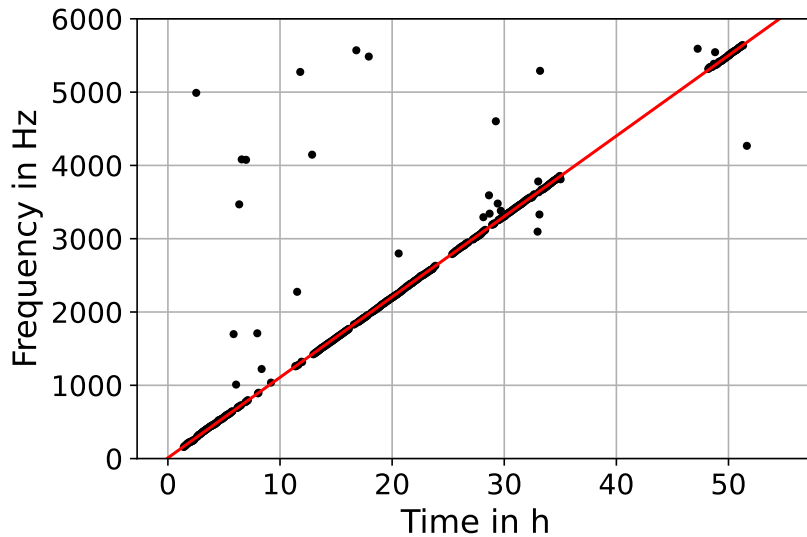


Figure 3.30: Measurement of the linear drift (black dots) due to spacer aging. A linear drift of  $30.5(1) \text{ mHz s}^{-1}$  (red line) is measured when the cavity is temperature stabilized. Isolated outliers in the frequency measurements and missing data points can occur when the optical comb is not stabilized or when the measured beat signal becomes too weak to track accurately.

instability (black and grey line) show the typical laser instability of the system. The difference between them is caused by different laboratory conditions and the settings of the stabilization systems.

At small Fourier frequencies below  $2 \times 10^{-3}$  Hz thermal stress is the dominant noise source. However, the measured laser instability is lower as the expectation from previous measurements of temperature fluctuations and the thermal stress sensitivity of the resonance frequency of the cavity. The reason could be given by a limitation of the measurement uncertainty including statistical uncertainty, changes of the laboratory conditions, changes in temperature inhomogeneity inside the cavity heat shield or an overestimation of the thermal stress due to single point measurements of the temperature sensors. At high Fourier frequencies above 6 Hz non-stabilized phase noise in the optical path and fibres are the dominant noise sources. The PSD of the measured laser instability is more than an order of magnitude higher as the measured phase noise in the presented setup. However, phase noise of the optical path between the reference cavity used for phase comparison and the optical comp is not included in the measurement. As the length of more than 100 m of the fibre connection between reference cavity and optical cavity is more than an order of magnitude longer than the one measured, it is reasonable that the measured laser instability at high frequencies is caused by phase noise in the optical fibers. For Fourier frequency in between the dominant noise sources are thermal noise, photo-thermal noise and seismic noise. The measured laser instability in these regime close to the expectation due to this noise sources. The slightly higher instability of the laser frequency could be caused by underestimation of these noise sources or different laboratory conditions and settings of the system. Furthermore, possible additional contributions could arise from birefringence noise.

Figure 3.31 (bottom) shows the fractional frequency instability of the two measurements calculated by the modified Allan deviation (black and grey line). Furthermore, the expected limitation due to the accumulated noise sources is shown (violet line) for comparison. The modified Allan deviation is calculated from the PSD using Equation 12. Additionally, the limitation due to the linear drift, which is removed from the data, is shown (purple line). The fractional frequency instability is on the order of  $2 \times 10^{-16}$  on a timescale between 0.2s and 200s and thus sufficient for second long probe times of the transportable  $^{27}\text{Al}^+$  clock.

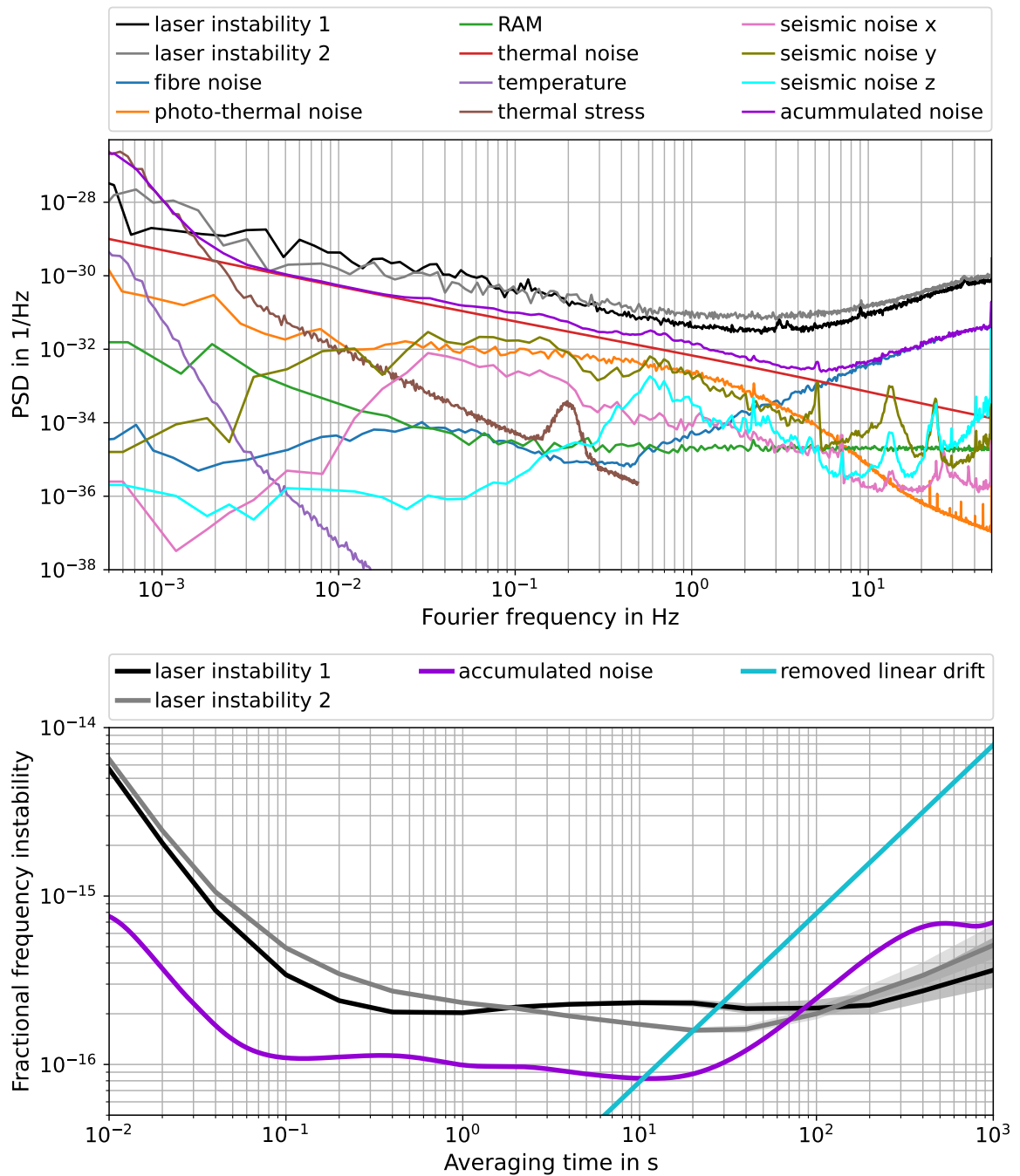


Figure 3.31: Frequency instability of the laser and the contribution of several noise sources. Top: PSD of the fractional frequency instability and the noise sources. Two measurements of the laser instability (black and grey line) with a slight difference due to different laboratory conditions and setting of the laser system are shown. In addition, the contribution of other noise sources are shown. Bottom: Fractional frequency instability calculated by the modified Allan deviation. The two measurements of the fractional frequency instability (black and grey line) are compared to the expected fractional frequency instability due to the accumulated noise sources (violet line). Additionally, the limitation due to the removed linear drift (purple line) is shown.

## 4 Generation of phase stable laser light at 267.4 nm

In the previous chapter, a laser system operating at a wavelength of 1069.6 nm has been discussed. This laser system is frequency stabilized using a highly stable optical cavity. However, the resonance frequency of the clock transition ( $^1S_0$  to  $^3P_0$ ) in  $^{27}\text{Al}^+$  is at 267.4 nm. Therefore it is necessary to quadruple the frequency of the laser light without compromising its phase stability. Consequently, phase fluctuations in the optical setup due to mechanical distortion, temperature, or pressure changes need to be suppressed. In this chapter, a frequency quadrupling system based on the publication titled “Phase-stabilized UV light at 267 nm through twofold second harmonic generation” [146] is presented. The compact system is part of the entire transportable clock laser system producing phase stabilized light at 267 nm.

The chapter is structured as follows: First, the concept of the frequency quadrupling setup is explained, followed by a detailed discussion of the cascaded frequency doubling process, involving two single-pass second harmonic generation stages and the optical setup. Subsequently, the system is characterized, especially phase stability is measured. The frequency quadrupling system is integrated in a rack alongside the stabilization cavity, the seed laser system, and all the necessary optical and electronic components. Furthermore, a second version of the frequency quadrupling system is presented, significantly reducing the size of the system.

### 4.1 Concept of frequency quadrupling setup

The clock transition of  $^{27}\text{Al}^+$ , as discussed in section 2.3, is probed at a wavelength of 267.4 nm. To generate light at this specific wavelength, the laser light delivered by a fibre laser at 1069.6 nm undergoes frequency quadrupling. In order to maintain a high level of phase stability for the resulting UV light, a phase stabilization scheme is integrated into the setup. It is worth noting that frequency doubling itself, achieved through second harmonic generation, does not alter the phase of the generated light [272].

Figure 4.1 provides an overview of the setup, which is constructed on an aluminum breadboard housed within a hermetically sealed aluminum box measuring 42 cm x 23 cm x 8.5 cm. This design ensures rigidity and stability against external disturbances such as temperature fluctuations, pressure changes, and vibrations. The box is sealed using a Viton<sup>®</sup> ring and can be evacuated through a flange on the lid to avoid refractive index changes of the air due to pressure and temperature fluctuations. Alternatively, to prevent damage to optical components from UV light, the box can be purged with clean gases such as oxygen or nitrogen [273]. The system is fiber-coupled, and optical access is provided through several windows sealed with indium. The robust and compact design enables high transportability and integration into a standard 19-inch rack. For frequency quadrupling, two single-pass second harmonic generation (SHG) stages are used. Each stage incorporates a nonlinear crystal housed in a custom-built oven for precise temperature control. The oven temperature is regulated using a PID controller to maintain a constant crystal temperature, which is essential to fulfill the

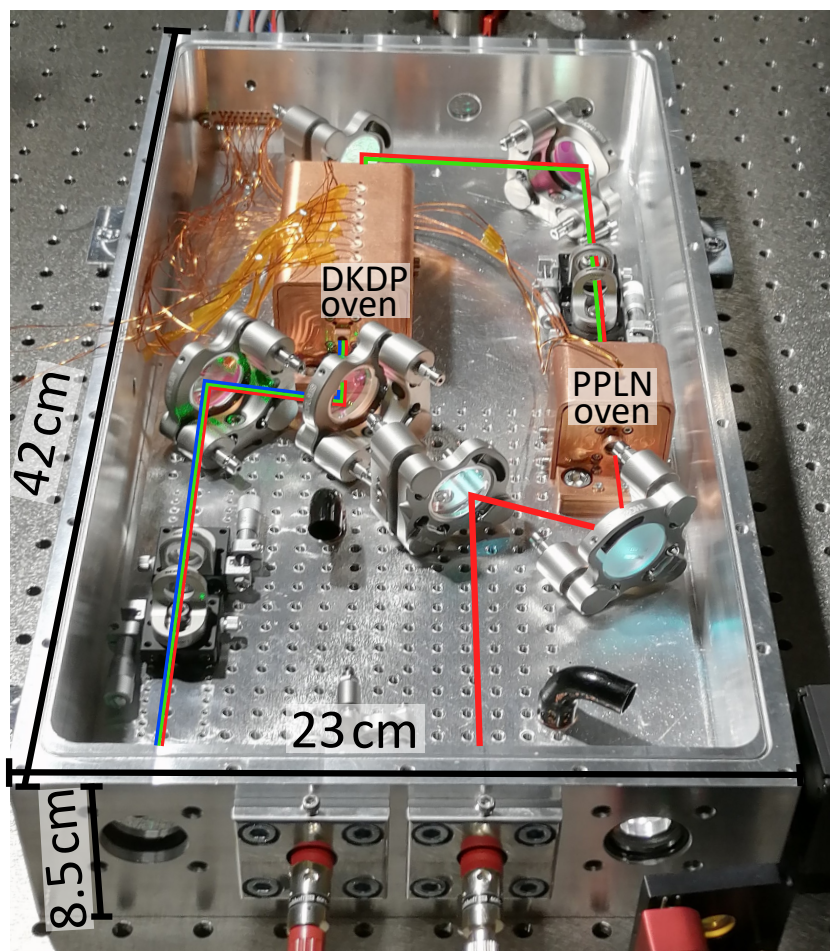


Figure 4.1: Image of the setup of the frequency quadrupling system including two cascaded non-linear crystals inside custom ovens covered by copper heat shields. The first oven (PPLN oven) contains a PPLN crystal waveguide, while the second oven (DKDP oven) contains a DKDP crystal. The beam path of IR light (red), green light (green) and UV light (blue) is schematically shown.

phase-matching condition.

A classical frequency quadrupling setup involves two resonant pump-beam power enhancement cavities for frequency doubling [129–144]. The challenge for a clock laser system is to transfer the phase stability from the cavity-stabilized IR laser through all optical paths including the frequency doubling stages to the UV light. While phase stabilization of the light in the optical cavities is not necessary, separated phase stabilization schemes before, between and after the frequency doubling stages is required. This significantly increases the complexity and size of the setup and results in a limited phase stability of the UV light. Furthermore, adjustment of the cavity length via the Hänsch-Couillaud locking technique [274] requires, additional elements. In contrast, a single-pass configuration of the SHG stages allows for a simple and compact design. This aspects benefit the approach of a transportable laser system. Moreover, interferometric phase stabilization of the IR light throughout the entire setup enables phase stabilization of the produced UV light. However, the single-pass approach involves a compromise, as the UV light power is relatively low due to the limited SHG conversion efficiency in the single-pass configuration. This does not pose a problem, since the required power for long clock probe times is very small ( $< 1 \mu\text{W}$ ).

## 4.2 Second harmonic generation stages

For the purpose of frequency quadrupling, two SHG stages are employed to convert the seed laser light at 1069.6 nm into UV light at 267.4 nm. In the following section, a brief explanation of the SHG process is provided, selection of crystals, and the temperature stabilization of the crystals in the oven sare discussed.

### 4.2.1 Second harmonic generation theory

Second harmonic generation is a nonlinear optical process in which two photons with the same frequency combine to generate a single photon with double the frequency. SHG is a specific case of harmonic generation, and a concise introduction to its fundamental concept is presented in standard textbooks. For a more comprehensive understanding, detailed information can be found in the work of Yariv [275].

When an electric field  $\vec{E}$  is applied to a bulk material, the elementary charges within it can be displaced from their equilibrium positions. This results in a dielectric polarization  $\vec{P}$ , which can be described by the following relation:

$$\vec{P}(\vec{E}) = \kappa_0 \vec{E} + \chi^{(2)} \vec{E}^2 + \chi^{(3)} \vec{E}^3 + O(\vec{E}^4), \quad (73)$$

where  $\kappa_0$  represents the linear dielectric susceptibility. The tensor terms  $\chi^{(i)}$  correspond to the higher-order nonlinear dielectric susceptibilities. When light with polarization along the x-axis is considered, its electric field vector can be described as



$$\vec{E} = \begin{pmatrix} E_x \cdot \sin(\nu t) \\ 0 \\ 0 \end{pmatrix} \quad (74)$$

the second term in equation 73 can be written as

$$P^{(2)}(\vec{E}) = \chi^{(2)} \vec{E}^2 = \begin{pmatrix} d_{11} \cdot \sin(\nu t)^2 \\ d_{21} \cdot \sin(\nu t)^2 \\ d_{31} \cdot \sin(\nu t)^2 \end{pmatrix} = \begin{pmatrix} d_{11} \\ d_{21} \\ d_{31} \end{pmatrix} \cdot E_x^2 \cdot \left( \frac{1}{2} + \sin(2\nu t) \right), \quad (75)$$

where  $d_{ij}$  is the nonlinear coefficient of the material. Following the convention  $\chi_{ij(k)} = 2d_{ij(k)}$ , the term  $E_x^2 \cdot \sin(2\nu t)$  represents polarization oscillations with twice the frequency of the initial electric field. The amplitude of these oscillations is proportional to the squared electric field. As a result of the movement of electric charges, an electric field with twice the frequency of the initial field is generated. This explains how nonlinear crystals can produce SHG light. Efficient harmonic generation requires a large effective nonlinear coefficient  $d_{\text{eff}}$ , which is the resulting nonlinear coefficient depending on the orientation of the crystal in respect to the propagation direction of the pump light. Additionally, phase-matching between the fundamental and second harmonic fields is necessary. When the SHG light and the pump light are in phase, they interfere constructively and contribute to the generation of SHG light. Conversely, in regions where SHG and pump light run out of phase, newly generated SHG light interference destructively with already present SHG light, thus limiting the efficiency of the process. In the non-depleted pump regime, assuming plane wave interaction, the generated SHG intensity  $I_{2\omega}$  scales quadratically with the pump intensity  $I_\omega$  [276]:

$$I_{2\omega} \propto d_{\text{eff}}^2 l^2 I_\omega^2 \nu^2 \frac{\sin^2(\Delta k l / 2)}{(\Delta k l / 2)^2}, \quad (76)$$

where  $l$  is the length of the crystal,  $\nu$  is the pump frequency, and  $\Delta k = k_{2\omega} - 2k_\omega$  represents the difference between the wavenumbers of the pump and SHG fields. In the strong conversion regime (pump depletion regime), the relation between SHG and pump intensity becomes linear. The maximum conversion efficiency is achieved when the phase-matching condition  $\Delta k = 0$  is fulfilled.

This can be achieved by utilizing, the birefringence commonly observed in nonlinear crystals. In terms of refractive index, the phase-matching condition can be expressed as  $n_{\parallel}(\nu) = n_{\perp}(2\nu)$ , where  $\parallel$  and  $\perp$  refer to the polarization with respect to the crystal's ordinary axis. In type I SHG, two photons with ordinary polarization are converted into one photon with extraordinary polarization, or two photons with extraordinary polarization are converted into one photon with ordinary polarization. This leads to the conditions  $n_o(\nu) = n_e(2\nu)$  or  $n_e(\nu) = n_o(2\nu)$ .

For type II SHG, one photon with ordinary polarization and one photon with extraordinary polarization are converted into one photon with extraordinary polarization or ordinary polarization. By selecting an appropriate crystal and polarization, the re-

fractive index can be tuned by controlling the crystal's temperature. This technique is known as non-critical phase-matching. Alternatively, the phase-matching condition can be achieved by adjusting the angle of the pump light beam with respect to the crystal. This is referred to as critical phase-matching. However, in critical phase-matching, the SHG field is often emitted at an angle to the pump light field, resulting in a walk-off of the laser beam. This limits the spatial overlap between the fields and therefore reduces the efficiency of SHG. In non-critical phase-matching, walkoff can be avoided, resulting in higher conversion efficiency and in an improvement in the laser beam quality.

Another approach to achieve phase-matching is given by quasi-phase-matching (QPM) [277]. In QPM, the sign of  $d_{\text{eff}}$  is periodically modulated in the crystal along the propagation direction. This is typically achieved by periodical poling the crystal. This modulation ensures that the generated SHG field coherently adds to the existing SHG field after running out of phase over a coherence length  $l_c = \frac{\lambda}{4(n(2\nu) - n(\nu))}$ . This results in a reduction of the SHG efficiency by a factor of  $2/\pi$ , but enables SHG generation even when the refractive indices do not match.

The quasi-phase-matching condition is expressed as  $\Delta k + G = 0$ , where  $G$  represents the reciprocal vector of the periodical poling with the period  $p$ . The relationship between  $G$  and  $p$  is given by  $|G| = 2\pi/p$ . By appropriately designing the period and tuning the refractive index through temperature control, the quasi-phase-matching condition can be achieved. Due to the linear expansion of the crystal with temperature, the period is also affected. In the case of QPM, it is also possible to convert two photons with extraordinary polarization to one photon with extraordinary polarization or two photons with ordinary polarization to one photon with ordinary polarization. This process is sometimes referred to as SHG type 0 phase-matching.

According to equation 76, the intensity of the generated SHG light scales quadratically with the intensity of the pump light in each layer of the crystal. For a Gaussian beam, the optimal beam geometry can be calculated for a given crystal length, taking into account factors such as absorption, divergence, and walk-off. Boyd and Kleinman et al. [276, 278] developed a theory that considers these factors and determines the optimal focus width  $\omega_0$  of the pump beam by maximizing the integral:

$$\frac{1}{4a} \int_{-a}^a \int_{-a}^a \frac{\exp \left[ ib(x-y) - \frac{B^2(x-y)^2}{a} \right]}{(1+ix)(1-iy)} dx dy. \quad (77)$$

The optimization parameter  $a = \frac{l}{\omega_0^2 k_\omega}$ , and  $b = \frac{1}{2} \Delta k \omega_0^2 k_\omega$  represents the focus strength of the beam and the phase matching parameter, respectively. Both depend on the the focus waist of the beam. If the beam waist decreases the Rayleigh length increases, the intensity at the focus increase, intensity decreases outside the focus. The parameter  $B = \frac{1}{2} \gamma \sqrt{l k_\omega}$  accounts for the expected walk-off with the walk-off angle  $\gamma$ . By maximizing this integral, the optimal focus width of the pump beam can be determined. The power of the SHG light  $P_{2\nu}$  also scales quadratically with the power of the pump light  $P_\nu$ , as given by the following equation:



$$P_\nu = \kappa P_{2\nu}^2. \quad (78)$$

The conversion coefficient  $\kappa$  depends on the beam geometry, absorption coefficient, and the nonlinear coefficient  $d_{\text{eff}}$  of the material.

To achieve higher pump light intensity in the crystal, integration of the crystal in the core of an optical waveguide can be utilized. The confinement of the electric field in the waveguide leads to a strong enhancement of the conversion coefficient, resulting in a highly efficient SHG process.

#### 4.2.2 Nonlinear crystals selection

In order to transfer the phase stability in the frequency quadrupling system from the IR to UV light, it is important both beams are spatial overlapping. If the beams are separated, different phase disturbances are acting on them and the phase relation between IR and UV light is compromised. To ensure optimal spatial overlap between the pump laser beam, the second harmonic generation (SHG) light beam, and the fourth harmonic generation (FHG) light beam, it is crucial to avoid walk-off in both SHG stages. This can be achieved through either quasi-phase-matching or non-critical phase-matching.

The available SHG generation efficiency is fundamentally limited due to the single-pass approach employed in both stages. Additionally, the UV output light power of the second SHG stage scales quadratically with the light power output of the first SHG stage. In order to achieve a sufficient UV output light power, the first SHG stage must provide a high conversion efficiency. This significantly restricts the choice of crystals. A periodically-poled lithium niobate (PPLN) ridge waveguide crystal<sup>5</sup> [279–285], has been selected for the first doubling stage, converting the wavelength from approximately 1069.6 nm to 534.8 nm. The waveguide crystal allows for QPM and facilitates a type 0 SHG process, resulting in the SHG light having the same polarization to the pump light. The waveguide crystal has a length of 10.3 mm, and both facets are coated with anti-reflection layers for the pump light and SHG light wavelengths. The crystal is specified with a conversion coefficient of  $\kappa \sim 125\% \text{ W}^{-1}$  at a quasi phase-matching temperature of 45(20)°C. The temperature tuning bandwidth  $\Delta T$  (FWHM) reflects the change in  $\Delta k$  caused by temperature and thus conversion variations according to Equation 76. For PPLN crystals,  $\Delta k$  depends not only on the temperature-induced changes in the refractive indices for both wavelengths but also on the linear expansion of the poling period. Taking all of these effects into account, the temperature tuning bandwidth,  $\Delta T$ , can be calculated using the following formula [277, 286]:

$$\Delta T = \frac{0.443}{l} \left( \frac{\delta \Delta n}{\delta T} + \alpha \Delta n \right)^{-1}. \quad (79)$$

Here,  $\Delta n = n_\nu - n_{2\nu}$ , where  $\alpha$  represents the linear thermal expansion coefficient.

---

<sup>5</sup>HC Photonics (HCP)

The effective refractive index of the waveguide crystal also depends on its geometry and the refractive index of the cladding. For simplification, the temperature tuning range of a 10.3 mm long bulk PPLN crystal with  $\alpha = 7 \times 10^{-6} \text{ K}^{-1}$  [287] is calculated, which yields  $\Delta T = 2.8 \text{ K}$ . The refractive index of the DKDP crystal is calculated with the Sellmeier equation [288, 289].

For the second doubling stage, a deuterated potassium dihydrogen phosphate (DKDP) crystal<sup>6</sup> [290] is selected to convert the wavelength from 534.8 nm to 267.4 nm. This crystal allows for non-critical phase-matching of type I at a phase-matching temperature of approximately 100 °C. However, the phase-matching temperature varies significantly with the deuterium content of the crystal. The crystal has a length of 50 mm, and both facets are anti-reflective (AR) coated for the pump light and SHG light wavelengths. The nonlinear coefficient of the crystal is approximately  $d_{\text{eff}} \approx 0.43 \text{ pm V}^{-1}$  [291] and its temperature tuning bandwidth is given as 3.2 K cm [291]. Using Boyd and Kleinman’s framework [278] and optimizing equation 77, the optimal focus waist is numerically calculated for the given crystal, resulting in an optimal waist focus of  $\omega_0 = 32 \text{ }\mu\text{m}$ . Consequently, a single-pass conversion coefficient of  $\kappa = 0.15 \% \text{ W}^{-1}$  can be achieved. Table 4.1 provides the key parameters for both crystals.

Table 4.1: Key crystal parameters.

Value	PPLN	DKDP
Length in mm	10.8	50
Facet dimensions in mm <sup>2</sup>	0.5 x 1.5	5.0 x 5.0
Transparency range bulk in nm	300... 5000	200... 2100
Absorption coefficient pump light in cm <sup>-1</sup>	$\approx 0.003$	$\approx 0.004 \dots 0.005$
Absorption coefficient SHG in cm <sup>-1</sup>	$\approx 0.03$	$\approx 0.004 \dots 0.005$
$d_{\text{eff}}$ in pm V <sup>-1</sup>	14... 16	$\approx 0.43$
Conversion coefficient in % W <sup>-1</sup>	125	0.15
Hygroscopicity	none	high
Expected phase-matching temperature in °C	45(20)	$\approx 100$
Temp. tuning bandw. in K cm	2.8	3.2
Manufacturer	HCP	Altechna

### 4.2.3 Crystal temperature controlling system

Effective SHG for both crystals only occurs at the phase-matching temperature as discussed in the previous sections. To ensure stable temperature in both crystals, precise temperature control is required. Therefore, custom ovens have been designed and built for each crystal. These ovens share a similar design, providing accurate, constant, and uniform temperature control up to 100 °C, limited by the used Peltier elements. Figure 4.2 (left) presents a cut-away drawing, while Figure 4.2 (right) illustrates an exploded

<sup>6</sup>Altechna

view of the oven. The oven’s dimensions do not exceed  $70 \times 46 \times 46$  mm.

Inside the oven, the waveguide (1) is positioned inside a copper socket (2). To prevent mechanical stress and ensure efficient thermal contact, the waveguide is enveloped in a single layer of  $100 \mu\text{m}$  indium foil. A spring-loaded copper plate applies pressure to hold the waveguide against the socket (3), avoiding mechanical tension. Two Peltier elements (4) are employed for heating. Temperature measurement is accomplished using two PT1000 temperature sensors (5), with one integrated into the top portion and the other in the bottom portion of the socket. Active temperature stabilization of the crystal oven is achieved by a PID controller, providing a resolution of 1 mK using one of the PT1000 temperature sensors. The second PT1000 temperature sensor serves as a monitoring sensor. The PT1000 temperature sensors and Peltier elements are connected to the PID controller (Meerstetter TEC-1091) via a vacuum-compatible sealed d-sub multi-pin feed-through, which is integrated into the box wall. To ensure thermal isolation of the crystal oven, an inner shield made of MACOR<sup>®</sup> (6) surrounds the socket. However, some temperature difference may persist between the crystal oven and the surrounding environment, potentially causing convection of the surrounding gas. This convection can lead to fluctuations in optical power due to beam pointing variations and phase distortions. To mitigate this, an additional outer shield (7) is added to the crystal oven. The outer shield, made of copper, maintains thermal contact with the breadboard through the copper ground plate of the oven. Apertures for the pump laser beam and SHG beam in the outer shield are incorporated as extensions of the copper shield to further minimize fluctuations in the gas along the pump light path. Importantly, the temperature of the outer shield does not exceed  $25^\circ\text{C}$  during normal oven operation. Furthermore, the first oven’s outer shield extrusion integrates two lenses (8) for directly coupling the IR light into the waveguide.

The design principle of the second oven closely resembles that of the first one, with the heating system located in the middle, surrounded by a MACOR<sup>®</sup> shield, and an outer copper shield. Figure 4.3 illustrates a drawing of this oven. Inside the oven, a 50 mm DKDP crystal is positioned. Consequently, the second oven is longer than the first, and has the dimensions  $110 \times 46 \times 46 \text{ mm}^3$ , making spatial temperature homogeneity more critical. To address this, three rows consisting of three Peltier elements and six PT1000 sensors are utilized, with three sensors placed in the bottom part of the socket and three in the top part. The two outer rows of Peltier elements operate in series with a fixed current, while the current to the middle row of Peltier elements is regulated by a PID controller for active temperature stabilization, using one of the PT1000 temperature sensors. The remaining PT1000 sensors can be employed for independent temperature monitoring to assess temperature inhomogeneity.

Unlike the PLLN Waveguide, the handling of the DKDP crystal is not as sensitive, making the spring-loaded mounting mechanism unnecessary. Instead, the DKDP crystal is wrapped with two layers of  $100 \mu\text{m}$  indium foil and placed inside the copper socket, establishing thermal contact via the indium foil. Unlike the first, the second oven does not integrate any lenses. However, extensions of the outer copper shield are added to shield the laser beam from pressure fluctuations caused by heating the oven

and the surrounding gas.

The parameters of the PID controller are optimized for both ovens using a standard step response test to determine the optimal PID settings. The goal is to minimize the temperature settling time, which indicates the timescale between reaching the settling temperature the first time and converging to stable temperature. For the first oven, a temperature settling time of less than 30 s is achieved, while the second oven has a settling time of less than 60 s. Furthermore, a maximum heating or cooling ramp of 1 °C/min is chosen for both ovens to ensure slow and uniform temperature changes, protecting the crystals from mechanical stress. Additionally, several tests are conducted to evaluate the oven performance. The thermalization timescale ( $1/e$  time constant of an exponential approach) is measured by operating the oven at its settling temperature using a constant heating power, without temperature control by the PID controller. By changing the heating power with a step function, the response of the oven is measured. The temperature of the oven shows an exponential convergence to the new settling temperature.

Figure 4.4 illustrates the typical response for both ovens, for increasing and decreasing heating power. The first oven exhibits a thermalization timescale of  $(280 \pm 30)$  s, while the larger second oven has a thermalization timescale of  $(610 \pm 30)$  s. Additionally, the long-term temperature stability of both ovens is assessed over several hours. In this case, the oven temperature is controlled by the PID controller, and an additional temperature sensor is used for out of loop measurement. The first oven demonstrates a temperature stability within 0.01 °C, while the second oven achieves a stability of 0.005 °C. All the important properties of both crystal ovens at their operational temperature are summarized in Table 4.2.

Table 4.2: Key parameters of the crystal ovens.

Measured value	PPLN-oven	DKDP-oven
Operational temp.	44 °C	76 °C
Long term temp. stability	0.01 °C	0.005 °C
Max. temp. ramp	1 °C/min	1 °C/min
Temp. settling time	30 s	60 s
Thermalization timescale	$(280 \pm 30)$ s	$(610 \pm 30)$ s

### 4.3 Optical setup

In this section, the optical setup of the frequency quadrupling system is discussed. The discussion begins with the coupling of light at a wavelength of 1069.6 nm and the first SHG stage for frequency doubling from 1069.6 nm to 534.8 nm, followed by a description of the second SHG stage for frequency doubling from 534.8 nm to 267.4 nm. Additionally, the optical phase stabilization scheme used in this setup is explained.

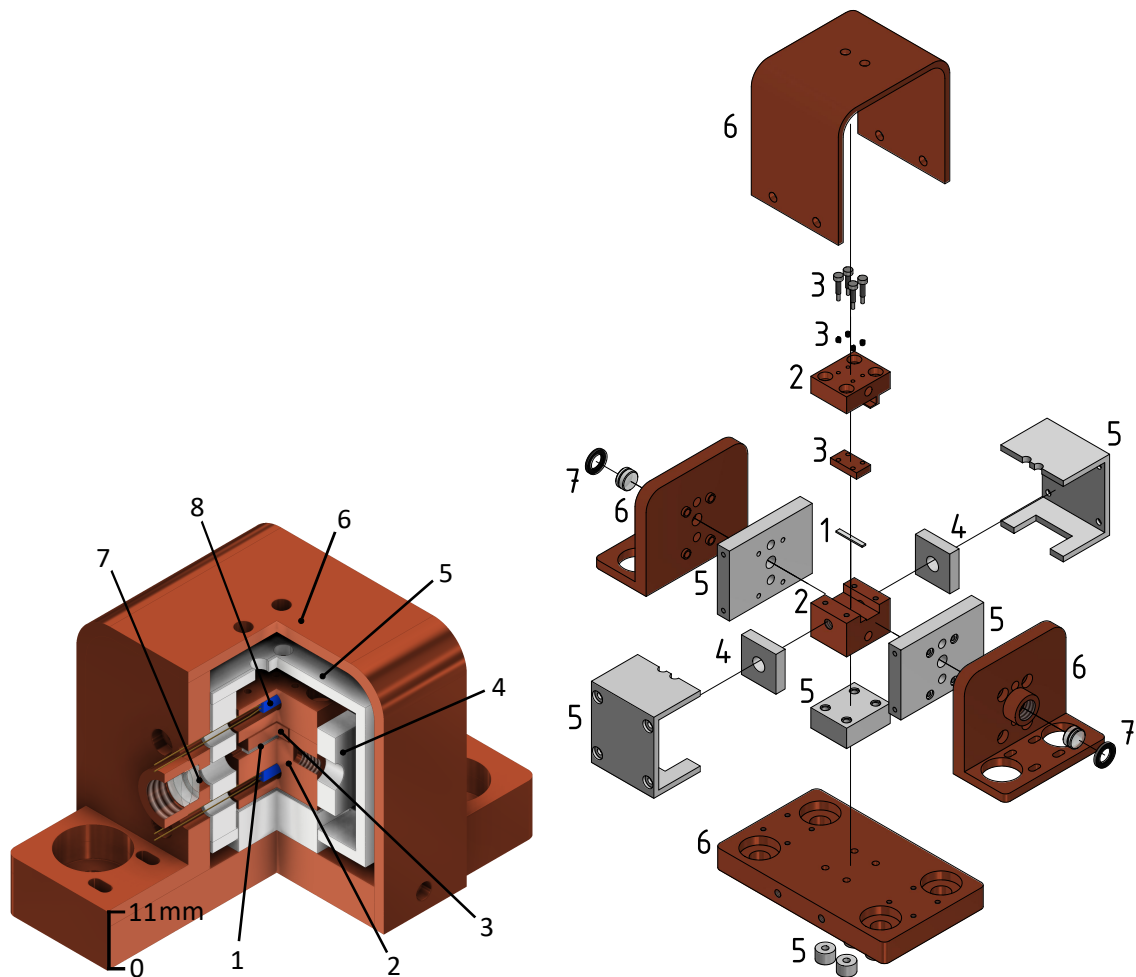


Figure 4.2: 3D drawing of the first crystal oven. Left: Cut-away drawing of the oven for the PPLN crystal. Right: Explosion drawing of the same oven. For both drawings: 1: waveguide, 2: parts of the socket, 3: fixation parts, 4: Peltier elements, 5: inner MACOR<sup>®</sup> shield, 6: outer copper shield, 7: lenses, 8: PT1000 temperature sensor.

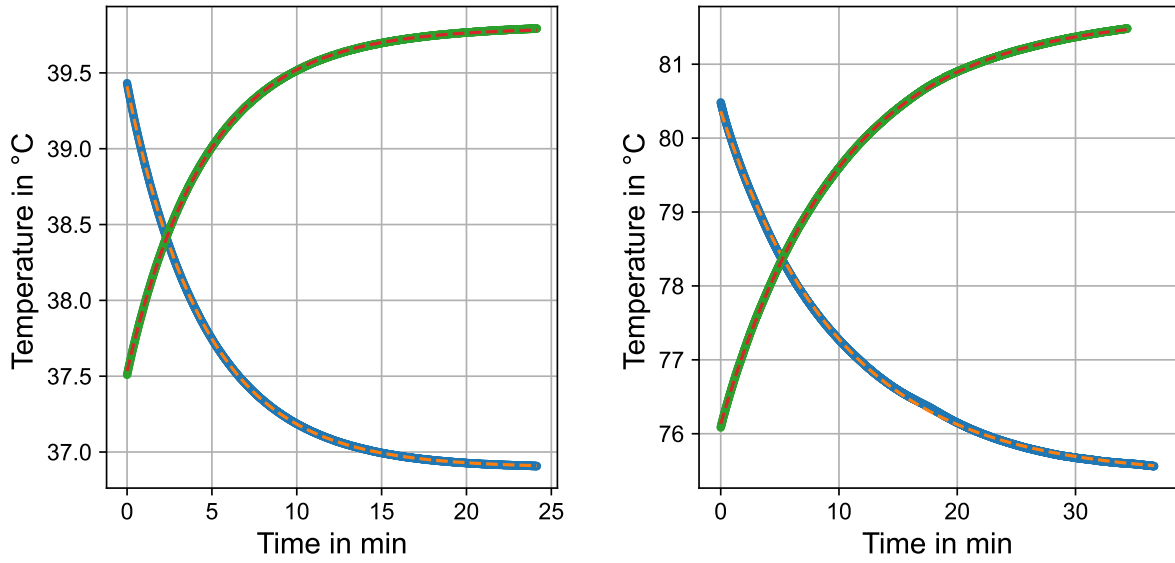


Figure 4.3: Thermalization time of the ovens for increased heating power (green line) and for decreased heating power (blue line) with exponential fits (dashed orange lines). Right: Measurement for the first crystal oven with a thermalization time  $\tau = (280 \pm 30)$  s. Left: Measurement for the second crystal oven with a thermalization time  $\tau = (610 \pm 30)$  s.

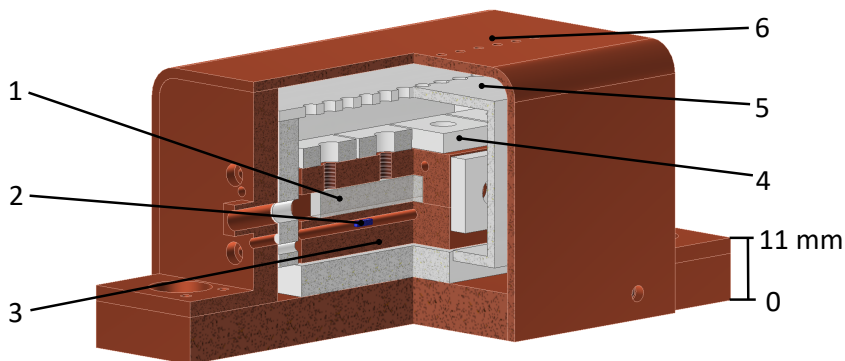


Figure 4.4: Cut-away CAD drawing of the second crystal oven. 1: DKDP crystal, 2: PT1000 temperature sensor, 3: socket, 4: Peltier elements, 5: inner MACOR<sup>®</sup> shield, 6: outer copper shield.

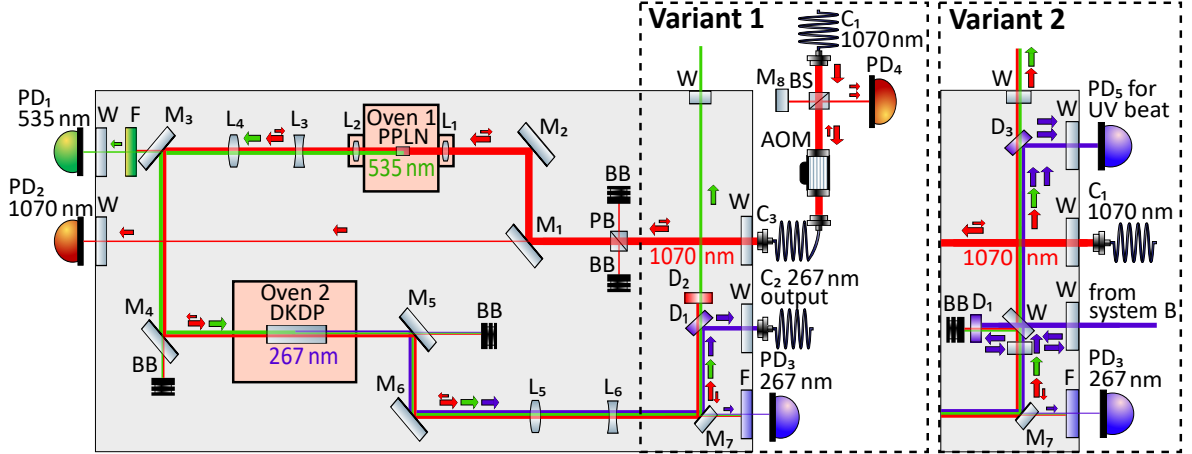


Figure 4.5: Schematic drawing of the setup showing an overview of the components used and the laser beam’s propagation direction. Variant 1: The setup is used as a length-stabilized UV light source. For details, see main text. Variant 2: The setup is expanded for a frequency instability measurement of the produced UV light in combination with a second UV light source.  $C_1$ : Collimator, IR light from Laser;  $C_2$ : Collimator, UV light output; PB: Polarizing beamsplitter; M: Mirror; L: Lens; BB: Beam block; PPLN: PPLN waveguide; DKDP: DKDP crystal; D: Dichroic mirror; PD: Photodiode; F: Filter; W: Window; BS: beamsplitter; AOM: Acousto-optic modulator.

### 4.3.1 First SHG stage from 1069.6 nm to 534.8 nm

A schematic drawing of the optical setup is shown in Figure 4.5, designed to handle an optical power of 1 watt of IR light at 1069.6 nm. The IR light is delivered to the setup through a polarization-maintaining fiber from the light distribution board (see section 3.2.2). A collimator positioned outside the box is employed to collimate the laser beam. The light enters the box via an AR-coated optical window. A polarizing beamsplitter is used to clean the polarization of the IR light. This pump light is horizontally polarised, corresponding to extraordinary polarisation in the crystal.

For the first SHG stage a PPLN-ridge waveguide is used for frequency doubling from 1069.6 nm to 534.8 nm. A power on the order of 200 mW of green light can be generated from 1 W of IR light. This waveguide is positioned in the first oven to maintain a constant temperature. It efficiently converts the IR laser light at 1069.6 nm into green light at 534.8 nm through SHG when actively temperature stabilized at the quasi phase-matching temperature  $T_{\text{pm}} \approx 44^\circ\text{C}$ . To couple the beam into the PPLN waveguide, two mirrors,  $M_1$  and  $M_2$ , are used. Highly stable adjustable mirror mounts<sup>7</sup> are used for all mirrors. Mirror  $M_1$  has a transparent backside, enabling the transmitted light to be detected by a photodiode  $P_1$ , located outside the box for monitoring the optical power of the IR light. To achieve mode matching of the IR beam and ensure optimal coupling into the waveguide, lens  $L_1$  with a focal length of  $f = +12.5$  mm is used. The combination of  $L_1$  and an adjustable lens with a focal length of  $f = +15$  mm inside the collimator guarantees overlap with the partial mode of the waveguide. The

<sup>7</sup>Thorlabs, Polaris line



numerical aperture (NA) of the waveguide for the pump light at 1069.6 nm is 0.16 in vertical direction and 0.14 in the horizontal direction. At 534.8 nm, the NA of the waveguide is specified as 0.8 in vertical direction and 0.7 in horizontal direction. The green light is horizontally polarized, as two extraordinary photons are converted into one extraordinary photon with double the frequency. This occurs due to the quasi phase-matching SHG process of type0. The outgoing green and IR light beams are collimated with an achromatic AR-coated lens  $L_2$ , with a focal length of  $f = +12.5$  mm. This results in a green light beam diameter of 2 mm. Additionally, a fraction of the non-converted IR light is transmitted through the waveguide. The IR light is collimated by the achromatic lens, resulting in a beam with a diameter of 4 mm, which spatially overlapped with the green light beam.

### 4.3.2 Second SHG stage 534.8 nm to 267.4 nm

For the second stage a DKDP crystal is used, which is placed inside the second oven. It converts green light on the order of 200 mW at 534.8 nm into up to 60  $\mu$ W of UV light at 267.4 nm. The DKDP crystal is 50 mm long and is AR-coated for both wavelengths.

For efficient conversion the crystal is heated to the phase-matching temperature by the actively temperature stabilized oven, which ensures a homogeneous phase-matching temperature along the crystal. It is worth noting, that the phase-matching temperature of the DKDP crystal strongly depends on the deuterium content of the crystal. When the exact composition of the crystal is not known a accurate prediction is not possible. A phase-matching temperature  $T_{\text{pm}} \approx 76^\circ\text{C}$  is measured for the crystal in this setup, which is reasonable for a highly deuterated DKDP crystal [292]. Following Boyd-Kleinman and solving the corresponding expression an optimal beam waist size of  $w_0 = 32 \mu\text{m}$  (radius at  $1/e^2$  intensity level of the Gaussian beam at the focus point) was found. Assuming a pump light beam at 534.8 nm with an optical power of 200 mW. For high SHG efficiency of the second stage, the pump beam is focused in the center of the crystal along its propagation direction. The calculated waist and optimum focus position for the green pump light are set by a telescope directly behind the first SHG stage. The telescope consists of two lenses  $L_3$  with  $f = -48$  mm and  $L_4$  with  $f = +75$  mm, which are placed on individual linear translation stages. The beam positioning can be adjusted with two additional mirrors  $M_3$  and  $M_4$ , which are placed behind the telescope and between the two SHG stages. The first mirror is backside-polished. Therefore, the pump light at 535 nm for the second SHG stage can be measured by the photodiode  $P_2$  placed outside the box.

In the second SHG stage a type 1 SHG process is used. The incoming green light is still horizontal polarized, which corresponds to ordinary polarization in the crystal. The generated UV light is vertically polarized, as two ordinary photons are converted into one extraordinary photon with twice the frequency. Even after the second SHG stage, the laser beams at all three wavelengths still spatially overlap. This is due to the negligible walk-off of the DKDP crystal, which is used with noncritical phase-matching. To adjust the position of the beams, two adjustable mirrors  $M_5$  and  $M_6$ , can be utilized. A second telescope, consisting of two lenses  $L_5$  and  $L_6$  placed on individual linear trans-



lation stages, is employed to recollimate the beams. Since achromatic lenses for deep UV light are not commercially available, complete suppression of chromatic aberration is not achievable. The power level of the generated UV light is monitored by photodiode  $P_3$  after transmission through a backside-polished mirror  $M_7$ , and a subsequent short-pass optical filter to eliminate any remaining green and IR light. In variant 1, the setup functions as a UV light source. In this configuration, the light reflected off  $M_7$  is split by a dichroic mirror  $D_1$ , with the green and IR light passing through and the UV light reflecting. The UV light exits the box through a window and can be coupled into a fiber, or directly used for the experiment.

### 4.3.3 Interferometric phase stabilization

The setup is designed to provide UV light source with phase stability bridging from the IR to the UV. To minimize phase noise contribution arising from pressure and temperature fluctuations, an air-sealed box is employed in the setup. However, for ultimate performance, an active phase stabilization scheme is still required. In this setup, interferometric phase stabilization is implemented for the IR light throughout the entire system, including both SHG stages and the majority of the optical path. Since the beams with all three wavelengths spatially overlap until they are separated by  $D_1$ , it is expected that these beams will experience similar phase and frequency disturbances. Therefore, the length stabilization of the IR light path serves as a reference for the UV light, accounting for common length changes. The IR length stabilization is realized according to the scheme depicted in Figure 4.5, variant 1. A short-pass dichroic mirror  $D_2$ , located closely behind  $D_1$ , is used to reflect the IR light. The green light, on the other hand, is transmitted through  $D_2$  and can be utilized outside the box via a window. The IR light follows the same path back to the first collimator  $C_1$ , and is coupled back into the fiber. The phase stabilization path for the IR light is localized in the distribution board and is already described in Section 3.1.4.

To compare the frequency stability of the system with a reference UV laser system, slight modifications to the light path are required. These modifications are depicted in Figure 4.5, variant 2. An additional UV beam from a second source is guided into the box through the output port of variant 1. Instead of using the dichroic mirror  $D_1$ , an uncoated window is installed and utilized as a beamsplitter to spatially overlap the two UV beams. The UV light generated in the FHG setup passes through the beamsplitter, while approximately 4% of the UV light from the second source is reflected. Since the second UV light source is expected to have a higher UV light power, this light splitting arrangement ensures that sufficient power is available from both sources to create a beat note for frequency comparison measurements. Next to the beamsplitter a dichroic mirror  $D_1$  is installed to reflect the UV light from the reference system, enabling phase stabilisation of the light up to this point. Optional, a beamsplitter can be installed in the light path of the frequency quadrupling system for backreflection of the IR light and setting the end point for the phase stabilisation scheme. To perform the frequency comparison, the UV light is reflected by the dichroic mirror  $D_3$  and detected by a photodiode located behind an optical window outside the box. The green and IR

light, on the other hand, are transmitted through the dichroic mirror  $D_3$  and can be further used outside the box after passing through a window. Further details regarding the frequency comparison measurement between two UV light sources are provided in section 4.4.2.

## 4.4 Characterization of the frequency quadrupling setup

The two main aspects of the UV laser system are the UV light output power and the phase stability of the UV light. The design of the system prioritizes achieving good phase stability at the expense of a lower output power due to the single pass approach. Both of these aspects are measured and will be thoroughly discussed in this section.

### 4.4.1 Second harmonic generation efficiency

The UV output power of the frequency quadrupling system is primarily determined by three factors: the IR input power from the laser, losses of optical power due to components in the light path, and the conversion efficiency of both SHG stages.

The IR optical input power of the frequency quadrupling system is limited to 1 W. This limitation is given by the limited pump light power of the PPLN waveguide used in the first SHG stage. The limitation is determined by the manufacturer, additionally a limitation of 200 mW of green light output power is stated by the manufacturer, while the stated output power depends on the input power through the expected conversion efficiency of the waveguide. From the physical view different damaging processes limit the maximum optical power for safe operation. Some important processes to mention are photoinduced effects such as photorefractive damage [293, 294] or green light-induced infrared absorption [295] inside the PPLN waveguide or optical induced thermal damaging [296] of the facets of the waveguide. For better performance and a higher damaging threshold, Mg enriched MgO:PPLN crystals can be used.

In any optical system, there are losses in optical power due to various factors such as absorption, unintentional reflection, limited reflectivity of optical mirrors and limited coupling efficiency into optical fibers or waveguides. In the presented setup, the main contribution to optical losses arises from the coupling efficiency of the free-space beam into the PPLN waveguide, which is limited to approximately 50% due to the waveguide's geometry, supporting an elliptical beam. It is important to note that the specification of the PPLN waveguide already accounts for these coupling losses. If the output light is coupled to an optical fiber, the coupling losses significantly increase the overall loss equation of optical power, with coupling efficiencies typically limited to 30% to 50%, in the deep UV regime. In the setup, all optics used have either high-reflective coatings (mirrors, dichroic beamsplitter) or antireflection coatings (crystals, windows, polarizing beamsplitter, lenses). As a result, the losses for each component are relatively small, mostly around 1% or below. However, it should be noted that there is an approximate 10% loss of UV light power due to optics in the UV light path. When measuring the UV light power, the output power of the UV light after the

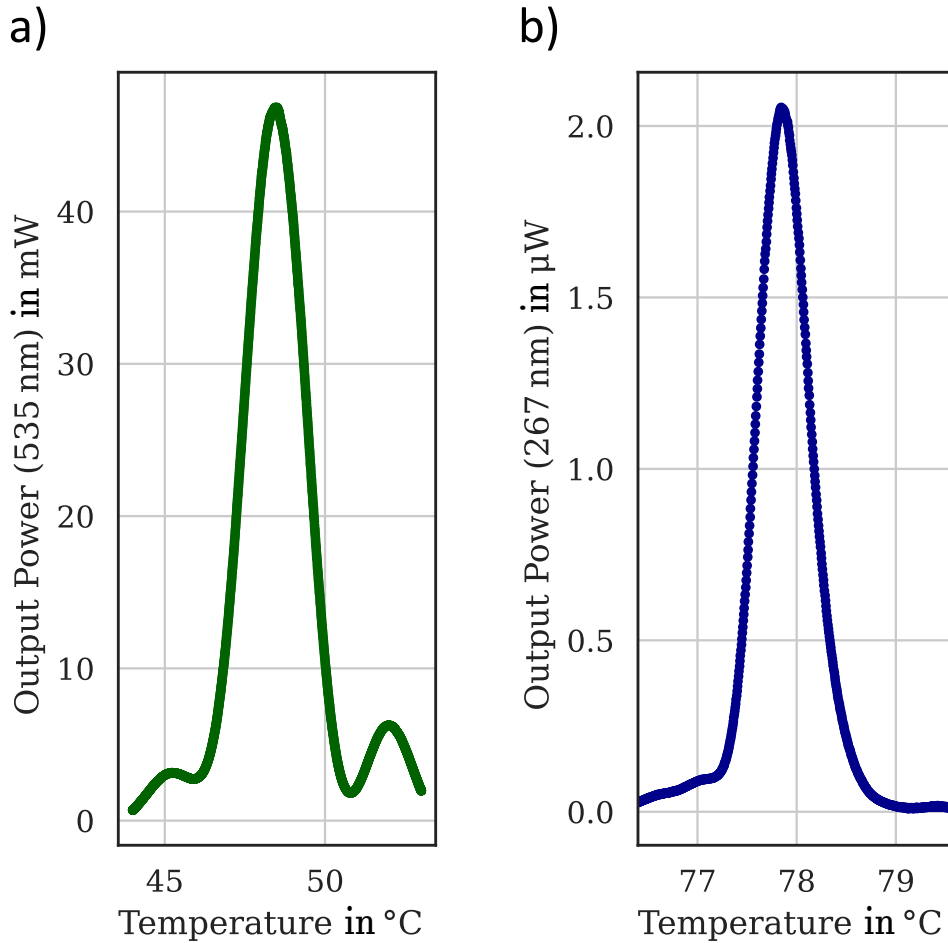


Figure 4.6: SHG output power of the crystal as a function of the oven Temperature. Left: Temperature dependency of the SHG efficiency for the first SHG stage at 534.8 nm. Left: Temperature dependency for the second SHG stage at 267.4 nm. Both are measured for an IR pump light power of 450 mW at 1069.6 nm

entire setup is considered, including the 10% losses. However, when considering the conversion efficiency of the second SHG stage, the measured optical power needs to be corrected for additional optical losses. The same applies to the losses in the green light path and the IR light power for the efficiency of both SHG stages. Photodiode  $P_2$  is used to measure the IR light power, while photodiode  $P_1$  is used to measure the green light power. The transition and reflection of mirrors  $M_1$  and  $M_3$  are taken into account in the analysis. An optical power sensor<sup>8</sup> is used to measure the optical power. The considerations of optical power and conversion efficiency for both SHG stages, losses due to optics in the IR and green light paths are neglected. Consequently, the given measurements of the optical light power for all three wavelengths are considered to be accurate within a range of approximately  $\pm 7\%$ , taking into account the losses and the limited measurement accuracy of the measurement devices.

<sup>8</sup>Thorlabs, S121C

Equation 76 in Section 4.2.1 gives a theoretical expectation of the efficiency of the SHG process, in respect of the phase mismatch ( $\Delta k$ ). For non-critical phase-matching, the value of  $\Delta k$  varies with the temperature, and the maximum conversion efficiency is achieved at the phase-matching temperature. In Figure 4.6 the measurement results are presented. The temperature dependence of the output power is shown for both the first and second SHG stages. For the first SHG stage, a maximum green light power of 47 mW is generated with an IR pump light power of 450 mW at an oven temperature of 48.5 °C. This temperature value falls within the manufacturer’s specification of (45 ± 20) °C, indicating agreement between the measurement and the expected temperature range. The full-width half maximum (FWHM) of the temperature tuning bandwidth is 2.2 °C, slightly smaller than the theoretically expected value of 2.7 °C for a 10.3 mm long bulk crystal. This difference may arise from a different effective refractive index in the waveguide compared to the bulk crystal.

For the second SHG stage, an output power of 2 μW is obtained at the phase-matching temperature of 77.84 °C, with a green pump light power of 47 mW. The FWHM of the temperature tuning bandwidth is 0.61 °C, which is in good agreement with the theoretically expected value of 0.62 °C. The measured oven temperature of approximately 78 °C differs from the expected value of around 100 °C. This discrepancy can be attributed to the dependence of the phase-matching temperature of DKDP crystals on the degree of deuteration, which influences the refractive index for both polarization. For a highly deuterated crystal, a phase-matching temperature of 78 °C at 1070 nm is reasonable, following the results of Ji et al. [292].

The phase-matching temperature has also been determined for different pump beam power levels. In the first SHG stage, the measured phase-matching temperature is found to decrease with higher pump light power. Specifically, for low pump light power around 50 mW, the measured phase-matching temperature is approximately  $T = 49$  °C, whereas for pump light power around 1 W, the temperature decreases to  $T = 47$  °C. The observed offset in the measured phase-matching temperature for different pump light powers in the first SHG stage can be attributed to an increasing temperature inhomogeneity between the crystal and the oven induced by pump beam absorption, resulting in localized heating within the crystal and thus requiring a lower external temperature for optimal phase-matching.

For the second SHG stage, where the green pump light power is limited to 200 mW, no significant changes in the phase-matching temperature were observed. A small deviation in the measured phase-matching temperature from 77.9 °C for 111 mW to 78.1 °C for 200 mW was observed. This slight increase in the measured phase-matching temperature with increasing pump light power contradicts the previous explanation. The reason for this discrepancy could be attributed to varying temperature homogeneity during the measurement process. The positioning of the sensors relative to the crystal may also lead to temperature variations, especially during temperature sweeps as performed in the measurements. Additionally, heating inside the crystal due to absorbed optical power can cause a temperature difference between the crystal and the oven. This effect is more significant in the first SHG stage due to higher pump light power

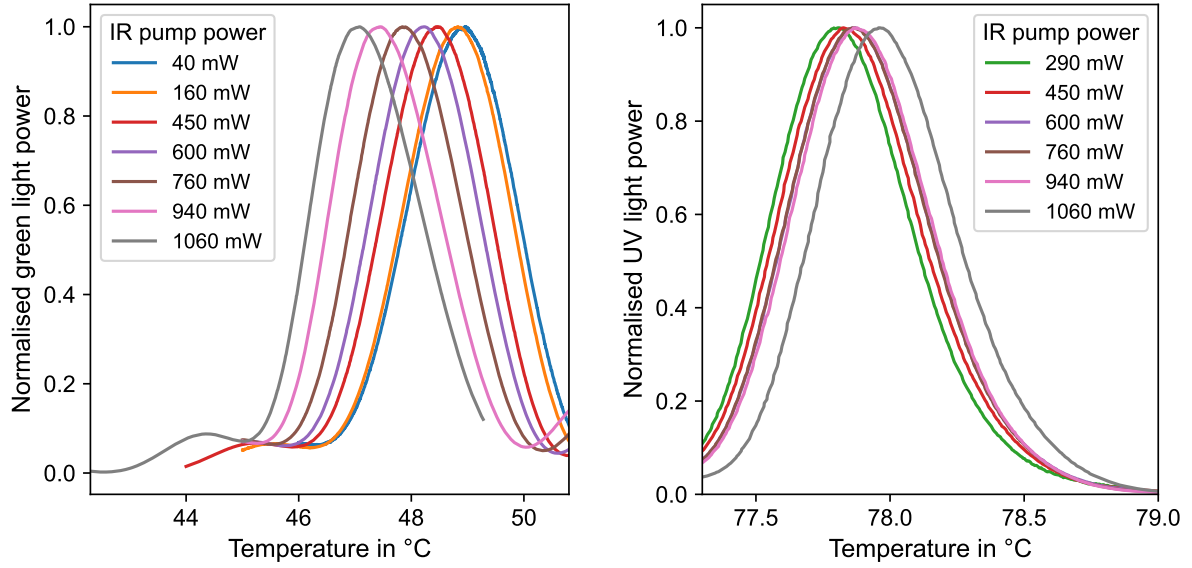


Figure 4.7: SHG output power as a function of the crystal oven Temperature and for different IR pump light power. Left: Output power of the first SHG stage as a function of the crystal oven temperature, considering different IR pump light powers. It demonstrates a noticeable drift in the measured phase-matching temperature. Right: Output power of the second SHG stage as a function of the crystal oven temperature, considering different IR pump light powers, with a non-significant drift in phase-matching temperature.

and a smaller crystal size compared to the second SHG stage. Overall, these factors contribute to the variability in the conversion efficiency and the temperature dependence of the UV laser system, and they need to be carefully considered.

Figure 4.7 presents the relationship between the converted optical power at the first SHG stage (534.8 nm) and the second SHG stage (267.4 nm) as a function of the pump light power (1069.6 nm). The inset focuses on the generated UV light power (267.4 nm) in relation to the green light power (534.8 nm). Throughout the measurement, the phase-matching temperatures of the two crystal ovens were optimized for each pump light power, considering the changing optimum oven temperature. For the maximum IR pump light power of 1050 mW, the first SHG stage produced 240 mW of green light. This green light was further converted into over 60  $\mu$ W of UV light by the second SHG stage. However, to ensure safe long time operation of the FHG system, the green light output power must be limited to 200 mW to prevent any damage to the waveguide according to the supplier.

In Section 4.2.1, it was established that the SHG light power follows a quadratic scaling with the pump light power in the low-intensity regime. To analyze the data in Figure 4.8, a quadratic function was fitted to the data points of the first SHG stage, restricting on data on the range where the green light output was below 120 mW and where the low-intensity regime applies. In this regime, the measured data closely aligns

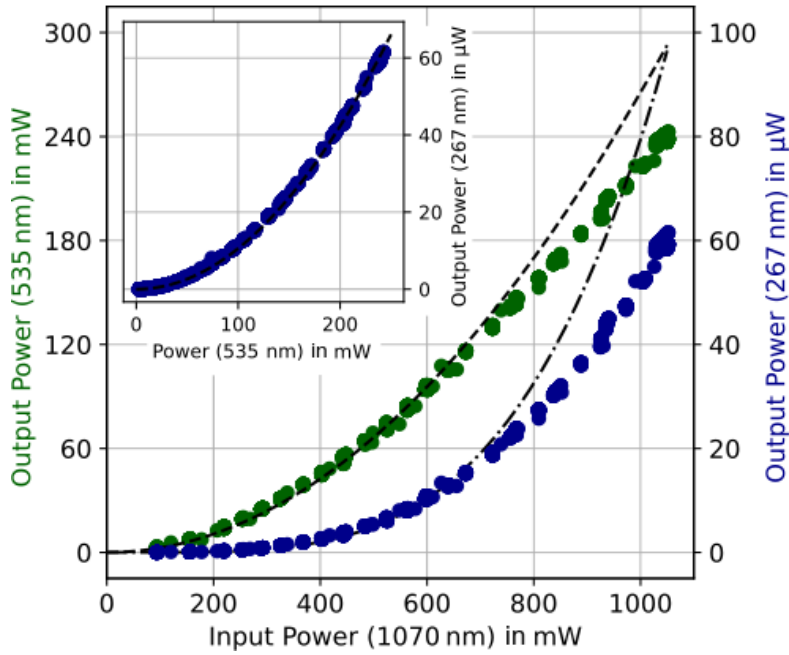


Figure 4.8: SHG output power as a function of the IR pump light power at 1069.6 nm. The the green light power at 534.8 nm (green dots) is generated by the first SHG stage. For the green light power the associated fit (dashed black line) represents a quadratic function. The UV light power at 267.4 nm (blue dots) is generated by the second SHG stage is presented. For the UV light power the associated fit (dashed black line) represents a fourth power function. For both fits the used data are restricted to the range below 120 mW. The inset shows the UV light power at 267.4 nm (blue dots) as a function of the green light power, which serves as the pump light for the second SHG stage at 534.8 nm. Here, a quadratic fit function is used. The coefficient of the quadratic functions represents the SHG efficiency  $\kappa$ .

with the fitted curve. For the low-power regime, the conversion efficiency can be determined from the coefficient of the quadratic fitting term, taking into account the measured coupling efficiency of the waveguide. The calculated conversion efficiency,  $\kappa = 119\% \text{ W}^{-1}$ , is in close agreement with the manufacturer's stated conversion coefficient of  $\kappa = 125\% \text{ W}^{-1}$ . The slight difference could be attributed to uncertainties in the measurements of light power and coupling efficiency of light to the waveguide. As the pump light power increases, the process transitions into a linear regime, as expected.

Regarding the FHG generation, the data was fitted to a fourth-power function, considering the same data range as before. When analyzing only the second SHG stage, the UV light power output exhibits a quadratic relationship with the green pump light, as demonstrated in the inset of Figure 4.8. Due to the low pump light power in the second SHG stage, all the data points align well with the quadratic fit. The obtained conversion coefficient is  $\kappa = 0.12\% \text{ W}^{-1}$ , which is close to the theoretically expected maximum value of  $\kappa = 0.15\% \text{ W}^{-1}$ . The slightly lower UV output power (around 80% of the expected value) indicates some diminished conversion efficiency, possibly due to

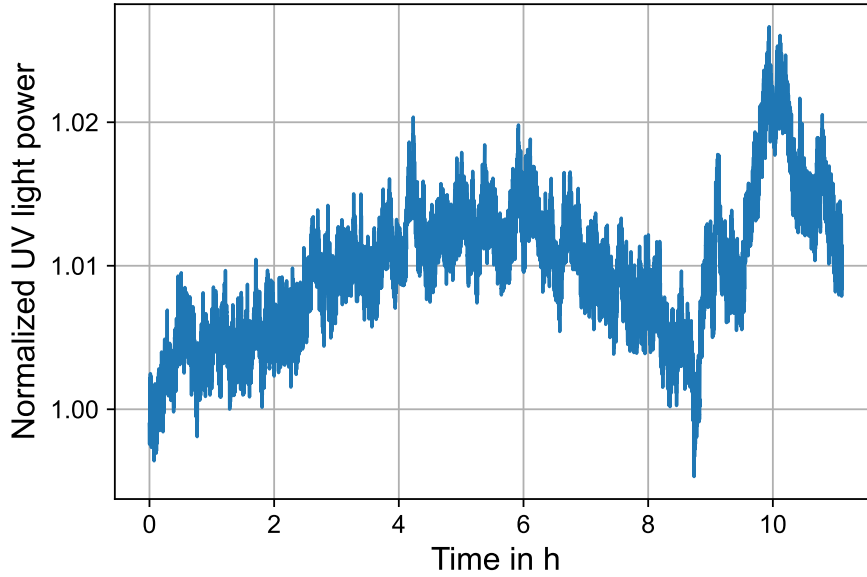


Figure 4.9: Normalized UV output power of the frequency quadrupling setup measured over more than 10 h. A fluctuation of UV light output power of maximal 3% is measured, mostly correlated with the pump light power fluctuation produced by the amplified fibre laser.

a non-optimal beam profile inside the crystal, deviation in the crystal composition, or impurities in crystal. Additionally, measurement accuracy is limited to  $\pm 7\%$  due to absorption in optical elements and accuracy of the device for optical power measurement.

To assess the long-term stability of the UV light power output from the laser system, the output power was continuously monitored for over 10 h with an IR pump light power of 800 mW. Throughout the measurement, the measured UV output power remained approximately  $30 \mu\text{W}$  as shown in figure 4.9. The results indicated a stability within 3%. The observed fluctuation in the UV light power output was primarily correlated with changes in the monitored IR pump light power from the laser source, which shows a stability within 1%. Since the UV output power strongly depends on the IR pump light power, the stability of the UV light power is mainly influenced by the power stability of the pump light laser itself. The stability of the output power can also be affected by variation of the conversion efficiency of the SHG process as non-critical phase-matching used in both SHG stages makes the converted output power sensitive to temperature variations of the nonlinear crystal. Optical degradation can also lead to a reduction in conversion efficiency. Additionally, beam pointing and resulting variation of the coupling efficiency of the waveguide and fibers might reduce the stability of optical power. Polarization fluctuations typically appear in optical fibre, while they are suppressed in the used polarization maintaining fibres, polarization fluctuations combined with a polarizing beamsplitter might further reduce the stability of the out-



put power. At present, an active power stabilization scheme has not been implemented in the system. However, it is planned to be installed in the final configuration. Such a scheme would actively adjust the system to counteract any fluctuations and maintain a consistent power level.

#### 4.4.2 Phase stability of the generated UV light

The produced UV laser will be utilized to interrogate the clock transition  $^1S_0$  to  $^3P_0$  of an  $^{27}\text{Al}^+$  quantum logic clock. As a clock laser, it is crucial to maintain high phase stability to enable long interrogation times and minimize statistical noise in clock operation. For this reason the IR laser source is stabilized to an ultra-stable reference cavity, described in Chapter 3. Subsequently, it is important to transfer the phase stability of the IR laser to the UV light. The frequency quadrupling system can introduce additional phase noise, which adds to the instability of the IR laser source. This is especially critical within the timescale of  $1 \times 10^{-2}\text{s}$  to  $1 \times 10^2\text{s}$  required for stabilizing the IR laser to the clock transition. On the other hand, when the laser source is stabilized to the clock transition, the IR light serves as a frequency reference for comparing with other clocks using an optical frequency comb or for stabilizing it. Phase noise generated by the quadrupling system directly affects the IR light when it is stabilized to the clock transition, thus limiting the phase stability of the IR light. It is essential to ensure that the instability of the quadrupling systems does not compromise the clock's performance, particularly on longer timescales where the frequency uncertainty of the clock approaches the systematic uncertainty limit, expected to be in the  $1 \times 10^{-18}$  regime.

To evaluate the system's performance, a theoretical analysis of the expected phase instability is provided. The phase shift in the absence of stabilization is determined by the phase shift of IR, green, and UV light propagating through different sections. Conservatively, the phase shift in each section is estimated, taking refractive index changes of air due to temperature and pressure effects into account. The calculations are carried out using the Edlen formula [257]. For the temperature dependence of the air along the free-space optical path in the system, a phase shift of  $1.3\text{rad K}^{-1}$  for the IR light path,  $3.6\text{rad K}^{-1}$  for the green light path, and  $8.9\text{rad K}^{-1}$  for the UV light path is calculated. Phase shifts of IR and green light are transferred to UV light when applying second harmonic generation (SHG). As a result, the total phase shift of the UV light, approximately  $14\text{rad K}^{-1}$ , is determined by the accumulated phase shift in all three sections. Regarding the pressure dependence, the estimated phase shift is approximately  $4\text{rad hPa}^{-1}$  ( $0.4\text{rad hPa}^{-1}$  for the IR light path,  $1.1\text{rad hPa}^{-1}$  for the green light path, and  $2.6\text{rad hPa}^{-1}$  for the UV light path).

Based on measurements conducted in the laboratory, temperature changes inside the box we expect less than  $10\text{mK s}^{-1}$  and pressure changes less than  $0.1\text{Pa s}^{-1}$ . Consequently, the resulting phase stability is approximately  $0.14\text{rad s}^{-1}$  for temperature changes and  $0.004\text{rad s}^{-1}$  for pressure changes. The corresponding fractional frequency change  $y(t) = \frac{\delta f}{f_0}(t)$  can be calculated using the equation:



$$y(t) = \frac{\delta\phi(t)}{2\pi t f_0}, \quad (80)$$

where  $\delta\phi(t)$  represents the expected phase shift of the UV light. This yields a value of  $y(1\text{ s}) \approx 2 \times 10^{-17}$  for temperature changes and  $y(1\text{ s}) \approx 6 \times 10^{-19}$  for pressure changes.

On timescales of a few seconds, the phase instability due to temperature and pressure changes does not pose a significant limitation to the frequency stability. However, for longer integration times, lower phase instability is necessary. Therefore, a phase stabilization scheme is implemented. In Section 4.3.3, the setup of the interferometric phase stabilization system is explained, which utilizes the optical path of the IR light to compensate for length fluctuations and phase instability in the UV light path. This is possible when a stable phase relation between IR light and UV light exists. However, it is important to consider that dispersion effects can disturb this phase relation and can introduce additional phase instability to the UV light. Other sources of remaining phase instability could arise from uncompensated optical paths in the setup, phase noise on the reference arm of the interferometric stabilization setup, or electrical noise in the control system.

By taking into account the dispersion of air, the remaining temperature-induced phase shift for UV light for the phase-stabilized system in the IR is estimated to be approximately  $0.8\text{ rad K}^{-1}$ , while the pressure-induced phase shift is approximately  $0.2\text{ rad hPa}^{-1}$  [257]. Assuming temperature changes of  $10\text{ mK s}^{-1}$  or pressure changes of  $0.1\text{ Pa s}^{-1}$ , the resulting fractional frequency instability at 1 s due to temperature and pressure changes in the air is on the order of  $1 \times 10^{-18}$  and  $3 \times 10^{-20}$ , respectively. These values are well within the acceptable range for the anticipated clock operation and do not limit its performance.

In order to measure the phase stability of the quadrupling system, a second UV light source is required as a reference. This reference UV light source is utilized to measure the stability of the phase difference between the light emitted by the two UV light sources. To obtain accurate results, it is crucial to have a reference system with significantly lower phase noise compared to the system being measured. Otherwise, it can not be distinguished which system is responsible for fluctuations in the phase relationship between the two UV laser beams. Unfortunately, such a system was not available at the time of the measurements. Alternatively, it is possible to perform a phase comparison between three systems and calculate the noise contribution from each system from noise correlations between the systems. However, a third system was also not available at the time of the measurements. Therefore, the beat measurements were conducted using a second UV laser system, referred to as system *B*, which consists of an existing quadrupling system with uncharacterized phase instability. As a result, the beat measurements provide only an upper limit for the phase stability of both systems. In contrast, the single-pass quadrupling setup described in section 4.1 is referred to as system *A*. The reference system, system *B*, is part of the clock laser system of an other  $^{40}\text{Ca}^+ / ^{27}\text{Al}^+$  clock and is described in [81]. For the sake of completeness, the setup of

system  $B$ , is also described here.

A schematic diagram of both setups in the beat note measurement configuration is presented in Figure 4.10. Both systems utilize the same fiber laser as common light source. The common light path between the setups is divided by a polarizing beam-splitter  $\text{PBS}_1$  (shown in Figure 4.10), and part of the power is directed to system  $A$  (single-pass FHG). This shared source configuration eliminates the phase noise originating from the laser itself, thereby obviating the need for stabilization of the fiber laser frequency in this measurement. The IR light coupled into system  $B$  is split into two paths. One is used as the short path of the interferometric stabilisation scheme. On the second path the IR light is amplified to approximately 600 mW by an additional amplifier. A specialized phase stabilization scheme is required, since the amplifier cannot operate bidirectionally. To achieve this, the IR light transmitted through  $\text{BS}_1$ ,  $\text{AOM}_1$ , the fiber amplifier, and the fiber-coupled waveguide doubler (SP-SHG) is reflected by the dichroic beamsplitter  $D$ . The reflection interferes with the reflection from mirror  $\text{Ref}_{1070\text{nm}}$  in the short path, which serves as the reference mirror for phase stabilization of the 1070 nm light. The optical interference is measured by  $\text{PD}_{1070\text{nm}}$  resulting in a beat note signal, which is phase-locked to a stable reference frequency by driving  $\text{AOM}_1$  via a tuneable direct digital synthesis (DDS) RF source<sup>9</sup>. A second output of the tracking oscillator is counted using a dead-time-free frequency counter. By minimizing the optical path length between the fiber output, and  $\text{Ref}_{1070\text{nm}}$  and enclosing it in a compact optical bench system, the phase at the reference point at  $\text{Ref}_{1070\text{nm}}$  coincides with the phase of the fiber output, which is then transferred to the green light at the dichroic mirror  $D$ . This green light is generated by the SP-SHG waveguide similar to the one used in system  $B$ .

The second doubling stage of system  $B$  is based on a pump-beam resonant second-harmonic generation cavity. Approximately 172 mW of 534.8 nm output from the waveguide is transmitted through dichroic mirror  $D$  and directed through a free-space  $\text{AOM}_2$  into the pump-beam resonant bow-tie cavity. Within the cavity, approximately 4 mW of 267 nm light is generated in a BBO crystal, exhibiting a quadratic scaling with input power. The length of the cavity is controlled by providing feedback to a piezo mirror inside the cavity, using 535 nm light reflected from the input window of the cavity in a Hänsch-Couillaud locking scheme [274].

Due to multipath interference, the stabilization of the green light through the cavity is not feasible. Therefore, the optical paths before and after the SHG cavity are independently length stabilized, with careful attention to keeping the unstabilized optical paths as short as possible. The phase stabilization in front of the cavity is realized in the following way: A small part of the green light is split and directed towards the photodiode  $\text{PD}_{535\text{nm}}$  using the mirror  $\text{Ref}_{535\text{nm}}$ , establishing the short path for the interferometric phase stabilization scheme. At this photodiode, the interference between the light reflected by  $\text{R}_{\text{VIS}}$  and the reference light is measured, thereby closing the phase-locked loop (PLL) by adjusting the frequency of  $\text{AOM}_2$ . A comprehensive

---

<sup>9</sup>Analog Devices, AD9956PCBZ

explanation of the interferometric phase stabilization technique is provided in Section 3.1.4. A similar phase stabilization scheme is also used for the UV light path behind the cavity. Although the described scheme was implemented in system *B*, it had not been characterized prior to these measurements. Furthermore, certain segments of the optical path, such as the path inside the frequency doubling waveguide and the frequency doubling cavity itself, were not subjected to phase stabilization. It is worth noting that the Hänsch–Couillaud locking scheme of the bow-tie cavities does not compensate phase changes in the direct path between in-coupling and out-coupling mirror. Consequently, vibrations and temperature fluctuations could introduce variations in the optical path length within reference system *B*, thereby limiting its phase stability. Moreover, the optical fiber 1, which guides the IR light towards system *B*, was not subject to stabilization during these measurements and is therefore suspected to contribute the majority of the observed residual phase noise.

The UV light generated by system *B* is subject to several frequency shifts. As a result, the light from system *B* accumulates a frequency offset of  $f_B - f_A = 251$  MHz compared to system *A*. To measure the phase stability, system *A* is utilized in the configuration depicted as variant 2 in Figure 4.5. The interference between the UV light generated by both systems is detected using photodiode PD<sub>5</sub>. The resulting beat signal is amplified, filtered by a tracking oscillator, and then counted by a dead-time free frequency counter<sup>10</sup>.

The beat-note signal between the UV light of the two systems was recorded over several hours. In the first measurement, system *A* was not actively phase stabilized, and system *B* was also not actively stabilized. The results of this measurement are shown in Figure 4.11 as the blue line, representing the fractional frequency difference using the modified Allan deviation for calculation. For an averaging time of 1 s, a fractional frequency instability limit of  $1 \times 10^{-15}$  was observed for the unstabilized systems.

In the second measurement, the active phase stabilization of system *B* was enabled. The resulting fractional frequency instability was calculated using the modified Allan deviation and is represented by the yellow line in Figure 4.11. With system *B* stabilized, the fractional frequency instability limit improved to  $5 \times 10^{-17}$  for an averaging time of 1 s, reaching down to  $10^{-18}$  for averaging times of  $10^3$  s. The second measurement demonstrates a significant reduction in fractional frequency uncertainty compared to the first measurement. This indicates that the measured fractional frequency instability in the first measurement was primarily caused by the unstabilized reference system *B*. As system *A* was not active phase stabilized during the measurements, only the passive phase stability of system *A* was measured.

To further characterize the intrinsic phase stability of system *A*, the free-running in-loop signal of the interferometric phase stabilization scheme is counted without active phase stabilization. Since the interferometric path contains any phase shift twice, the result is divided by two. This measurement provides a lower limit for the passive

---

<sup>10</sup>K+K Messtechnik, FXE Phase + Frequency Meter

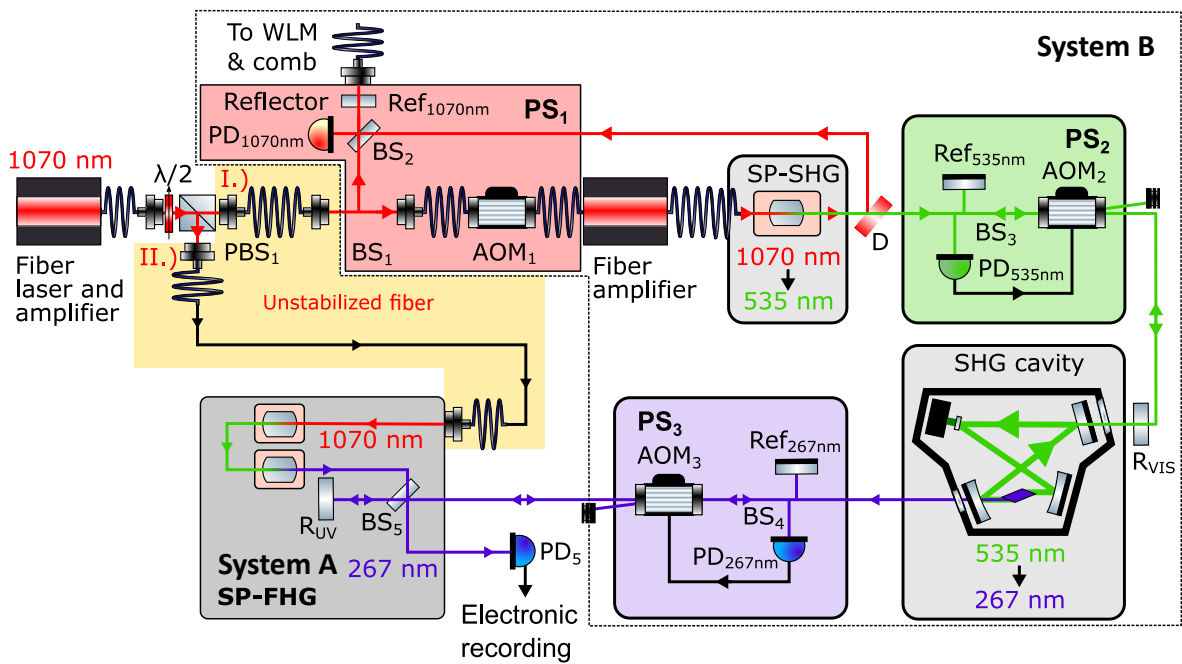


Figure 4.10: Simplified scheme for phase stability measurement with a second fourth harmonic generation system (system *B*). System *B* consists of a waveguide doubler and a frequency doubling cavity for frequency conversion. A phase stabilization scheme is implemented before, between, and after the two SHG stages in system *B*. By analyzing the interference signal obtained from photodiode PD<sub>5</sub>, the relative phase stability between system A and system B can be determined.

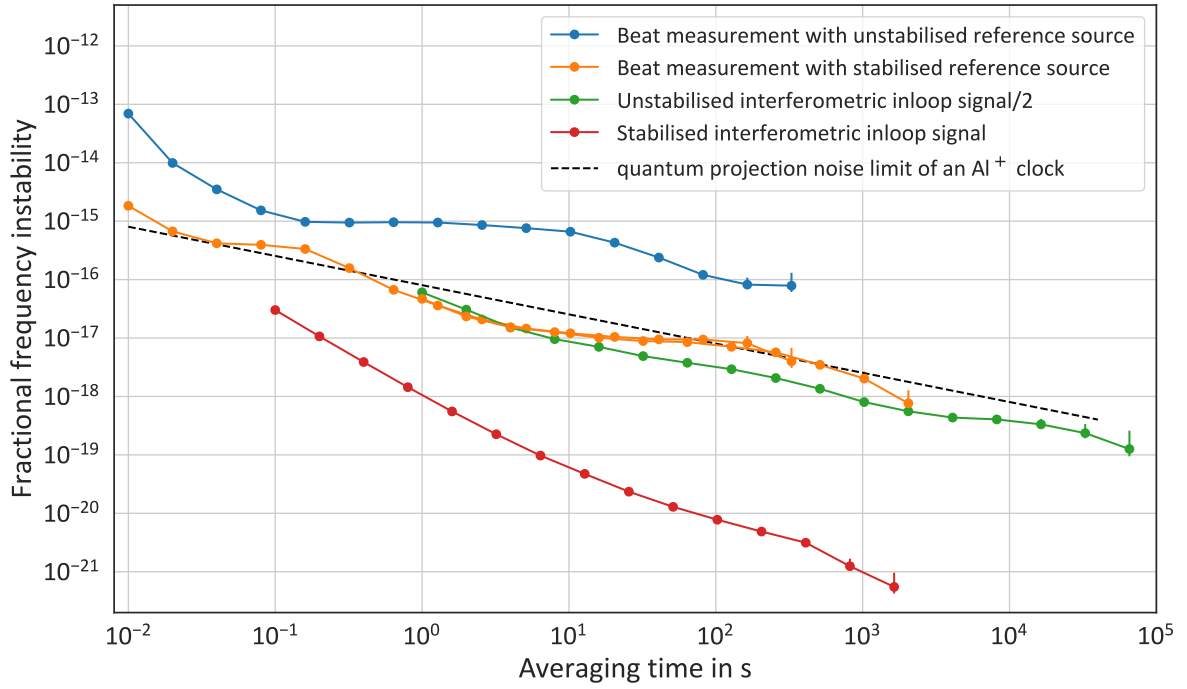


Figure 4.11: Measurements of the fractional frequency instability of the FHG system expressed as the modified Allan deviation. The blue (yellow) line results from a beat-note measurement with the unstabilized (stabilized) external UV source (system B), representing an upper fractional frequency instability limit for the single-pass FHG system. The green line shows the free-running signal of the interferometric phase stabilization scheme divided by two without active phase stabilization. A lower bound is given by electronic measurement noise of the in-loop error signal of the active phase stabilization (red line). For comparison, the lifetime-limited quantum projection noise (dashed black line) for Ramsey spectroscopy limit of the clock transition of  $^{27}\text{Al}^+$  at 267.4 nm (see text for details).

phase instability of system *A*. However, this measurement does not take into account frequency noise caused by non-stabilized light paths, such as the optical fiber 2. Additionally, dispersion effects leading to phase instability are also not included. From the measurement data, the modified Allan deviation of the fractional frequency instability is calculated and shown as the green line in Figure 4.11. At an integration time of 1 s, a fractional frequency instability of  $7 \times 10^{-17}$  is observed, which is consistent with the previous measurement using the stabilized external UV light source (system *B*) as a reference. Both measurements are at the same order of magnitude as the expected instability due to temperature fluctuations, while they are higher than the expected instability, implying the presence of other frequency noise sources. For longer averaging times, the fractional frequency stability of the free-running signal is lower compared to the measured fractional frequency instability with the reference system. This could indicate a limitation of the phase stability of the reference system or may be caused by different laboratory conditions during the measurements. The remaining non-stabilized fibers in both systems shown in Figure 4.10 are also likely to contribute to the observed level of measurement limitations.

To assess the phase stability of the system, it is compared to the quantum projection noise (dashed black line) obtained through Ramsey spectroscopy of an  $^{27}\text{Al}^+$  ion with a probe time equivalent to the excited state lifetime of 20.6 s [85]. The fractional frequency instability of the passive FHG system is already below the quantum projection noise limit, indicating favorable performance. However, further enhancements in phase stability are anticipated by implementing active phase stabilization.

The measured error signal from the interferometric phase measurement in the IR is employed for active phase stabilization, as detailed in corresponding Section 4.3.3. The signal-to-noise ratio of more than 40 dB, is considered appropriate for the phase stabilization scheme following electrical amplification. Evaluating the residual in-loop signal of the active phase stabilization scheme establishes a lower limit for the achievable fractional frequency instability. The remaining instability can be attributed to electronic noise in the system. This measurement is presented as the red line in Figure 4.11. It is important to note that this in-loop measurement does not account for phase instability resulting from non-stabilized light paths, dispersion effects, or any undetected phase shifts in the controlling system.

## 4.5 Rack integration of the clock laser system

The frequency quadrupling system, along with the stabilization cavity, are part of the clock laser system for a transportable optical  $^{27}\text{Al}^+$  clock. To ensure portability, standalone operation, and compactness, all optical and electronic components are housed within a standard 19-inch rack. The complete setup, as depicted in Figure 4.12, was used during laboratory measurements. The electrical systems are installed in the upper section on both sides of the rack, as they generate significant heat and are less susceptible to vibration and temperature fluctuations. This section includes the electronics for Pound-Drever-Hall locking, referenced RF frequency sources, RF amplifiers



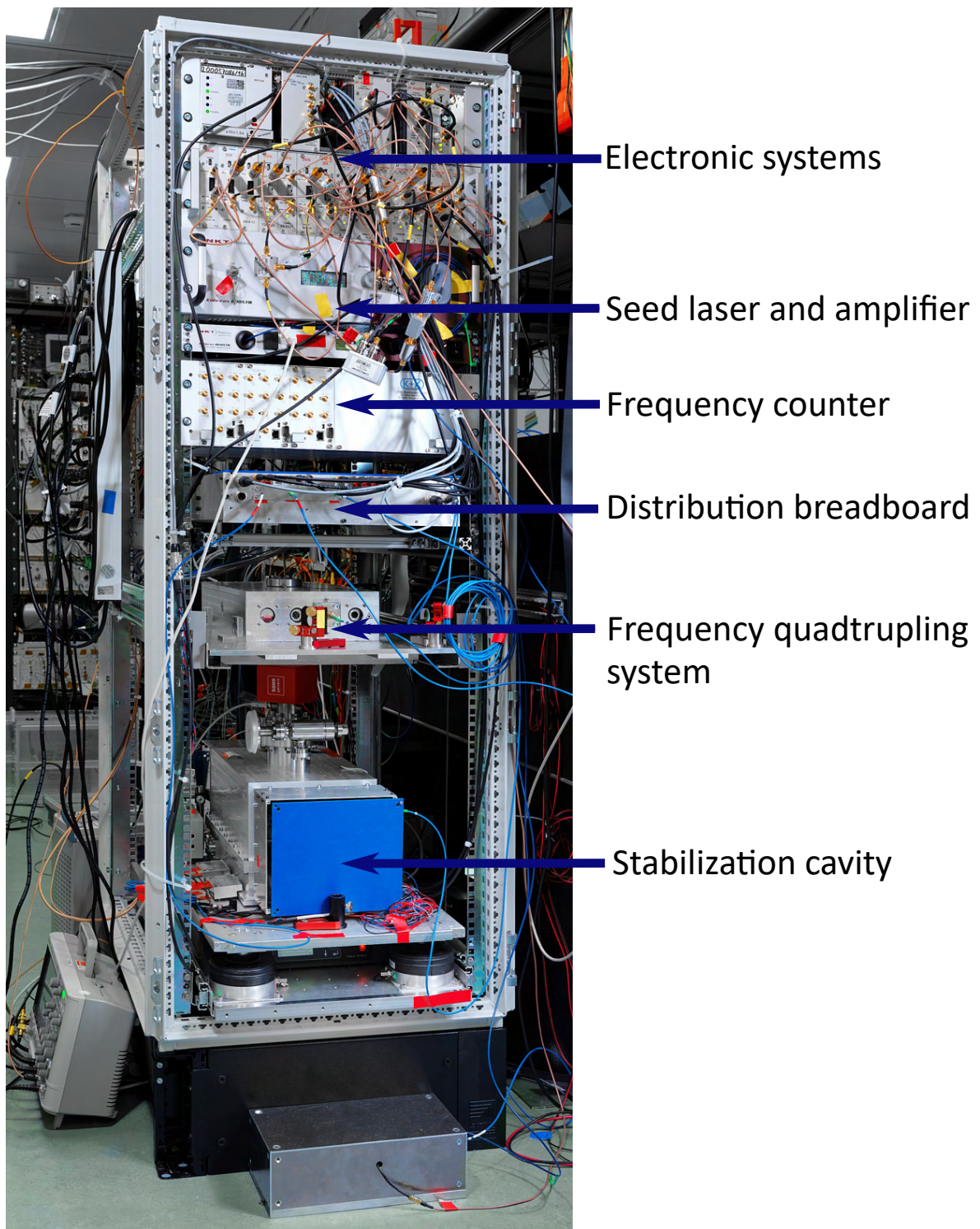


Figure 4.12: Image of the front side of the transportable clock laser system. Electronic system and the seed laser with laser amplifier on top of the rack. Below, in the following order, the distribution board, the frequency quadrupling system, and the cavity are placed. [PTB Mediengestaltung]

for fiber length stabilization, temperature controllers, and a counter for measuring RF frequency beats. Also located in the upper half of the rack are the laser source and the fiber laser amplifier. Below, in the following order, the distribution board, frequency quadrupling system, and stabilization cavity are positioned. Placing them at the bottom of the rack helps shield these systems from temperature fluctuations caused by the heat generated by the electrical systems at the top.

The frequency quadrupling system, like the optical cavity and distribution board, is mounted on an additional breadboard installed on rails within the 19-inch rack. This configuration allows the system to be easily slid out of the rack when access is required for optical readjustments or maintenance. Furthermore, a separate isolation shield surrounds both the frequency quadrupling system and the cavity to minimize any remaining temperature fluctuations from the surrounding environment. Optical fibers are employed to guide the laser light throughout the setup. These fibers transmit the laser light from the laser source to the fiber laser amplifier, then to the distribution board, and further on to the stabilization cavity and frequency quadrupling system. The resulting UV light at a wavelength of 267.4 nm is guided through a fiber to the ion interrogation breadboard, where the vacuum chamber containing the ion trap is located.

The overall performance of the clock laser system has not been measured yet, as no reference system with the required frequency stability is currently available during this thesis is written. However, the fractional frequency instability of each subsystem has been measured. For averaging times of 1 s and longer, the frequency instability of the optical reference cavity is the main limiting factor for the frequency instability of the UV laser system. The remaining phase instability of the optical paths on the distribution board and the frequency instability of the frequency quadrupling system have a negligible impact on the overall stability for longer averaging times. Therefore, the fractional frequency instability of the transportable  $^{27}\text{Al}^+$  clock laser is estimated to be around  $2 \times 10^{-16}$  for averaging times between 1 s and more than 100 s.

## 4.6 A simplified frequency quadrupling system

In order to independently verify the phase instability of the actively stabilized quadrupling system, it is necessary to have a reference system operating with a lower phase instability. Alternatively, a phase comparison between three systems can be used to accurately calculate the phase noise introduced by each system. This was one of the motivations behind building a second quadrupling system that is similar to the first one. While the previously performed measurements using system *B* can only provide limited information on the phase stability of *A*, it is expected that by comparing two similar and highly stable systems, a lower instability of the phase difference of both systems can be achieved, especially if both systems are actively phase stabilized.

Another advantage of having a second quadrupling system is the availability of a spare system in case the first system experiences a breakdown and becomes inoperable. This ensures continuity in the operation of the clock laser system. Additionally, the



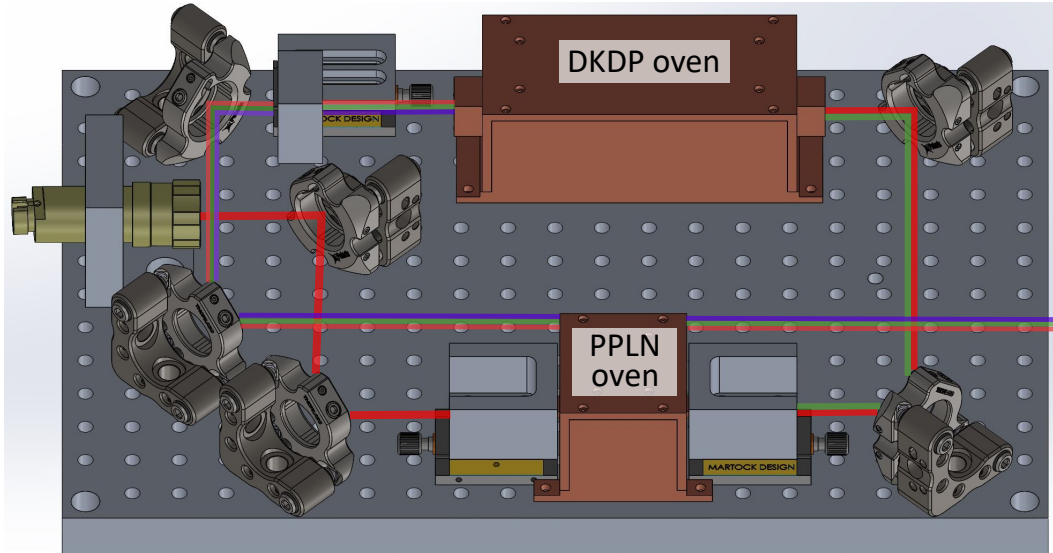


Figure 4.13: 3D drawing of the miniaturized frequency quadrupling system. The setup uses half inch optics and is more compact compared to the first system.

second quadrupling system is smaller in size compared to the first system, making it more compact and easier to handle. Although the miniaturization process may pose challenges in construction, it offers the potential for significant size reduction in the optical clock setup. Furthermore, the smaller size allows for the use of the frequency quadrupling system in a free-space configuration, eliminating the power loss that occurs when coupling the UV light into an optical UV fiber.

The principle of the second setup follows a similar approach to the first one. Like all other optical setups, this frequency quadrupling system is designed and created virtually using a 3D drawing program. The 3D drawing of the setup is depicted in Figure 4.13, and a photograph of the completed setup is shown in Figure 4.14. In contrast to the first setup, the collimators are placed on a bracket directly on a breadboard with a thickness of 10 mm and a grid of M4 threads with 12.5 mm separation between each. The breadboard is also enclosed within a sealing box. Polaris half-inch adjustable mirrors are utilized for beam position adjustments.

The first oven in the second setup is designed similarly to the one in the first generation, but smaller in size, measuring  $38 \times 30 \times 27 \text{ mm}^3$ . The spring-loaded copper plate is omitted in this design, and instead, the socket, which holds the waveguide, is created with additional space to accommodate wrapping the waveguide in indium foil twice. The soft indium foil serves to protect the waveguide from potential damage caused by mechanical stress. In this oven, the Peltier elements establish direct thermal contact between the copper socket on one side and the outer copper shield on the other side. This arrangement allows for more efficient heating of the socket while the outer shield is cooled by the Peltier element, effectively countering the heating effect on the outer shield. Moreover, if necessary, it is also possible to cool the socket using this configuration.

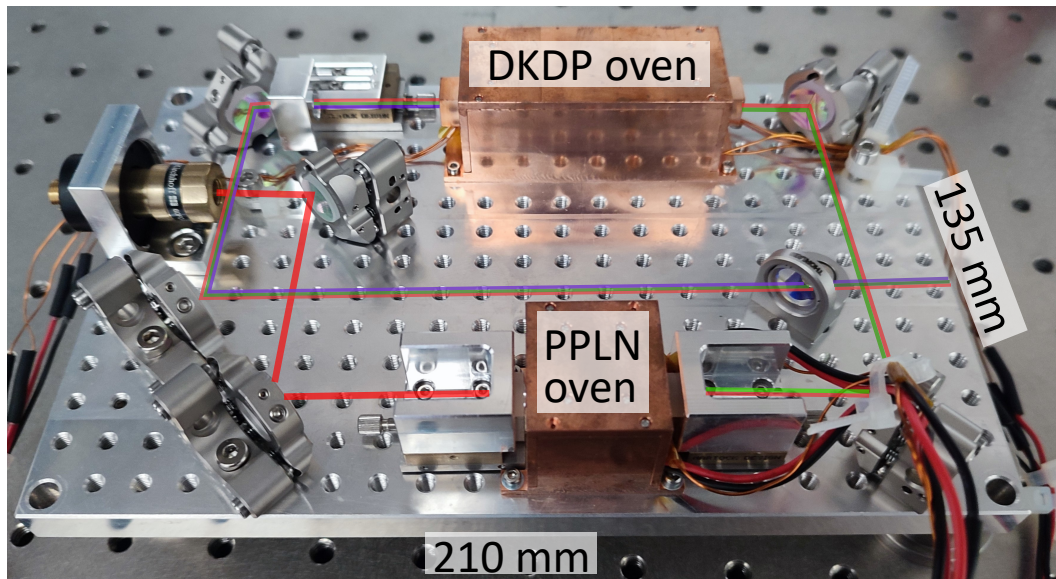


Figure 4.14: Image of the miniaturized FHG setup with reworked design of the two SHG stages inside more compact custom-made ovens. The beam path of IR light (red), green light (green) and UV light (blue) is schematically shown. For better view the system is depicted without the sealed box

The second isolation shield is made of PEEK instead of MACOR<sup>®</sup> as it is easier to machine. The oven's thermalization time is faster due to the improved thermal contact and the smaller volume of the oven interior. Unlike the first-generation design, the oven does not contain lenses within the outer shield. Instead, a lens with a focal length of 12 mm is positioned on a small translation stage in front of the oven. This allows for easier adjustment of the lens position and simplifies the coupling of the IR light to the waveguide. Another translation stage with a similar lens is placed behind the oven, serving as a replacement for the telescope used in the first frequency quadrupling setup. This lens is directly responsible for refocusing the beam onto the DKDP crystal in the second oven, ensuring the correct beam geometries for efficient conversion of the green light to UV light. Two additional half-inch mirrors are employed for beam position adjustments.

The second oven in the setup also follows a similar design to the first one, with dimensions of  $78 \times 30 \times 27 \text{ mm}^3$ . Within this oven, a DKDP crystal is placed, but unlike the crystal used in the first setup, the phase-matching temperature for the second crystal is  $117^\circ\text{C}$ , corresponding to a DKDP crystal with a low deuterium content [292]. Due to the relatively high phase-matching temperature, Peltier elements cannot be utilized. Instead, a resistive heater is installed inside the copper sockets, enabling heating of up to 15 W to achieve temperatures of up to  $260^\circ\text{C}$ .

Behind the oven, two half-inch mirrors are employed for beam position adjustments, and a lens on a translation stage is used to collimate the UV beam. Additional optics

can be used to separate the light with fundamental wavelength and the light with FHG wavelength. Similar to the first setup, the UV light can be coupled into a UV optical fiber or used in free space. A 50:50 beamsplitter on the breadboard allows for overlapping of the UV light beam from the first setup with the UV light beam from the second setup, enabling potential beat measurements outside the system enclosure. However, at the time of writing this thesis, this measurement has not yet been conducted, as no laser with sufficient light power for both frequency quadrupling systems was available.

## 5 Clock setup

The primary focus of this work is the development of a transportable clock laser system for a  $^{40}\text{Ca}^+ / ^{27}\text{Al}^+$  quantum logic clock. However, the quantum logic spectroscopy of  $^{40}\text{Ca}^+$  and  $^{27}\text{Al}^+$  ions requires several laser systems for cooling, detection and manipulation of the internal states of  $^{40}\text{Ca}^+$  as well as optical pumping of  $^{27}\text{Al}^+$ . The setup of these lasers are not discussed in this thesis. This chapter presents the physics package, which consists of a segmented linear Paul trap within a vacuum chamber. The vacuum chamber is mounted on a rack-integrated breadboard, which incorporates all the necessary optics for ion manipulation. The physics package also encompasses an imaging system for collecting the fluorescence light of the ion. All the systems are integrated into racks to ensure the transportability of the optical  $^{40}\text{Ca}^+ / ^{27}\text{Al}^+$  clock setup. At the time of writing this thesis, the construction of a carrier board and the integration of the tap onto the carrier board are in progress. Moreover, the fabrication of the mu-metal shield has not been completed at this stage. The description of the other parts of the setup reflects the current status and will be optimized once the trap is integrated.

### 5.1 Vacuum system

Experiments with trapped ions require ultra-high vacuum to minimize background gas collisions, which can result in ion loss and heating and disturb the coherence during clock interrogation. In addition, the excited Al ion is susceptible to molecule formation with residual hydrogen gas. Ideally, a pressure below  $10^{-11}$  mbar should be achieved for the  $^{40}\text{Ca}^+ / ^{27}\text{Al}^+$  ion clock. The vacuum system (shown in Figure 5.1) is designed to fulfill these requirements.

The octagonal vacuum chamber<sup>11</sup> is constructed from aluminium. On one side of the octagon, a T-tube with a CF 40 viewport and a valve is installed. The valve allows for connection to a vacuum pump for initial pumping down of the vacuum chamber. On the opposite side, an extension is welded to the vacuum chamber, and a combined ion and NEG pump<sup>12</sup> is installed. The remaining six sides of the octagon feature CF 40 viewports<sup>13</sup>. They have anti-reflection coated windows for optical access to the ion trap center within a titanium frame. On the top side, a titanium CF 100 flange<sup>14</sup> provides two sub-D25 electrical feedthroughs for electrical connection to the ion trap. This flange also includes a feedthrough for the RF drive of the trap, featuring low RF losses and low capacity. Additionally, a helical resonator is mounted on top of the flange and connected to the RF feedthrough. On the bottom of the vacuum chamber, an inverted CF 100 viewport with an anti-reflection coated window (diameter of 68 mm) facilitates imaging of the trapped ions, as described in Chapter 5.6.

---

<sup>11</sup>VACOM, custom design

<sup>12</sup>SAES, Nextorr Z200

<sup>13</sup>MPF Products, custom design

<sup>14</sup>MPF Products, custom design

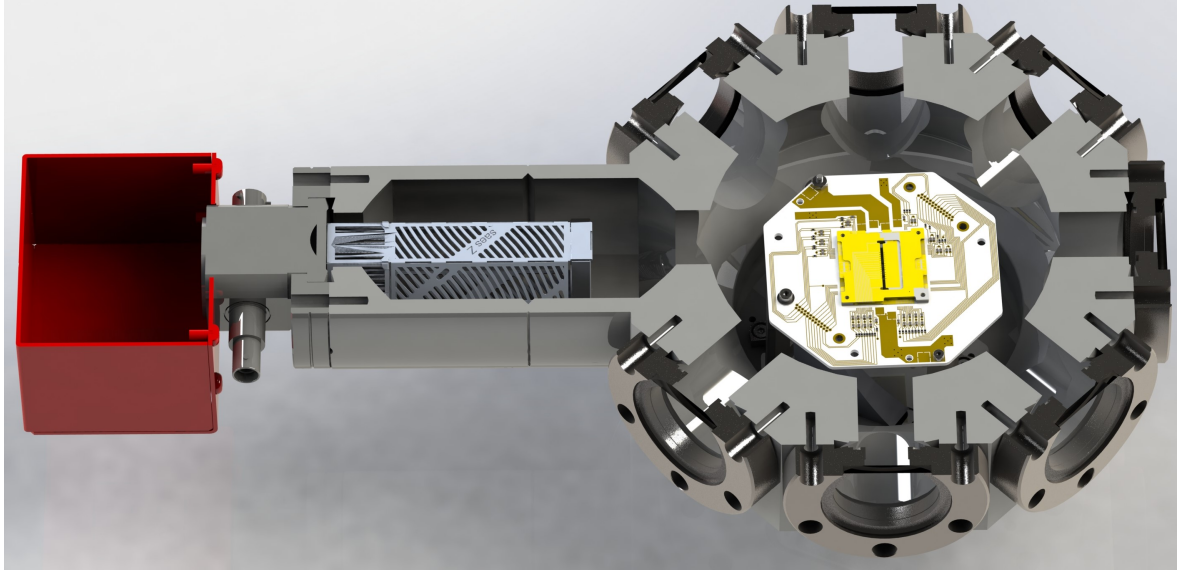


Figure 5.1: 3D Drawing of the vacuum chamber with ion trap. A NEG and ion pump combination is used to ensure ultra-high vacuum inside the titanium octagon vacuum chamber. A multi-segment, micro-fabricated linear Paul trap is installed inside the vacuum chamber.

## 5.2 The ion trap

Typically, a  $^{40}\text{Ca}^+ / ^{27}\text{Al}^+$  clock is operated with a single  $^{40}\text{Ca}^+$  co-trapped with a single  $^{27}\text{Al}^+$  ion. However, multi-ion quantum logic optical clock schemes have also been proposed, allowing for the inclusion of additional ions [297]. In this setup, a linear Paul trap was chosen to confine the two ions. The trap is similar to the one presented [298] in and is fabricated by the group of Tanja Mehlstäubler at the Physikalisch-Technische Bundesanstalt in Brunswick. This trap geometry is designed to provide nearly micromotion-free confinement even for multiple ions along the trap axis. The trap consists of multiple microfabricated segments, as shown in Figure 5.1. Having multiple segments allows for distinct loading and spectroscopy zones, as well as the storage of ions in different regions of the trap. The trap chip will be mounted on a carrier board. To ensure excellent thermal conductivity, the trap and the carrier board are constructed using aluminum nitride (AlN). Temperature sensors are integrated into the trap, allowing for precise measurement of the temperature around the ion and enabling the calculation of the black body radiation shift. The original design of the carrier board is credited to Malte Brinkmann [299]. Electric low-pass filters are placed on the carrier board and wired to the trap chip. The carrier board is electrically connected to the feedthroughs on the top flange through Kapton-insulated wiring. To support the carrier board, three titanium supports are placed on the top flange. These supports provide mechanical stability and allow heat transfer towards the top flange, which acts as a heat sink.



### 5.3 Magnetic field generation

A magnetic field is necessary to project the magnetic sublevels and prevent degeneration of these states. The direction of the magnetic field aligns with the trap axis, and its magnitude determines the Zeeman splitting of the magnetic sublevels. This is particularly crucial for the  $^{27}\text{Al}^+$  clock transition and the  $^{40}\text{Ca}^+$  logic transition from the  $S_{1/2}$  to  $D_{5/2}$  levels at 729 nm. For optimal access to the RSB of the  $|S_{1/2}, m_j = -1/2\rangle$  to  $|D_{5/2}, m - j = -5/2\rangle$  transition during sideband cooling and quantum logic spectroscopy requires a magnetic field strength between 180  $\mu\text{T}$  and 250  $\mu\text{T}$ . The magnetic field must remain stable within 30 nT to enable the interrogation of the  $^{40}\text{Ca}^+$  logic transition [79]. Additionally, the magnetic field induces a Zeeman shift on the clock transition, and fluctuations in the magnetic field can increase the uncertainty of this shift, limiting the performance of the optical clock. Therefore, it is essential to suppress fluctuations in the magnetic field. To achieve this, an approach using permanent magnets, a mu-metal shield and compensation coils is chosen instead of magnetic field coils, as the latter are susceptible to noise.

Two permanent ring magnets made of samarium cobalt alloy are used to achieve a stable magnetic field aligned with the trap axes. These magnets are positioned outside the vacuum chamber and aligned with the trap axis in a distance of 165 mm from the trap center. The measured magnetic field is 200  $\mu\text{T}$  at the trap center. The configuration with two ring magnets allows minimal magnetic field inhomogeneity at the center of the trap. The temperature drift of the magnetic field generated by the magnets is measured for heating and cooling of the magnets. A constant drift of the relative magnetic field of  $3.6 \times 10^{-4} \text{ K}^{-1}$  was observed. To achieve a magnetic field stability of 1 nT, a measurement of the magnet temperature with an uncertainty in the order of 10 mK is necessary and can be achieved with standard temperature sensors next to the temperature isolated magnet. With the choice of permanent magnets, the high frequency noise of magnetic field coils is exchanged for slow temperature drifts. The latter can be corrected by regular calibration of the magnetic field within clock operation. To compensate for deviations from the axial direction at the trap center, two coils are employed for each axis, resulting in a total of six coils. Each coil consists of 20 turns with insulated copper wire and is placed on the flanges of the vacuum chamber. These coils allow for fine adjustments to the magnetic field to tailor the Zeeman shift splitting in the experiment. It is planned to use two mu-metal shields to shield the experiment from external magnetic field fluctuations [300]. The mu-metal shields attenuates external magnetic fields, minimizing their influence on the trapped ions. Inside the mu-metal shield, materials with low magnetic susceptibility are selected to prevent any interference or generation of inhomogeneity in the magnetic field.

### 5.4 Ablation and ionization calcium and aluminium

An ablation loading technique is employed to load  $^{40}\text{Ca}^+$  and  $^{27}\text{Al}^+$  ions into the trap. A specially designed target is positioned inside the vacuum chamber above the ion trap on the topside flange. In Figure 5.2 the target is shown. It features a designated position where calcium granulate can be affixed. The target is made of aluminum,

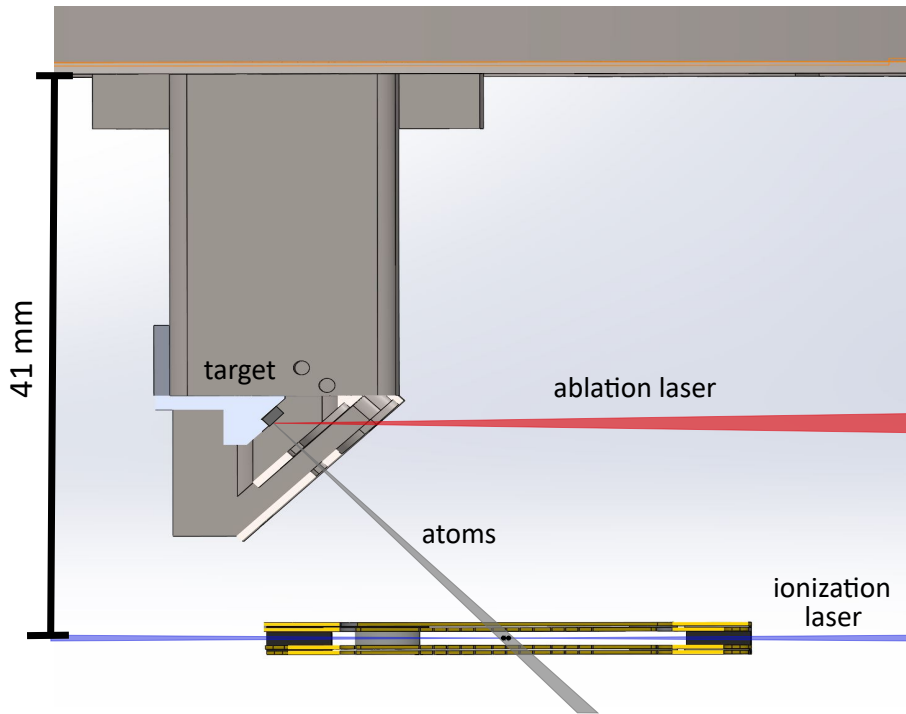


Figure 5.2: Image of the ablation target and the ion trap. The ablation laser hits the target and Ca and Al atoms are evaporated towards the ion trap. In the trap the atoms get ionized by the ionization lasers and trapped.

allowing ablation of Al atoms at a second spot. Two apertures are placed in front of the target, allowing a portion of the accelerated atoms to pass. Also, the ablation laser can pass through the apertures. The focus of the ablation laser beam is on the target, allowing minimum beam waist and maximum intensity.

A Q-switched laser<sup>15</sup> at a wavelength of 1064 nm and a pulse duration of less than 1.5 ns is used for ablation. It has a repetition rate of up to 1 kHz and provides a pulse energy of more than 90  $\mu\text{J}$ . The pulsed Q-switch diode laser is coupled into a multi-mode fiber. To collimate the beam, a collimator with a lens having an optical focal length of 40 mm is used. In order to ensure a small waist at the focus on the target, a lens with a focal length of  $f = 150$  mm is employed. At the target position, a pulse energy of up to 20  $\mu\text{J}$  is available, which is more than sufficient for ablating atoms from the surface. A portion of the accelerated atoms passes through two apertures which are used to collimate the neutral atom beam. The atoms moves towards the trapping region. The position of the laser beam on the target can be adjusted to switch between ablation of calcium and aluminum, enabling the loading of both ions into the trap. This functionality is achieved through a motorized mount equipped with two stepper motors<sup>16</sup> which holds the collimator.

At the trap center, the atoms are photo-ionized and subsequently trapped by the

<sup>15</sup>CryLas, DSS1064-Q4

<sup>16</sup>Thorlabs, Z812

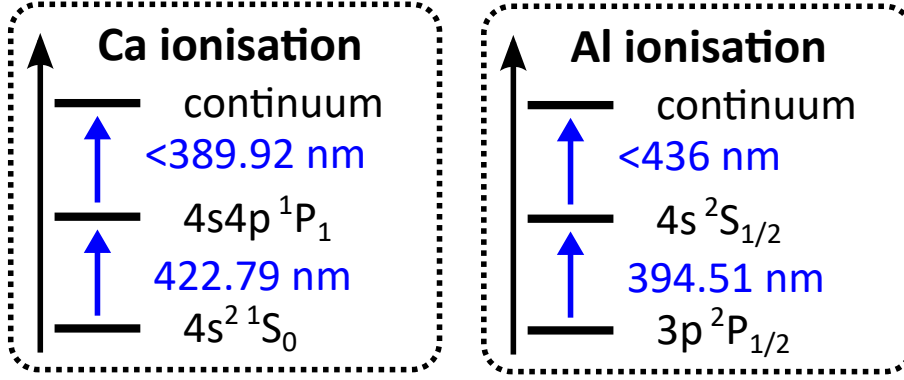


Figure 5.3: Level scheme for the two step ionization process of  $^{40}\text{Ca}^+$  and  $^{27}\text{Al}^+$ . A detailed description is given in the text. Taken from [80].

ion trap. For the ionization of Ca atoms, a two-step ionization process is employed. The level scheme for ionization  $^{40}\text{Ca}^+$  is shown in Figure 5.3 (left). In the first step, laser light at a wavelength of 422 nm is used to excite the transition from the  $4s^2 1S_0$  state to the  $4s4p 1P_1$  state of the Ca atom. In the second step, the electron is removed from the atom. The remaining ionization energy is provided by the transition from the  $4s4p 1P_1$  state to the continuum, which occurs at a wavelength of less than 390 nm. A diode laser operating at 375 nm is used for this step.

Similarly, for the ionization of Al atoms, a two-step ionization process from the  $3p^2 P_{1/2}$  state to the  $4s^2 S_{1/2}$  state of the Al atom is used, as shown in 5.3 (right). This transition can be driven by a diode laser operating at 394 nm. In the second step of the ionization process, light with a wavelength shorter than 436 nm is required, which can also be provided by the laser operating at 394 nm.

## 5.5 Integration of the physics package

The vacuum chamber is mounted on a rack-integrated breadboard, along with the optical setup for focusing the laser beams on the ions at the trap center. The aluminium breadboard has dimensions of  $700 \times 350 \text{ mm}^2$ . The vacuum chamber is positioned at its center. A hole with a diameter of 110 mm allows for direct optical access to the ions from the bottom through the inverted viewport. The permanent magnets are also mounted on the breadboard in their appropriate positions.

The optical design for each laser path follows a similar principle. The laser light is coupled into an optical single-mode fiber, which is connected to an optical collimator for each path. The collimator is mounted in a piezo motor-driven mount<sup>17</sup> on the breadboard, allowing for automated adjustment of the laser beam alignment. After polarization cleaning and preparation using a combination of polarizer and lambda/2 plates, the light is split, and a small portion is directed to a photodiode for intensity stabilization.

<sup>17</sup>Newport, 8821 Picomotor Mounts



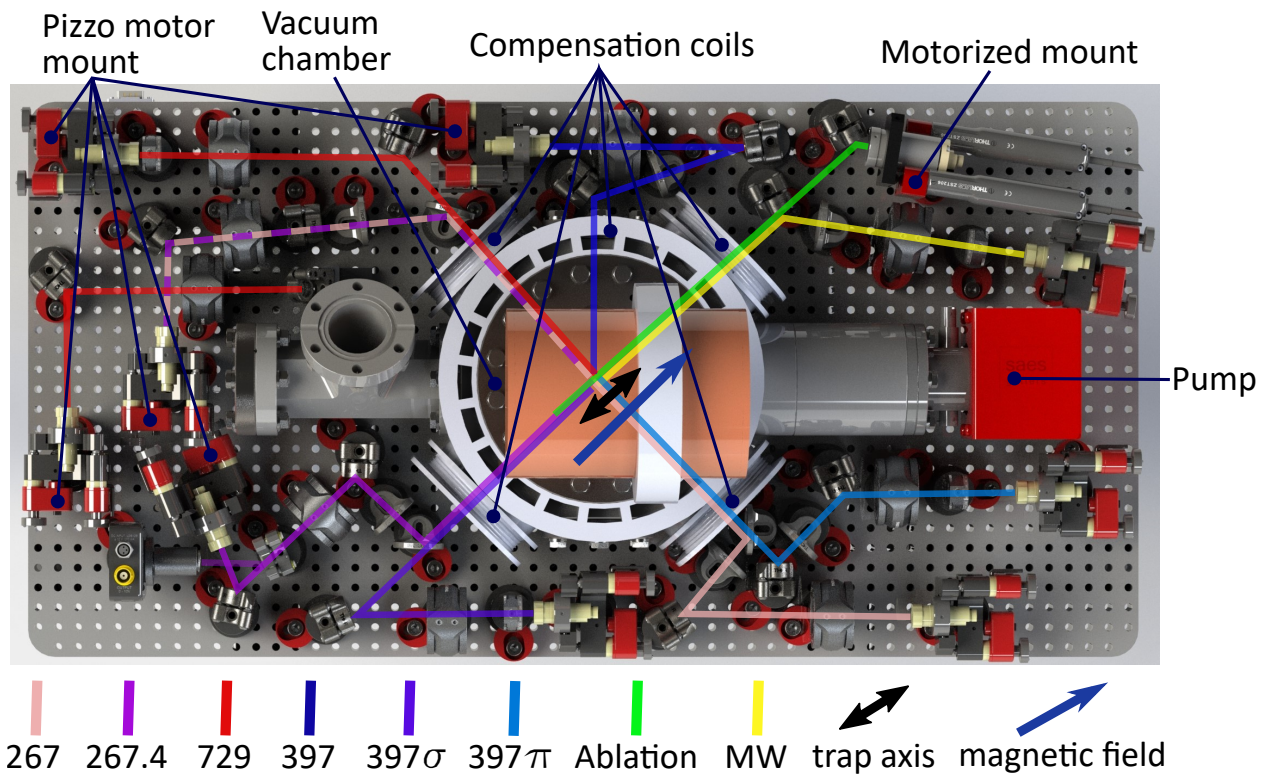


Figure 5.4: Optical beam path driving the optical transitions of the ions. The optics are placed on a breadboard together with the vacuum system. 267: clock laser at 267 nm, 267.4:  $^{27}\text{Al}^+$  logic laser at 267.4 nm, 729:  $^{40}\text{Ca}^+$  logic laser at 729 nm, 397: doubler cooling at 397 nm, 397 $\sigma$ :  $\sigma$  polarized light at 397 nm. 397 $\pi$ :  $\pi$  polarized light at 397 nm, Ablation: ablation laser, MW: laser beam with multiple wavelength. Further explanation is provided in the text.

Each laser path includes mirrors and a lens to focus the laser beam onto the ion at the trap center. Some of the laser beams are overlapped using dichroic beamsplitters. The beam paths for all lasers are depicted in Figure 5.4. The geometric setup for each laser is as follows:

- Orthogonal to the trap axis and the magnetic bias field direction, the  $^{40}\text{Ca}^+$  cooling laser with  $\pi$  polarized light at 397 nm is overlapped with the clock laser at 267.4 nm.
- On the opposite side, the  $^{40}\text{Ca}^+$  laser at 729 nm is overlapped with a secondary path for the clock laser at 267.4 nm.
- Aligned with the trap axis, a second laser beam at 267 nm is used for state preparation and quantum logic implementation of  $^{27}\text{Al}^+$ . This beam is overlapped with another cooling laser beam with  $\sigma$  polarized light at 397 nm.
- Also aligned with the trap axis, laser beams with different wavelengths are overlapping from the opposite side. These laser beams include the Ca ionization laser at 375 nm and 422 nm, the cooling laser at 397 nm, the Al ionization laser at 394 nm, the  $^{40}\text{Ca}^+$  quantum logic laser at 729 nm, and the repumper lasers for  $^{40}\text{Ca}^+$  at 854 nm and 866 nm. All these laser beams are coupled together into a large-mode-area (LMA) fiber, which is connected to the collimator on the breadboard.
- Additionally, a third  $^{40}\text{Ca}^+$  quantum logic laser at 729 nm is guided to the bottom side of the breadboard using a periscope through a hole in the breadboard. Here, the laser beam is focused onto the trap center with an oblique angle of incidence relative to the trap axis for out-of-plane micromotion determination. Another  $^{40}\text{Ca}^+$  cooling laser at 397 nm is guide horizontally to the trap with an angle of  $45^\circ$  in respect to the trap axis for Doppler cooling of all motional modes.

The breadboard is further reinforced with aluminum profiles located at the bottom, providing a lightweight support. These profiles are equipped with holes to accommodate the optical beam path and imaging system. To facilitate its integration, the breadboard is placed within an extra rack using a similar mounting approach as the one employed for the cavity and frequency quadrupling system. The system can be easily pulled out from the rack when necessary. It comprises two cross braces and two stainless steel angle rails (see Figure 5.5). Each angle rail is connected to a pull-out rail, which is linked to the rack through a strut. Vibration absorption connectors are also utilized to minimize vibrations between the aluminum profiles and the mounting system. Moreover, the breadboard is designed to be encased in two mu-metal shields, effectively shielding the experiment from fluctuations in the surrounding magnetic field. The entire setup, including the breadboard, is integrated into a standard 19-inch rack, along with various laser and electronic components, as depicted in Figure 5.6.

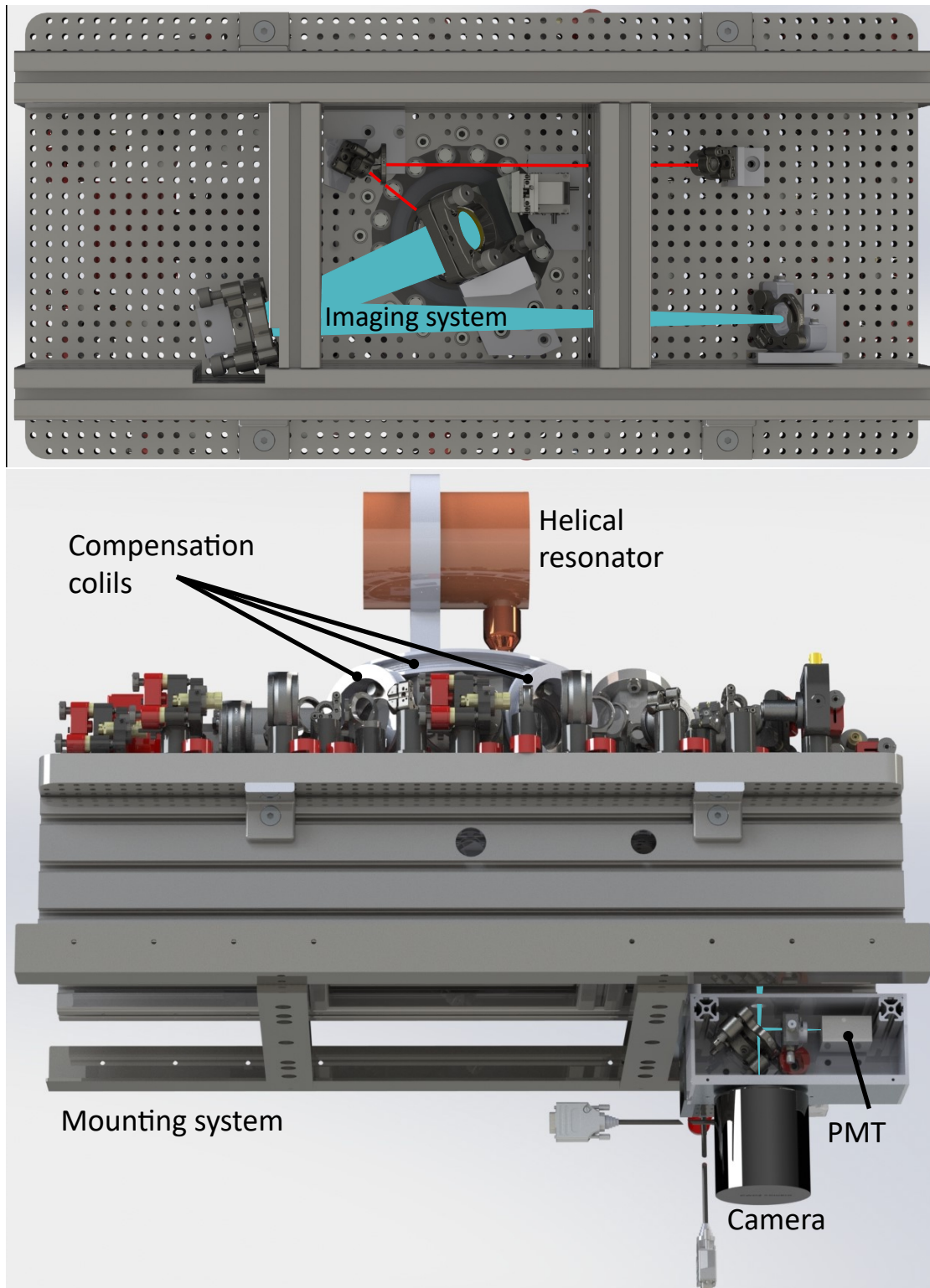


Figure 5.5: Rendering of the physics package from bottom view and side view showcases the imaging system with the line of view highlighted in cyan for the camera and photomultiplier tube. The breadboard features a mounting design for integration into a rack. It holds the optical setup, which includes all the necessary optical components for delivering light to the ions (also see Figure 5.4). The laser beam for exciting the  $^{40}\text{Ca}^+$  logic transition at 729 nm is shown in red.



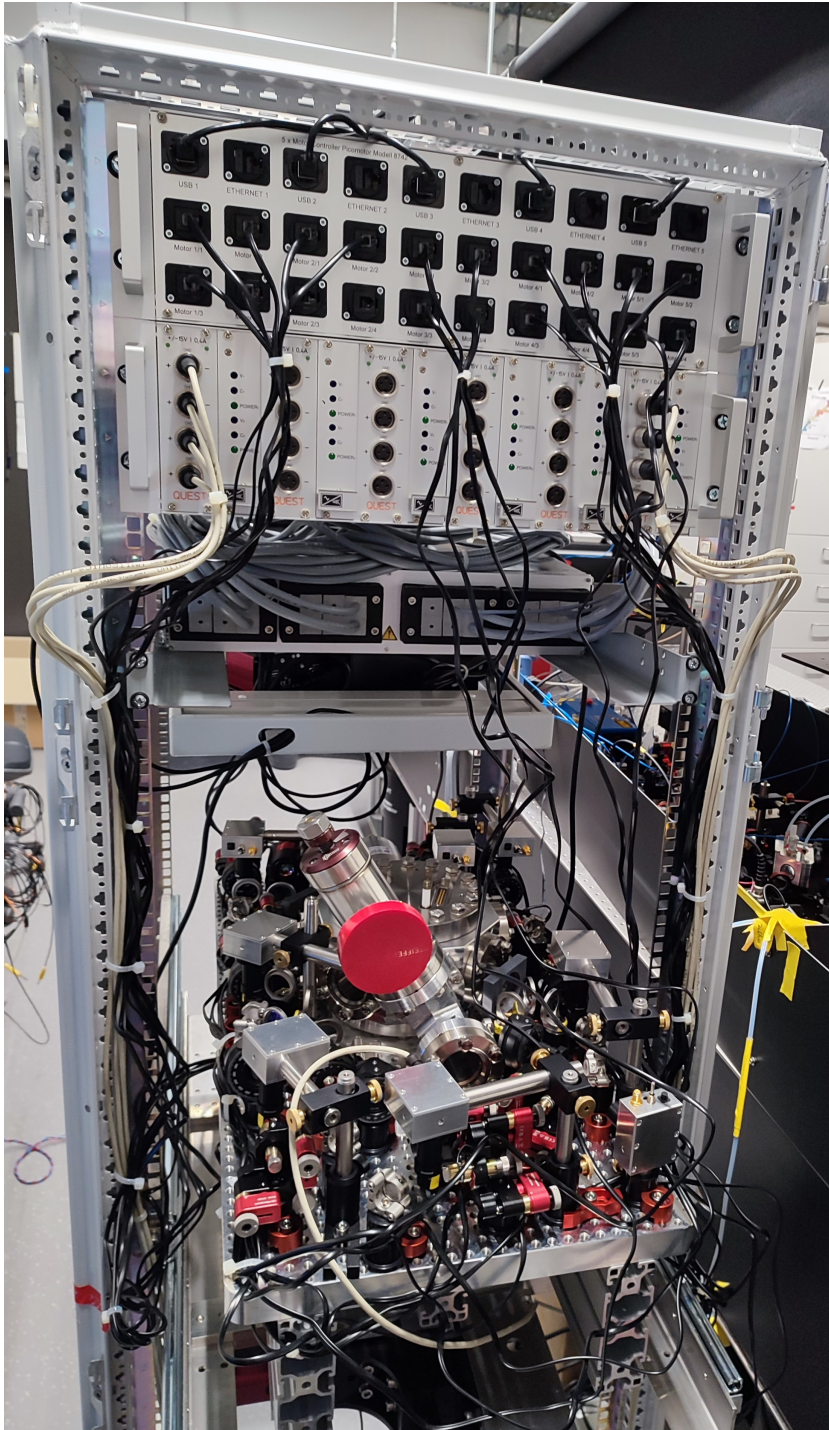


Figure 5.6: The physics package of a  $^{40}\text{Ca}^+ / ^{27}\text{Al}^+$  quantum logic clock inside a standard rack. The board with the vacuum chamber and optics is placed inside the rack on rails, which makes it possible to pull it out for better access. A detailed explanation of the physics package is given in the text

## 5.6 The imaging system

The imaging system is positioned at the bottom of the breadboard. It consists of a two-inch aspheric lens, which is located outside the vacuum chamber beneath the inverted viewport. The inverted viewport configuration allows for a distance of 40 mm between the ion and the aspheric lens. The use of a large lens size in close proximity to the ion enables a high numerical aperture (NA) of approximately 0.5, ensuring high resolution of the ions as well as high percentage of collected fluorescence photons. The aspheric lens is mounted on a piezo-driven stage<sup>18</sup> with three axes, enabling automated adjustment of its position and facilitating imaging of different segments of the ion trap. To achieve an optical path length of over 800 mm between the aspheric lens and the camera<sup>19</sup>, as required for optimal imaging performance of the lens, three mirrors are employed on the bottom of the breadboard (see Figure 5.5). This compact design allows for efficient utilization of space within the 19-inch rack while maintaining the required optical path length. The mu-metal shields and aluminum profiles are equipped with holes to provide unobstructed line of sight for the imaging system. The camera is mounted on a box, which contains a beamsplitter, an adjustable aperture, and a photomultiplier tube (PMT). This setup enables the splitting of imaging light from the ions, with simultaneous detection on both the camera and the PMT. Both the box and the camera are mounted on a motor-driven three-axis stage, positioned beneath the breadboard.

---

<sup>18</sup>Thorlabs, PD1D and PD1

<sup>19</sup>QHYCCD, QHY 183 mono

## 6 Discussion and conclusion

A highly stable cavity for the stabilization of an IR laser operating at a wavelength of 1069.8 nm is presented. To facilitate transportability, the cavity is integrated into a standard 19-inch rack. Together with the cavity, two breadboards are utilized to facilitate the stabilization of the coupled power and implementation of the RAM stabilization scheme. Another fiber-coupled breadboard is constructed to distribute the IR light to the cavity, the actual experiment, and an optical comb. Optical path stabilization is implemented for each port, ensuring stable and precise delivery of light. The performance of the optical path stabilization is evaluated for each path, and it demonstrates a stability of  $7 \times 10^{-17}$  after a duration of 0.1 s. The primary sources of frequency noise for the cavity are investigated. These include thermal noise, vibration noise, photo-thermal noise, RAM, spacer aging drift, and the influence of temperature drifts.

A thermal noise limit of  $7-8 \times 10^{-17}$  is calculated for the cavity with single crystal GaAs/AlGaAs coatings. Additionally, the cavity's finesse, linewidth, and birefringence line splitting are characterized. The vibration sensitivity of the cavity is determined to be  $S_{v,x} = 1(1) \times 10^{-11} g^{-1}$ ,  $S_{v,y} = 4(2) \times 10^{-11} g^{-1}$ , and  $S_{v,z} = 3(2) \times 10^{-11} g^{-1}$ , consistent with previous measurements of an identical cavity. When the cavity is placed on an active vibration isolation table, the fractional frequency instability due to the residual vibration along each axis is below the thermal noise limit for average times exceeding 0.1 s .

Fluctuations in optical power absorbed by the mirrors contribute to frequency fluctuations. To mitigate this noise source, optical power stabilization is employed. Furthermore, the impact of optical power-induced birefringence line splitting is investigated. The fast polarization mode experiences enhanced sensitivity to fluctuations in optical power, resulting in photo-birefringence noise. However, photo-thermal noise and photo-birefringence noise cancel each other partially for the slow polarization mode. By leveraging this behavior, a fractional frequency instability below  $3 \times 10^{-17}$  is obtained due to the combined effects of photo-thermal noise and photo-birefringence noise.

An active residual amplitude modulation (RAM) stabilization scheme is integrated into the cavity setup. The frequency instability attributed to RAM is evaluated both with and without active stabilization. Remarkably, even without active stabilization, a fractional frequency instability below  $7 \times 10^{-17}$  is achieved, which is exceptionally low compared to other highly stable cavities. With active RAM stabilization, the residual fractional frequency instability due to RAM is suppressed below the  $1 \times 10^{-17}$  level for average times exceeding 0.1 s.

The cavity's CTE zero crossing temperature is measured to be  $26.2^\circ\text{C}$ , and the cavity is temperature stabilized to this temperature. Two passive heat shields protect the cavity from temperature fluctuations, while active temperature stabilization is implemented at the active heat shield. A fractional frequency instability due to the remaining temperature fluctuations below thermal noise is achieved for average

times below 500 s. However, additional frequency changes resulting from thermal fluctuations inside the system have been observed, likely due to thermal stress within the heat shield. Nevertheless, the frequency instability due to thermal stress remains below the thermal noise limit for averaging times below 20 s and below  $1 \times 10^{-15}$  for averaging times below 5000 s. The performance of the system can be further enhanced by improving the temperature stability of the cavity. This can be accomplished through additional thermal isolation of the cavity or the entire system, stabilizing the environmental temperature, or improving the active temperature stabilization. The latter can be achieved by implementing homogeneous heating using additional Peltier elements and temperature sensors positioned at different locations. Additionally, it is crucial to investigate frequency fluctuations caused by thermal stress, which may necessitate optimizing the mounting process.

To assess the stability of the stabilization cavity, its frequency is compared to a more stable reference cavity via an optical comb. The fractional frequency instability of the cavity is measured to be on the order of  $2 \times 10^{-16}$  over an averaging time between 0.2 s and 200 s. This level of stability makes it well-suited for stabilizing the clock laser of a portable optical  $^{40}\text{Ca}^+ / ^{27}\text{Al}^+$  quantum logic clock. The measured fractional frequency instability is close to the thermal noise limit of the cavity and other evaluated noise sources. The performance of the ultra stable cavity is on the same level as the best transportable ultra stable cavities [107, 239, 301] built so far.

The clock transition of the  $^{27}\text{Al}^+$  ion is in the ultraviolet at 267.4 nm, requiring frequency quadrupling of the IR laser light. A single-pass frequency quadrupling system with good passive phase stability has been demonstrated. Its output power of approximately 50  $\mu\text{W}$  is sufficient for probing the highly forbidden clock transition of  $^{27}\text{Al}^+$  [22]. In scenarios where additional power is required while maintaining phase stability, the single-pass FHG system can serve as a phase reference for a separate and more efficient enhancement cavity-based FHG system. An upper bound for the passive phase stability of the unstabilized setup is obtained through frequency comparisons with a stabilized external UV light source and by observing the free-running signal of the interferometric phase stabilization loop. Both measurements reveal a phase stability of  $5\text{-}7 \times 10^{-17}$  at an averaging time of 1 s, approaching the lifetime-limited quantum projection noise limit of an aluminum ion clock with a 8 mHz narrow clock transition. At averaging times of 1 s or longer, the fractional frequency instability of the frequency quadrupling system is negligible compared to the stabilization cavity. A fractional frequency instability below  $1 \times 10^{-18}$  is achieved for averaging times exceeding 2000 s, enabling the transfer of the expected frequency stability of the  $^{27}\text{Al}^+$  ion spectroscopy back to the IR light and optical comb. Active phase stabilization is implemented and expected to further reduce the fractional frequency instability of the system. Furthermore, a more compact system has already been developed.

The frequency quadrupling system, stabilization cavity, light distribution board, laser, and all necessary electronics fits into a standard 19-inch rack. The complete system exhibits a fractional frequency instability of around  $2 \times 10^{-16}$  for averaging times between 1 s and more than 100 s, primarily limited by the performance of the cavity.



With this level of frequency stability, the system is well-suited for interrogating the clock laser transition of the  $^{27}\text{Al}^+$  ion and can be utilized for a transportable optical  $^{40}\text{Ca}^+ / ^{27}\text{Al}^+$  quantum logic clock.

The vacuum system required for the clock system has been established and tested. A dedicated breadboard has been designed and implemented to hold the physics package and optics for all necessary lasers. This transportable system is integrated into a second standard 19-inch rack along with additional electronic systems. The assembly of the carrier board and ion trap chip is currently in progress. Laser systems for cooling  $^{40}\text{Ca}^+$ , state preparation of  $^{40}\text{Ca}^+$  and  $^{27}\text{Al}^+$ , and quantum logic spectroscopy are already set up or under preparation. To enable automated clock operation, implementation within the experimental control system is essential. Once the optical clock system is fully set up, the next steps involve trapping and cooling  $^{40}\text{Ca}^+$  ions and optimizing this process. Characterization of residual micromotion and heating rate of the trap using the  $^{40}\text{Ca}^+$  ion is necessary to determine the limitations of clock accuracy. Trapping and implementation of the quantum logic scheme for  $^{27}\text{Al}^+$  ions are crucial for progressing toward clock operation. Finally, the clock laser system can be utilized to spectroscopically probe the clock transition from the  $^1\text{S}_0$  to  $^3\text{P}_0$  state of the  $^{27}\text{Al}^+$  ion.

## References

- <sup>1</sup>N. Huntemann, C. Sanner, B. Lipphardt, C. Tamm, and E. Peik, “Single-Ion Atomic Clock with  $3 \times 10^{-18}$  Systematic Uncertainty”, [Physical Review Letters \*\*116\*\*, 063001 \(2016\)](#).
- <sup>2</sup>I. Ushijima, M. Takamoto, M. Das, T. Ohkubo, and H. Katori, “Cryogenic optical lattice clocks”, en, [Nature Photonics \*\*9\*\*, 185–189 \(2015\)](#).
- <sup>3</sup>S. M. Brewer, J.-S. Chen, A. M. Hankin, E. R. Clements, C. W. Chou, D. J. Wineland, D. B. Hume, and D. R. Leibrandt, “ $^{27}\text{Al}^+$  Quantum-logic clock with a systematic uncertainty below  $10^{-18}$ ”, [Phys. Rev. Lett. \*\*123\*\*, Publisher: American Physical Society, 033201 \(2019\)](#).
- <sup>4</sup>C. Sanner, N. Huntemann, R. Lange, C. Tamm, E. Peik, M. S. Safronova, and S. G. Porsev, “Optical clock comparison for Lorentz symmetry testing”, en, [Nature \*\*567\*\*, 204–208 \(2019\)](#).
- <sup>5</sup>W. F. McGrew, X. Zhang, R. J. Fasano, S. A. Schäffer, K. Beloy, D. Nicolodi, R. C. Brown, N. Hinkley, G. Milani, M. Schioppo, T. H. Yoon, and A. D. Ludlow, “Atomic clock performance enabling geodesy below the centimetre level”, En, [Nature \*\*564\*\*, 87 \(2018\)](#).
- <sup>6</sup>T. L. Nicholson, S. L. Campbell, R. B. Hutson, G. E. Marti, B. J. Bloom, R. L. McNally, W. Zhang, M. D. Barrett, M. S. Safronova, G. F. Strouse, W. L. Tew, and J. Ye, “Systematic evaluation of an atomic clock at  $2 \times 10^{-18}$  total uncertainty”, en, [Nature Communications \*\*6\*\*, 6896 \(2015\)](#).
- <sup>7</sup>N. Ohmae, M. Takamoto, Y. Takahashi, M. Kokubun, K. Araki, A. Hinton, I. Ushijima, T. Muramatsu, T. Furumiya, Y. Sakai, N. Moriya, N. Kamiya, K. Fujii, R. Muramatsu, T. Shiimado, and H. Katori, “Transportable Strontium Optical Lattice Clocks Operated Outside Laboratory at the Level of  $10^{-18}$  Uncertainty”, en, [Advanced Quantum Technologies \*\*2021\*\*, 2100015 \(2021\)](#).
- <sup>8</sup>T. Bothwell, D. Kedar, E. Oelker, J. M. Robinson, S. L. Bromley, W. L. Tew, J. Ye, and C. J. Kennedy, “JILA SrI optical lattice clock with uncertainty of  $2.0 \times 10^{-18}$ ”, en, [Metrologia \*\*56\*\*, Publisher: IOP Publishing, 065004 \(2019\)](#).
- <sup>9</sup>M. Takamoto, I. Ushijima, N. Ohmae, T. Yahagi, K. Kokado, H. Shinkai, and H. Katori, “Test of general relativity by a pair of transportable optical lattice clocks”, en, [Nature Photonics \*\*14\*\*, Publisher: Nature Publishing Group, 411–415 \(2020\)](#).
- <sup>10</sup>O. Intergouvernementale and d. l. C. d. Mètre, *SI Brochure: The International System of Units (SI)*, 2019.
- <sup>11</sup>V. Gerginov, N. Nemitz, S. Weyers, R. Schröder, D. Griebisch, and R. Wynands, “Uncertainty evaluation of the caesium fountain clock ptb-csf2”, [Metrologia \*\*47\*\*, 65 \(2009\)](#).
- <sup>12</sup>T. P. Heavner, E. A. Donley, F. Levi, G. Costanzo, T. E. Parker, J. H. Shirley, N. Ashby, S. Barlow, and S. R. Jefferts, “First accuracy evaluation of nist-f2”, [Metrologia \*\*51\*\*, 174 \(2014\)](#).

- <sup>13</sup>S. R. Jefferts, T. P. Heavner, T. E. Parker, J. H. Shirley, E. A. Donley, N. Ashby, F. Levi, D. Calonico, and G. A. Costanzo, “High-accuracy measurement of the black-body radiation frequency shift of the ground-state hyperfine transition in  $^{133}\text{Cs}$ ”, [Phys. Rev. Lett. \*\*112\*\*, 050801 \(2014\)](#).
- <sup>14</sup>S. Weyers, V. Gerginov, M. Kazda, J. Rahm, B. Lipphardt, G. Dobrev, and K. Gibble, “Advances in the accuracy, stability, and reliability of the ptb primary fountain clocks”, [Metrologia \*\*55\*\*, 789 \(2018\)](#).
- <sup>15</sup>F. Riehle, “Towards a redefinition of the second based on optical atomic clocks”, [Comptes Rendus Physique, The measurement of time / La mesure du temps \*\*16\*\*, 506–515 \(2015\)](#).
- <sup>16</sup>F. Riehle, P. Gill, F. Arias, and L. Robertsson, “The CIPM list of recommended frequency standard values: guidelines and procedures”, en, [Metrologia \*\*55\*\*, 188 \(2018\)](#).
- <sup>17</sup>J. Lodewyck, “On a definition of the SI second with a set of optical clock transitions”, en, [Metrologia \*\*56\*\*, Publisher: IOP Publishing, 055009 \(2019\)](#).
- <sup>18</sup>P. Gill, “When should we change the definition of the second?”, [Philosophical Transactions of the Royal Society A: Mathematical, Physical and Engineering Sciences \*\*369\*\*, 4109–4130 \(2011\)](#).
- <sup>19</sup>T. Kobayashi, D. Akamatsu, Y. Hisai, T. Tanabe, H. Inaba, T. Suzuyama, F. Hong, K. Hosaka, and M. Yasuda, “Uncertainty Evaluation of an  $^{171}\text{Yb}$  Optical Lattice Clock at NMIJ”, [IEEE Transactions on Ultrasonics, Ferroelectrics, and Frequency Control \*\*65\*\*, 2449–2458 \(2018\)](#).
- <sup>20</sup>Z. Barber, C. Hoyt, C. Oates, L. Hollberg, A. Taichenachev, and V. Yudin, “Direct Excitation of the Forbidden Clock Transition in Neutral  $\text{Yb}^{174}$  Atoms Confined to an Optical Lattice”, [Physical Review Letters \*\*96\*\*, 10.1103/PhysRevLett.96.083002 \(2006\)](#).
- <sup>21</sup>K. Yamanaka, N. Ohmae, I. Ushijima, M. Takamoto, and H. Katori, “Frequency ratio of  $^{199}\text{Hg}^+$  and  $^{87}\text{Sr}$  optical lattice clocks beyond the SI limit”, [Physical Review Letters \*\*114\*\*, 230801 \(2015\)](#).
- <sup>22</sup>K. Cui, S. Chao, C. Sun, S. Wang, P. Zhang, Y. Wei, J. Yuan, J. Cao, H. Shu, and X. Huang, “Evaluation of the systematic shifts of a  $^{40}\text{Ca}^+ - ^{27}\text{Al}^+$  optical clock”, [The European Physical Journal D \*\*76\*\*, 140 \(2022\)](#).
- <sup>23</sup>J. Keller, D. Kalincev, T. Burgermeister, A. P. Kulosa, A. Didier, T. Nordmann, J. Kiethe, and T. Mehlstäubler, “Probing Time Dilation in Coulomb Crystals in a High-Precision Ion Trap”, [Physical Review Applied \*\*11\*\*, 011002 \(2019\)](#).
- <sup>24</sup>T. Rosenband, D. B. Hume, P. O. Schmidt, C. W. Chou, A. Brusch, L. Lorini, W. H. Oskay, R. E. Drullinger, T. M. Fortier, J. E. Stalnaker, S. A. Diddams, W. C. Swann, N. R. Newbury, W. M. Itano, D. J. Wineland, and J. C. Bergquist, “Frequency ratio of  $^{27}\text{Al}^+$  and  $^{199}\text{Hg}^+$  single-ion optical clocks; metrology at the 17<sup>th</sup> decimal place”, [Science \*\*319\*\*, 1808–1812 \(2008\)](#).
- <sup>25</sup>K. J. Arnold, R. Kaewuam, S. R. Chanu, T. R. Tan, Z. Zhang, and M. D. Barrett, “Precision Measurements of the  $^{138}\text{Ba}^+ 6s^2S_{1/2} - 5d^2D_{5/2}$  Clock Transition”, [Physical Review Letters \*\*124\*\*, Publisher: American Physical Society, 193001 \(2020\)](#).

- <sup>26</sup>P. Dubé, J. E. Bernard, and M. Gertsvolf, “Absolute frequency measurement of the 88 Sr + clock transition using a GPS link to the SI second”, en, [Metrologia](#) **54**, 290 (2017).
- <sup>27</sup>Y. Huang, B. Zhang, M. Zeng, H. Zhang, Y. Hao, Z. Chen, M. Wang, H. Guan, and K. Gao, “Nearly continuous Ca<sup>+</sup> optical clocks with stability at the 10<sup>-18</sup> level”, en, [10.21203/rs.3.rs-120082/v1](#) (2021).
- <sup>28</sup>Z. Zhiqiang, K. J. Arnold, R. Kaewuam, and M. D. Barrett, “176Lu+ clock comparison at the 10-18 level via correlation spectroscopy”, [Science Advances](#) **9**, Publisher: American Association for the Advancement of Science, eadg1971 (2023).
- <sup>29</sup>S. Dörscher, N. Huntemann, R. Schwarz, R. Lange, E. Benkler, B. Lipphardt, U. Sterr, E. Peik, and C. Lisdat, “Optical frequency ratio of a <sup>171</sup>Yb<sup>+</sup> single-ion clock and a <sup>87</sup>Sr lattice clock”, en, [Metrologia](#) **58**, Publisher: IOP Publishing, 015005 (2021).
- <sup>30</sup>K. Pyka, N. Herschbach, J. Keller, and T. E. Mehlstäubler, “A high-precision segmented Paul trap with minimized micromotion for an optical multiple-ion clock”, en, [Applied Physics B](#) **114**, 231–241 (2014).
- <sup>31</sup>J. Keller, T. Burgermeister, D. Kalincev, A. Didier, A. P. Kulosa, T. Nordmann, J. Kiethe, and T. E. Mehlstäubler, “Controlling systematic frequency uncertainties at the 10<sup>-19</sup> level in linear Coulomb crystals”, [Physical Review A](#) **99**, 013405 (2019).
- <sup>32</sup>L. Pelzer, “Robust artificial clock transition by continuous dynamical decoupling in multi-ion calcium crystals”, eng, DoctoralThesis (Hannover : Institutionelles Repository der Leibniz Unversität Hannover, 2023).
- <sup>33</sup>D. J. Wineland, J. J. Bollinger, W. M. Itano, F. L. Moore, and D. J. Heinzen, “Spin squeezing and reduced quantum noise in spectroscopy”, [Physical Review A](#) **46**, R6797–6800 (1992).
- <sup>34</sup>K. Arnold, E. Hajiyev, E. Paez, C. H. Lee, M. D. Barrett, and J. Bollinger, “Prospects for atomic clocks based on large ion crystals”, [Physical Review A](#) **92**, 032108 (2015).
- <sup>35</sup>T. R. Tan, R. Kaewuam, K. J. Arnold, S. R. Chanu, Z. Zhang, M. S. Safronova, and M. D. Barrett, “Suppressing inhomogeneous broadening in a lutetium multi-ion optical clock”, [Phys. Rev. Lett.](#) **123**, 063201 (2019).
- <sup>36</sup>E. Pedrozo-Peñafiel, S. Colombo, C. Shu, A. F. Adiyatullin, Z. Li, E. Mendez, B. Braverman, A. Kawasaki, D. Akamatsu, Y. Xiao, and V. Vuletić, “Entanglement on an optical atomic-clock transition”, en, [Nature](#) **588**, Number: 7838 Publisher: Nature Publishing Group, 414–418 (2020).
- <sup>37</sup>P. Micke, T. Leopold, S. A. King, E. Benkler, L. J. Spieß, L. Schmöger, M. Schwarz, J. R. C. López-Urrutia, and P. O. Schmidt, “Coherent laser spectroscopy of highly charged ions using quantum logic”, en, [Nature](#) **578**, 60–65 (2020).
- <sup>38</sup>S. A. King, L. J. Spieß, P. Micke, A. Wilzewski, T. Leopold, J. R. Crespo López-Urrutia, and P. O. Schmidt, “Algorithmic Ground-State Cooling of Weakly Coupled Oscillators Using Quantum Logic”, [Physical Review X](#) **11**, Publisher: American Physical Society, 041049 (2021).

- <sup>39</sup>S. A. King, L. J. Spieß, P. Micke, A. Wilzewski, T. Leopold, E. Benkler, R. Lange, N. Huntemann, A. Surzhykov, V. A. Yerokhin, J. R. Crespo López-Urrutia, and P. O. Schmidt, “An optical atomic clock based on a highly charged ion”, en, [Nature](#) **611**, Number: 7934 Publisher: Nature Publishing Group, 43–47 (2022).
- <sup>40</sup>B. Seiferle, L. v. d. Wense, P. V. Bilous, I. Amersdorffer, C. Lemell, F. Libisch, S. Stellmer, T. Schumm, C. E. Düllmann, A. Pálffy, and P. G. Thirolf, “Energy of the 229 Th nuclear clock transition”, en, [Nature](#) **573**, 243–246 (2019).
- <sup>41</sup>L. von der Wense and B. Seiferle, “The <sup>229</sup>Th isomer: prospects for a nuclear optical clock”, [arXiv:2009.13633 \[nucl-ex, physics:physics\]](#), [arXiv: 2009.13633](#) (2020).
- <sup>42</sup>B. Seiferle, D. Moritz, K. Scharl, S. Ding, F. Zacherl, L. Löbell, and P. G. Thirolf, “Extending Our Knowledge about the 229Th Nuclear Isomer”, en, [Atoms](#) **10**, Number: 1 Publisher: Multidisciplinary Digital Publishing Institute, 24 (2022).
- <sup>43</sup>E. Peik, B. Lipphardt, H. Schnatz, T. Schneider, C. Tamm, and S. Karshenboim, “Limit on the Present Temporal Variation of the Fine Structure Constant”, [Physical Review Letters](#) **93**, 170801 (2004).
- <sup>44</sup>X. Calmet and M. Keller, “Cosmological evolution of fundamental constants: From theory to experiment”, en, [Modern Physics Letters A](#) **30**, 1540028 (2015).
- <sup>45</sup>R. Schwarz, S. Dörscher, A. Al-Masoudi, E. Benkler, T. Legero, U. Sterr, S. Weyers, J. Rahm, B. Lipphardt, and C. Lisdat, “Long term measurement of the <sup>87</sup>Sr clock frequency at the limit of primary Cs clocks”, [Physical Review Research](#) **2**, Publisher: American Physical Society, 033242 (2020).
- <sup>46</sup>R. M. Godun, P. B. R. Nisbet-Jones, J. M. Jones, S. A. King, L. A. M. Johnson, H. S. Margolis, K. Szymaniec, S. N. Lea, K. Bongs, and P. Gill, “Frequency Ratio of Two Optical Clock Transitions in <sup>171</sup>Yb<sup>+</sup> and Constraints on the Time Variation of Fundamental Constants”, [Physical Review Letters](#) **113**, 210801 (2014).
- <sup>47</sup>N. Huntemann, B. Lipphardt, C. Tamm, V. Gerginov, S. Weyers, and E. Peik, “Improved Limit on a Temporal Variation of  $m_p/m_e$  from Comparisons of Yb<sup>+</sup> and Cs Atomic Clocks”, [Physical Review Letters](#) **113**, 210802 (2014).
- <sup>48</sup>R. Lange, N. Huntemann, J. M. Rahm, C. Sanner, H. Shao, B. Lipphardt, C. Tamm, S. Weyers, and E. Peik, “Improved Limits for Violations of Local Position Invariance from Atomic Clock Comparisons”, [Physical Review Letters](#) **126**, Publisher: American Physical Society, 011102 (2021).
- <sup>49</sup>A. Derevianko and M. Pospelov, “Hunting for topological dark matter with atomic clocks”, en, [Nature Physics](#) **10**, 933–936 (2014).
- <sup>50</sup>A. Arvanitaki, J. Huang, and K. Van Tilburg, “Searching for dilaton dark matter with atomic clocks”, [Physical Review D](#) **91**, 015015 (2015).
- <sup>51</sup>M. S. Safronova, D. Budker, D. DeMille, D. F. J. Kimball, A. Derevianko, and C. W. Clark, “Search for new physics with atoms and molecules”, [Reviews of Modern Physics](#) **90**, 025008 (2018).

- <sup>52</sup>K. Beloy, M. I. Bodine, T. Bothwell, S. M. Brewer, S. L. Bromley, J.-S. Chen, J.-D. Deschênes, S. A. Diddams, R. J. Fasano, T. M. Fortier, Y. S. Hassan, D. B. Hume, D. Kedar, C. J. Kennedy, I. Khader, A. Koepke, D. R. Leibbrandt, H. Leopardi, A. D. Ludlow, W. F. McGrew, W. R. Milner, N. R. Newbury, D. Nicolodi, E. Oelker, T. E. Parker, J. M. Robinson, S. Romisch, S. A. Schäffer, J. A. Sherman, L. C. Sinclair, L. Sonderhouse, W. C. Swann, J. Yao, J. Ye, X. Zhang, and B. A. C. O. N. (Collaboration, “Frequency ratio measurements at 18-digit accuracy using an optical clock network”, en, [Nature](#) **591**, Number: 7851 Publisher: Nature Publishing Group, 564–569 (2021).
- <sup>53</sup>B. M. Roberts, P. Delva, A. Al-Masoudi, A. Amy-Klein, C. Bærentsen, C. F. A. Baynham, E. Benkler, S. Bilicki, S. Bize, W. Bowden, J. Calvert, V. Cambier, E. Cantin, E. A. Curtis, S. Dörscher, M. Favier, F. Frank, P. Gill, R. M. Godun, G. Grosche, C. Guo, A. Hees, I. R. Hill, R. Hobson, N. Huntemann, J. Kronjäger, S. Koke, A. Kuhl, R. Lange, T. Legero, B. Lipphardt, C. Lisdat, J. Lodewyck, O. Lopez, H. S. Margolis, H. Álvarez-Martínez, F. Meynadier, F. Ozimek, E. Peik, P.-E. Pottie, N. Quintin, C. Sanner, L. D. Sarlo, M. Schioppo, R. Schwarz, A. Silva, U. Sterr, C. Tamm, R. L. Targat, P. Tuckey, G. Vallet, T. Waterholter, D. Xu, and P. Wolf, “Search for transient variations of the fine structure constant and dark matter using fiber-linked optical atomic clocks”, en, [New Journal of Physics](#) **22**, Publisher: IOP Publishing, 093010 (2020).
- <sup>54</sup>P. Wcisło, P. Ablewski, K. Beloy, S. Bilicki, M. Bober, R. Brown, R. Fasano, R. Ciuryło, H. Hachisu, T. Ido, J. Lodewyck, A. Ludlow, W. McGrew, P. Morzyński, D. Nicolodi, M. Schioppo, M. Sekido, R. L. Targat, P. Wolf, X. Zhang, B. Zjawin, and M. Zawada, “New bounds on dark matter coupling from a global network of optical atomic clocks”, en, [Science Advances](#) **4**, eaau4869 (2018).
- <sup>55</sup>C. W. Chou, D. B. Hume, J. C. J. Koelemeij, D. J. Wineland, and T. Rosenband, “Frequency comparison of two high-accuracy  $^{27}\text{Al}^+$  optical clocks”, [Phys. Rev. Lett.](#) **104**, Publisher: American Physical Society, 070802 (2010).
- <sup>56</sup>T. E. Mehlstäubler, G. Grosche, C. Lisdat, P. O. Schmidt, and H. Denker, “Atomic clocks for geodesy”, en, [Reports on Progress in Physics](#) **81**, 064401 (2018).
- <sup>57</sup>J. Müller, M. Soffel, and S. A. Klioner, “Geodesy and relativity”, en, [Journal of Geodesy](#) **82**, 133–145 (2008).
- <sup>58</sup>C. W. Chou, D. B. Hume, T. Rosenband, and D. J. Wineland, “Optical Clocks and Relativity”, [Science](#) **329**, 1630–1633 (2010).
- <sup>59</sup>M. Vermeer, *Chronometric levelling*, Reports of the Finnish Geodetic Institute 83(2) (Geodeettinen Laitos, Geodetiska Institutet, 1983), pp. 1–7.
- <sup>60</sup>C. Voigt, H. Denker, and L. Timmen, “Time-variable gravity potential components for optical clock comparisons and the definition of international time scales”, en, [Metrologia](#) **53**, 1365 (2016).

- <sup>61</sup>C. Lisdat, G. Grosche, N. Quintin, C. Shi, S. M. F. Raupach, C. Grebing, D. Nicolodi, F. Stefani, A. Al-Masoudi, S. Dörscher, S. Häfner, J.-L. Robyr, N. Chiodo, S. Bilicki, E. Bookjans, A. Koczwara, S. Koke, A. Kuhl, F. Wiotte, F. Meynadier, E. Camisard, M. Abgrall, M. Lours, T. Legero, H. Schnatz, U. Sterr, H. Denker, C. Chardonnet, Y. Le Coq, G. Santarelli, A. Amy-Klein, R. Le Targat, J. Lodewyck, O. Lopez, and P.-E. Pottie, “A clock network for geodesy and fundamental science”, en, [Nature Communications](#) **7**, 12443 (2016).
- <sup>62</sup>S. M. F. Raupach, A. Koczwara, and G. Grosche, “Brillouin amplification supports  $1 \times 10^{-20}$  uncertainty in optical frequency transfer over 1400 km of underground fiber”, [Physical Review A](#) **92**, 021801 (2015).
- <sup>63</sup>F. Riehle, “Optical clock networks”, en, [Nature Photonics](#) **11**, 25–31 (2017).
- <sup>64</sup>W.-K. Lee, F. Stefani, A. Bercy, O. Lopez, A. Amy-Klein, and P.-E. Pottie, “Hybrid fiber links for accurate optical frequency comparison”, en, [Applied Physics B](#) **123**, 161 (2017).
- <sup>65</sup>M. Fujieda, M. Kumagai, S. Nagano, A. Yamaguchi, H. Hachisu, and T. Ido, “All-optical link for direct comparison of distant optical clocks”, [Optics Express](#) **19**, 16498–16507 (2011).
- <sup>66</sup>M. Fujieda, S.-H. Yang, T. Gotoh, S.-W. Hwang, H. Hachisu, H. Kim, Y. K. Lee, R. Tabuchi, T. Ido, W.-K. Lee, M.-S. Heo, C. Y. Park, D.-H. Yu, and G. Petit, “Advanced Satellite-based Frequency Transfer at the  $10^{-16}$  Level”, [arXiv:1710.03147 \[physics\]](#), [arXiv: 1710.03147](#) (2017).
- <sup>67</sup>S. B. Koller, J. Grotti, S. Vogt, A. Al-Masoudi, S. Dörscher, S. Häfner, U. Sterr, and C. Lisdat, “Transportable Optical Lattice Clock with  $7 \times 10^{-17}$  Uncertainty”, [Physical Review Letters](#) **118**, 073601 (2017).
- <sup>68</sup>J. Cao, P. Zhang, J. Shang, K. Cui, J. Yuan, S. Chao, S. Wang, H. Shu, and X. Huang, “A compact, transportable single-ion optical clock with  $7.8 \times 10^{-17}$  systematic uncertainty”, en, [Applied Physics B](#) **123**, 112 (2017).
- <sup>69</sup>S. Falke, N. Lemke, C. Grebing, B. Lipphardt, S. Weyers, V. Gerginov, N. Hunte-  
mann, C. Hagemann, A. Al-Masoudi, S. Häfner, S. Vogt, U. Sterr, and C. Lisdat, “A strontium lattice clock with  $3 \times 10^{-17}$  inaccuracy and its frequency”, [New Journal of Physics](#) **16**, 073023 (2014).
- <sup>70</sup>T. Abbasov, K. Makarenko, I. Sherstov, M. Axenov, I. Zalivako, I. Semerikov, K. Khabarova, N. Kolachevsky, S. Chepurov, A. Taichenachev, S. Bagaev, and A. Tausenev, “Compact transportable  $^{171}\text{Yb}^+$  single-ion optical fully automated clock with  $4.9\text{E-}16$  relative instability”, [arXiv:2010.15244 \[physics, physics:quant-ph\]](#), [arXiv: 2010.15244](#) (2020).
- <sup>71</sup>G. Mura, T. Franzen, C. A. Jaoudeh, A. Görlitz, H. Luckmann, I. Ernsting, A. Nevsky, and S. Schiller, “A transportable optical lattice clock using  $^{171}\text{Yb}$ ”, in [2013 Joint European Frequency and Time Forum International Frequency Control Symposium \(EFTF/IFC\)](#) (July 2013), pp. 376–378.



- <sup>72</sup>M. Zeng, Y. Huang, B. Zhang, Y. Hao, Z. Ma, R. Hu, H. Zhang, Z. Chen, M. Wang, H. Guan, and K. Gao, “Toward a Transportable  $\text{Ca}^+$  Optical Clock with a Systematic Uncertainty of  $4.8 \times 10^{-18}$ ”, [Physical Review Applied](#) **19**, Publisher: American Physical Society, 064004 (2023).
- <sup>73</sup>S. Ritter, M. A. Hafiz, B. Arar, A. Bawamia, K. Bergner, M. Biethahn, S. Brakhane, S. Brakhane, A. Didier, J. Fortágh, M. Halder, R. Holzwarth, N. Huntemann, M. Johanning, R. Jördens, W. Kaenders, F. Karlewski, F. Kienle, M. Krutzik, M. Lessing, T. E. Mehlstäubler, D. Meschede, E. Peik, A. Peters, A. Peters, P. O. Schmidt, H. Siebeneich, J. Stuhler, C. Tamm, E. Vogt, A. Wicht, and C. Wunderlich, “Opticlock: Transportable and Easy-to-Operate Optical Single-Ion Clock”, EN, in [OSA Quantum 2.0 Conference \(2020\)](#), paper QTh5B.6 (Sept. 2020), QTh5B.6.
- <sup>74</sup>W. F. McGrew, X. Zhang, H. Leopardi, R. J. Fasano, D. Nicolodi, K. Beloy, J. Yao, J. A. Sherman, S. A. Schäffer, J. Savory, R. C. Brown, S. Römisch, C. W. Oates, T. E. Parker, T. M. Fortier, and A. D. Ludlow, “Towards the optical second: verifying optical clocks at the SI limit”, EN, [Optica](#) **6**, 448–454 (2019).
- <sup>75</sup>J. Grotti, S. Koller, S. Vogt, S. Häfner, U. Sterr, C. Lisdat, H. Denker, C. Voigt, L. Timmen, A. Rolland, F. N. Baynes, H. S. Margolis, M. Zampaolo, P. Thoumany, M. Pizzocaro, B. Rauf, F. Bregolin, A. Tampellini, P. Barbieri, M. Zucco, G. A. Costanzo, C. Clivati, F. Levi, and D. Calonico, “Geodesy and metrology with a transportable optical clock”, en, [Nature Physics](#) **14**, 437–441 (2018).
- <sup>76</sup>T. Takano, M. Takamoto, I. Ushijima, N. Ohmae, T. Akatsuka, A. Yamaguchi, Y. Kuroishi, H. Munekane, B. Miyahara, and H. Katori, “Geopotential measurements with synchronously linked optical lattice clocks”, en, [Nature Photonics](#) **10**, 662–666 (2016).
- <sup>77</sup>C. Reigber, R. Schmidt, F. Flechtner, R. König, U. Meyer, K.-H. Neumayer, P. Schwintzer, and S. Y. Zhu, “An Earth gravity field model complete to degree and order 150 from GRACE: EIGEN-GRACE02S”, [Journal of Geodynamics](#) **39**, 1–10 (2005).
- <sup>78</sup>R. Bondarescu, M. Bondarescu, G. Hetényi, L. Boschi, P. Jetzer, and J. Balakrishna, “Geophysical applicability of atomic clocks: direct continental geoid mapping”, [Geophysical Journal International](#) **191**, 78–82 (2012).
- <sup>79</sup>S. Hannig, “Development and characterization of a transportable aluminum ion quantum logic optical clocksetup”, PhD Thesis (Leibniz Universität Hannover, 2018).
- <sup>80</sup>S. Hannig, L. Pelzer, N. Scharnhorst, J. Kramer, M. Stepanova, Z. T. Xu, N. Spethmann, I. D. Leroux, T. E. Mehlstäubler, and P. O. Schmidt, “Towards a transportable aluminium ion quantum logic optical clock”, [Review of Scientific Instruments](#) **90**, 053204 (2019).
- <sup>81</sup>J. A. Kramer, “An aluminum optical clock setup and its evaluation using  $\text{Ca}^+$ ”, ger, DoctoralThesis (Hannover : Institutionelles Repositorium der Leibniz Universität Hannover, 2023).
- <sup>82</sup>P. O. Schmidt, T. Rosenband, C. Langer, W. M. Itano, J. C. Bergquist, and D. J. Wineland, “Spectroscopy Using Quantum Logic”, [Science](#) **309**, 749–752 (2005).

- <sup>83</sup>A. D. Ludlow, M. M. Boyd, J. Ye, E. Peik, and P. O. Schmidt, “Optical atomic clocks”, [Reviews of Modern Physics](#) **87**, 637–701 (2015).
- <sup>84</sup>I. D. Leroux, N. Scharnhorst, S. Hannig, J. Kramer, L. Pelzer, M. Stepanova, and P. O. Schmidt, “On-line estimation of local oscillator noise and optimisation of servo parameters in atomic clocks”, [Metrologia](#) **54**, 307 (2017).
- <sup>85</sup>E. Peik, T. Schneider, and C. Tamm, “Laser frequency stabilization to a single ion”, [Journal of Physics B: Atomic, Molecular and Optical Physics](#) **39**, 145–158 (2006).
- <sup>86</sup>E. Riis and A. G. Sinclair, “Optimum measurement strategies for trapped ion optical frequency standards”, [Journal of Physics B: Atomic, Molecular and Optical Physics](#) **37**, 4719–4732 (2004).
- <sup>87</sup>W. M. Itano, J. C. Bergquist, J. J. Bollinger, J. M. Gilligan, D. J. Heinzen, F. L. Moore, M. G. Raizen, and D. J. Wineland, “Quantum projection noise: population fluctuations in two-level systems”, [Physical Review A](#) **47**, 3554–3570 (1993).
- <sup>88</sup>J. Alnis, A. Matveev, N. Kolachevsky, T. Udem, and T. W. Hänsch, “Subhertz linewidth diode lasers by stabilization to vibrationally and thermally compensated ultralow-expansion glass fabry-pérot cavities”, [Physical Review A](#) **77**, 10.1103/PhysRevA.77.053809 (2008).
- <sup>89</sup>Y. Y. Jiang, A. D. Ludlow, N. D. Lemke, R. W. Fox, J. A. Sherman, L.-S. Ma, and C. W. Oates, “Making optical atomic clocks more stable with  $10^{-16}$ -level laser stabilization”, [Nat Photon](#) **5**, 158–161 (2011).
- <sup>90</sup>T. Kessler, C. Hagemann, C. Grebing, T. Legero, U. Sterr, F. Riehle, M. J. Martin, L. Chen, and J. Ye, “A sub-40-mHz-linewidth laser based on a silicon single-crystal optical cavity”, [Nature Photonics](#) **6**, 687–692 (2012).
- <sup>91</sup>D. R. Leibrandt, M. J. Thorpe, M. Notcutt, R. E. Drullinger, T. Rosenband, and J. C. Bergquist, “Spherical reference cavities for frequency stabilization of lasers in non-laboratory environments”, [Optics Express](#) **19**, 3471–3482 (2011).
- <sup>92</sup>J. Millo, D. Magalhães, C. Mandache, Y. Le Coq, E. English, P. Westergaard, J. Lodewyck, S. Bize, P. Lemonde, and G. Santarelli, “Ultrastable lasers based on vibration insensitive cavities”, [Physical Review A](#) **79**, 053829 (2009).
- <sup>93</sup>J. M. Robinson, E. Oelker, W. R. Milner, W. Zhang, T. Legero, D. G. Matei, F. Riehle, U. Sterr, and J. Ye, “Crystalline optical cavity at 4k with thermal-noise-limited instability and ultralow drift”, [Optica](#) **6**, 240–243 (2019).
- <sup>94</sup>M. J. Thorpe, D. R. Leibrandt, T. M. Fortier, and T. Rosenband, “Measurement and real-time cancellation of vibration-induced phase noise in a cavity-stabilized laser”, [Optics Express](#) **18**, 18744–18751 (2010).
- <sup>95</sup>S. Vogt, C. Lisdat, T. Legero, U. Sterr, I. Ernsting, A. Nevsky, and S. Schiller, “Demonstration of a transportable 1 hz-linewidth laser”, [Applied Physics B](#) **104**, 741–745 (2011).
- <sup>96</sup>M. Swallows, M. Martin, M. Bishof, C. Benko, Y. Lin, S. Blatt, A. Rey, and J. Ye, “Operating a  $^{87}\text{Sr}$  optical lattice clock with high precision and at high density”, [IEEE Transactions on Ultrasonics, Ferroelectrics and Frequency Control](#) **59**, 416–425 (2012).

- <sup>97</sup>S. Webster and P. Gill, “Force-insensitive optical cavity”, *Optics Letters* **36**, 3572–3574 (2011).
- <sup>98</sup>S. Webster, M. Oxborrow, S. Pugla, J. Millo, and P. Gill, “Thermal-noise-limited optical cavity”, *Physical Review A* **77**, 10.1103/PhysRevA.77.033847 (2008).
- <sup>99</sup>A. D. Ludlow, X. Huang, M. Notcutt, T. Zanon-Willette, S. M. Foreman, M. M. Boyd, S. Blatt, and J. Ye, “Compact, thermal-noise-limited optical cavity for diode laser stabilization at  $1 \times 10^{-15}$ ”, *Optics letters* **32**, 641 (2007).
- <sup>100</sup>W. Zhang, J. M. Robinson, L. Sonderhouse, E. Oelker, C. Benko, J. L. Hall, T. Legero, D. G. Matei, F. Riehle, U. Sterr, and J. Ye, “Ultrastable silicon cavity in a continuously operating closed-cycle cryostat at 4 k”, *Phys. Rev. Lett.* **119**, Publisher: American Physical Society, 243601 (2017).
- <sup>101</sup>T. Nazarova, F. Riehle, and U. Sterr, “Vibration-insensitive reference cavity for an ultra-narrow-linewidth laser”, *Applied Physics B* **83**, 531–536 (2006).
- <sup>102</sup>B. C. Young, F. C. Cruz, W. M. Itano, and J. C. Bergquist, “Visible lasers with subhertz linewidths”, *Physical Review Letters* **82**, 3799–3802 (1999).
- <sup>103</sup>S. T. Dawkins, R. Chicireanu, M. Petersen, J. Millo, D. V. Magalhães, C. Mandache, Y. Le Coq, and S. Bize, “An ultra-stable referenced interrogation system in the deep ultraviolet for a mercury optical lattice clock”, *Applied Physics B* **99**, 41–46 (2009).
- <sup>104</sup>A. Didier, S. Ignatovich, E. Benkler, M. Okhapkin, and T. E. Mehlstäubler, “946-nm nd:YAG digital-locked laser at  $1.1 \times 10^{-16}$  in 1 s and transfer-locked to a cryogenic silicon cavity”, *Optics Letters* **44**, 1781–1784 (2019).
- <sup>105</sup>P. Dubé, A. A. Madej, J. E. Bernard, L. Marmet, and A. D. Shiner, “A narrow linewidth and frequency-stable probe laser source for the  $^{88}\text{Sr}^+$  single ion optical frequency standard”, *Applied Physics B* **95**, 43–54 (2009).
- <sup>106</sup>S. Häfner, S. Falke, C. Grebing, S. Vogt, T. Legero, M. Merimaa, C. Lisdat, and U. Sterr, “ $8 \times 10^{-17}$  fractional laser frequency instability with a long room-temperature cavity”, *Optics Letters* **40**, 2112 (2015).
- <sup>107</sup>S. Häfner, S. Herbers, S. Vogt, S. Vogt, C. Lisdat, and U. Sterr, “Transportable interrogation laser system with an instability of  $\text{mod } \sigma_y = 3 \times 10^{-16}$ ”, *Optics Express* **28**, Publisher: Optical Society of America, 16407–16416 (2020).
- <sup>108</sup>D. G. Matei, T. Legero, S. Häfner, C. Grebing, R. Weyrich, W. Zhang, L. Sonderhouse, J. M. Robinson, J. Ye, F. Riehle, and U. Sterr, “ $1.5 \mu\text{m}$  lasers with sub-10 mHz linewidth”, *Physical Review Letters* **118**, 263202 (2017).
- <sup>109</sup>J. Borregaard and A. S. Sørensen, “Efficient atomic clocks operated with several atomic ensembles”, *Physical Review Letters* **111**, 090802 (2013).
- <sup>110</sup>D. B. Hume and D. R. Leibbrandt, “Probing beyond the laser coherence time in optical clock comparisons”, *Physical Review A* **93**, 032138 (2016).
- <sup>111</sup>E. M. Kessler, P. Kómár, M. Bishof, L. Jiang, A. S. Sørensen, J. Ye, and M. D. Lukin, “Heisenberg-limited atom clocks based on entangled qubits”, *Physical Review Letters* **112**, 190403 (2014).

- <sup>112</sup>T. Rosenband and D. R. Leibbrandt, “Exponential scaling of clock stability with atom number”, [arXiv:1303.6357 \(2013\)](#).
- <sup>113</sup>M. Takamoto, T. Takano, and H. Katori, “Frequency comparison of optical lattice clocks beyond the dick limit”, [Nat Photon 5, 288–292 \(2011\)](#).
- <sup>114</sup>M. Schioppo, R. C. Brown, W. F. McGrew, N. Hinkley, R. J. Fasano, K. Beloy, T. H. Yoon, G. Milani, D. Nicolodi, J. A. Sherman, N. B. Phillips, C. W. Oates, and A. D. Ludlow, “Ultrastable optical clock with two cold-atom ensembles”, [Nature Photonics 11, 48–52 \(2017\)](#).
- <sup>115</sup>S. Dörscher, A. Al-Masoudi, M. Bober, R. Schwarz, R. Hobson, U. Sterr, and C. Lisdat, “Dynamical decoupling of laser phase noise in compound atomic clocks”, [Communications Physics 3, Number: 1 Publisher: Nature Publishing Group, 1–9 \(2020\)](#).
- <sup>116</sup>E. R. Clements, M. E. Kim, K. Cui, A. M. Hankin, S. M. Brewer, J. Valencia, J.-S. Chen, C.-W. Chou, D. R. Leibbrandt, and D. B. Hume, “Lifetime-limited interrogation of two independent  $^{27}\text{Al}^+$  clocks using correlation spectroscopy”, [Phys. Rev. Lett. 125, 243602 \(2020\)](#).
- <sup>117</sup>D. Leibbrandt, S. Brewer, J.-S. Chen, A. Hankin, D. Hume, D. Wineland, and C.-W. Chou, “Trapped-ion optical atomic clocks at the quantum limits”, in [Proceedings of the 48th annual precise time and time interval systems and applications meeting, monterey, CA \(2017\)](#).
- <sup>118</sup>K.-F. C. Si-Jia Chao and K.-F. C. Si-Jia Chao, “Observation of  $^1\text{S}_0 \rightarrow ^3\text{P}_0$  transition of a  $^{40}\text{Ca}^+ - ^{27}\text{Al}^+$  quantum logic clock”, [Chinese Physics Letters 36, 120601 \(2019\)](#).
- <sup>119</sup>T. Rosenband, P. O. Schmidt, D. B. Hume, W. M. Itano, T. M. Fortier, J. E. Stalnaker, K. Kim, S. A. Diddams, J. C. J. Koelemeij, J. C. Bergquist, and D. J. Wineland, “Observation of the  $^1\text{S}_0 \rightarrow ^3\text{P}_0$  clock transition in  $^{27}\text{Al}^+$ ”, [Phys. Rev. Lett. 98, Publisher: American Physical Society, 220801 \(2007\)](#).
- <sup>120</sup>H. Leopardi, K. Beloy, and T. Bothwell et al., “Measurement of the  $^{27}\text{Al}^+$  and  $^{87}\text{Sr}$  absolute optical frequencies”, [Metrologia 58, Publisher: IOP Publishing, 015017 \(2021\)](#).
- <sup>121</sup>S. A. Diddams, T. Udem, J. C. Bergquist, E. A. Curtis, R. E. Drullinger, L. Hollberg, W. M. Itano, W. D. Lee, C. W. Oates, K. R. Vogel, and D. J. Wineland, “An optical clock based on a single trapped  $^{199}\text{Hg}^+$  ion”, [Science 293, 825 \(2001\)](#).
- <sup>122</sup>W. Oskay, S. Diddams, E. Donley, T. Fortier, T. Heavner, L. Hollberg, W. Itano, S. Jefferts, M. Delaney, K. Kim, F. Levi, T. Parker, and J. Bergquist, “Single-atom optical clock with high accuracy”, [Physical Review Letters 97, 020801 \(2006\)](#).
- <sup>123</sup>N. Ohtsubo, Y. Li, K. Matsubara, T. Ido, and K. Hayasaka, “Frequency measurement of the clock transition of an indium ion sympathetically-cooled in a linear trap”, [Optics Express 25, 11725–11735 \(2017\)](#).
- <sup>124</sup>N. Ohtsubo, Y. Li, N. Nemitz, H. Hachisu, K. Matsubara, T. Ido, and K. Hayasaka, “Frequency ratio of an  $^{115}\text{In}^+$  ion clock and a  $^{87}\text{Sr}$  optical lattice clock”, [Optics Letters 45, Publisher: Optical Society of America, 5950–5953 \(2020\)](#).

- <sup>125</sup>Y. Wang, R. Dumke, T. Liu, A. Stejskal, Y. Zhao, J. Zhang, Z. Lu, L. Wang, T. Becker, and H. Walther, “Absolute frequency measurement and high resolution spectroscopy of  $^{115}\text{In}^+ 5S^2 1S_0 - 5s5p 3P_0$  narrowline transition”, *Optics Communications* **273**, 526–531 (2007).
- <sup>126</sup>J. J. McFerran, L. Yi, S. Mejri, S. Di Manno, W. Zhang, J. Guéna, Y. Le Coq, and S. Bize, “Neutral atom frequency reference in the deep ultraviolet with fractional uncertainty= $5.7 \times 10^{-15}$ ”, *Physical Review Letters* **108**, 183004 (2012).
- <sup>127</sup>N. Ohmae, F. Bregolin, N. Nemitz, and H. Katori, “Direct measurement of the frequency ratio for hg and yb optical lattice clocks and closure of the hg/yb/sr loop”, *Optics Express* **28**, Publisher: Optical Society of America, 15112–15121 (2020).
- <sup>128</sup>M. Takamoto, I. Ushijima, M. Das, N. Nemitz, T. Ohkubo, K. Yamanaka, N. Ohmae, T. Takano, T. Akatsuka, A. Yamaguchi, and H. Katori, “Frequency ratios of sr, yb, and hg based optical lattice clocks and their applications”, *Comptes Rendus Physique*, 10.1016/j.crhy.2015.04.003 (2015).
- <sup>129</sup>K.-H. Ko, Y. Kim, H. Park, Y.-H. Cha, T.-S. Kim, L. Lee, G. Lim, J. Han, K.-H. Ko, and D.-Y. Jeong, “High-power continuous-wave tunable 544- and 272-nm beams based on a diode-oscillator fiber-amplifier for calcium spectroscopy”, *Applied Physics B* **120**, 233–238 (2015).
- <sup>130</sup>Y. Kaneda, M. Fallahi, J. Hader, J. V. Moloney, S. W. Koch, B. Kunert, and W. Stoltz, “Continuous-wave single-frequency 295 nm laser source by a frequency-quadrupled optically pumped semiconductor laser”, *Optics letters* **34**, 3511–3513 (2009).
- <sup>131</sup>Y. Kaneda, J. M. Yarborough, L. Li, N. Peyghambarian, L. Fan, C. Hessenius, M. Fallahi, J. Hader, J. V. Moloney, Y. Honda, M. Nishioka, Y. Shimizu, K. Miyazono, H. Shimatani, M. Yoshimura, Y. Mori, Y. Kitaoka, and Y. Sasaki, “Continuous-wave all-solid-state 244 nm deep-ultraviolet laser source by fourth-harmonic generation of an optically pumped semiconductor laser using CsLiB<sub>6</sub>O<sub>10</sub> in an external resonator”, *Opt. Lett.* **33**, Publisher: OSA, 1705–1707 (2008).
- <sup>132</sup>M. Scheid, F. Markert, J. Walz, J. Wang, M. Kirchner, and T. W. Hänsch, “750 mW continuous-wave solid-state deep ultraviolet laser source at the 253.7 nm transition in mercury”, *Optics letters* **32**, 955–957 (2007).
- <sup>133</sup>P. Herskind, J. Lindballe, C. Clausen, J. L. Sørensen, and M. Drewsen, “Second-harmonic generation of light at 544 and 272 nm from an ytterbium-doped distributed-feedback fiber laser”, *Optics Letters* **32**, 268–270 (2007).
- <sup>134</sup>J. Sakuma, Y. Asakawa, and M. Obara, “Generation of 5-W deep-UV continuous-wave radiation at 266 nm by an external cavity with a CsLiB<sub>6</sub>O<sub>10</sub> crystal”, en, *Optics Letters* **29**, 92 (2004).
- <sup>135</sup>T. Freearde and C. Zimmermann, “On the design of enhancement cavities for second harmonic generation”, *Optics Communications* **199**, 435–446 (2001).
- <sup>136</sup>C. Zimmermann, V. Vuletić, A. Hemmerich, and T. W. Hänsch, “All solid state laser source for tunable blue and ultraviolet radiation”, *Applied Physics Letters* **66**, 2318–2320 (1995).



- <sup>137</sup>H.-Y. Lo, J. Alonso, D. Kienzler, B. C. Keitch, L. E. d. Clercq, V. Negnevitsky, and J. P. Home, “All-solid-state continuous-wave laser systems for ionization, cooling and quantum state manipulation of beryllium ions”, *Applied Physics B* **114**, 17–25 (2014).
- <sup>138</sup>Z. Wang, F. Yang, G. Zhang, Y. Bo, S. Liu, S. Xie, Y. Xu, N. Zong, F. Li, B. Liu, J. Xu, Q. Peng, J. Zhang, D. Cui, Y. Wu, and Z. Xu, “High-power ultraviolet 278 nm laser from fourth-harmonic generation of a nd:YAG laser in CsB<sub>3</sub>O<sub>5</sub>”, *Optics Letters* **37**, Publisher: Optical Society of America, 2403–2405 (2012).
- <sup>139</sup>D. B. Hume, “Two-species ion arrays for quantum logic spectroscopy and entanglement generation”, PhD thesis (University of Colorado, Boulder, USA, 2010), 129 pp.
- <sup>140</sup>S. Hannig, J. Mielke, J. A. Fenske, M. Misera, N. Beev, C. Ospelkaus, and P. O. Schmidt, “A highly stable monolithic enhancement cavity for second harmonic generation in the ultraviolet”, *Review of Scientific Instruments* **89**, 013106 (2018).
- <sup>141</sup>T. Schmitt, T. A. Puppe, A. Nendel, F. Lison, W. G. Kaenders, and M. Le Flohic, “Single mode tunable all solid-state UV laser at the 281.6 nm clock transition of <sup>199</sup>Hg<sup>+</sup>”, *Optical Society of America, Conference on Lasers and Electro-Optics/International Quantum Electronics Conference, CTuR5* (2009).
- <sup>142</sup>S. Manzoor, J. N. Tinsley, S. Bandarupally, M. Chiarotti, and N. Poli, “High-power, frequency-quadrupled UV laser source resonant with the <sup>1</sup>S<sub>0</sub>-<sup>3</sup>P<sub>1</sub> narrow intercombination transition of cadmium at 326.2 nm”, *arXiv:2203.08510 [physics]*, *arXiv:2203.08510* (2022).
- <sup>143</sup>J. C. Shaw, S. Hannig, and D. J. McCarron, “Stable 2 W continuous-wave 261.5 nm laser for cooling and trapping aluminum monochloride”, EN, *Optics Express* **29**, Publisher: Optical Society of America, 37140–37149 (2021).
- <sup>144</sup>Z. Burkley, A. D. Brandt, C. Rasor, S. F. Cooper, and D. C. Yost, “Highly coherent, watt-level deep-UV radiation via a frequency-quadrupled Yb-fiber laser system”, EN, *Applied Optics* **58**, 1657–1661 (2019).
- <sup>145</sup>J.-S. Chen, “Ticking near the Zero-Point Energy: Towards 1x10<sup>-18</sup> Accuracy in Al<sup>+</sup> Optical Clocks”, PhD Thesis (University of Colorado, Boulder, USA, Jan. 2017).
- <sup>146</sup>B. Kraus, F. Dawel, S. Hannig, J. Kramer, C. Nauk, and P. O. Schmidt, “Phase-stabilized UV light at 267 nm through twofold second harmonic generation”, EN, *Optics Express* **30**, Publisher: Optica Publishing Group, 44992–45007 (2022).
- <sup>147</sup>N. Poli, C. Oates, P. Gill, and G. Tino, “Optical atomic clocks”, *La Rivista del Nuovo Cimento* **36**, 555–624 (2013).
- <sup>148</sup>J. Lodewyck, S. Bilicki, E. Bookjans, J.-L. Robyr, C. Shi, G. Vallet, R. L. Targat, D. Nicolodi, Y. L. Coq, J. Guéna, M. Abgrall, P. Rosenbusch, and S. Bize, “Optical to microwave clock frequency ratios with a nearly continuous strontium optical lattice clock”, en, *Metrologia* **53**, Publisher: IOP Publishing, 1123–1130 (2016).
- <sup>149</sup>S. V. Chepurov, N. A. Pavlov, A. A. Lugovoy, S. N. Bagayev, and A. V. Taichenachev, “Optical frequency standard with a single 171Yb<sup>+</sup> ion”, en, *Quantum Electronics* **51**, Publisher: IOP Publishing, 473 (2021).

- <sup>150</sup>K. J. Arnold, R. Kaewuam, A. Roy, T. R. Tan, and M. D. Barrett, “Blackbody radiation shift assessment for a lutetium ion clock”, en, [Nature Communications](#) **9**, 1–6 (2018).
- <sup>151</sup>T. W. Hänsch and A. L. Schawlow, “Cooling of gases by laser radiation”, [Optics Communications](#) **13**, 68–69 (1975).
- <sup>152</sup>D. J. Wineland, R. E. Drullinger, and F. L. Walls, “Radiation-pressure cooling of bound resonant absorbers”, [Physical Review Letters](#) **40**, 1639–1642 (1978).
- <sup>153</sup>D. J. Wineland and W. M. Itano, “Laser cooling of atoms”, [Physical Review A](#) **20**, 1521 (1979).
- <sup>154</sup>D. J. Wineland, “Trapped ions, laser cooling, and better clocks”, [Science](#) **226**, 395 (1984).
- <sup>155</sup>D. J. Wineland, W. M. Itano, J. C. Bergquist, and R. G. Hulet, “Laser-cooling limits and single-ion spectroscopy”, [Physical Review A](#) **36**, 2220–2232 (1987).
- <sup>156</sup>S. Herbers, “Transportable ultra-stable laser system with an instability down to  $10^{-16}$ ”, en, 10.15488/11624, PhD Thesis (Leibniz Universität Hannover, Hannover, Dec. 2021).
- <sup>157</sup>S. Häfner, “Ultra-stabile Lasersysteme für Weltraum- und Bodenanwendungen”, PhD Thesis (Leibniz Universität Hannover, Hannover, 2015).
- <sup>158</sup>S. Amairi, “A Long Optical Cavity For Sub-Hertz Laser Spectroscopy”, PhD Thesis (Leibniz Universität Hannover, July 2014).
- <sup>159</sup>T. Hänsch, “Nobel Lecture: Passion for precision”, [Reviews of Modern Physics](#) **78**, 1297–1309 (2006).
- <sup>160</sup>J. Hall, “Nobel Lecture: Defining and measuring optical frequencies”, [Reviews of Modern Physics](#) **78**, 1279–1295 (2006).
- <sup>161</sup>F. Riehle, *Frequency standards: basics and applications* (Wiley-VCH, Weinheim, 2004).
- <sup>162</sup>D. W. Allan, “Statistics of atomic frequency standards”, [Proceedings of the IEEE](#) **54**, 221–230 (1966).
- <sup>163</sup>J. Rutman and F. Walls, “Characterization of frequency stability in precision frequency sources”, [Proceedings of the IEEE](#) **79**, 952–960 (1991).
- <sup>164</sup>P. Lesage and C. Audoin, “Characterization of frequency stability: uncertainty due to the finite number of measurements”, [IEEE Transactions on Instrumentation and Measurement](#) **22**, 157–161 (1973).
- <sup>165</sup>P. Lesage and C. Audoin, “Effect of dead-time on the estimation of the two-sample variance”, [IEEE Transactions on Instrumentation and Measurement](#) **28**, 6–10 (1979).
- <sup>166</sup>P. Lesage and T. Ayi, “Characterization of frequency stability: analysis of the modified allan variance and properties of its estimate”, [IEEE Transactions on Instrumentation and Measurement](#) **33**, 332–336 (1984).
- <sup>167</sup>W. J. Riley, *Handbook of frequency stability analysis*, Vol. 1065, NIST Special Publications (US Department of Commerce, National Institute of Standards and Technology, Boulder, USA, 2008).



- <sup>168</sup>G. J. Dick, “Local Oscillator Induced Instabilities in Trapped Ion Frequency Standards”, in [Proc. 19th Annual Precise Time and Time Interval \(PTTI\) Application and Planning Meeting](#) (1987), pp. 133–147.
- <sup>169</sup>G. J. Dick, J. D. Prestage, C. A. Greenhall, and L. Maleki, “Local oscillator induced degradation of medium-term stability in passive atomic frequency standards”, in [Proceedings of the 22nd Annual Precise Time and Time Interval \(PTTI\) Applications and Planning Meeting](#) (May 1990).
- <sup>170</sup>E. Oelker, R. B. Hutson, C. J. Kennedy, L. Sonderhouse, T. Bothwell, A. Goban, D. Kedar, C. Sanner, J. M. Robinson, G. E. Marti, D. G. Matei, T. Legero, M. Giunta, R. Holzwarth, F. Riehle, U. Sterr, and J. Ye, “Demonstration of  $4.8 \times 10^{-17}$  stability at 1 s for two independent optical clocks”, en, [Nature Photonics](#), 1–6 (2019).
- <sup>171</sup>M. Schulte, C. Lisdat, P. O. Schmidt, U. Sterr, and K. Hammerer, “Prospects and challenges for squeezing-enhanced optical atomic clocks”, en, [Nature Communications](#) **11**, Number: 1 Publisher: Nature Publishing Group, 5955 (2020).
- <sup>172</sup>C. A. Greenhall, “A derivation of the long-term degradation of a pulsed atomic frequency standard from a control-loop model”, [IEEE Transactions on Ultrasonics, Ferroelectrics, and Frequency Control](#) **45**, 895–898 (1998).
- <sup>173</sup>G. Santarelli, C. Audoin, A. Makdissi, P. Laurent, G. Dick, and A. Clairon, “Frequency stability degradation of an oscillator slaved to a periodically interrogated atomic resonator”, [IEEE Transactions on Ultrasonics, Ferroelectrics and Frequency Control](#) **45**, 887–894 (1998).
- <sup>174</sup>R. Schwarz, “A cryogenic Strontium lattice clock”, eng, DoctoralThesis (Hannover : Institutionelles Repositorium der Leibniz Universität Hannover, 2022).
- <sup>175</sup>S. Falke, H. Schnatz, J. S. R. V. Winfred, T. Middelmann, S. Vogt, S. Weyers, B. Lipphardt, G. Grosche, F. Riehle, U. Sterr, and C. Lisdat, “The  $^{87}\text{Sr}$  optical frequency standard at PTB”, [Metrologia](#) **48**, 399–407 (2011).
- <sup>176</sup>T. Rosenband, W. M. Itano, P. O. Schmidt, D. B. Hume, J. C. J. Koelemeij, J. C. Bergquist, and D. J. Wineland, “Blackbody radiation shift of the  $^{27}\text{Al}^+ \ ^1\text{S}_0 - \ ^3\text{P}_0$  transition”, in [Proceedings of the 20th European Frequency and Time Forum](#) (2006), pp. 289–291.
- <sup>177</sup>S. G. Porsev and A. Derevianko, “Multipolar theory of blackbody radiation shift of atomic energy levels and its implications for optical lattice clocks”, [Physical Review A](#) **74**, 020502 (2006).
- <sup>178</sup>T. Middelmann, S. Falke, C. Lisdat, and U. Sterr, “High Accuracy Correction of Blackbody Radiation Shift in an Optical Lattice Clock”, [Physical Review Letters](#) **109**, 263004 (2012).
- <sup>179</sup>T. Middelmann, C. Lisdat, S. Falke, J. Winfred, F. Riehle, and U. Sterr, “Tackling the Blackbody Shift in a Strontium Optical Lattice Clock”, [IEEE Transactions on Instrumentation and Measurement](#) **60**, 2550–2557 (2011).

- <sup>180</sup>A. M. Hankin, E. R. Clements, Y. Huang, S. M. Brewer, J.-S. Chen, C. W. Chou, D. B. Hume, and D. R. Leibbrandt, “Systematic uncertainty due to background-gas collisions in trapped-ion optical clocks”, *Physical Review A* **100**, 033419 (2019).
- <sup>181</sup>J. Davis, P. Dubé, and A. C. Vutha, “Improved estimate of the collisional frequency shift in Al<sup>+</sup> optical clocks”, *Physical Review Research* **1**, Publisher: American Physical Society, 033137 (2019).
- <sup>182</sup>K. Gibble, “Scattering of Cold-Atom Coherences by Hot Atoms: Frequency Shifts from Background-Gas Collisions”, *Physical Review Letters* **110**, 180802 (2013).
- <sup>183</sup>B. J. Bloom, T. L. Nicholson, J. R. Williams, S. L. Campbell, M. Bishof, X. Zhang, W. Zhang, S. L. Bromley, and J. Ye, “An optical lattice clock with accuracy and stability at the 10<sup>-18</sup> level”, en, *Nature* **506**, 71–75 (2014).
- <sup>184</sup>S. M. Brewer, J.-S. Chen, K. Bely, A. M. Hankin, E. R. Clements, C. W. Chou, W. F. McGrew, X. Zhang, R. J. Fasano, D. Nicolodi, H. Leopardi, T. M. Fortier, S. A. Diddams, A. D. Ludlow, D. J. Wineland, D. R. Leibbrandt, and D. B. Hume, “Measurements of <sup>27</sup>Al<sup>+</sup> and <sup>25</sup>Mg<sup>+</sup> magnetic constants for improved ion-clock accuracy”, *Physical Review A* **100**, 013409 (2019).
- <sup>185</sup>D. J. Berkeland, J. D. Miller, J. C. Bergquist, W. M. Itano, and D. J. Wineland, “Minimization of ion micromotion in a Paul trap”, *Journal of Applied Physics* **83**, 5025–5033 (1998).
- <sup>186</sup>N. Scharnhorst, “Multi-mode ground state cooling of trapped ions”, PhD thesis (Leibniz Universität Hannover, 2018).
- <sup>187</sup>J. B. Wübbena, “Controlling Motion in Quantum Logic Clocks”, PhD Thesis (Leibniz Universität Hannover, July 2014).
- <sup>188</sup>A. D. Ludlow, N. D. Lemke, J. A. Sherman, C. W. Oates, G. Quémener, J. von Stecher, and A. M. Rey, “Cold-collision-shift cancellation and inelastic scattering in a Yb optical lattice clock”, *Physical Review A* **84**, 052724 (2011).
- <sup>189</sup>P. Lemonde and P. Wolf, “Optical lattice clock with atoms confined in a shallow trap”, *Phys. Rev. A* **72**, 033409 (2005).
- <sup>190</sup>B. Merkel, K. Thirumalai, J. E. Tarlton, V. M. Schäfer, C. J. Ballance, T. P. Harty, and D. M. Lucas, “Magnetic field stabilization system for atomic physics experiments”, *Review of Scientific Instruments* **90**, 044702 (2019).
- <sup>191</sup>M. Scholz, D. Opalevs, P. Leisching, W. Kaenders, G. Wang, X. Wang, R. Li, and C. Chen, “1.3-mw tunable and narrow-band continuous-wave light source at 191 nm”, *Opt. Express* **20**, 18659–18664 (2012).
- <sup>192</sup>M. D. Whitfield, S. P. Lansley, O. Gaudin, R. D. McKeag, N. Rizvi, and R. B. Jackman, “High-speed diamond photoconductors: a solution for high rep-rate deep-uv laser applications”, *Diamond and related materials* **10**, 650–656 (2001).
- <sup>193</sup>J.-J. Li, F.-F. Zhang, Z.-M. Wang, Y.-C. Xu, X.-C. Liu, N. Zong, S.-J. Zhang, F.-L. Xu, F. Yang, L. Yuan, Y. Kou, Y. Bo, D.-F. Cui, Q.-J. Peng, X.-Y. Wang, L.-J. Liu, C.-T. Chen, and Z.-Y. Xu, “High-energy single-frequency 167 nm deep-ultraviolet laser”, en, *Optics Letters* **43**, 2563 (2018).

- <sup>194</sup>C. Roos, T. Zeiger, H. Rohde, H. C. Nägerl, J. Eschner, D. Leibfried, F. Schmidt-Kaler, and R. Blatt, “Quantum State Engineering on an Optical Transition and Decoherence in a Paul Trap”, *Physical Review Letters* **83**, 4713–4716 (1999).
- <sup>195</sup>D. J. Larson, J. C. Bergquist, J. J. Bollinger, W. M. Itano, and D. J. Wineland, “Sympathetic cooling of trapped ions: A laser-cooled two-species nonneutral ion plasma”, *Physical Review Letters* **57**, 70 (1986).
- <sup>196</sup>M. Barrett, B. DeMarco, T. Schaetz, V. Meyer, D. Leibfried, J. Britton, J. Chiaverini, W. Itano, B. Jelenković, J. Jost, C. Langer, T. Rosenband, and D. Wineland, “Sympathetic cooling of  $^9\text{Be}^+$  and  $^{24}\text{Mg}^+$  for quantum logic”, *Physical Review A* **68**, 042302 (2003).
- <sup>197</sup>J. B. Wübbena, S. Amairi, O. Mandel, and P. O. Schmidt, “Sympathetic cooling of mixed-species two-ion crystals for precision spectroscopy”, *Physical Review A* **85**, 043412 (2012).
- <sup>198</sup>M. Guggemos, D. Heinrich, O. A. Herrera-Sancho, R. Blatt, and C. F. Roos, “Sympathetic cooling and detection of a hot trapped ion by a cold one”, en, *New Journal of Physics* **17**, 103001 (2015).
- <sup>199</sup>K.-f. Cui, J.-j. Shang, S.-j. Chao, S.-m. Wang, J.-b. Yuan, P. Zhang, J. Cao, Hua-lin Shu, and X.-r. Huang, “Sympathetic sideband cooling of a  $^{40}\text{Ca}^+ - ^{27}\text{Al}^+$  pair toward a quantum logic clock”, en, *Journal of Physics B: Atomic, Molecular and Optical Physics* **51**, 045502 (2018).
- <sup>200</sup>N. Scharnhorst, J. Cerrillo, J. Kramer, I. D. Leroux, J. B. Wübbena, A. Retzker, and P. O. Schmidt, “Multi-mode double-bright EIT cooling”, [arXiv:1711.00738 \[physics, physics:quant-ph\]](https://arxiv.org/abs/1711.00738), [arXiv: 1711.00738](https://arxiv.org/abs/1711.00738) (2017).
- <sup>201</sup>N. Scharnhorst, J. Cerrillo, J. Kramer, I. D. Leroux, J. B. Wübbena, A. Retzker, and P. O. Schmidt, “Experimental and theoretical investigation of a multimode cooling scheme using multiple electromagnetically-induced-transparency resonances”, *Physical Review A* **98**, 023424 (2018).
- <sup>202</sup>M. Ramm, T. Pruttivarasin, M. Kokish, I. Talukdar, and H. Häffner, “Precision Measurement Method for Branching Fractions of Excited  $P_{1/2}$  States Applied to  $^{40}\text{Ca}^+$ ”, *Physical Review Letters* **111**, 023004 (2013).
- <sup>203</sup>P. A. Barton, C. J. S. Donald, D. M. Lucas, D. A. Stevens, A. M. Steane, and D. N. Stacey, “Measurement of the lifetime of the  $3d\ ^2D_{5/2}$  state in  $^{40}\text{Ca}^+$ ”, *Physical Review A* **62**, 032503 (2000).
- <sup>204</sup>A. Kreuter, C. Becher, G. P. T. Lancaster, A. B. Mundt, C. Russo, H. Häffner, C. Roos, W. Hänsel, F. Schmidt-Kaler, R. Blatt, and M. S. Safronova, “Experimental and theoretical study of the  $3d^2D$  -level lifetimes of  $^{40}\text{Ca}^+$ ”, *Physical Review A* **71**, 032504 (2005).
- <sup>205</sup>J. Benhelm, G. Kirchmair, U. Rapol, T. Körber, C. F. Roos, and R. Blatt, “Measurement of the hyperfine structure of the  $S_{1/2} - D_{5/2}$  transition in  $^{43}\text{Ca}^+$ ”, *Physical Review A* **75**, 032506 (2007).

- <sup>206</sup>M. Chwalla, K. Kim, T. Monz, P. Schindler, M. Riebe, C. F. Roos, and R. Blatt, “Precision spectroscopy with two correlated atoms”, *Applied Physics B: Lasers and Optics* **89**, 483–488 (2007).
- <sup>207</sup>M. Guggemos, M. Guevara-Bertsch, D. Heinrich, O. A. Herrera-Sancho, Y. Colombe, R. Blatt, and C. F. Roos, “Frequency measurement of the  $^1S_0, F=5/2 - ^3P_1, F=7/2$  transition of  $^{27}\text{Al}^+$  via quantum logic spectroscopy with  $^{40}\text{Ca}^+$ ”, en, *New Journal of Physics* **21**, 103003 (2019).
- <sup>208</sup>B. Zhang, Y. Huang, H. Zhang, Y. Hao, M. Zeng, H. Guan, and K. Gao, “Progress on the  $^{40}\text{Ca}^+$  ion optical clock”, en, *Chinese Physics B*, [10.1088/1674-1056/ab9432](https://doi.org/10.1088/1674-1056/ab9432) (2020).
- <sup>209</sup>L. Pelzer, K. Dietze, J. Kramer, F. Dawel, L. Krinner, N. Spethmann, V. Martinez, N. Aharon, A. Retzker, K. Hammerer, and P. O. Schmidt, “Tailored optical clock transition in  $^{40}\text{Ca}^+$ ”, en, *Measurement: Sensors* **18**, 100326 (2021).
- <sup>210</sup>M. C. T. Bahaa E. A. Saleh, *Fundamentals of Photonics* (John Wiley & Sons, Ltd, 1991) Chap. 9, pp. 310–341.
- <sup>211</sup>R. V. Pound, “Electronic Frequency Stabilization of Microwave Oscillators”, *Review of Scientific Instruments* **17**, 490–505 (1946).
- <sup>212</sup>R. W. P. Drever, J. L. Hall, F. V. Kowalski, J. Hough, G. M. Ford, A. J. Munley, and H. Ward, “Laser phase and frequency stabilization using an optical resonator”, *Applied Physics B: Lasers and Optics* **31**, 97–105 (1983).
- <sup>213</sup>E. D. Black, “An introduction to Pound–Drever–Hall laser frequency stabilization”, *American Journal of Physics* **69**, Publisher: American Association of Physics Teachers, 79–87 (2001).
- <sup>214</sup>N. Wong and J. Hall, “Servo control of amplitude modulation in frequency-modulation spectroscopy: demonstration of shot-noise-limited detection”, *Journal of The Optical Society of America* **2**, [10.1364/JOSAB.2.001527](https://doi.org/10.1364/JOSAB.2.001527) (1985).
- <sup>215</sup>E. A. Whittaker, M. Gehrtz, and G. C. Bjorklund, “Residual amplitude modulation in laser electro-optic phase modulation”, *J. Opt. Soc. Am. B* **2**, 1320–1326 (1985).
- <sup>216</sup>H. Shen, L. Li, J. Bi, J. Wang, and L. Chen, “Systematic and quantitative analysis of residual amplitude modulation in Pound-Drever-Hall frequency stabilization”, *Physical Review A* **92**, 063809 (2015).
- <sup>217</sup>L. Jin, “Suppression of residual amplitude modulation of adp electro-optical modulator in pound-drever-hall laser frequency stabilization”, *Optics & Laser Technology* **136**, 106758 (2021).
- <sup>218</sup>W. Zhang, M. J. Martin, C. Benko, J. L. Hall, J. Ye, C. Hagemann, T. Legero, U. Sterr, F. Riehle, G. D. Cole, and M. Aspelmeyer, “Reduction of residual amplitude modulation to  $1 \times 10^{-6}$  for frequency modulation and laser stabilization”, en, *Optics Letters* **39**, 1980 (2014).
- <sup>219</sup>L. Li, H. Shen, J. Bi, C. Wang, S. Lv, and L. Chen, “Analysis of frequency noise in ultra-stable optical oscillators with active control of residual amplitude modulation”, en, *Applied Physics B* **117**, 1025–1033 (2014).

- <sup>220</sup>J. F. Diehl, C. E. Sunderman, J. M. Singley, V. J. Urick, and K. J. Williams, “Control of residual amplitude modulation in lithium niobate phase modulators”, *Opt. Express* **25**, 32985–32994 (2017).
- <sup>221</sup>J. Hall, W. Zhang, and J. Ye, “Accurate removal of ram from fm laser beams”, in (Apr. 2015), pp. 713–716.
- <sup>222</sup>J. C. Bergquist, W. M. Itano, and D. J. Wineland, “Frontiers in laser spectroscopy”, in Proceedings of the international school of physics “enrico fermi”, Hansch, T. W. and Inguscio, M. (1992), p. 359.
- <sup>223</sup>L.-S. Ma, P. Jungner, J. Ye, and J. L. Hall, “Delivering the same optical frequency at two places: accurate cancellation of phase noise introduced by an optical fiber or other time-varying path”, *Optics Letters* **19**, 1777–1779 (1994).
- <sup>224</sup>D. R. Leibbrandt, J. C. Bergquist, and T. Rosenband, “Cavity-stabilized laser with acceleration sensitivity below  $10^{-12} \text{ g}^{-1}$ ”, *Physical Review A* **87**, 023829 (2013).
- <sup>225</sup>X. Chen, Y. Jiang, B. Li, H. Yu, H. Jiang, T. Wang, Y. Yao, and L. Ma, “Laser frequency instability of  $6 \times 10^{-16}$  using 10-cm-long cavities on a cubic spacer”, *Chinese Optics Letters* **18**, 030201 (2020).
- <sup>226</sup>Q.-F. Chen, A. Nevsky, M. Cardace, S. Schiller, T. Legero, S. Häfner, A. Uhde, and U. Sterr, “A compact, robust, and transportable ultra-stable laser with a fractional frequency instability of  $1 \times 10^{-15}$ ”, *Review of Scientific Instruments* **85**, 113107, 10.1063/1.4898334 (2014).
- <sup>227</sup>J. Davila-Rodriguez, F. N. Baynes, A. D. Ludlow, T. M. Fortier, H. Leopardi, S. A. Diddams, and F. Quinlan, “Compact, thermal-noise-limited reference cavity for ultra-low-noise microwave generation”, *Opt. Lett.* **42**, 1277–1280 (2017).
- <sup>228</sup>D. Świerad, S. Häfner, S. Vogt, B. Venon, D. Holleville, S. Bize, A. Kulosa, S. Bode, Y. Singh, K. Bongs, E. M. Rasel, J. Lodewyck, R. Le Targat, C. Lisdat, and U. Sterr, “Ultra-stable clock laser system development towards space applications”, *Scientific Reports* **6**, 33973 (2016).
- <sup>229</sup>B. Argence, E. Prevost, T. Lévêque, R. Le Goff, S. Bize, P. Lemonde, and G. Santarelli, “Prototype of an ultra-stable optical cavity for space applications”, *Optics Express* **20**, 25409–25420 (2012).
- <sup>230</sup>H. B. Callen and T. A. Welton, “Irreversibility and generalized noise”, *Physical Review* **83**, 34–40 (1951).
- <sup>231</sup>H. B. Callen and R. F. Greene, “On a Theorem of Irreversible Thermodynamics”, *Physical Review* **86**, 702–710 (1952).
- <sup>232</sup>K. Numata, A. Kemery, and J. Camp, “Thermal-Noise Limit in the Frequency Stabilization of Lasers with Rigid Cavities”, *Physical Review Letters* **93**, 250602 (2004).
- <sup>233</sup>J. Dickmann, L. S. Neto, M. Gaedtke, and S. Kroker, “Levitating the noise performance of ultra-stable laser cavities assisted by a deep neural network: the non-intuitive role of the mirrors”, EN, *Optics Express* **31**, Publisher: Optica Publishing Group, 15953–15965 (2023).

- <sup>234</sup>T. Kessler, T. Legero, and U. Sterr, “Thermal noise in optical cavities revisited”, [Journal of the Optical Society of America B](#) **29**, 178–184 (2012).
- <sup>235</sup>G. M. Harry, A. M. Gretarsson, P. R. Saulson, S. E. Kittelberger, S. D. Penn, W. J. Startin, S. Rowan, M. M. Fejer, D. R. M. Crooks, G. Cagnoli, J. Hough, and N. Nakagawa, “Thermal noise in interferometric gravitational wave detectors due to dielectric optical coatings”, [Classical and Quantum Gravity](#) **19**, 897 (2002).
- <sup>236</sup>F. Bondu, P. Hello, and J.-Y. Vinet, “Thermal noise in mirrors of interferometric gravitational wave antennas”, [Physics Letters A](#) **246**, 227–236 (1998).
- <sup>237</sup>Y. Levin, “Internal thermal noise in the LIGO test masses: A direct approach”, [Physical Review D](#) **57**, 659–663 (1998).
- <sup>238</sup>N. Nakagawa, A. M. Gretarsson, E. K. Gustafson, and M. M. Fejer, “Thermal noise in half infinite mirrors with nonuniform loss: A Slab of excess loss in a half infinite mirror”, [Phys. Rev. D](#) **65**, 102001 (2002).
- <sup>239</sup>S. Herbers, S. Häfner, S. Häfner, S. Dörscher, T. Lücke, U. Sterr, and C. Lisdat, “Transportable clock laser system with an instability of  $1.6 \times 10^{-16}$ ”, EN, [Optics Letters](#) **47**, Publisher: Optica Publishing Group, 5441–5444 (2022).
- <sup>240</sup>V. B. Braginsky, M. L. Gorodetsky, and S. P. Vyatchanin, “Thermodynamical fluctuations and photothermal shot noise in gravitational wave antennae”, [Phys. Lett. A](#) **264**, 1 (1999).
- <sup>241</sup>M. Gorodetsky, “Thermal noises and noise compensation in high-reflection multi-layer coating”, [Physics Letters, Section A: General, Atomic and Solid State Physics](#) **372**, 10.1016/j.physleta.2008.09.056 (2008).
- <sup>242</sup>H. J. Kimble, B. L. Lev, and J. Ye, “Optical interferometers with reduced sensitivity to thermal noise”, [Phys. Rev. Lett.](#) **101**, 260602 (2008).
- <sup>243</sup>M. Evans, S. Ballmer, M. Fejer, P. Fritschel, G. Harry, and G. Ogin, “Thermo-optic noise in coated mirrors for high-precision optical measurements”, [Phys. Rev. D](#) **78**, 102003 (2008).
- <sup>244</sup>V. Braginsky, M. Gorodetsky, and S. Vyatchanin, “Thermo-refractive noise in gravitational wave antennae”, [Physics Letters A](#) **271**, 303–307 (2000).
- <sup>245</sup>E. D. Black, A. Villar, and K. G. Libbrecht, “Thermoelastic-damping noise from sapphire mirrors in a fundamental-noise-limited interferometer”, [Phys. Rev. Lett.](#) **93**, 241101 (2004).
- <sup>246</sup>E. D. Black, A. Villar, K. Barbary, A. Bushmaker, J. Heefner, S. Kawamura, F. Kawazoe, L. Matone, S. Meidt, S. R. Rao, K. Schulz, M. Zhang, and K. G. Libbrecht, “Direct observation of broadband coating thermal noise in a suspended interferometer”, [Physics Letters A](#) **328**, 1–5 (2004).
- <sup>247</sup>T. Chalermongsak, F. Seifert, E. D. Hall, K. Arai, E. K. Gustafson, and R. X. Adhikari, “Broadband measurement of coating thermal noise in rigid fabry–pérot cavities”, [Metrologia](#) **52**, 17 (2014).



- <sup>248</sup>T. Chalermongsak, E. D. Hall, G. D. Cole, D. Follman, F. Seifert, K. Arai, E. K. Gustafson, J. R. Smith, M. Aspelmeyer, and R. X. Adhikari, “Coherent cancellation of photothermal noise in GaAs/Al<sub>0.92</sub>Ga<sub>0.08</sub>As bragg mirrors”, [Metrologia](#) **53**, 860 (2016).
- <sup>249</sup>M. M. Fejer, S. Rowan, G. Cagnoli, D. R. M. Crooks, A. Gretarsson, G. M. Harry, J. Hough, S. D. Penn, P. H. Sneddon, and S. P. Vyatchanin, “Thermoelastic dissipation in inhomogeneous media: loss measurements and displacement noise in coated test masses for interferometric gravitational wave detectors”, [Phys. Rev. D](#) **70**, 082003 (2004).
- <sup>250</sup>M. Cerdonio, L. Conti, A. Heidmann, and M. Pinard, “Thermoelastic effects at low temperatures and quantum limits in displacement measurements”, [Physical Review D](#) **63**, 082003 (2001).
- <sup>251</sup>Y. T. Liu and K. Thorne, “Thermoelastic noise and homogeneous thermal noise in finite sized gravitational-wave test masses”, [Physical Review D](#) **62**, 10.1103/PhysRevD.62.122002 (2000).
- <sup>252</sup>C. J. Hood, H. J. Kimble, and J. Ye, “Characterization of high-finesse mirrors: loss, phase shifts, and mode structure in an optical cavity”, [Phys. Rev. A](#) **64**, 033804 (2001).
- <sup>253</sup>A. Farsi, M. Cumis, F. Marino, and F. Marin, “Photothermal and thermo-refractive effects in high reflectivity mirrors at room and cryogenic temperature”, [Journal of Applied Physics](#) **111**, 043101 (2012).
- <sup>254</sup>M. De Rosa, F. Marin, F. Marino, O. Arcizet, A. Heidmann, and M. Pinard, “Experimental investigation of dynamic photo-thermal effect”, [Classical and Quantum Gravity](#) **23**, S259 (2006).
- <sup>255</sup>U. Sterr and C. Lisdat, “Millihertz-linewidth lasers: A sharper laser”, [Nature Physics](#) **5**, 382–383 (2009).
- <sup>256</sup>I. Ito, A. Silva, T. Nakamura, and Y. Kobayashi, “Stable CW laser based on low thermal expansion ceramic cavity with 4.9 mHz/s frequency drift”, [EN, Optics Express](#) **25**, 26020–26028 (2017).
- <sup>257</sup>B. Edlén, “The Refractive Index of Air”, [Metrologia](#) **2**, 71–80 (1966).
- <sup>258</sup>J. Yu, “Cryogenic silicon Fabry-Perot resonator with Al<sub>0.92</sub>Ga<sub>0.08</sub>As/GaAs mirror coatings”, en, PhD Thesis (Leibniz Universität Hannover, 2023).
- <sup>259</sup>J. Yu, D. Kedar, S. Häfner, T. Legero, F. Riehle, S. Herbers, D. Nicolodi, C. Y. Ma, J. M. Robinson, E. Oelker, J. Ye, and U. Sterr, *Excess noise in highly reflective crystalline mirror coatings*, arXiv:2210.15671 [astro-ph, physics:physics], Oct. 2022.
- <sup>260</sup>T. Legero, T. Kessler, and U. Sterr, “Tuning the thermal expansion properties of optical reference cavities with fused silica mirrors”, [JOSA B](#) **27**, 914–919 (2010).
- <sup>261</sup>G. D. Cole, W. Zhang, M. J. Martin, J. Ye, and M. Aspelmeyer, “Tenfold reduction of Brownian noise in high-reflectivity optical coatings”, en, [Nature Photonics](#) **7**, 644–650 (2013).



- <sup>262</sup>G. D. Cole, W. Zhang, B. J. Bjork, D. Follman, P. Heu, C. Deutsch, L. Sonderhouse, J. Robinson, C. Franz, A. Alexandrovski, M. Notcutt, O. H. Heckl, J. Ye, and M. Aspelmeyer, “High-performance near- and mid-infrared crystalline coatings”, en, [Optica](#) **3**, 647 (2016).
- <sup>263</sup>G. D. Cole, S. Ballmer, G. Billingsley, S. B. Cataño-Lopez, M. Fejer, P. Fritschel, A. M. Gretarsson, G. M. Harry, D. Kedar, T. Legero, C. Makarem, S. D. Penn, D. Reitze, J. Steinlechner, U. Sterr, S. Tanioka, G.-W. Truong, J. Ye, and J. Yu, *Substrate-transferred GaAs/AlGaAs crystalline coatings for gravitational-wave detectors: A review of the state of the art*, arXiv:2301.02687 [astro-ph, physics:physics], Jan. 2023.
- <sup>264</sup>E. A. Klocke, “Design und Charakterisierung eines Breadboards zur Laserfrequenzverteilung mit relativen Instabilitäten von unter  $10^{-16}$  in einer transportablen optischen Uhr”, de, MA thesis (Leibniz Universität Hannover, Hannover, 2020).
- <sup>265</sup>D. Babic and S. Corzine, “Analytic expressions for the reflection delay, penetration depth, and absorptance of quarter-wave dielectric mirrors”, [Quantum Electronics, IEEE Journal of](#) **28**, 514–524 (1992).
- <sup>266</sup>S. Herbers, *Private communication* (2023).
- <sup>267</sup>R. W. Fox, “Fabry-Perot temperature dependence and surface-mounted optical cavities”, in Proc. SPIE, Vol. 7099 (2008).
- <sup>268</sup>X. Dai, Y. Jiang, C. Hang, Z. Bi, and L. Ma, “Thermal analysis of optical reference cavities for low sensitivity to environmental temperature fluctuations”, [Optics Express](#) **23**, 5134–5146 (2015).
- <sup>269</sup>J. Zhang, Y. Luo, B. Ouyang, K. Deng, Z. Lu, and J. Luo, “Design of an optical reference cavity with low thermal noise limit and flexible thermal expansion properties”, en, [The European Physical Journal D](#) **67**, 1–9 (2013).
- <sup>270</sup>W. Wei, X. Qi, H. Deng, L. Shang, Y. Zhang, and H. Liu, “Determination of the coefficient of thermal expansion of ultra-low-expansion glass using an ultrasonic immersion testing method”, [Appl. Opt.](#) **62**, 3347–3356 (2023).
- <sup>271</sup>C. Weigel, V. Cherkasova, M. Holz, H. B. Phi, C. Görner Tenorio, B. Wilbertz, L. Voßgrag, T. Fröhlich, and S. Strehle, “Ultralow expansion glass as material for advanced micromechanical systems”, [Advanced Engineering Materials](#) **25**, 2201873 (2023).
- <sup>272</sup>S. Herbers, S. Dörscher, E. Benkler, and C. Lisdat, “Phase noise of frequency doublers in optical clock lasers”, [Opt. Express](#) **27**, Publisher: OSA, 23262–23273 (2019).
- <sup>273</sup>H. Schröder, P. Wagner, D. Kokkinos, W. Riede, and A. Tighe, “Laser-induced contamination and its impact on laser damage threshold”, in [Laser-Induced Damage in Optical Materials: 2013](#), Vol. 8885 (Nov. 2013), 88850R.
- <sup>274</sup>T. W. Hänsch and B. Couillaud, “Laser frequency stabilization by polarization spectroscopy of a reflecting reference cavity”, [Optics Communications](#) **35**, 441–444 (1980).
- <sup>275</sup>A. Yariv, *Quantum Electronics*, Englisch, 3rd ed. (John Wiley & Sons, New York, Jan. 1989).

- <sup>276</sup>G. D. Boyd, A. Ashkin, J. M. Dziedzic, and D. A. Kleinman, “Second-harmonic generation of light with double refraction”, *Phys. Rev.* **137**, Publisher: American Physical Society, A1305–A1320 (1965).
- <sup>277</sup>M. M. Fejer, G. A. Magel, D. H. Jundt, and R. L. Byer, “Quasi-phase-matched second harmonic generation: tuning and tolerances”, *Quantum Electronics, IEEE Journal of* **28**, 2631–2654 (1992).
- <sup>278</sup>G. D. Boyd and D. A. Kleinman, “Parametric interaction of focused gaussian light beams”, *Journal of Applied Physics* **39**, eprint: <https://doi.org/10.1063/1.1656831>, 3597–3639 (1968).
- <sup>279</sup>K. R. Parameswaran, J. R. Kurz, R. V. Roussev, and M. M. Fejer, “Observation of 99% pump depletion in single-pass second-harmonic generation in a periodically poled lithium niobate waveguide”, *Optics Letters* **27**, 43–45 (2002).
- <sup>280</sup>M. Iwai, T. Yoshino, S. Yamaguchi, M. Imaeda, N. Pavel, I. Shoji, and T. Taira, “High-power blue generation from a periodically poled MgO:LiNbO<sub>3</sub> ridge-type waveguide by frequency doubling of a diode end-pumped Nd:Y<sub>3</sub>Al<sub>5</sub>O<sub>12</sub> laser”, *Applied Physics Letters* **83**, 3659–3661 (2003).
- <sup>281</sup>S. Sunstov, C. E. Rüter, D. Brüske, and D. Kip, “Watt-level 775 nm SHG with 70% conversion efficiency and 97% pump depletion in annealed/reverse proton exchanged diced PPLN ridge waveguides”, EN, *Optics Express* **29**, Publisher: Optical Society of America, 11386–11393 (2021).
- <sup>282</sup>C.-Y. Cho, J.-Y. Lai, J.-Y. Lai, C.-S. Hsu, Y.-T. Huang, J.-H. Jang, and M.-H. Chou, “Power scaling of continuous-wave second harmonic generation in a MgO:PPLN ridge waveguide and the application to a compact wavelength conversion module”, EN, *Optics Letters* **46**, Publisher: Optical Society of America, 2852–2855 (2021).
- <sup>283</sup>K. A. Fedorova, G. S. Sokolovskii, M. Khomylev, D. A. Livshits, and E. U. Rafailov, “Efficient yellow-green light generation at 561 nm by frequency-doubling of a QD-FBG laser diode in a PPLN waveguide”, *Opt. Lett.* **39**, Publisher: OSA, 6672–6674 (2014).
- <sup>284</sup>J. Sun and C. Xu, “466 mW green light generation using annealed proton-exchanged periodically poled MgO:LiNbO<sub>3</sub> ridge waveguides”, *Optics Letters* **37**, 2028–2030 (2012).
- <sup>285</sup>J. Sun, Y. Gan, and C. Xu, “Efficient green-light generation by proton-exchanged periodically poled MgO:LiNbO<sub>3</sub> ridge waveguide”, *Optics Letters* **36**, 549–551 (2011).
- <sup>286</sup>H. Zhao, K. Sukhoy, J. I T Lima, and A. Major, “Generation of green second harmonic with 60% conversion efficiency from a q-switched microchip laser in mgo:ppln crystal”, *Laser Physics Letters* **9**, 355 (2012).
- <sup>287</sup>F. Pignatiello, M. De Rosa, P. Ferraro, S. Grilli, P. De Natale, A. Arie, and S. De Nicola, “Measurement of the thermal expansion coefficients of ferroelectric crystals by a moiré interferometer”, *Optics Communications* **277**, 14–18 (2007).
- <sup>288</sup>O. Gayer, Z. Sacks, E. Galun, and A. Arie, “Temperature and wavelength dependent refractive index equations for mgo-doped congruent and stoichiometric LiNbO<sub>3</sub>”, *Applied Physics B: Lasers and Optics* **91**, 343–348 (2008).

- <sup>289</sup>L. Deng, X. Gao, Z. Cao, W. Chen, Y. Yuan, W. Zhang, and Z. Gong, “Improvement to sellmeier equation for periodically poled LiNbO<sub>3</sub> crystal using mid-infrared difference-frequency generation”, *Optics Communications* **268**, 110–114 (2006).
- <sup>290</sup>Y. S. Liu, W. B. Jones, and J. P. Chernoch, “High-efficiency high-power coherent uv generation at 266 nm in 90° phase-matched deuterated KDP”, *Applied Physics Letters* **29**, 32–34 (2008).
- <sup>291</sup>*SNLO nonlinear optics code available from A. V. Smith, AS-Photonics, Albuquerque, NM, en-US.*
- <sup>292</sup>S. Ji, S. Zhang, M. Xu, B. Liu, L. Zhu, L. Zhang, X. Xu, Z. Wang, and X. Sun, “Non-critical phase-matching conditions for fourth harmonic generation of DKDP crystal”, *Optical Materials Express* **2**, 735–739 (2012).
- <sup>293</sup>J. Villarroel, J. Carnicero, F. Luedtke, M. Carrascosa, A. García-Cabañes, J. M. Cabrera, A. Alcazar, and B. Ramiro, “Analysis of photorefractive optical damage in lithium niobate: application to planar waveguides”, *Opt. Express* **18**, 20852–20861 (2010).
- <sup>294</sup>M. Aillerie, P. Bourson, M. Mostefa, F. Abdi, and M. D. Fontana, “Photorefractive damage in congruent linbo<sub>3</sub>. part i. zinc doped lithium niobate crystals”, *Journal of Physics: Conference Series* **416**, 012001 (2013).
- <sup>295</sup>J. Sun and C.-q. Xu, “Green-induced infrared absorption in annealed proton-exchanged MgO:LiNbO<sub>3</sub> waveguides”, *J. Opt. Soc. Am. B* **31**, Publisher: OSA, 2779–2785 (2014).
- <sup>296</sup>Z. Lou, K. Han, C. Zhang, M. Chen, B. Yan, Y. Yang, H. Liu, J. Chen, and X. Li, “The characterization of laser-induced thermal damage mechanism of mid-infrared optical coatings with surface contaminants”, *Physica Scripta* **95**, 035507 (2020).
- <sup>297</sup>M. Schulte, N. Lörch, I. D. Leroux, P. O. Schmidt, and K. Hammerer, “Quantum Algorithmic Readout in Multi-Ion Clocks”, *Physical Review Letters* **116**, 013002 (2016).
- <sup>298</sup>M. Doležal, P. Balling, P. B. R. Nisbet-Jones, S. A. King, J. M. Jones, H. A. Klein, P. Gill, T. Lindvall, A. E. Wallin, M Merimaa, C. Tamm, C. Sanner, N. Huntemann, N. Scharnhorst, I. D. Leroux, P. O. Schmidt, T. Burgermeister, T. E. Mehlstäubler, and E. Peik, “Analysis of thermal radiation in ion traps for optical frequency standards”, en, *Metrologia* **52**, 842 (2015).
- <sup>299</sup>M. Brinkmann, “Design und fabrikation skalierbarer ionenfallen für neuartige anwendungen der quantenmetrologie.”, de, MA thesis (2020).
- <sup>300</sup>T. Ruster, H. Kaufmann, M. A. Luda, V. Kaushal, C. T. Schmiegelow, F. Schmidt-Kaler, and U. G. Poschinger, “Entanglement-Based dc Magnetometry with Separated Ions”, *Physical Review X* **7**, 031050 (2017).
- <sup>301</sup>R. Xiao, Y. Xu, Y. Wang, H. Sun, and Q. Chen, “Transportable 30 cm optical cavity based ultrastable lasers with beating instability of  $2 \times 10^{-16}$ ”, en, *Applied Physics B* **128**, 220 (2022).

## List of publications

- **B. Kraus**, F. Dawel, S. Hannig, J. Kramer, C. Nauk, and P. O. Schmidt: Phase-stabilized UV light at 267 nm through twofold second harmonic generation.



# Curriculum vitae

## PERSONAL DETAILS

Name	Benjamin Kraus
Date of birth	12.08.1991
Place of birth	Speyer, Germany

## POSTGRADUATE STUDIES

Since 2019	Doctoral studies at the QUEST Institute for Experimental Quantum Metrology, PTB and Leibniz Universität Hannover, Braunschweig, Germany
2018	Master of Science from Universität Heidelberg, Germany
2016-2018	Master student of physics at Universität Heidelberg, Germany

## UNDERGRADUATE STUDIES

2016	Bachelor of Science from Universität Heidelberg, Germany
2013-2016	Bachelor student of physics at Universität Heidelberg, Germany

## FORMAL EDUCATION

2013	Fachgebundene Hochschulreife from Carl-Engler Schule Karlsruhe, Germany
2011-2013	Carl-Engler Schule Karlsruhe, Germany

## PROFESSIONAL EDUCATION

2011	Completed vocational training as a mechatronics technician
2008-2011	SEW-Eurodrive Graben Neudorf, Germany